İbrahim Deneme

A Ph.D. Thesis

AGU 2024

DEVELOPMENT OF NOVEL FUNCTIONAL ORGANIC MATERIALS FOR OPTOELECTRONIC APPLICATIONS

A THESIS
SUBMITTED TO THE DEPARTMENT OF MATERIALS SCIENCE
AND MECHANICAL ENGINEERING
AND THE GRADUATE SCHOOL OF ENGINEERING AND SCIENCE
OF ABDULLAH GUL UNIVERSITY
IN PARTIAL FULFILLMENT OF THE REQUIREMENTS
FOR THE DEGREE OF
DOCTOR OF PHILOSOPHY

By
İbrahim Deneme
December 2024

DEVELOPMENT OF NOVEL FUNCTIONAL ORGANIC MATERIALS FOR OPTOELECTRONIC APPLICATIONS

A THESIS
SUBMITTED TO THE DEPARTMENT OF MATERIALS SCIENCE AND MECHANICAL ENGINEERING
AND THE GRADUATE SCHOOL OF ENGINEERING AND SCIENCE OF ABDULLAH GUL UNIVERSITY
IN PARTIAL FULFILLMENT OF THE REQUIREMENTS
FOR THE DEGREE OF
DOCTOR OF PHILOSOPHY

By
İbrahim Deneme
December 2024

SCIENTIFIC ETHICS COMPLIANCE

I hereby declare that all information in this document has been obtained in accordance with academic rules and ethical conduct. I also declare that, as required by these rules and conduct, I have fully cited and referenced all materials and results that are not original to this work.

Name-Surname: İbrahim Deneme

Signature:

REGULATORY COMPLIANCE

Ph.D. thesis titled Development of Novel Functional Organic Materials for Optoelectronic Applications has been prepared in accordance with the Thesis Writing Guidelines of the Abdullah Gül University, Graduate School of Engineering & Science.

Prepared By	Advisor
İbrahim Deneme	Prof. Dr. Hakan Usta

Head of the Materials Science and Mechanical Engineering Program
Assist. Prof. Zeliha Soran Erdem

ACCEPTANCE AND APPROVAL

Ph.D. thesis titled Development of Novel Functional Organic Materials for Optoelectronic Applications and prepared by İbrahim Deneme has been accepted by the jury in the Materials Science and Mechanical Engineering Graduate Program at Abdullah Gül University, Graduate School of Engineering & Science.

25 /12 /2024

(Thesis Defense Exam Date)

JURY:

Advisor : (Prof. Dr. Hakan Usta)

Member : (Prof. Dr. Gökhan Demirel)

Member : (Asst. Prof. Fahri Alkan)

Member : (Prof. Dr. M. Serdar Önses)

Member : (Prof. Dr. Mehmet Şahin)

APPROVAL:

The acceptance of this Ph.D. thesis has been approved by the decision of the Abdullah Gül University, Graduate School of Engineering & Science, Executive Board dated ….. /….. / …….. and numbered ……..…… .

…….. /…….. / ……..

(Date)

Graduate School Dean
Prof. Dr. İrfan ALAN

ABSTRACT

DEVELOPMENT OF NOVEL FUNCTIONAL ORGANIC MATERIALS FOR OPTOELECTRONIC APPLICATIONS

İbrahim Deneme
Ph.D. in Materials Science and Mechanical Engineering
Advisor: Prof. Dr. Hakan Usta

December 2024

In the first chapter, we review the historical and recent advances in the design and proposal of organic semiconductors and their (opto)electronic applications. In the second chapter of this thesis, we discovered the nanostructured film construction and Raman signal enhancement capabilities of a π-electron deficient low-LUMO BTBT molecule, 1,10-(benzo[b]benzo[4,5]thieno[2,3-d]thiophene-2,7-diyl)bis(octan-1-one) **(D(C$_7$CO)-BTBT)**, which includes 2,7-dicarbonyl functionalization along with n-heptyl (-n-C_7H_{15}) substituents. This molecule is arranged on the gram-scale in ambient via simplistic Friedel-Crafts acylation and precipitation/solvent washing without demanding any high-cost transition-metal catalyst and monotonous chromatographic/sublimation-based purification. In the third chapter of this thesis, we demonstrated the Hansen solubility approach to study the solubility behavior of an ambient-stable *n*-type semiconductor, 2,2'-(2,8-bis(3-dodecylthiophen-2-yl)indeno[1,2-b]fluorene-6,12-diylidene)dimalononitrile (**β,β'-C$_{12}$-TIFDMT**), and to analyze potential green solvents for thin-film processing. In the fourth chapter of this thesis, present a unique molecular engineering on the BTBT π-system by employing *mono*-(aryl)carbonyl functionalization with one hexyl (*n*-C_6H_{13}) substituent, and demonstrate the design, synthesis, and characterization of a new asymmetric BTBT semiconductor, ***m*-C$_6$PhCO-BTBT**. The new molecule was produced in gram-scale through a two-step transition-metal-free synthesis, and the detailed structural, physicochemical, and (opto)electronic characterizations were performed.

Keywords: Organic Semiconductor, Small Molecule, P-type (hole transporting), Surface Enhanced Raman Spectroscopy(SERS) , Organic Field Effect Transistors (OFETs).

ÖZET

OPTOELEKTRONİK UYGULAMALAR İÇİN YENİ FONKSİYONEL ORGANİK MALZEMELERİN GELİŞTİRİLMESİ

İbrahim Deneme

Malzeme Bilimi ve Makine Mühendisliği Anabilim Dalı Doktora
Tez Yöneticisi: Prof. Dr. Hakan Usta

Aralık 2024

İlk bölümde, organik yarı iletkenlerin tasarımı ve uygulanmasındaki ve bunların (opto)elektronik uygulamalarındaki tarihsel ve güncel gelişmeleri gözden geçiriyoruz. Bu tezin ikinci bölümünde, π-elektron eksikliği olan düşük LUMO'lu bir **BTBT** molekülü olan 1,10-(benzo[b]benzo[4,5]thieno[2, 3-d]tiyofen-2,7-diil)bis(oktan-1-on) **(D(C$_7$CO)-BTBT)**, ki bu, n-heptil (-n-C_7H_{15}) süpstitüe edicileri ile birlikte 2,7-dikarbonil fonksiyonel grupları içeren bu molekül, herhangi bir yüksek maliyetli geçiş metali katalizörü ve uğraştırıcı kromatografik/süblimasyon bazlı saflaştırma gerektirmeden, kolay Friedel-Crafts asilasyonu ve çökeltme/çözücü yıkama yoluyla, hava ortamında gram ölçeğinde hazırlanmıştır. Bu tezin üçüncü bölümünde, ortam kararlı bir n-tipi yarı iletken olan 2,2'-(2,8-bis(3-dodesiltiofen-2-il)indeno[1,2-b]floren-6,12-diyliden)dimalononitrilin **(β,β'-C$_{12}$-TIFDMT)** çözünürlük davranışını incelemek ve ince film işleme için potansiyel yeşil çözücüleri analiz etmek için Hansen çözünürlük yaklaşımını gösterdik. Bu tezin dördüncü bölümünde, bir heksil (n-C_6H_{13}) sübstitüenti ile mono-(aril)karbonil fonksiyonelleştirmesi kullanılarak **BTBT** π-sistemi üzerinde benzersiz bir moleküler mühendislik sunulmuş ve yeni bir asimetrik BTBT yarı iletkeni olan ***m*-C$_6$PhCO-BTBT'nin** tasarımı, sentezi ve karakterizasyonu gösterilmiştir. Yeni molekül, iki aşamalı geçiş metali içermeyen bir sentez yoluyla gram ölçeğinde üretildi ve (opto) elektronik karakterizasyonlar gerçekleştirildi.

Anahtar kelimeler: Organik yarıieletken, Küçük Molekül, P-Tipi (boşluk taşıma), Yüzeyi geliştirilmiş Raman spektroskopisi(SERS), Organik Alan Etkili Transistörler(OFET).

Acknowledgements

I would like to take a moment to thank everyone who helped me along with this long journey.

First, I wish to express my sincere gratitude to my advisor, Prof. Hakan Usta, for his patience and continuous support of my Ph.D study. He has such immense knowledge which helped me in all the time of research. His enthusiasm and passion for science have made an intense impact on my life. My Ph.D study would not have been possible without his supervision, motivation and inspiration.

I would like to thank my thesis committee: Prof. Gökhan Demirel and Asst. Prof. Fahri Alkan, Prof. Dr. Mustafa Serdar Önses and Prof. Dr. Mehmet Şahin for their insights and hard questions which helped me to widen my research vision from different perspectives. Without their feedback, I would not have made it.

I thank my fellow labmates in Usta Research Group, Asst. Prof. Resul Özdemir, Ayça Yıldız, and Nilgün Kayacı: for their help and supports during my lab sessions and for their kind friendships.

My sincere and endless thanks to my lovely parents, my mom, my dad and my sister who believe in me and always encourage me to reach my goals.

Finally, to my caring, loving and supportive wife, Erinç, and my cheerful son, Ömer Tuna: your love and endless support helped me through the tough times. Without you guys, I would not have made it. It is time to celebrate; you earned this degree right along with me.

This Ph.D study was supported by the Scientific and Technological Research Council of Turkey (TUBITAK), grant number of 121C261.

TABLE OF CONTENTS

LIST OF FIGURES

LIST OF TABLES

LIST OF ABBREVIATIONS

AFM	Atomic Force Microscopy
BTBT	[1]benzothieno[3,2-b][1]benzothiophene
DSC	Differential Scanning Calorimetry
GIXD	Grazing Incidence X-ray Diffraction
HOMO	Highest Occupied Molecular Orbital
LUMO	Lowest Unoccupied Molecular Orbital
N-Type	Electron Transporting Semiconductor
OFETs	Organic Fiel Effect tTransistors
P-Type	Hole Transporting Semiconductor
PVD	Physical Vapor Deposition
TGA	Thermogravimetric Analysis

Chapter 1

Introduction

The discovery of conductive polymers in the 1970s marked a significant turning point in the field of materials science and electronics. Prior to this discovery, plastics were primarily known for their insulating properties, making them ideal for a wide range of applications requiring electrical isolation. However, the breakthrough in conductive polymers, particularly with the discovery that certain carbon-based materials could achieve levels of electrical conductivity comparable to metals when doped with halogens, opened up a new realm of possibilities. The recognition of the potential of these materials sparked widespread interest among researchers in both academia and industry. This led to the emergence of a new research field known as "organic electronics," which explores the development and application of electronic devices based on organic materials, including conductive polymers. In 2000, this groundbreaking work was honored with the Nobel Prize in Chemistry, awarded to Alan J. Heeger, Alan G. MacDiarmid, and Hideki Shirakawa for their contributions to the discovery and development of conductive polymers. Their work not only expanded our understanding of the fundamental properties of materials but also paved the way for innovations in various fields, including electronics, energy storage, and biomedical devices.

The term "organic" in organic electronics refers to the use of carbon-based polymers and small molecules as active semiconducting materials. While silicon has long been the cornerstone of microelectronics due to its exceptional properties, including its abundance and usefulness, the high infrastructure and fabrication costs

associated with silicon-based technology can limit its applicability in certain contexts. Organic semiconductors offer several advantages over silicon, making them attractive alternatives in various applications. Their low fabrication costs, compatibility with flexible plastic substrates, ability for large area coverage, and flexibility are particularly advantageous. Moreover, organic semiconductors boast facile synthesis methods and, crucially, exhibit tunable physicochemical and optoelectronic properties, allowing for customization based on specific application requirements. These characteristics make organic semiconductors particularly well-suited for applications where silicon may not be feasible or cost-effective, such as flexible electronics, wearable devices, large-area displays, and organic photovoltaics. As research and development in the field of organic electronics continue to advance, we can expect to see even more innovative applications emerge, further expanding the realm of possibilities for electronic devices.

It's fascinating to envision the potential impact of organic electronic technologies on our daily lives, particularly in the realm of RFID and other applications. Radio Frequency Identification (RFID) holds great promise for streamlining processes such as checkout in retail settings, eliminating the need to individually scan items and significantly speeding up the shopping experience. The ability of RFID tags to provide real-time information, such as expiration dates on perishable items, could revolutionize inventory management and consumer convenience. Moreover, the integration of organic electronic materials into everyday objects opens up a wealth of possibilities. Imagine foldable electronic papers that function like traditional newspapers but are lightweight, portable, and easily customizable. These could offer a sustainable and convenient alternative to printed media. Additionally, wearable polymer solar cells could provide a novel way to charge devices on the go, harnessing energy from ambient light sources to power electronics such as smartphones. This could offer greater flexibility and freedom for users, reducing dependence on traditional charging methods. Key advancements in organic electronic technologies, including Organic Complementary Metal Oxide Semiconductor (OCMOS) (Figure 1.1), Organic Field Effect Transistors (OFETs), Organic Photovoltaics (OPVs), and Organic Light-Emitting Diodes (OLEDs), are driving these innovations forward. These technologies have made significant strides in recent years, paving the way for practical applications in various fields, from consumer electronics to healthcare and beyond. As these technologies continue to mature and become more widespread, we can expect to see a proliferation of organic electronic

devices and systems that enhance our daily lives in ways we may not yet fully appreciate. The future of electronics is exciting, with organic materials playing a central role in shaping the next generation of innovative technologies.

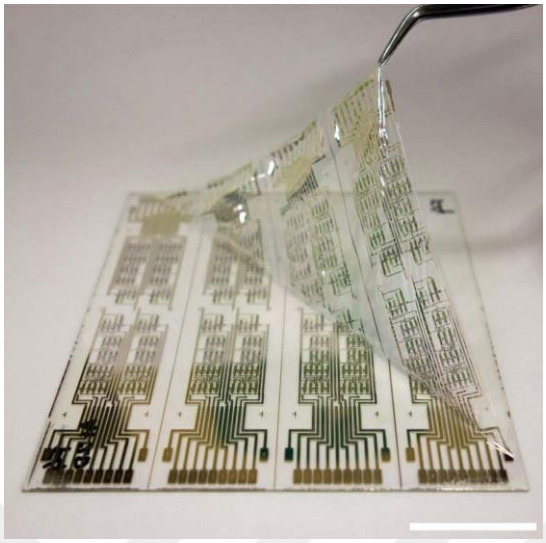

Figure 1.1 Photograph of organic CMOS logic circuit on a one-micron-thick (μm) substrate. The total thickness is less than 3 μm. Scale bar, 25 mm.[3]

Organic Field-Effect Transistors (OFETs) have been the focus of research for quite some time due to their potential applications in flexible and low-cost electronics. However, in recent years, there has been a notable increase in industrial interest in OFETs, primarily driven by advancements in new organic semiconductor materials that exhibit higher charge carrier mobility compared to traditional amorphous silicon-based (a-Si) materials.[4]

Inorganic semiconductors such as silicon (Si), germanium (Ge), and gallium arsenide (GaAs) have long been the cornerstone of modern electronics, particularly in the form of Metal Oxide Semiconductor Field Effect Transistors (MOSFETs), which are integral components of microprocessors and other semiconductor devices.

Today, inorganic crystals like doped silicon and gallium arsenide have demonstrated exceptional hole mobility, with values exceeding 1000 cm^2/Vs at room temperature. This high mobility is crucial for achieving high-performance electronic devices, such as those found in microprocessors and high-speed communication systems. However, despite their impressive performance characteristics, inorganic semiconductors have limitations, particularly in terms of manufacturing processes and compatibility with flexible substrates. The high-temperature manufacturing processes required for inorganic semiconductor fabrication are not conducive to large-area

coverage or compatibility with plastic substrates, which hinders the development of flexible and lightweight electronics. On the other hand, thermally evaporated amorphous silicon thin films are commonly used for applications such as active matrix addressing in displays. While these films offer the advantage of compatibility with corresponding substrates and lower-temperature processing compared to crystalline silicon, they typically exhibit lower hole mobility, ranging from 0.1 to 1 cm^2/Vs. The limitations of inorganic semiconductors in terms of manufacturing processes and substrate compatibility have fueled interest in organic semiconductors, which offer advantages such as lower fabrication costs, compatibility with flexible substrates, and tunable properties. Organic electronics, including Organic Field-Effect Transistors (OFETs), Organic Photovoltaics (OPVs), and Organic Light-Emitting Diodes (OLEDs), hold promise for realizing large-area covered electronics and flexible devices, paving the way for the development of next-generation electronics with enhanced functionality and form factors.

The journey of Organic Field-Effect Transistors (OFETs) has seen significant progress since their inception in the late 1980s.[5] The first OFETs, based on polythiophene as the semiconducting material, demonstrated promising characteristics but suffered from relatively low charge carrier mobility, around $\sim 10^{-5}$ cm^2/Vs. Since then, there has been remarkable improvement in the electronic performance of OFETs, driven by advancements in materials design, device fabrication techniques, and understanding of device physics (Figure 1.2). Researchers have explored a wide range of polymeric and molecular semiconductors, as well as engineering strategies to enhance charge transport within the transistor channel. Today, OFETs with charge carrier mobility approaching the performance of amorphous silicon-based transistors have been achieved.[4] This achievement represents a significant milestone in the development of organic electronics, as it brings these devices closer to practical applications in various fields, including flexible displays, sensors, and integrated circuits. The continuous improvement in the electronic performance of OFETs underscores the potential of organic semiconductors as viable alternatives to traditional inorganic materials. As research in this field continues to advance, we can expect further enhancements in device performance and the realization of even more sophisticated organic electronic devices with a wide range of functionalities.

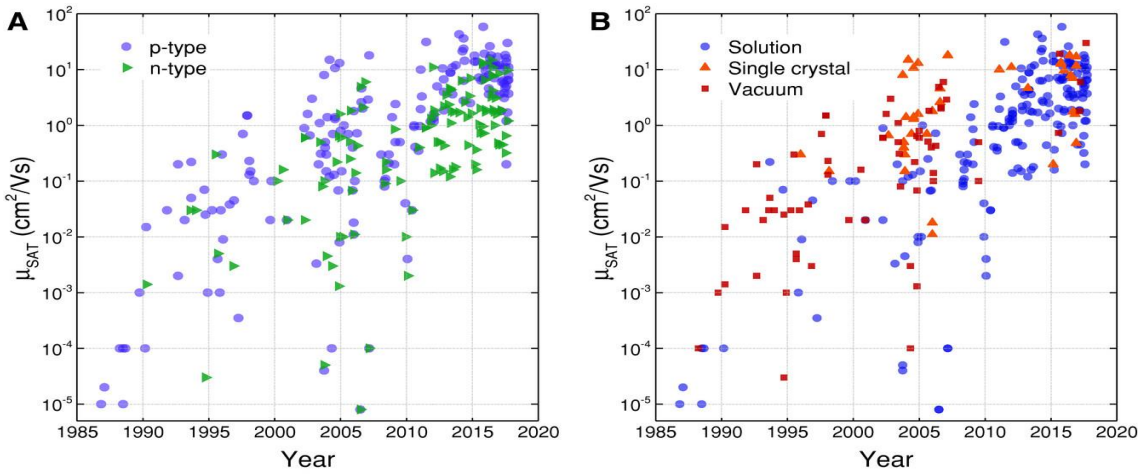

Figure 1.2 Plots of field-effect carrier mobility values over time. The data has been separated into the following categories: a) Charge carrier type: p-type and n-type. b) Processing technique: solution processed, single crystal, and vacuum.[6]

Particularly in the field of organic electronics, here are some important advantages of using carbon-based materials as active components in Field Effect Transistors (FETs). Large Area Coverage: Carbon-based materials, such as organic semiconductors, can be processed into thin films using solution-based techniques like spin-coating and inkjet printing. These methods enable the fabrication of transistors over large areas, making them suitable for applications where conventional inorganic semiconductors may be impractical due to size limitations. Flexibility and Mechanical Properties: Organic semiconductors offer superior mechanical properties and flexibility compared to traditional inorganic materials. This flexibility, combined with the compatibility of carbon-based materials with plastic substrates, enables the development of flexible and bendable electronic devices. This is particularly advantageous for applications such as wearable electronics and flexible displays. Low-Temperature Fabrication: Unlike many inorganic semiconductors, carbon-based materials do not require high-temperature fabrication processes. This significantly reduces the manufacturing costs associated with electronic devices, making them more cost-effective to produce. Additionally, the lower processing temperatures open up the possibility of using a wider range of substrates, including flexible plastics.

While these advantages are clear, determining the precise cost of carbon-based electronic devices can be challenging. The cost calculation would involve factors such as material costs, fabrication process complexity, yield rates, and market demand. Given the rapid pace of research and development in organic electronics, as well as

ongoing improvements in manufacturing techniques, it may be difficult to provide a definitive cost analysis at this time. However, as the technology matures and production processes become more optimized, the cost of carbon-based electronic devices is expected to become more predictable and competitive with traditional semiconductor technologies.

The roll-to-roll (R2R) production process holds tremendous potential for the large-scale manufacturing of electronic devices, particularly those based on organic electronics such as Organic Field-Effect Transistors (OFETs) (Figure 1.3). Unlike traditional batch processing methods, R2R production enables continuous and high-throughput fabrication of electronic circuits on flexible substrates, such as plastic films, at a significantly lower cost. OFETs offer several advantages for R2R production, including compatibility with flexible substrates, low-temperature processing requirements, and the ability to print circuits using solution-based techniques like inkjet printing or roll-to-roll printing. This makes them well-suited for integration into complex micro-systems and low-cost applications, including RFID tags, smart cards, and flexible displays. Replacing conventional pixel driver circuits in Liquid Crystal Displays (LCDs) with OFET-based circuits not only opens up new possibilities for flexible display technologies but also paves the way for the widespread adoption of RFID tags and smart cards in our daily lives. These advancements in manufacturing processes and materials deposition techniques are driving the transition towards more flexible, lightweight, and cost-effective electronic devices, ushering in a new era of ubiquitous and interconnected smart systems.

Figure 1.3 Example of a roll-to-roll coated OPV device on a PET foil (Polyethylene Terephthalate) substrate.[7]

Organic materials typically exhibit weak intermolecular interactions, primarily Van der Waals forces, which can result in poor self-organization in the solid state. As a result, the final morphology and microstructure of organic thin films are highly dependent on the fabrication technique used. Solution-processed thin films, such as those produced via spin-coating or inkjet printing, often exhibit poorly ordered structures due to the random arrangement of molecules during film deposition. In contrast, vacuum deposition techniques, such as thermal evaporation or sputtering, can produce well-organized thin films with a more uniform molecular arrangement. However, achieving high-performance Field-Effect Transistors (FETs) with large-area coverage requires a delicate balance between favorable solid-state packing and good solubility in common organic solvents. Ideally, the organic semiconductor materials should be capable of forming ordered structures in the solid state to facilitate efficient charge transport while also being soluble in organic solvents to enable solution-based processing techniques. By optimizing both the material properties and fabrication processes, it is possible to achieve high-performance FETs with large-area coverage, paving the way for the realization of next-generation organic electronic devices with enhanced functionality and scalability[7].

Organic electronic systems primarily consisting of carbon, hydrogen, and occasionally other heteroatoms like sulfur, oxygen, or nitrogen, simplifies the integration process and reduces fabrication costs. This uniformity in material composition enables the seamless integration of various components within the same fabrication process, leading to more efficient manufacturing processes and lower overall costs. Ongoing research and development efforts in improving the performance of organic FETs are critical for advancing the commercial viability and widespread adoption of integrated organic electronic systems. By enhancing the performance and reliability of FETs, organic electronic devices can continue to revolutionize various industries and enable innovative applications that leverage the unique properties of organic materials.

Organic Field Effect Transistors (OFETs) operate on principles similar to those of other field-effect transistors, such as Metal-Oxide-Semiconductor Field-Effect Transistors (MOSFETs). Here's a breakdown of the working principles:

Gate Voltage Application: When a voltage is applied to the gate electrode, which is separated from the semiconductor layer by a dielectric material, it creates an electric field. This electric field modulates the conductivity of the semiconductor layer.

Threshold Voltage: Above a certain threshold voltage, typically a few volts, the electric field is strong enough to induce charge carriers (either holes for p-type semiconductors, electrons for n-type semiconductors, or both for ambipolar materials) in the semiconductor layer adjacent to the dielectric.

Channel Formation: The induced charge carriers create a conductive channel, typically 5-10 nanometers thick, in the semiconductor layer beneath the gate electrode. This channel serves as a path for current flow between the source and drain electrodes.

Source-Drain Voltage Application: When a potential difference is applied between the source and drain electrodes, it creates an electric field along the channel. This electric field allows charge carriers to move from the source to the drain, resulting in current flow through the channel.

Controlled Current Flow: By varying the voltage applied to the gate electrode, the conductivity of the channel can be modulated, thereby controlling the current flow between the source and drain electrodes. This allows for the precise regulation of current in OFETs, enabling them to function as switches or amplifiers in electronic circuits.

Overall, OFETs offer flexibility, scalability, and compatibility with flexible substrates, making them promising candidates for a wide range of applications in organic electronics, including displays, sensors, and integrated circuits.

There are several key parameters essential for the electrical characterization of Organic Field-Effect Transistors (OFETs) and their significance in determining device performance:

Charge Carrier Mobility: The charge carrier mobility of an OFET refers to the ability of charge carriers (either holes or electrons) to move through the semiconductor channel in response to an applied electric field. It is a critical parameter that determines the speed at which the transistor can switch on and off, as well as its overall performance in various applications. Average device performance typically falls within the range of 0.01 to 1.0 cm^2/Vs for hole mobility, though higher values are desirable for certain high-performance applications.

Current Modulation Ratio (Ion/Ioff Ratio): The current modulation ratio, often expressed as the Ion/Ioff ratio, measures the ratio of the maximum current when the transistor is turned on (Ion) to the minimum current when it is turned off (Ioff). A high Ion/Ioff ratio indicates good switching behavior and minimal leakage current when the transistor is in the off state. OFETs with Ion/Ioff ratios in the range of 10^5 to 10^6 are considered to have excellent performance for most applications.

Threshold Voltage: The threshold voltage of an OFET is the gate voltage at which the transistor begins to conduct appreciable current. It is a crucial parameter that determines the onset of transistor operation and influences the switching characteristics of the device. Typical threshold voltages for OFETs range from 10 to 40 volts, though lower values are desirable for minimizing power consumption and enhancing device efficiency.

Advancements in the synthesis and fabrication techniques of polymeric and molecular semiconductors are driving improvements in OFET performance. By achieving higher charge carrier mobilities and optimizing device structures, researchers aim to enhance the capabilities of OFETs for a broader range of applications, including analog circuits. Higher charge carrier mobilities enable faster switching speeds and improved device performance, thereby expanding the potential applications of OFETs in areas such as displays, sensors, and integrated circuits.

Here, the basic equations describing the charge carrier mobility (μ) in Field-Effect Transistors (FETs) and its relationship with conductivity (σ) and density of states (n). Let's break down these equations:

Mobility (μ):

The mobility (μ) of charge carriers in a semiconductor material refers to how fast they move in response to an electric field. In the context of FETs, it describes the speed at which electrons or holes travel through the channel when a voltage is applied across the source and drain electrodes.

$$\mu = \frac{V_d}{E} \tag{1.1}$$

Equation (1.1) describes the relationship between mobility, drift velocity (Vd), and electric field (E). It states that mobility is proportional to the ratio of drift velocity to electric field, with the proportionality constant having units of cm^2/Vs.

$$\mu = \frac{\sigma}{n\,e} \tag{1.2}$$

Equation (1.2) relates mobility to conductivity (σ), where n represents the density of charge carriers (electrons or holes) and e is the elementary charge. It shows that mobility is inversely proportional to conductivity, with a higher density of charge carriers leading to lower mobility.

To enhance the performance of Organic Field-Effect Transistors (OFETs), particularly in terms of charge carrier mobility, researchers can focus on either developing novel organic semiconductors or refining device fabrication techniques. Here's a detailed look at both approaches, particularly focusing on the types of organic materials used.

Polymeric semiconductors are long chains of repeating molecular units (monomers) that form π-conjugated systems. They are often processed from solution, which makes them suitable for techniques like spin-coating and inkjet printing. However, they typically exhibit certain limitations. Disordered/Amorphous Thin-Film Morphology, solution-processable polymers often result in thin films with a disordered or amorphous structure, which impedes efficient charge transport and results in poor charge carrier mobility.Secoundly purification challenges. Polymers can have residual extrinsic dopants that are difficult to completely remove, leading to high intrinsic conductivity. This can negatively affect the On/Off (Ion/Ioff) ratio of the transistor, as the off-state current remains undesirably high. Other challenges is batch variability, synthesis of polymeric semiconductors can lead to significant batch-to-batch variations, making it challenging to achieve consistent device performance.

Small molecular semiconductors are composed of relatively low molecular weight compounds with conjugated π-electron systems. They offer several advantages over polymeric semiconductors: High Solubility and Purity, small molecules generally exhibit higher solubility in organic solvents, which facilitates solution processing. Additionally, they can be purified to a high degree, ensuring minimal residual doping. High Degree of Crystallinity, small molecules can form highly ordered crystalline structures, which enhance charge transport and result in higher charge carrier mobility. Reproducibility, small molecules typically exhibit less batch-to-batch variation due to their well-defined molecular structures, leading to more consistent device performance. Scalability, the synthetic processes for small molecules can be more easily controlled and scaled up compared to polymers, which is beneficial for commercial applications.

Beyond material synthesis, advancements in fabrication techniques can significantly impact device performance.For instance, Controlled Deposition Methods: Techniques such as vacuum deposition and epitaxial growth can help in forming highly ordered thin films with minimal defects, which is crucial for achieving high mobility. Optimizing Annealing Processes: Post-deposition thermal annealing can improve the crystallinity and molecular ordering of the thin films, thereby enhancing charge transport properties. Surface Treatment and Interface Engineering: Modifying the surface properties of substrates and optimizing the interfaces between different layers can reduce trap states and improve charge carrier injection and transport. Nanoimprint Lithography and Other Patterning Techniques: These can help in precisely controlling the morphology and structure of the semiconductor layers, leading to better device performance.

By focusing on both the development of novel organic semiconductors and the refinement of fabrication techniques, significant improvements in OFET performance can be achieved. Small molecular π-conjugated systems, in particular, offer promising properties that address many of the limitations associated with polymeric semiconductors. These advances will continue to drive the adoption of OFETs in various applications, including flexible electronics, displays, sensors, and more.

1.1 Organic Materials for Field-Effect Transistors

Molecular and polymeric organic compounds that possess extended π-orbitals and exhibit photophysical and electrical properties typical of semiconductor materials are known as organic semiconductors.[8], [9] π-Conjugation is essential for organic compounds to exhibit semiconducting properties. It involves the overlap of properly aligned p orbitals of sp^2-hybridized atoms in an organic compound with an alternating single and double bond pattern. An example of this is polyacetylene, the simplest π-conjugated semiconducting polymer.(Figure 1.4A). Following this atomic orbital overlapping, a set of π-molecular orbitals is formed, allowing π-electrons to become delocalized over these orbitals due to π-conjugation. The highest occupied molecular orbital (HOMO) and the lowest unoccupied molecular orbital (LUMO) are the frontier π-molecular orbitals, analogous to the valence and conduction band edges in an inorganic semiconductor. (Figure 1.4B) These frontier orbitals are essential for the

optical (e.g., light absorption and emission) and electrical (e.g., charge carrier transport) processes in organic semiconductors. The degree of π-electron delocalization and the arrangement of π-electrons determine the energy levels of the HOMO and LUMO, making them suitable for electronic processes linked to semiconducting properties. This allows the material to absorb and emit visible light and have energy levels compatible with the work function of metal electrodes, enabling the injection of holes or electrons into the frontier orbitals. To provide a general idea about the chemical structure of organic semiconductors, some examples are shown in Figure 1.5. Typically, organic semiconductors consist of fused or linked five- or six-membered ring systems, olefinic, or acetylenic groups. For instance, tetracene is a fused carbocyclic ring system, while terthiophene is a linked heterocyclic ring system. Semiconductors, whether based on inorganic or organic materials, are undeniably among the most crucial advanced materials driving unprecedented advancements in electronics and computer technologies. None of these achievements would have been possible without semiconductor technology. Organic optoelectronic devices, such as organic light-emitting diodes (OLEDs), organic field-effect transistors (OFETs), and organic photovoltaics (OPVs), represent a rapidly growing field. In these devices, π-conjugated organic molecules and polymers serve as the semiconducting layer, thus they are referred to as organic (opto)electronic devices. Advantages of electronic devices containing an electro-active organic layer compared to traditional inorganic-based devices. Cost-effectiveness, devices with electro-active organic layers often utilize cheaper materials and manufacturing processes compared to inorganic-based devices. This can lead to lower production costs and more affordable final products. Lower processing temperatures, organic materials typically have lower processing temperature requirements compared to inorganic materials. This allows for the fabrication of electronic devices on flexible substrates or even plastic, expanding their potential applications. Mechanical flexibility, organic electronic devices can be inherently flexible due to the flexible nature of organic materials. This flexibility enables the development of bendable or stretchable electronic devices, opening up possibilities for wearable electronics, rollable displays, and conformal electronics for various applications. Compatibility with molecular engineering, Organic molecules can be chemically modified with various substitutions, allowing for precise control over their electronic and solid-state properties. This molecular engineering flexibility enables the

design of custom electronic and solid-state structures tailored to specific applications, such as organic light-emitting diodes (OLEDs) or organic photovoltaic cells (OPVs). Overall, electronic devices incorporating electro-active organic layers offer a compelling alternative to conventional inorganic-based devices, thanks to their cost-effectiveness, low-temperature processing, mechanical flexibility, and compatibility with molecular engineering. These advantages make them particularly attractive for applications where traditional electronic devices may be impractical or too costly, such as wearable electronics, flexible displays, and organic electronics.[10]

The semiconducting properties of organic compounds differ significantly from those of conventional inorganic semiconductors. Organic semiconductors behave differently and how their electrical conductivity is achieved, difference in semiconducting properties, organic semiconductors are typically π-conjugated organic compounds, which means they have alternating single and multiple bonds along their molecular backbone. This π-conjugation leads to delocalized electron clouds, giving rise to unique electronic properties compared to inorganic semiconductors. in contrast, conventional inorganic semiconductors, such as silicon or gallium arsenide, rely on the crystalline structure of the material and the movement of charge carriers (electrons or holes) within the crystal lattice. Electrical Conductivity Mechanisms, charge injection via doping, organic semiconductors can achieve electrical conductivity through doping, where charge carriers (electrons or holes) are injected into the material. doping can occur through various methods such as chemical doping (introducing dopant molecules), electrochemical doping (applying a voltage to introduce dopants), or photo-doping (using light to induce doping). These mechanisms highlight the versatility of organic semiconductors in achieving electrical conductivity and their compatibility with various doping techniques and device configurations. Additionally, the ability to tailor organic semiconductor properties through molecular design and synthesis offers opportunities for customizing their electronic behavior for specific applications, such as organic electronics, sensors, and energy devices.[11], [12]

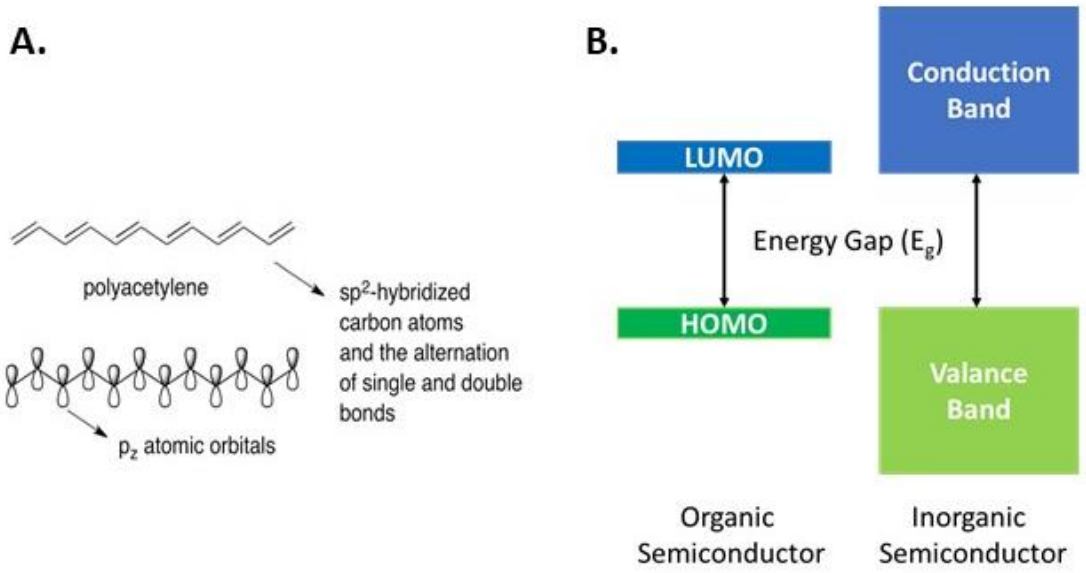

Figure 1.4 (A) The chemical structure of polyacetylene and the formation of π-conjugation along its backbone. (B) The pictorial representation of electronic energy levels of an organic semiconductor and of electron band structure of an inorganic semiconductor.

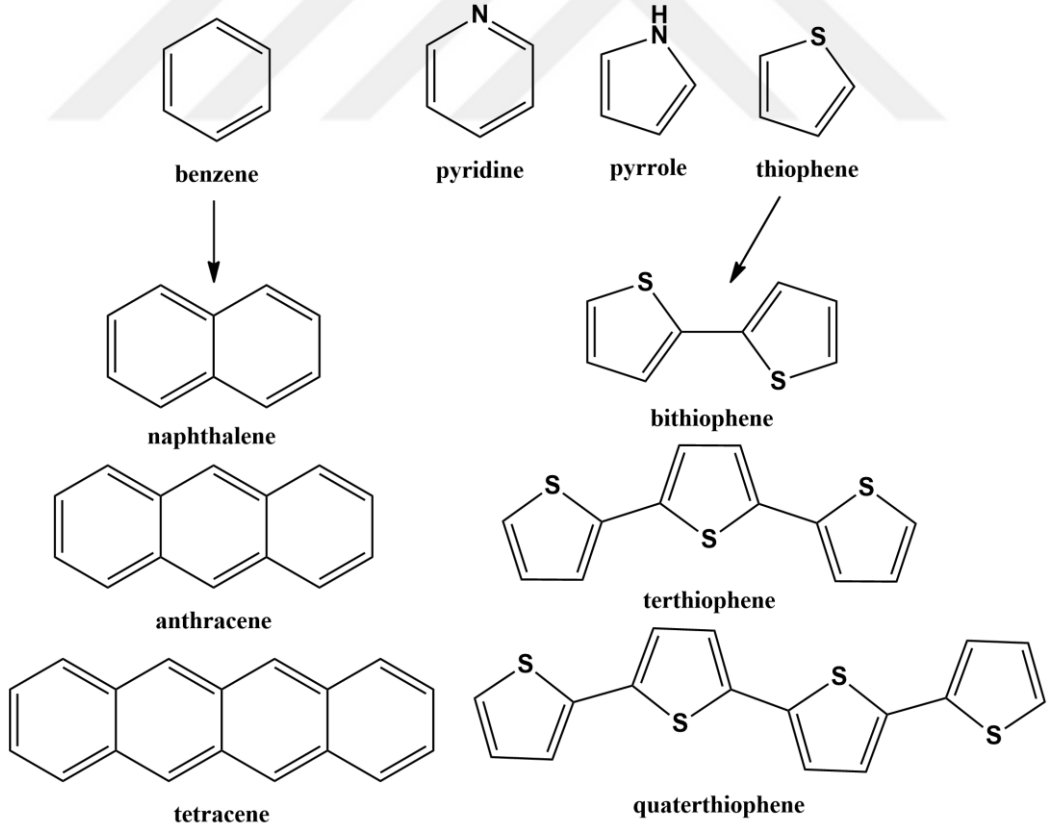

Figure 1.5 The chemical structures of some of the carbocyclic and heterocyclic rings taking part in the formation of organic semiconducting compounds.

We can discuss some of the essential requirements for organic semiconducting materials. These are; Band gap energies, the band gap energy determines whether a material can conduct electricity and, if so, how well. For organic semiconductors, it's crucial that the energy gap between the highest occupied molecular orbital (HOMO) and the lowest unoccupied molecular orbital (LUMO) falls within a certain range. This range allows for efficient electron transport while also preventing excessive leakage of current. Alignment of p orbitals, organic molecules often contain π orbitals, which can overlap to form what's known as a π-conjugated system. This arrangement facilitates the movement of electrons along the molecular backbone, enabling charge transport. Proper alignment of these p orbitals is essential for maintaining the integrity of the π-conjugation system and ensuring efficient charge transport. solid-state stacking arrangements**: In organic semiconductors, molecules or polymer chains need to be properly arranged in the solid-state to facilitate charge transport. This often involves stacking the molecules or chains in a way that allows for efficient electron hopping between adjacent units. The stacking arrangement affects parameters such as charge mobility and crystallinity, which in turn impact the overall performance of the semiconductor material.By fulfilling these prerequisites, organic semiconducting materials can exhibit desirable electronic properties, making them suitable for various applications such as organic electronics, flexible displays, and organic photovoltaics.[13] In this context, research in organic (opto)electronics has predominantly concentrated on polycyclic conjugated systems like acenes, fullerenes, and oligo- and polythiophenes over the past few decades. This focus is driven by their inherent π-conjugation and the extent of electron delocalization they offer, resulting in favorable structural and (opto)electronic characteristics.[14], [15] Furthermore, the advancement of new π-conjugated systems is a crucial aspect to broaden the scope of alternative organic semiconductors documented in the literature. This expansion facilitates deeper insights into the mechanisms governing charge transport, separation, and recombination within (opto)electronic devices.

1.2 OFET Architecture and Operation

The structure of an Organic Field-Effect Transistor (OFET) can be understood by examining its key components and their roles: Gate Electrode, function: Controls the formation of the conductive channel in the semiconductor layer by applying an electric field. The gate electrode is electrically isolated from the semiconductor by the dielectric layer. Dielectric Insulating Layer, function is serving as an insulating barrier between the gate electrode and the semiconductor layer. It allows the gate voltage to induce an electric field in the semiconductor without direct electrical contact. Common materials for the dielectric layer include silicon dioxide (SiO_2), aluminum oxide (Al_2O_3), and various organic insulators. The other part is the organic Semiconducting Material, acts as the active layer where charge carriers (electrons or holes) move to create the current flow when a voltage is applied between the source and drain electrodes. And there are two types can be made of small molecular semiconductors or polymeric semiconductors, each with distinct properties that influence device performance.Finally, Source and Drain Contacts as a provide the electrical connections for injecting and collecting charge carriers into and out of the semiconductor channel. Both the source and drain electrodes are in direct contact with the organic semiconductor material, allowing charge carriers to enter and exit the channel.

The architecture of Organic Field-Effect Transistors (OFETs) varies, with several common configurations, each having its own advantages and drawbacks. The most frequently used geometries are top-contact/bottom-gate (TC/BG) and bottom-contact/bottom-gate (BC/BG) configurations, but top-contact/top-gate (TC/TG) and bottom-contact/top-gate (BC/TG) structures are also employed for specific applications (Figure 1.6).Top-Contact/Bottom-Gate (TC/BG) Configuration (Figure 1.6A). The organic semiconductor is first deposited on the dielectric/gate substrate, followed by the deposition of metallic source and drain electrodes using techniques such as shadow masking. Bottom-Contact/Bottom-Gate (BC/BG) Configuration (Figure 1.6B). The source and drain metal contacts are deposited first, followed by the deposition of the organic semiconductor layer. Top-Contact/Top-Gate (TC/TG) Configuration (Figure 1.6C). Both the source/drain electrodes and the gate electrode are deposited on top of the organic semiconductor, with the gate separated by a dielectric layer. Bottom-

Contact/Top-Gate (BC/TG) Configuration (Figure 1.6D). The metal contacts are deposited first, followed by the organic semiconductor and then the gate electrode on top, separated by a dielectric layer. Dielectric Layer, in these configurations, the dielectric layer is typically made of thermally grown silicon dioxide (SiO_2) with a thickness of 200-300 nm. This layer serves as the insulating barrier that allows the gate electrode to control the semiconductor channel without direct electrical contact.

Each OFET configuration has its unique set of advantages and disadvantages, making them suitable for different applications and fabrication methods. The choice of architecture depends on factors such as desired device performance, fabrication complexity, and specific application requirements. Advances in material science and fabrication techniques continue to optimize these configurations, enhancing the overall performance and reliability of OFETs in various electronic applications.

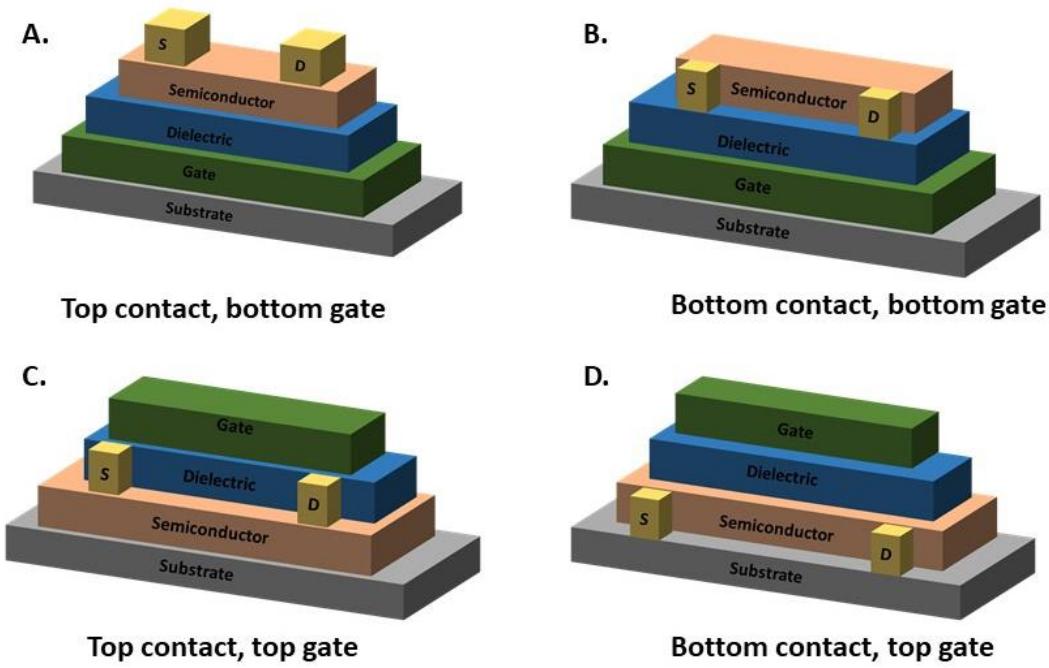

Figure 1.6 Schematic view of various device architecture in OFETs, top contact/bottom gate (A), bottom contact/bottom gate (B), top contact/top gate (C), bottom contact/top gate (D).

The OFET functions as an "electronic valve," where the conductance of the semiconductor channel is controlled by applying voltages to the gate and drain electrodes. Semiconductor Types; the semiconductor in OFETs can be either a small molecule or a polymer. These materials are chosen for their ability to modulate conductivity when an electric field is applied. Carrier Concentration; to maintain high current modulation, the organic semiconductor used in OFETs is typically not intentionally doped. This ensures a very low intrinsic carrier concentration, usually less than (10^{14} cm^{-3}). Device States; off State; when the gate-source voltage(V_G) is zero (i.e., the gate potential is zero relative to the grounded source electrode), the source-drain current (I_{SD}) is very low, indicating that the device is in the "off" state. On State; when a voltage is applied between the gate and the source (V_{SG}), it induces an accumulation of charge carriers at the interface between the gate dielectric and the semiconductor. This increases the carrier concentration significantly (to greater than (10^{20} cm^{-3})), resulting in an increase in the source-drain current (I_{SD}). This is the "on" state of the transistor (Figure 1.7).

Basic Relationships Describing OFET Drain Currents; The behavior of the drain current in OFETs can be described using two fundamental equations, depending on the operation regime (linear or saturation). Linear (Ohmic) Region, when the drain-source voltage (V_{SD}) is small, the OFET operates in the linear region (eq. 1.3). The drain current (I_{SD}) is given by:

$$(I_{SD})_{lin} = \left(\frac{W}{L}\right) \mu_{FET} C_i \left(\frac{V_{SG} - V_T - V_{SD}}{2}\right) V_{SD} \quad (1.3)$$

where:

- (W) is the channel width.
- (L) is the channel length.
- (μ) is the charge carrier mobility.
- (C_i) is the capacitance per unit area of the gate dielectric.
- (V_{SG}) is the gate-source voltage.
- (V_T) is the threshold voltage.

Saturation Region, when the drain-source voltage (V_{SD}) is high enough that the channel is pinched off, the OFET operates in the saturation region (eq. 1.4). The drain current (I_{SD}) is given by:

$$(I_{SD})_{sat} = \left(\frac{W}{2L}\right) \mu_{FET} C_i (V_{SG} - V_T)^2 \quad (1.4)$$

In these equations:

- (V_{SG}) (gate-source voltage) controls the accumulation of charge carriers in the channel.
- (V_{SD}) (drain-source voltage) drives the current through the channel.
- The mobility (μ) and capacitance (C_i) are critical parameters that influence the device performance.

OFETs operate based on the modulation of the semiconductor channel conductance through gate and drain voltages. Understanding the basic equations and principles behind their operation helps in designing and optimizing these devices for various applications, such as display drivers, memory circuits, and sensors. The ability

to achieve high current modulation with low intrinsic carrier concentration in the semiconductor is essential for the effective functioning of OFETs.

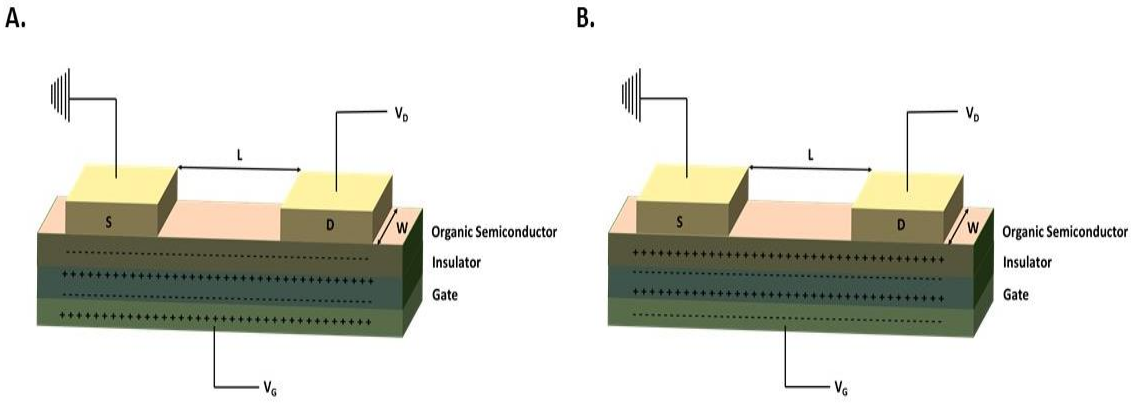

Figure 1.7 On-state of OFETs and corresponding polarization in insulator layer and accumulation of charge carriers in organic semiconductor layer when positive gate voltage is applied (A), and negative gate voltage is applied (B).

The term "field-effect" originates from the control exerted by the gate voltage over the transistor's channel conductance, which is mediated through an electric field. This principle is visually represented through energy band diagrams, which illustrate how the energy levels of the organic semiconductor shift in response to an applied gate voltage. Figure 1.8 depicts these energy band diagrams during the operation of a field-effect transistor. Highest Occupied Molecular Orbital (HOMO) and Lowest Unoccupied Molecular Orbital (LUMO), HOMO: Analogous to the valence band in inorganic semiconductors, the HOMO level represents the highest energy level that is fully occupied by electrons at zero Kelvin. LUMO: Analogous to the conduction band, the LUMO level is the lowest energy level that is empty and can accept electrons.

Source and Drain Electrodes: The Fermi level in the source and drain metallic electrodes represents the energy level at which the probability of finding an electron is 50%. This level is crucial for determining the alignment of energy bands when a voltage is applied.

Gate Voltage Application: When a gate voltage (VG) is applied, it creates an electric field that influences the energy levels of the semiconductor. Positive Gate Voltage (for n-type semiconductors): When a positive gate voltage is applied, it lowers

the energy levels of the semiconductor's conduction band relative to the Fermi level of the source and drain. This shift enables electrons to accumulate at the semiconductor/dielectric interface, forming a conductive channel. Negative Gate Voltage (for p-type semiconductors): When a negative gate voltage is applied, it raises the energy levels of the semiconductor's valence band relative to the Fermi level of the source and drain. This shift enables holes to accumulate at the semiconductor/dielectric interface, forming a conductive channel.

Off State (No Gate Voltage Applied): In the off state, when no gate voltage is applied, the energy levels of the HOMO and LUMO are aligned such that there is minimal overlap with the Fermi levels of the source and drain electrodes. As a result, there is minimal charge carrier accumulation at the interface between the semiconductor and the gate dielectric. This results in a very low source-drain current (ISD), indicating that the transistor is in the "off" state.

On State (Gate Voltage Applied): Positive Gate Voltage (n-type OFETs): When a positive gate voltage is applied, it lowers the energy levels of the LUMO with respect to the Fermi level of the source and drain electrodes. This shift facilitates the accumulation of electrons at the semiconductor/dielectric interface, forming an electron-rich conductive channel. The increase in electron concentration significantly enhances the source-drain current (ISD), turning the transistor "on" state (Figure 1. 8C and E respectively). Negative Gate Voltage (p-type OFETs): When a negative gate voltage is applied, it raises the energy levels of the HOMO with respect to the Fermi level of the source and drain electrodes.This shift facilitates the accumulation of holes at the semiconductor/dielectric interface, forming a hole-rich conductive channel. The increase in hole concentration significantly enhances the source-drain current (ISD), turning the transistor "on" state(Figure 1. 8B and D respectively).

The field-effect in OFETs is a result of the gate-induced modulation of the energy levels of the semiconductor. By applying a gate voltage, the energy levels of the HOMO and LUMO are shifted, allowing for the accumulation of charge carriers at the semiconductor/dielectric interface. This accumulation of charges forms a conductive channel between the source and drain electrodes, enabling the flow of current and thus turning the transistor "on." The energy band diagrams help visualize this process, showing how the application of a gate voltage can control the conductance of the semiconductor channel in an OFET.

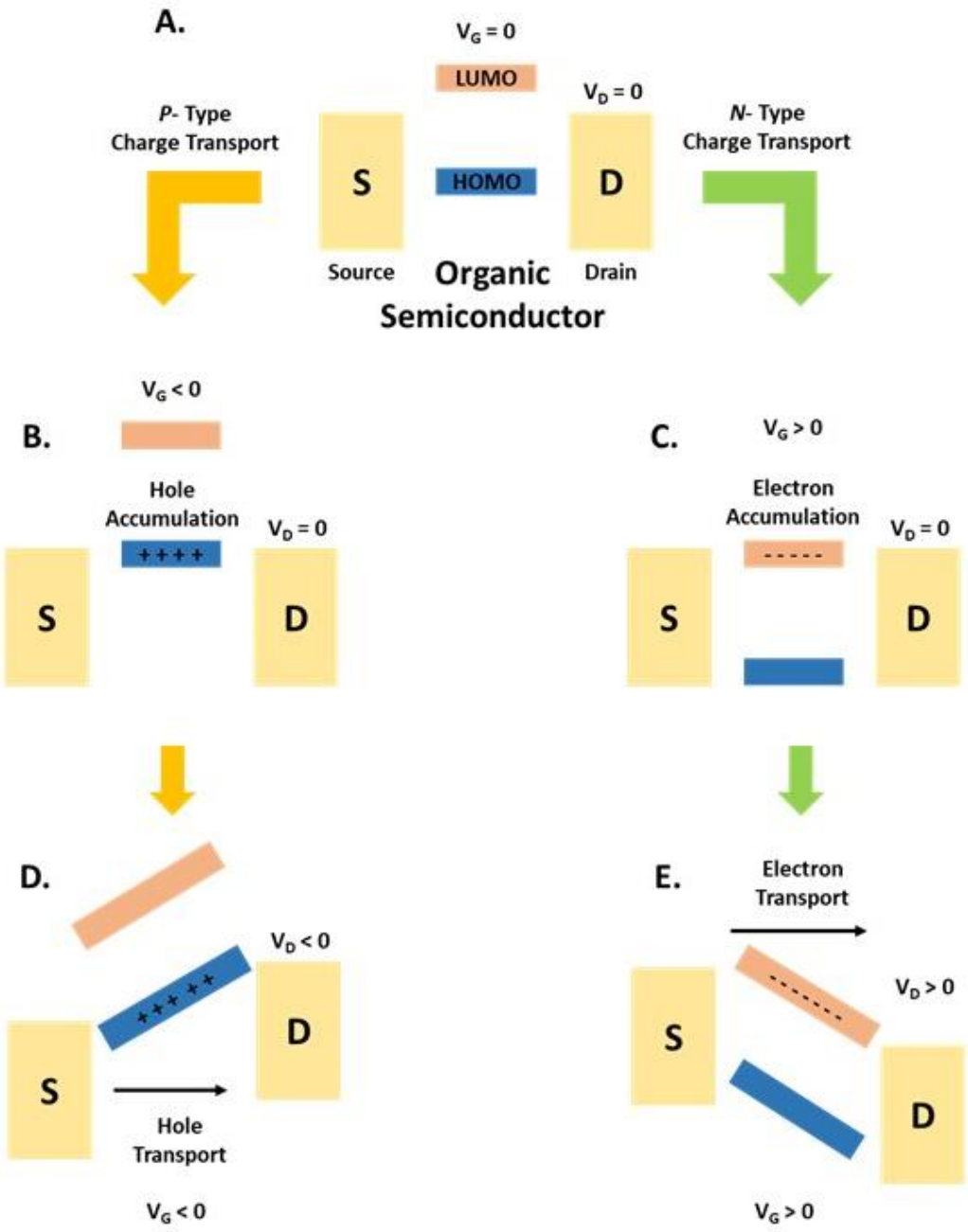

Figure 1.8 Energy band diagrams of HOMO and LUMO levels at V_G=0 (A), during *p*-channel device operation (B and D), and *n*-channel device operation (C and E).

To deepen understand these formations, it is rather to identify the threshold voltage (V_T). The threshold voltage (V_T) is a crucial parameter in the operation of OFETs, defining the minimum gate voltage required to create a conductive channel of mobile charge carriers at the semiconductor/dielectric interface. Understanding (V_T) and the factors that influence it is essential for optimizing the performance of OFETs. For

example, doping an n-type semiconductor material moves the (V_T) to more negative values. Additionally, a mismatch between the Fermi level of the metal contacts and the LUMO energy level of the organic semiconductor can shift (V_T) either negatively or positively, depending on the nature of the misalignment.

OFETs are primarily characterized using two methods. First, by keeping the gate bias at zero and sweeping the drain bias, resulting in an (I_D)-(V_D) curve, also known as the "output curve" (Figure 1.9C). Second, by holding the drain bias at a constant value and sweeping the gate bias, producing an (I_D)-(V_G) curve, or "transfer curve" (Figure 1.9A and B).

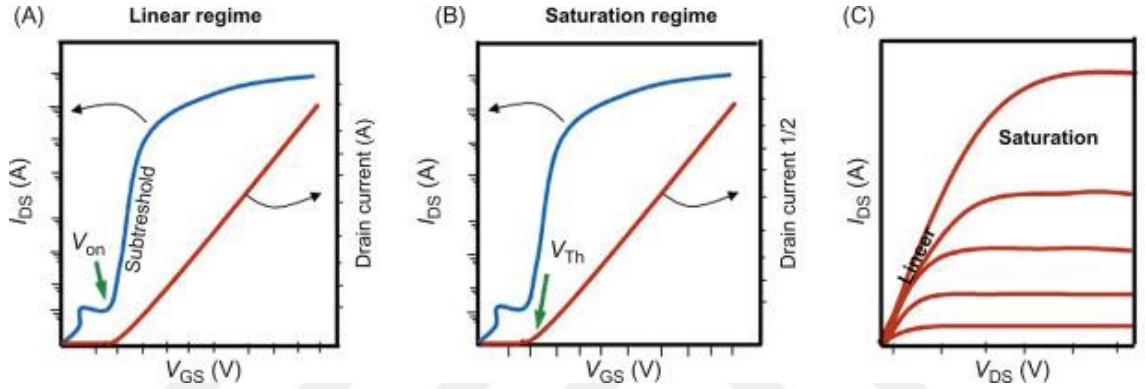

Figure 1.9 Illustrative current–voltage characteristics of an OFET: (A, B) transfer characteristics in both systems (linear/saturation) and (C) output characteristics indicating the linear and saturation regimes in the same graph. OFET.[16]

1.3 Fabrication Methods

Organic semiconducting materials differ significantly from their inorganic counterparts in terms of mechanical properties, solubility, and melting point. Processing bulky organics is typically challenging; for example, their single crystals are highly brittle. Consequently, the fabrication processes for organic thin films are highly dependent on the physicochemical properties of the materials. Therefore, it is not feasible to fabricate organic optoelectronic devices using the same techniques as conventional microelectronics. However, some early OFET fabrication methods were modeled after conventional techniques like thermal oxidation and photolithography. Typically, organic field-effect transistors (OFETs) consisted of a heavily doped silicon substrate (p++-Si or n--Si) as the gate, with a thermally grown oxide layer (≈200-300

nm) serving as the dielectric layer, and lithographically patterned metal electrodes (e.g., Au, Ag) as the source and drain. To minimize production risks, organic semiconductors are deposited at the final stage of the fabrication process.

Thin-film growth and patterning, ranging from 1 to 200 nm in thickness, are crucial for achieving high-performance optoelectronic devices. The most common techniques for creating thin films include spin-coating, thermal evaporation, and chemical vapor deposition. The fabrication of optoelectronic components with nanoscale resolution varies depending on the chosen deposition technique.

1.3.1 Solution-Processed Deposition

Solution-processed deposition techniques are widely employed in forming semiconducting layers, which serve as active channels in optoelectronic devices. These techniques leverage the benefits of organic materials, such as low cost and large area coverage. While doping in physical vapor deposition (PVD) under vacuum involves the simultaneous deposition of different materials, solution-based deposition allows for a more practical approach. In this method, organic materials are mixed in a solvent medium, simplifying the doping process.

Spin-coating is a solution-processed deposition technique used to fabricate optoelectronic devices by coating a substrate with an organic small molecular or polymeric solution. The substrate is spun for a specific period to achieve the desired thickness, and a thin film is formed as the solvent evaporates. For this technique, the material must be highly soluble in common organic solvents like chloroform, dichloromethane, tetrahydrofuran, and toluene. However, many organic semiconductors are not naturally soluble. To address this, small molecules with linear or branched alkyl chains and polymers grafted with solubilizing groups are often used. Solvents with low boiling points or vapor pressures are preferred to decrease the drying time.

The advantages of spin-coating include producing ultrathin films with uniform morphology at low cost, simplicity, and easy operation conditions. High spin speeds result in shorter drying times and consistent film thickness on both macro and nanoscale levels. However, the main drawback of this technique is the significant material wastage, as excess solution is flung off during spinning.

Langmuir-Blodgett (LB) is an alternative technique for fabricating homogeneous ultra-thin films of organic small molecules, allowing for precise control over the structure and thickness of the resulting film. This method involves spreading amphiphilic molecules at the water-air interface as a single layer. However, this is not applicable for most small molecules used in OFETs. Amphiphilic small molecules, which have a hydrophilic head and a hydrophobic chain, exhibit strong dipole moments and can form hydrogen bonds due to functional groups like –OH, -COOH, and -NH2. The hydrophilic parts of these molecules tend to sink in water, while the hydrophobic parts orient towards the air. Once homogeneity and surface balance are achieved, the deposition process can proceed. The hydrophilic and hydrophobic properties of organic molecules are crucial for the fabrication of LB films. Additionally, the stability of surface-active molecules is important for the deposition of multiple single layers using this method.

Langmuir-Blodgett films are arranged by dissolving a unimportant amount of an amphiphilic compound in a unstable solvent, which is then deposited on the surface of purified water. As the solvent evaporates, the organic molecules can be compressed to form a floating two-dimensional solid. During the compression of these monolayer films, a variety of phases can appear, similar to the mesophase of liquid crystals. When the substrate is absorbed in the liquid, it interrelates with the monolayer, causing the Langmuir film to adhere to the substrate and coat it as a monolayer.

Printing technology offers significant advantages for producing large volumes of organic electronics, leveraging its adaptability and efficiency. Among the various printing techniques, inkjet printing stands out for its ability to fabricate optoelectronic devices such as organic photovoltaics (OPVs) and organic light-emitting diodes (OLEDs). Inkjet printing's non-contact patterning capability and mask-free operation make it highly appealing for the production of organic electronics. Non-Contact Patterning, Inkjet printing does not require physical contact with the substrate, which reduces the risk of contamination and damage to delicate electronic materials. This is particularly beneficial for handling sensitive organic compounds used in OPVs and OLEDs. Mask-Free Operation, Unlike traditional lithographic techniques, inkjet printing does not require masks. This simplifies the fabrication process and reduces production costs and time. It also allows for greater flexibility and ease of prototyping and small-scale production. Direct Printing Capability, Inkjet printing can deposit

materials directly onto the substrate in precise patterns. This direct approach enables the creation of complex designs and the integration of multiple functional layers in a single printing step. Versatility in Design, The ability to easily change designs from print to print is a significant advantage. It allows for rapid iteration and customization, making it suitable for both research and commercial applications. This flexibility supports the development of tailored optoelectronic devices for specific applications or user requirements. Scalability, Inkjet printing can be scaled up for mass production, making it a viable option for producing large volumes of organic electronics. The scalability of this technology is essential for meeting the growing demand for optoelectronic devices in various industries. Inkjet printing can be used to fabricate OPVs with complex multi-layer structures. It allows for precise control over the thickness and composition of each layer, which is crucial for optimizing the efficiency and performance of these devices. The technology is also suitable for producing OLEDs, where uniformity and precision in the deposition of organic layers are critical for device performance and lifespan. Inkjet printing can achieve high-resolution patterns required for displays and lighting applications. Overall, the adaptability, precision, and efficiency of inkjet printing make it a highly attractive technology for the production of organic electronics, paving the way for innovative optoelectronic devices with enhanced performance and functionality.

The inkjet printing process and its suitability for liquid-phase materials, particularly in the context of organic electronics Inkjet printing offers significant material savings compared to traditional fabrication methods. This is because it precisely deposits only the required amount of material onto the substrate, minimizing waste and reducing material costs. Inkjet inks typically consist of a solute, which could be a semiconductor or other functional material, dissolved or dispersed in a solvent or carrier fluid. These inks can be tailored to meet the specific requirements of the printing process and the desired properties of the final device. Inkjet printing relies on the piezoelectric effect to eject droplets of ink from a nozzle. By applying an external voltage to the solution-filled reservoir, the volume of the droplet can be controlled, ensuring precise deposition onto the substrate. Once ejected from the nozzle, the ink droplet experiences gravity and air resistance as it travels towards the substrate. Upon impact, the droplet spreads due to its momentum and flows across the surface, guided by surface tension. The solvent then begins to evaporate, allowing the deposited

material to solidify and form the desired pattern. The viscosity of the ink is a critical factor that influences the printing process and the quality of the deposited layers. Materials with favorable viscosity properties, such as highly soluble polymers, macromolecules, or small molecules, are well-suited for inkjet printing. The concentration and molar mass of the solute also play a role in determining the ink's viscosity and overall performance. In summary, inkjet printing offers a versatile and efficient approach for depositing liquid-phase materials in the fabrication of organic electronics. By optimizing ink composition and printing parameters, researchers and manufacturers can achieve precise control over the deposition process, leading to the production of high-performance optoelectronic devices.

The utilization of green solvents in the solution processing of molecular semiconductors has garnered significant attention in recent years, driven by the growing imperative to minimize the environmental impact of chemical manufacturing processes. Traditional solvents used in the fabrication of organic electronic devices, such as chloroform, dichloromethane, and toluene, are often toxic, volatile, and harmful to both human health and the environment. As the demand for sustainable and eco-friendly technologies rises, the search for alternative solvents that are less hazardous and more sustainable becomes critical. Green solvents, characterized by their reduced toxicity, biodegradability, and lower environmental footprint, offer a promising pathway to achieve this goal.

In the context of organic electronics, where solution processing techniques like spin-coating and inkjet printing are prevalent, the choice of solvent plays a pivotal role in determining the quality and performance of the resulting thin films. The physicochemical properties of the solvent, including its boiling point, polarity, and solubility parameters, directly influence the morphology, crystallinity, and electronic properties of the semiconducting layers. Therefore, the integration of green solvents into the fabrication process not only addresses environmental concerns but also opens new avenues for optimizing device performance. Exploreing the potential of green solvents in the solution processing of molecular semiconductors, highlighting their benefits, challenges, and the recent advancements in this field. By adopting sustainable solvent systems, the organic electronics industry can move towards more environmentally friendly practices without compromising the efficiency and functionality of the devices.

In recent years, the utilization of green solvents in the solution processing of molecular semiconductors has emerged as a crucial research direction for advancing the future development of organic optoelectronics. Despite the significant potential and growing interest in this area, there are still very limited examples of green solvent applications specifically for Organic Field-Effect Transistors (OFETs). This gap underscores the need for further investigation and innovation in developing environmentally friendly processing techniques that do not compromise the performance and functionality of these advanced electronic devices. As the field of organic optoelectronics continues to evolve, the integration of green solvents holds promise for achieving sustainable and high-performance solutions, driving the industry towards more eco-friendly practices. The utilization of green solvents in the solution processing of molecular semiconductors, particularly in the context of Organic Field-Effect Transistors (OFETs), represents a significant stride towards sustainable and environmentally friendly manufacturing practices in the field of organic optoelectronics.

OFETs, as key components in various electronic devices such as sensors, displays, and flexible circuits, rely on the deposition of semiconducting layers onto substrates to facilitate the controlled flow of charge carriers. Traditionally, the fabrication process involves the use of solvents like chloroform, dichloromethane, and toluene, which are known to be toxic, volatile, and detrimental to human health and the environment. The widespread adoption of these solvents poses significant environmental and health risks, making their replacement with greener alternatives imperative.

Green solvents, characterized by their reduced toxicity, biodegradability, and lower environmental footprint, offer a promising solution to these challenges. Solvents such as ethanol, ethyl lactate, and supercritical carbon dioxide (CO2) have gained attention for their eco-friendly properties and compatibility with OFET fabrication processes. The adoption of green solvents in OFET fabrication presents several advantages. Firstly, these solvents offer a safer working environment for researchers and technicians, minimizing health risks associated with exposure to toxic fumes and chemicals. Additionally, they contribute to reducing air and water pollution, as they are less harmful to ecosystems and do not pose risks to aquatic life when released into the environment.

Furthermore, green solvents can enhance the performance and properties of OFET devices. By promoting the formation of uniform and high-quality semiconducting thin films, these solvents contribute to improved charge transport characteristics, higher carrier mobilities, and enhanced device reliability. The use of green solvents also enables finer control over film morphology and crystallinity, leading to more precise tuning of device parameters and performance optimization.

Despite these benefits, the widespread adoption of green solvents in OFET fabrication still faces challenges. One such challenge is the limited availability and compatibility of green solvents with specific molecular semiconductor materials. Many existing OFET materials may have limited solubility in green solvents, necessitating the development of new semiconducting materials or modification of existing ones to be compatible with eco-friendly solvent systems. Moreover, the optimization of processing parameters and techniques for green solvent-based OFET fabrication requires thorough investigation and experimentation. Parameters such as solvent concentration, deposition method, drying conditions, and annealing processes may need to be adjusted to achieve optimal device performance while minimizing solvent waste and environmental impact.

In conclusion, the integration of green solvents in the solution processing of molecular semiconductors for OFET fabrication holds tremendous promise for advancing the field of organic optoelectronics towards sustainability. With ongoing research and innovation, the development of greener solvent systems tailored to the specific requirements of OFETs will contribute to a more environmentally conscious and socially responsible approach to electronic device manufacturing.

1.3.2 Physical Vapor Deposition

The spin-coating technique necessitates solutions with high viscosity, which can pose challenges for small molecular semiconductors. In contrast, Physical Vapor Deposition (PVD) emerges as the ideal method for fabricating thin films using these materials. In principle, the Physical Vapor Deposition (PVD) technique involves heating an organic material within a high vacuum chamber (approximately 10^{-6} to 10^{-9} torr). The organic semiconducting material is placed in a metal boat made of materials like tungsten (W), molybdenum (Mo), or tantalum (Ta), which is then heated using Joule heating. As the material reaches its evaporation temperature, it begins to

evaporate from the source in molecular form. These molecules eventually deposit onto the substrate, which is positioned a few centimeters above the boat. However, this method is not suitable for polymers, as they can easily decompose due to cracking when heated. The main advantages of this method include straightforward and well-controlled thickness management and the production of highly-ordered thin films with high purity. The growth rate and substrate temperature can be adjusted to achieve the desired properties of the resulting thin film. Multi-layered coatings and very thick films can also be achieved using this system. However, its primary drawbacks include the high cost and complexity of the instrumentation compared to spin-coating, as well as the challenges associated with cleaning the vacuum chamber. In organic electronic devices such as OFETs, OLEDs, and OPVs, small molecules typically evaporate under reduced pressure ($<10^{-6}$ torr) with a low growth rate of 0.1-3 Å/s. This method facilitates the modeling of deposition masks and pixels. Consequently, vacuum equipment, already in use in the semiconductor industry, can be readily adapted for the fabrication of organic optoelectronic devices.

Chapter 2

Enabling three-dimensional porous architectures via carbonyl functionalization and molecular specific organic-SERS platforms

2.1 Introduction

Noncovalent intermolecular interactions play an exceptional role in nature to define the supramolecular arrangement of organic structures, and to govern chemical reactions and different states of matter.[17], [18], [19] While the double helix structure of DNA and protein secondary structures are formed via multiple strong hydrogen bonds, carbonyl···carbonyl interactions as well as dipolar/London dispersion forces determine three-dimensional structures and functions these biomaterials.[20], [21], [22], [23] Molecular recognition in biological processes (e.g., between and within peptides, proteins, and enzyme-inhibitor complexes) also rely on varied noncovalent interactions.1 With the advent of synthesis methodologies and characterization tools, varied π-units, heteroatoms, functional groups, and substituents have been employed in the rational design of (semi)synthetic organic structures, which has allowed for the precise control of noncovalent intermolecular interactions in the solid-state to achieve desired supramolecular arrangements, microstructures, and morphologies in various nanotechnology fields. In this perspective, among carbon-based material families developed in the recent decades, semiconducting small molecules have become a key player in thin-film optoelectronic devices.[24], [25] Their ability to form nano-/micro-structured thin-films from solution or vapor phase with tunable morphologies and optoelectronic properties has greatly benefited the research for next-generation

optoelectronic devices.[26], [27], [28] Although most of these device technologies, such as organic field-effect transistors (OFETs)[29] or light-emitting diodes (OLEDs)[30], have now become a conventional application avenue for molecular semiconductors, they hold huge promise also for unconventional applications such as surface-enhanced Raman spectroscopy (SERS). As we have recently disclosed in our pioneering studies, the nanostructured organic films of π-electron deficient fluorinated oligothiophene semiconductors DFH-4T[31] and DFP-4T[32], fabricated via physical vapor deposition (PVD), enabled the Raman detection of organic analytes (e.g., methylene blue and rhodamine 6G) without needing a metallic or an inorganic layer. Our initial findings have convincingly demonstrated that low-LUMO oligothiophene semiconductors in their nanostructured films could enhance Raman signals via chemical enhancement mechanism. In these perspective, perfluoro-alkyl/-aryl substituents attached directly to the quaterthiophene π-core do not only lower the lowest unoccupied molecular orbital (LUMO) energy of the π-system (-3.2 – -3.4 eV) for effective charge-transfer interactions with analyte molecules but also enable a high favorable crystal growth dynamics during the PVD processes. To this end, from a molecular engineering perspective, non-fluorinated molecular structures and π-frameworks other than oligothiophenes are yet to be studied. Exploring additional molecular structures is important not only to widen the scope of SERS-active organic films for potential molecule-specific sensing, but also to reveal key molecular parameters that controls Raman enhancement mechanisms.

In search of π-frameworks as the building blocks of organic-SERS platforms, [1]benzothieno[3,2-b][1]benzothiophenes (BTBTs) stand out as an attractive molecular family. BTBTs have been one of the most attractive semiconductor families of this decade.[33], [34] This is mainly a result of their favorable charge-transport characteristics in thin-films, as well as structural and functional properties including facile synthesis/functionalization in small number of steps, solubility in common organic solvents, optical transparency, and convenient film preparation via vacuum- or solution-processing.[35], [36] As a result of their completely coplanar electron-rich fused thienoacene π-system, and highly delocalized frontier orbital wave functions with polarizable S-atoms, BTBTs are generally hole-transporting (p-type) semiconductors and have convincingly demonstrated high hole mobilities of >1.0-2.0 cm2/Vs in OFETs for a wide range of alkyl and aryl substituents.[37] Despite their great properties,

BTBTs had not been preferred as organic-SERS platforms in our previous studies since they are quite π-electron rich systems with high-lying LUMOs (>-2.2 eV). In the only reported SERS study based on a BTBT derivative,24 we have fabricated 2,7-dioctyl[1]benzothieno[3,2-b][1]benzothiophene (C8-BTBT) film as a micro-structured organic template to deposit Au nanoparticulates for plasmonic Raman enhancement. As the research to tailor BTBT π-framework continues in the optoelectronics field, we have recently developed highly π-electron deficient BTBTs via 2,7-functionalizations.[38], [39] Our study demonstrated that carbonyl functionalities could adopt in-plane conformations (θtorsions < 2-3°) with the BTBT π-system, which extends and stabilizes (ΔELUMO = -1.5 eV) LUMO significantly leading to the first examples of electron-transporting (n-type, electron mobility ~ 0.6 cm2/V·s) BTBT semiconductors in the literature. Furthermore, carbonyl functionalities were observed to induce strong dipolar and π-interactions between the BTBTs leading to enhanced cohesive energetics relative to non-functionalized analogues.[37], [39] These results have not only revealed the great potential of functionalized low-LUMO BTBTs in n-type OFETs and complementary circuits, but also made this thienoacene molecular family, as pure organic films, quite attractive for nanostructured SERS-active platforms.

Herein, we explore the nanostructured film formation and Raman signal enhancement abilities of a π-electron deficient low-LUMO BTBT molecule, 1,10-(benzo[b]benzo[4,5]thieno[2,3-d]thiophene-2,7-diyl)bis(octan-1-one) (D(C_7CO)-BTBT, Figure 1a), which includes 2,7-dicarbonyl functionalization along with n-heptyl (-n-C_7H_{15}) substituents. This molecule is prepared on the gram-scale in ambient via facile Friedel-Crafts acylation and precipitation/solvent washing without requiring any high-cost transition-metal catalyst and tedious chromatographic/sublimation-based purification. While the good chemical/thermal stabilities allow for stable semiconductor film deposition, carbonyl functionalization induces favorable out-of-plane crystal growth via zigzag motif of dipolar C=O···C=O interactions, hydrogen bonds, and strengthened π-interactions. A unique two-stage film growth behavior is identified by a transition from an initial densely packed 2D island-based (Volmer-Weber (VW)) morphology into a highly porous 3D surface consisting of vertically oriented nanoplates. This transition is accompanied by an “edge-on” to “face-on” molecular orientational switch driven by the surface hydrophobicity of the initially formed island-based morphology. A non-functionalized BTBT analogue, C_8-BTBT, provides a straight

comparison at molecular level to study the effects of carbonyl functionalization and stabilized/extended frontier π-orbitals on nanostructured film formation and Raman signal enhancements. Three-dimensional highly crystalline nanostructured D(C_7CO)-BTBT films showed strong Raman signal enhancements in Surface-Enhanced Raman Spectroscopy (SERS) with four different analyte molecules having varied electronic structures. Molecular sensitivity for Raman signal enhancement is also achieved on the non-functionalized (high-LUMO) organic-SERS platform. The analysis of the electronic structures and the ratio of the anti-Stokes to Stokes SERS, suggests that the π-extended and stabilized LUMOs with crystalline face-on orientations in varied directions, all of which are the direct results of carbonyl functionalization, are key to the realization of strong chemical enhancement mechanism.

2.2 Results

2.2.1 Synthesis and purification of D(C7CO)-BTBT

As shown in Figure 2.1, gram-scale synthesis of **D(C_7CO)-BTBT** was carried out in one step from the **BTBT** π-core via Friedel-Crafts acylation following a slightly modified procedure from the literature (60-70% yield).[37], [40] Most importantly, this reaction was performed in ambient without requiring an inert atmosphere although the yield is ~8% lower than the reaction performed under nitrogen. The target compound was precipitated from the reaction mixture as a result of its low solubility in common organic solvents, which was filtered and purified via simple solvent washing to yield pure **D(C_7CO)-BTBT** solid (Figure 2. 1b). Therefore, tedious chromatographic purification or thermal gradient sublimation, as typically used in organic semiconductors including our previous SERS-active molecules **DFH-4T** and **DFP-4T**, were not needed. The chemical structure and purity of **D(C_7CO)-BTBT** solid were characterized and established by using ^{1}H/^{13}C-nuclear magnetic resonance (NMR) spectroscopy (Figures 2.8. and 2.9.), mass spectrometry (Figures 2.10.), thin layer chromatography, and elemental analysis. This solid was directly used for the PVD fabrication of nanostructured SERS-active organic films. The synthesis of **D(C_7CO)-BTBT** did not require any high-cost transition-metal catalyst as used in the synthesis of

our previously reported SERS-active molecules **DFH-4T**[31] and **DFP-4T**[41] (i.e., $Pd(PPh_3)_4$ and $Pd(PPh_3)_2Cl_2$). Instead, relatively low-cost $AlCl_3$ Lewis acid catalyst was used. From a functional materials development standpoint with an aim for low-cost sensing/detection, **D(C$_7$CO)-BTBT** stands out as a promising material that could be industrially scalable at low production costs. On the other hand, **C$_8$-BTBT** was synthesized in accordance with the reported procedure.[37] The only structural difference between **C$_8$-BTBT** and **D(C$_7$CO)-BTBT** is the electron-withdrawing (EWD) carbonyl units, and this comparative study at molecular level provides a solid understanding of the effects of carbonyl functionalization and stabilized/extended frontier π-orbitals on nanostructured film formation and SERS ability of molecular π-systems.

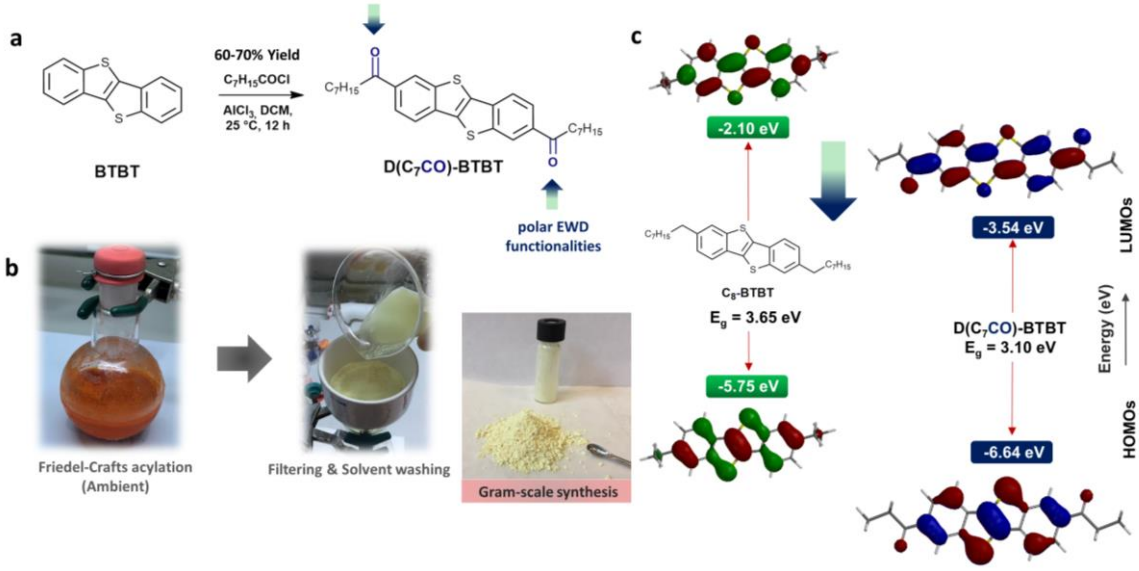

Figure 2.1. Synthesis and purification of D(C7CO)-BTBT, and computational analysis. **a** Chemical structure and synthesis of **D(C7CO)-BTBT** from the BTBT π-core via Friedel-Crafts acylation reaction in ambient. **b** Photos taken during the ambient reaction and the simple work-up (filtering and washing with water/methanol/dichloromethane), and the photo of the gram-scale solid obtained after drying. **c** Chemical structure of **C8-BTBT**, experimental HOMO/LUMO energy levels of **C8-BTBT** and **D(C7CO)-BTBT** determined via electrochemical methods combined with the optical band gaps (E_g's),[39] and the DFT(B3LYP/6-31G**)-calculated topographical frontier orbital representations.

2.2.2 Fabrication of nanostructured D(C7CO)-BTBT and C8-BTBT films

The micron-thick films of **D(C7CO)-BTBT** (~5.5±0.2 μm thick) and **C8-BTBT** (~2.3±0.2 μm thick) were deposited onto Si(001) substrates under high vacuum (1×10^{-6} Torr) via a modified PVD technique (Figure 2. 2a). Different than conventional slow thermal evaporation process used for the fabrication of layer-by-layer grown semiconducting thin-films (≤ 100 nm) in organic optoelectronics, the formation of out-of-plane oriented crystalline nano-structures in a micron-thick film was enabled by employing modified parameters of fast molecular deposition rate (~ 40 nm/s), short source-to-substrate distance (~ 7 cm), and low substrate temperature (~ 25-30 °C). This film deposition condition enables ballistic molecular transport from source to substrate surface and promotes the formation of out-of-plane morphologies by minimizing in-

plane crystal growth.[24], [42] However, using modified PVD technique does not always guarantee a desired morphology in organic films; the characteristics of intermolecular interactions in the out-of-plane direction is also crucial, which is strongly correlated with the molecular structure and functional units.

2.2.3 Microstructures, morphologies, and film growth mechanisms of nanostructured D(C7CO)-BTBT and C8-BTBT films

The semiconductor film morphologies were characterized using field emission scanning electron microscopy (FE-SEM) (Figure 2. 2). The top-view FE-SEM analysis of **D(C_7CO)-BTBT** (Figure 2. 2f) film showed uniformly distributed and highly interconnected vertically oriented nano-plates with lateral sizes of ~50-70 nm. On the other hand, as shown in Figure 2. 2c, the **C_8-BTBT** film showed a significant amount of face-on oriented 2D plate formation with limited density of vertical plates (~100-200 nm lateral sizes). When compared with **C_8-BTBT**, the surface of **D(C_7CO)-BTBT** film showed a much higher density of vertically oriented thin nano-plates with an extensive porosity. The wettability of these films were studied by water contact-angle measurements (Figures 2. 2b and 2e insets), which showed hydrophobic surfaces ($CA_{water} \geq 90°$) for both films with a much larger contact angle of 142.5±5.3° for **D(C_7CO)-BTBT**. Despite its highly polar nature,[43], [44], [45] adding carbonyl units to the BTBT π-system significantly increased the hydrophobicity of the corresponding films. Since both **C_8-BTBT** and **D(C_7CO)-BTBT** have the same hydrophobic BTBT π-system and medium-length alkyl chains, much larger hydrophobicity (ΔCA_{water} ~ 50-55°) of the **D(C_7CO)-BTBT** film is attributed to carbonyl-induced (*vide infra*) growth of three-dimensional highly porous nanostructured morphology on the film surface.

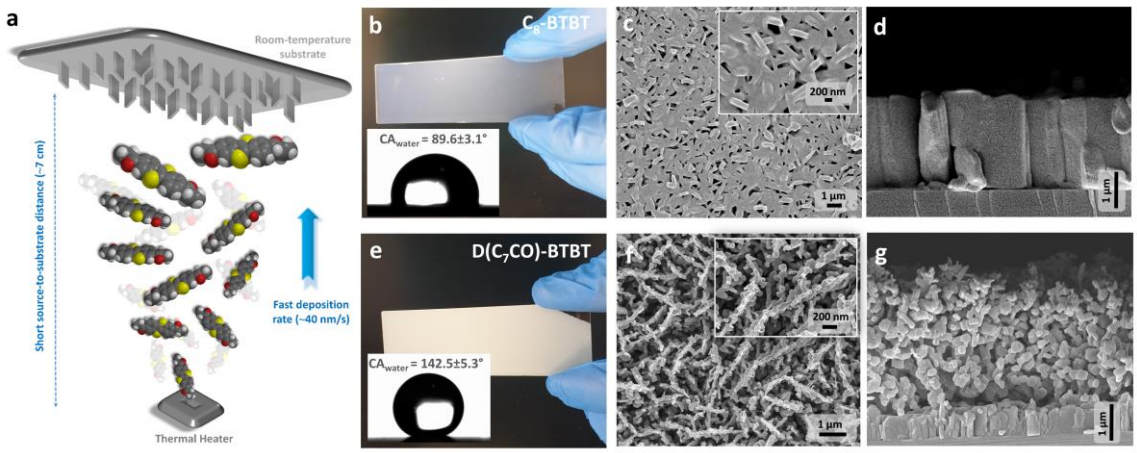

Figure 2.2. Fabrication and characterization of D(C7CO)-BTBT and C8-BTBT films. a Schematic illustration of the physical vapor deposition (PVD) method and the key deposition parameters used for the fabrication of nanostructured SERS films. Photos (**b** and **e**) of the nanostructured films and a water droplet on them, water contact angles (CA_{water}), top-view and cross-sectional SEM images of the nanostructured films for **C8-BTBT** (**c** and **d**) and **D(C7CO)-BTBT** (**f** and **g**). Scale bars are shown separately for each SEM image.

The crystallinity and microstructure of the current films were characterized by conventional θ-2θ diffraction scans which, in combination with the reported single-crystal unit cells and the simulated powder patterns (Figures 2. 2. and 2.11),[37], [39] revealed out-of-plane diffraction planes, intermolecular interactions, and the corresponding molecular orientations relative to the substrate surface. As shown in Figure 3a, **D(C7CO)-BTBT** film showed five strong high-angle diffraction peaks in the out-of-plane direction corresponding to various crystalline planes (i.e., (111), (511), (020), (021), and (131)), all with nearly face-on oriented molecular π-backbones (Figure 2. 3b). However, **C8-BTBT** film showed only two high angle diffraction peaks (i.e., (020) and (111) planes) with much lower intensities. For both **D(C7CO)-BTBT** and **C8-BTBT** films, some degree of edge-on (i.e., (200) and (001), respectively, and higher order peaks) molecular orientations were evident in the XRDs. The BFDH (Bravais, Friedel, Donnay, and Harker) theoretical crystal morphologies[46], [47] predicted plate-like morphologies for both molecules with in-plane crystal growth for edge-on molecular orientations and out-of-plane oriented crystalline domains for face-on oriented molecules (Figure 2. 3b). In **C8-BTBT** film, the relatively large intensity of the (001) first-order diffraction peak as compared to (111) and (020) is very consistent with

the observed SEM morphology (Figure 2. 2c), which indicates that **C8-BTBT** molecules favor to remain in the edge-on molecular orientation during the entire PVD process and promote in-plane crystal growth in an island-based morphology. On the other hand, the presence of strong high-angle diffraction peaks (i.e., (111), (511), (020), (021), and (131)) leading to vertically oriented nano-plates (according to BFDH) in **D(C_7CO)-BTBT** film correlates perfectly with the observed SEM morphology (Figure 2. 2f). The obvious improvement in the morphology of **D(C_7CO)-BTBT** as compared to **C_8-BTBT** originates from presence of highly polar ($\mu \sim 2.9$ D) and electron-deficient carbonyl functionalities, which apparently induces very favorable out-of-plane crystal growth. The analysis of the crystalline planes in the **D(C_7CO)-BTBT** film forming the top-lying 3D morphology revealed that this 3D morphological region has a continuous zigzag motif of *head-to-tail* C=O(δ^-)···(δ^+)C=O (3.52 Å) (∠ O···C=O ~ 95.8° and ∠ C=O···C ~ 139.9°) interactions (Figure 2.3c). In addition, the acidity of the aliphatic α-methylene hydrogens seems to yield weak (α-*methylene*) C-H···O=C (*carbonyl*) (2.87 Å) hydrogen bonds along the slipped stacked molecular packing (Figure2. 3c).[48], [49], [50] The out-of-plane crystal growth was also found to involve strong (*Ph*) C-H···π (*BTBT*)/S···π (*thiophene*) (a = 3.27 Å and c = 2.78 Å < r_{vdw}(H) + r_{vdw}(C) = 2.90 Å/b = 3.22 Å < r_{vdw}(S) + r_{vdw}(C) = 3.50 Å) and S···S (3.43 Å < r_{vdw}(S) + r_{vdw}(S) = 3.60 Å) interactions (Figure 2. 3c).[51] The minimum (*Ar*) C-H···π/S···S interaction distances were found to be ~ 0.2 Å smaller than those in **C_8-BTBT**, which is undoubtedly due to the electronic effect of carbonyl presence (i.e., deshielding on the aromatic π-system and increased acidity for the α-methylene hydrogens).[39] On the basis of the measured distance, carbonyl···carbonyl interactions in **D(C_7CO)-BTBT** film are found to be of dipolar nature,[43], [45], [52] rather than n-π* interactions (typical distances < 3.1-3.2 Å)[20], [44]. These dipolar head-to-tail carbonyl interactions were reported to be strong non-covalent interactions that could be competitive with hydrogen bonds in some biological molecules.[43], [44], [45] On the basis of these findings, the presence of carbonyl units in **D(C_7CO)-BTBT** clearly strengthens intermolecular interactions and facilitate crystal growth into the out-of-plane direction. As a direct evidence of enhanced cohesive energetics in the solid-state after carbonyl functionalization, one should also note the large melting point increase of ~135 °C in **D(C_7CO)-BTBT** as compared to its non-carbonyl analogue **C_8-BTBT**. Our film deposition attempts using unsubstituted **BTBT** (Figure 2. 1a) also yielded only

dense 2D island-based film morphologies with very limited out-of-plane features (Figures 2. 2. and 2.12), which is consistent with the previous reports on thin-films of BTBTs.[37]

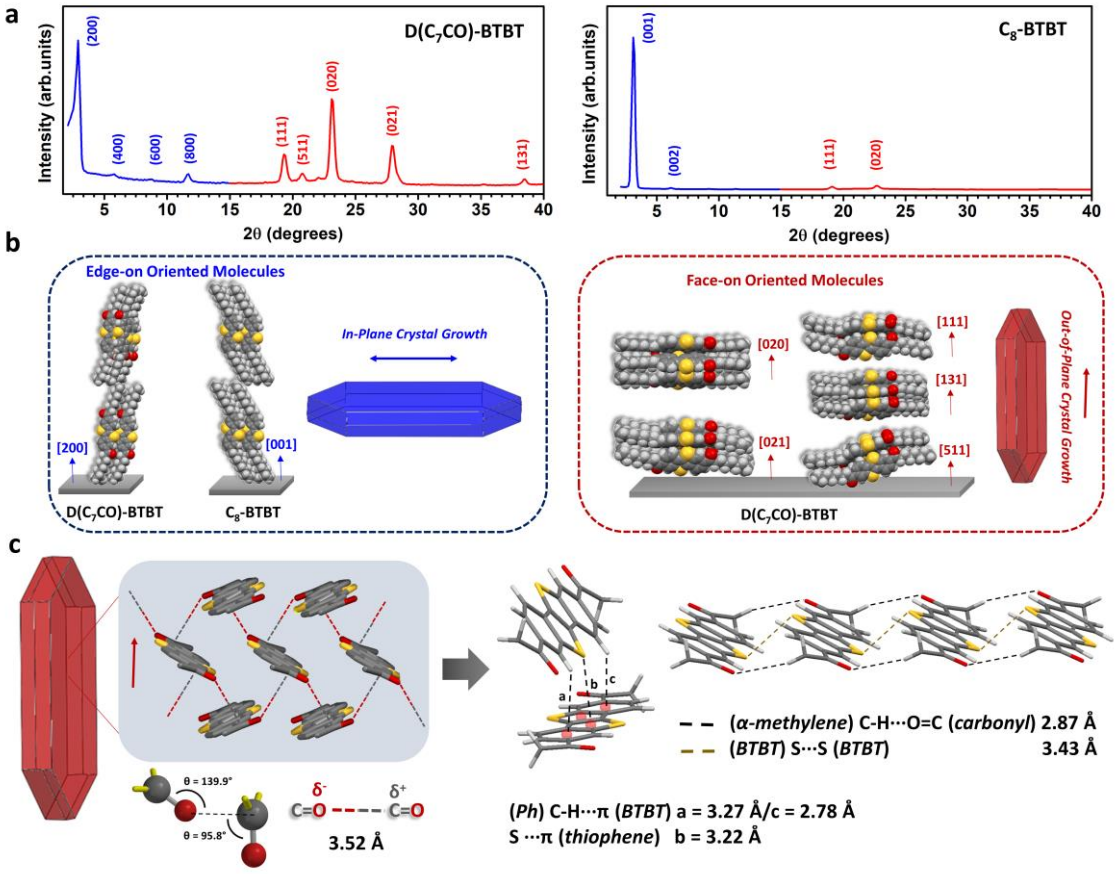

Figure 2.3. XRD characterization and crystal packing in D(C7CO)-BTBT and C8-BTBT films. a The θ-2θ XRD patterns of the **D(C7CO)-BTBT** and **C8-BTBT** films and the assigned out-of-plane crystallographic planes. **b** The schematic packing illustrations of the diffraction planes identified in the out of plane direction and BFDH (Bravais, Friedel, Donnay, and Harker) theoretical crystal growth morphologies formed along these crystallographic directions. **c** The zigzag structural motif of *head-to-tail* carbonyl···carbonyl interactions in the out-of-plane direction with the corresponding (δ^-)O···C(δ^+) distance and angles. Perspective views of the herringbone and slipped-stacked molecular packings and key intermolecular interactions in the out-of-plane direction.

The cross-sectional SEM images reveal the film growth behaviors of the current molecules. While **C_8-BTBT** (Figure 2. 2d) showed a consistent growth of densely packed island-based morphology (Volmer-Weber (VW) growth mode)[47], [53] during the course of the entire film deposition process, a quite unique two-stage film growth behavior was evident for **D(C_7CO)-BTBT** (Figure 2. 2g). Two distinct growth modes were identified for **D(C_7CO)-BTBT**. Similar to that observed in **C_8-BTBT**, the initial ~600 nm of the **D(C_7CO)-BTBT** film showed dense packing of island-based morphology (VW growth mode), which is obviously a direct result of our modified PVD film growth dynamics[42], [47] and the tendency of the crystal growth with lowest energy surfaces ((200) for **D(C_7CO)-BTBT** and (001) for **C_8-BTBT** based on BFDH)[54] covering the high-energy substrate surface (γ = 52.5 mJ/m^2 for native oxide)[55]. Once this dense film is formed, growth mode in **D(C_7CO)-BTBT** shows transition into a highly porous 3D morphology forming loosely connected and vertically oriented nanoplates in the top-lying ~4.5-5.0 μm.

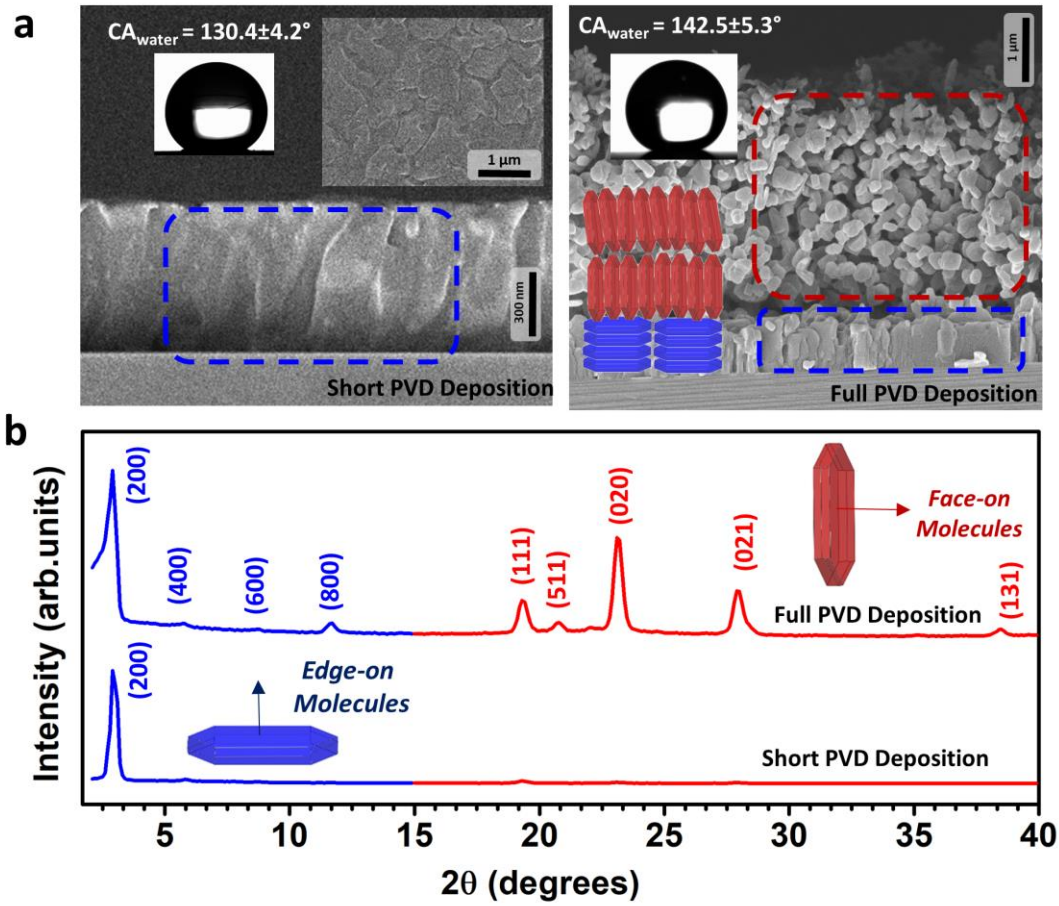

Figure 2.4. Characterization of two-stage film growth in D(C7CO)-BTBT film. a Cross-sectional and top-view SEM images of the nanostructured films of **D(C7CO)-BTBT** for short (~600±50 nm thick film) and full (~5.5±0.2 µm thick film) deposition conditions, photos of the water droplets on them with the corresponding contact angles (CA_{water}). The corresponding edge-on and face-on oriented molecular domains are shown in blue and red, respectively. Scale bars are shown separately for each SEM image. **b** The θ-2θ XRD patterns of the nanostructured films of **D(C7CO)-BTBT** for short (~600±50 nm thick film) and full (~5.5±0.2 µm thick film) deposition conditions along with the assigned out-of-plane crystallographic planes, BFDH (Bravais, Friedel, Donnay, and Harker) theoretical crystal morphologies and the relative directions of "edge-on" and "face-on" oriented molecular packings. Note that herein the terms "edge-on (shown in dark blue)" and "face-on (shown in red)" refer to the molecular orientations with respect to the substrate plane.

In order to understand the origin of this dynamic growth behavior for **D(C7CO)-BTBT**, we first identified the distinct molecular packing in each morphological layer. A controlled short PVD deposition onto Si(001) substrate yielded the first ~600±50 nm layer of densely packed island-based morphology without forming the top-lying 3D morphology (Figure 2. 4a). The out-of-plane XRD characterization of this film (Figure 2. 4b) confirmed that this initial layer consists of mainly edge-on oriented molecules

that shows 2D crystalline growth on the substrate plane as also predicted by the BFDH (Bravais, Friedel, Donnay, and Harker)[46], [47] theoretical crystal morphology (shown in blue in Figures2. 3. and 2. 4). On the basis of this finding, the higher angle diffractions (2θ = 15-40°) in thick **D(C$_7$CO)-BTBT** films are assigned to the top-lying highly porous 3D morphological layer, which is also consistent with the BFDH theoretical crystal morphology (shown in red in Figures 2. 3 and 2. 4). The short PVD deposition allowed us to understand that the initial layer of densely packed island-based morphology gives a highly hydrophobic surface (CA_{water} = 130.4±4.2°, γ = 25.43 mJ/m^2) which further increases to a CA_{water} value of 142.5±5.3° (γ = 22.99 mJ/m^2)) with the contribution of the top-lying 3D porous morphology. Since surface energy and hydrophobicity of the active deposition area are very likely to affect molecular orientation, nucleation/crystal growth, and film morphology,[53], [56], [57] we performed additional depositions on freshly-prepared hydrophobic (CA_{water} ~ 93.5±2.4° and γ = 41.03 mJ/m^2) polystyrene (PS, M_n = 5.2 kDa/PDI = 1.06) grafted SiO_2(300 nm)-Si(100) substrates,[58], [59] and compared these SEM images (Figure 2. 5) to those fabricated directly on the native oxide silicon substrates (Figures 2. 2d and 2. 2g). **D(C$_7$CO)-BTBT** formed porous 3D morphology from the beginning of the film growth when deposited onto the hydrophobic PS-grafted surface. This suggests that the growth of the porous 3D morphology is induced by the surface hydrophobicity onto which molecules are deposited, which could be provided either with a PS-grafted layer or initially deposited island-based **D(C$_7$CO)-BTBT** layer itself. Similar morphology/crystallinity transitions were observed previously for pentacene film deposition (from thin-film phase to bulk phase) after a critical organic layer thickness was reached.[57], [60] Also, various *n*- and *p*-type molecular semiconductors showed a 2D-to-3D transition on graphene in their growth modes during film deposition under vacuum.[42] Here, an interesting question arises as to why such a thick (~ 600 nm) **D(C$_7$CO)-BTBT** layer is needed to induce 3D morphological growth. We note that this layer was formed in only 15 seconds based on the ultra-high film growth rate (~ 40 nm/s) of our PVD process. Therefore, this densely packed initial layer was formed in a relatively short time before the deposition process reaches a thermodynamic equilibrium to induce the continued 3D growth. We believe that this initial layer could be made much thinner with a more controlled deposition rate, which seems not to be important for our study at this point since the top ~1-2 μm morphology is crucial for SERS

activity. On the other hand, the PS-grafted hydrophobic surface still resulted in dense island-based film growth for **C_8-BTBT** with no porous 3D morphology. Therefore, it seems that there are threshold surface properties (i.e., surface energy and hydrophobicity), probably unique to each molecular structure, essential to induce 3D porous morphological growth. A crystal growth on a substrate that does not meet these properties would induce only 2D crystal growth since it requires the lowest-energy crystalline surface, that is the largest area surface in the BFDH morphology,[54] to be on the substrate plane. The combination of intrinsic factors such as intermolecular (dipolar carbonyl, strong C-H···π/S···π/S···S, and weak C-H···C=O hydrogen bonding) interactions along the crystal growth direction and extrinsic factors such as surface energy and hydrophobicity onto which molecules are deposited were found to be the key factors in the formation of porous 3D morphology for **D(C_7CO)-BTBT** film with vertical oriented nanoplates. The top morphology of the **D(C_7CO)-BTBT** film is highly favorable for SERS detection since it enables a large surface area for the analyte deposition and allows for effective π-interactions between analyte and face-on **D(C_7CO)-BTBT** molecules in varied crystalline orientations.[31], [41]

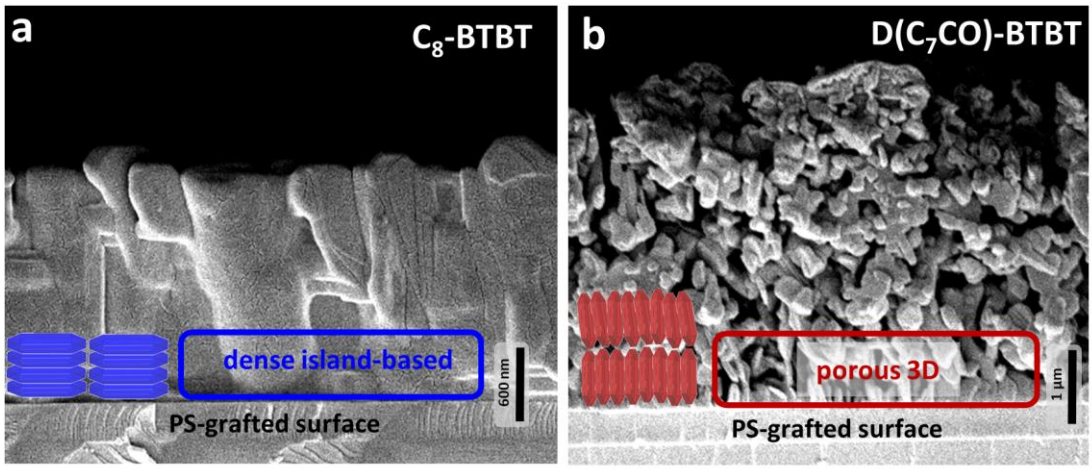

Figure 2.5. SEM characterization of C_8-BTBT *vs.* D(C_7CO)-BTBT films on PS-grafted surfaces. Cross-sectional SEM images of the nanostructured films of **C_8-BTBT** (**a**) and **D(C_7CO)-BTBT** (**b**) on hydrophobic PS-grafted surfaces. The corresponding dense island-based (in blue) and porous 3D (in red) morphologies, and the relative directions of "face-on" (in blue) and "edge-on" (in red) oriented BFDH (Bravais, Friedel, Donnay, and Harker) theoretical crystal morphologies were shown for the initial stages of the organic film growths. Scale bars are shown separately for each SEM image.

2.2.4 Raman Signal Enhancements For Nanostructured D(C_7CO)-BTBT And C_8-BTBT Films, And The Origins Of The Chemical Enhancement Mechanism

The effects of BTBT molecular design, carbonyl-functionalization, and electronic structure on intermolecular interactions and film growth (microstructure/morphology) mechanisms have been discussed in detail in the previous section. In this section, the Raman signal enhancement abilities of the current 3D-nanostructured **D(C_7CO)-BTBT** and 2D-morphology dominant **C_8-BTBT** films were investigated using four different analyte molecules (i.e., methylene blue (MB)[61], rhodamine 6G (R6G)[62], crystal violet (CV)[63], and malachite green (MG)[64]) with varied electronic structures and HOMO/LUMO levels spanning 1.0 and 1.5 eV energy ranges, respectively (Figure 2. 6). These molecules were drop-casted from their aqueous solutions (1×10^{-3} M) onto semiconductor films, and a Raman laser excitation

wavelength of 785 nm (1.58 eV) was employed in the SERS experiments, at which both semiconductors and the analyte molecules exhibit no electronic transitions ($\lambda_{abs}^{\text{low-energy onset}}$'s < 700 nm, Figures 2. 2. And 2. 13). Therefore, purely analyte electronic excitation (μ_{mol}) or semiconductor exciton (band gap) resonances ($\mu_{semiconductor}$) could not contribute to the Raman enhancement in the current analyte/*o*-SERS systems.

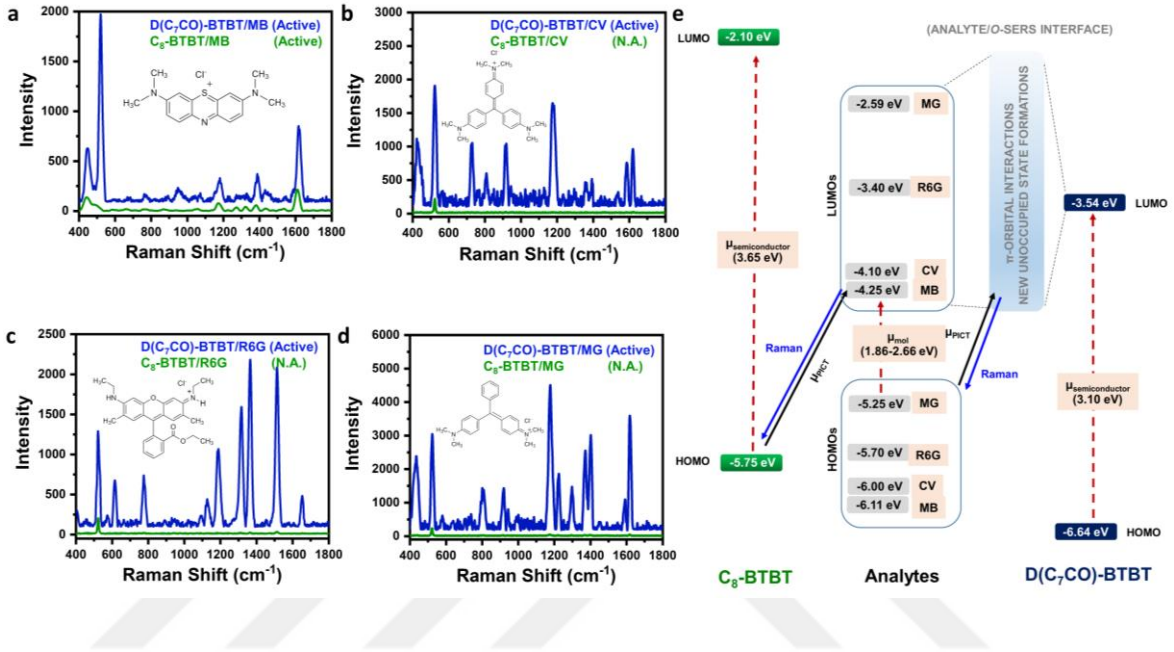

Figure 2.6. Raman enhancement for D(C7CO)-BTBT and C8-BTBT films, and chemical enhancement mechanism. SERS spectra of methylene blue (MB) (**a**), crystal violet (CV) (**b**), rhodamine 6G (R6G) (**c**), and malachite green (MG) (**d**) analytes on **D(C7CO)-BTBT** and **C8-BTBT** films. Insets depict the molecular structures of the analyte molecules. **e** Energy level diagram for the current analyte/*o*-SERS systems for **D(C7CO)-BTBT** and **C8-BTBT** showing the frontier molecular orbital (HOMO/LUMO) energies and plausible (shown with solid black arrow)/non-plausible (shown with dashed red arrows) transitions. μ_{PICT} stands for photo-induced charge-transfer between analyte and semiconductor under the excitation of 785 nm. Raman signals were produced during the transitions shown with blue solid arrows.

As shown in Figures 2. 6 and Figures 2.14, while 2D-morphology dominant **C8-BTBT** films did not show any Raman signal enhancement with R6G, CV, and MG analyte molecules and showed SERS signals only for MB (green spectrum in Figure 2. 6a) with low intensities (I's < 250), nanostructured **D(C7CO)-BTBT** films showed substantial Raman enhancements for all analyte molecules with I's of up to 4,000-5,000. The Raman shifts and the assignments for the observed bands are listed in Table

2. 1. The prominent Raman peaks for MB (ν(C–C) ring stretches at 1,621 cm^{-1}, δ(C-N-C) skeletal deformation at 445 cm^{-1}, and ν(C-N) symmetric/asymmetric stretches at 1,391/1,435 cm^{-1}) are slightly different than those observed on metallic platforms[31], [47] indicating the presence of analyte-semiconductor interaction specific signal enhancements.[65] We note that, despite the low performance on **C_8-BTBT** films, a molecular-specific (i.e., among a sample of four analyte molecules) Raman enhancement is achieved on an organic-SERS platform.[66] Considering that undoped π-conjugated organic semiconductors have a low intrinsic free carrier density (10^{13} carrier/cm^3)[31], which is much lower than those of metals (10^{22} – 10^{23} carrier/cm^3)[67], electromagnetic contribution to SERS is an implausible mechanism for the current organic films. Therefore, as demonstrated in the previous reports by Lombardi et al.[65], [68], [69] and our research groups[31], [41] on (in)organic SERS platforms, charge-transfer (CT) resonance occurred at the analyte/semiconductor interface should be the key player to enhance the polarizability derivative tensor for analyte vibrational modes, which consequently leads to Raman signal enhancements. We also note that the CT resonances could couple with 3D-morphology-driven Mie scattering to further benefit from the porous nanostructured morphology in **D(C_7CO)-BTBT** films.[70] The formation of CT resonances requires strong π-orbital interactions (mixing) between analyte and semiconductor molecules at the interface. When the semiconductor molecules have a properly oriented π-orbital system for effective spatial overlap, which is a face-on orientation towards the analyte-semiconductor interface, and there is a small energy difference between the corresponding (i.e., analyte and semiconductor) wave functions, a strong interfacial state formation could be expected. Our previous studies revealed that π-electron deficient (π-delocalized LUMOs with E_{LUMO} < -3 eV) **DFH-4T** and **DFP-4T** molecules, in their properly oriented nanostructured films, formed resonant CT-states with MB and R6G analytes.[31], [41] As evidenced by the microstructural analysis for **C_8-BTBT** (*vide supra*), the edge-on π-backbone dominant orientation with σ-insulating alkyl substituents pointing towards the analyte-semiconductor interface precludes an efficient π-π mixing in the case of analyte/**C_8-BTBT** pair for the majority of this semiconductor film. Therefore, on **C_8-BTBT** film surface, there is only a limited region with face-on semiconductor π-backbones, which in the first place deteriorates Raman enhancements (I's < 250). Secondly, the only Raman enhancement observed on **C_8-BTBT** was with the lowest-LUMO (-4.25 eV)

analyte molecule, MB, in which an energetically feasible resonant transition (~1.50 eV based on vacuum energy levels) could be defined from semiconductor to analyte frontier π-orbitals ($\psi_{HOMO(C8\text{-}BTBT)} \rightarrow \psi_{LUMO(MB)}$, μ_{PICT} in Figure 2. 6e). However, when it comes to the nanostructured **D(C$_7$CO)-BTBT** film, energetically feasible transitions in resonance with the incident photon energy (1.58 eV (785 nm)) could not be identified between the pristine analyte and **D(C$_7$CO)-BTBT** frontier π-orbitals since **D(C$_7$CO)-BTBT**'s HOMO is stabilized by ~0.9 eV. As a result, all plausible transitions would require energies larger than 2 eV. Despite this energetic mismatch, the fact that all four analyte molecules showed strong Raman enhancements suggests that there should be strong frontier π-orbital interaction at the semiconductor-analyte interface on **D(C$_7$CO)-BTBT** film forming new interfacial states. In order to understand the origin of these frontier π-orbital interactions, the energy level diagram for both semiconductors and the analyte molecules are depicted in Figure 2. 6e. The first point to be made from this diagram is that, going from **C$_8$-BTBT** to **D(C$_7$CO)-BTBT**, the semiconductor's HOMO is stabilized by ~0.9 eV that results in energy mismatch between the HOMOs. If the π-orbital interactions at the analyte/semiconductor interface were to occur between the HOMOs, from an energetic standpoint, one would expect an exact opposite SERS finding that **C$_8$-BTBT** film shows SERS activity with all analyte molecules and **D(C$_7$CO)-BTBT** is SERS-inactive with these analytes. This, however, is not the case in our SERS measurements. Therefore, based on our SERS results, the key interfacial π-orbital mixing should be between the LUMO's of the semiconductor and analyte molecules. From a purely quantum mechanical perspective, the higher energy and larger spatial extension of LUMO levels, when compared to HOMOs, make them more likely to be perturbed and interact in complex π-systems, especially for intermolecular orbital interactions that requires spatial overlap of the corresponding wave functions.[71] Consistent with the discussions made earlier for **D(C$_7$CO)-BTBT** *vs.* **C$_8$-BTBT**, while the LUMO energy level of **C$_8$-BTBT** is much higher (up to ~ 2 eV energy mismatch) than those of analyte molecules, **D(C$_7$CO)-BTBT**'s LUMO is more π-extended and stabilized due to carbonyls, and becomes energetically close to those of the analytes. As shown in Figure 6e, **D(C$_7$CO)-BTBT**'s LUMO lies symmetrically with respect to those of all analyte molecules. This enables significant wave function mixing with the π-conjugated analyte molecules to yield new interfacial unoccupied states for low-energy CT-transitions. The Raman enhancements observed in the nanostructured **D(C$_7$CO)-**

BTBT films most likely benefits from photoinduced "$\psi_{HOMO(analyte)} \rightarrow \psi_{new\ unoccupied\ states}$" charge transfers ($\mu_{PICT}$ in Figure 2. 6e). It is noteworthy that since **D(C$_7$CO)-BTBT** film surface includes varied crystalline planes (i.e., (111), (511), (020), (021), and (131)) with all nearly face-on oriented molecules, semiconductor-analyte π-interactions could occur in various geometries to find the most favorable orientation for each vibrational mode.

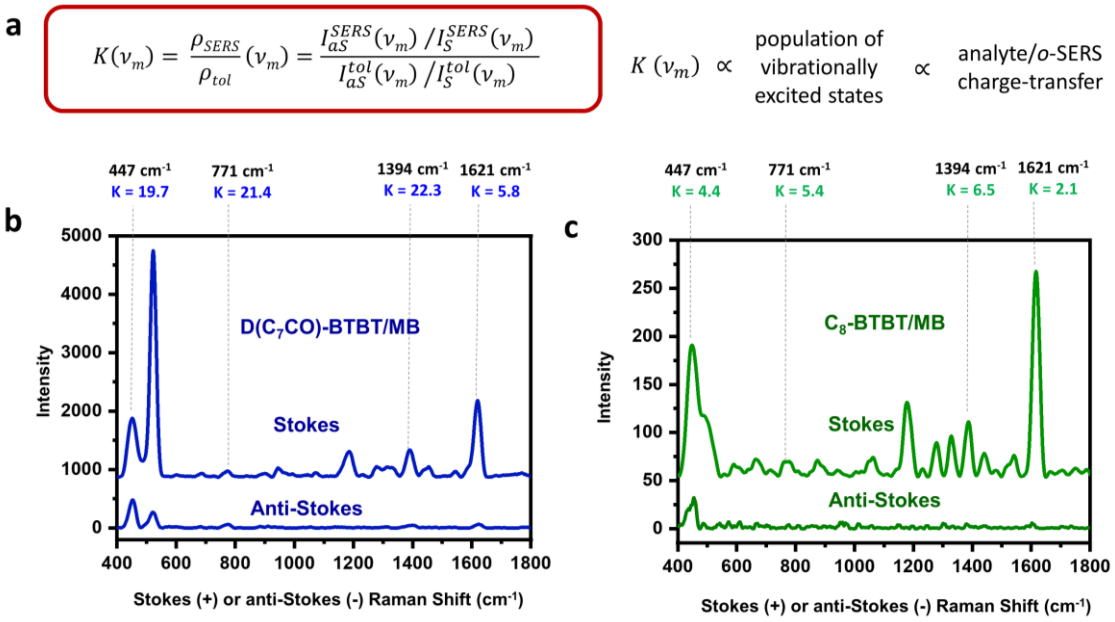

Figure 2.7. Stokes *vs.* anti-Stokes Raman spectra for D(C$_7$CO)-BTBT and C$_8$-BTBT films. a The equation describing the degree (*K*) by which the SERS anti-Stokes signal exceeded the expectation of the Boltzmann distribution. Stokes and anti-Stokes Raman spectra for **D(C$_7$CO)-BTBT/MB** (**b**) and **C$_8$-BTBT/MB** (**c**) analyte/*o*-SERS systems, and the calculated *K* values for selected Raman peaks (ν_m). I_{aS}^{SERS} and I_S^{SERS} are the observed anti-Stokes and Stokes signal intensities, respectively, for the analyte molecule on the current films. I_{aS}^{tol} and I_S^{tol} are the anti-Stokes and Stokes signal intensities, respectively, for toluene.

As previously demonstrated by Linic and co-workers, charge-transfer processes within a complex metal-adsorbate system can be identified experimentally via SERS.[72] This identification is mainly based on elevation of anti-Stokes Raman signal intensities, which is the direct result of increased population of excited vibrational states compared to the equilibrated states when charge excitation occurs on a π-system.[73], [74] Therefore, for a defined vibrational mode, the ratio of anti-Stokes to Stokes signal intensities indicates charge-transfer efficiency. To make a direct comparison, MB

analyte was employed since it is the only molecule to exhibit SERS activity on both semiconductor surfaces. The Stokes and anti-Stokes SERS spectra were collected under the laser excitation of 1.58 eV. As shown in Figure 2. 7, we first note that the anti-Stokes signal intensities collected on **D(C$_7$CO)-BTBT** film are much higher than those on **C$_8$-BTBT** film. To better understand these observations, the ratios of anti-Stokes/Stokes Raman signal intensities (ρ_{SERS}) for specific MB vibrational modes (ν_m) were calculated and compared with the ratio for a similar energy mode in liquid toluene (ρ_{tol}) as demonstrated earlier.[75], [76] The calculations were carried out using the equation shown in Figure 2. 7a, in which *K* describes the degree by which the SERS anti-Stokes signal exceeded the expectation of the Boltzmann distribution. While I_{aS}^{SERS} and I_S^{SERS} are the observed anti-Stokes and Stokes signal intensities, respectively, for the analyte molecule on the current films, I_{aS}^{tol} and I_S^{tol} are the anti-Stokes and Stokes signal intensities, respectively, for toluene. The calculated *K* values for **D(C$_7$CO)-BTBT/MB** were found to be large and in the range of 5.8 to 22.3, whereas those of **C$_8$-BTBT/MB** were much smaller (2.1-6.5). These results provide further evidence that interfacial charge-transfer processes are more effective within the **D(C$_7$CO)-BTBT/MB** system when compared with the **C$_8$-BTBT/MB** system.

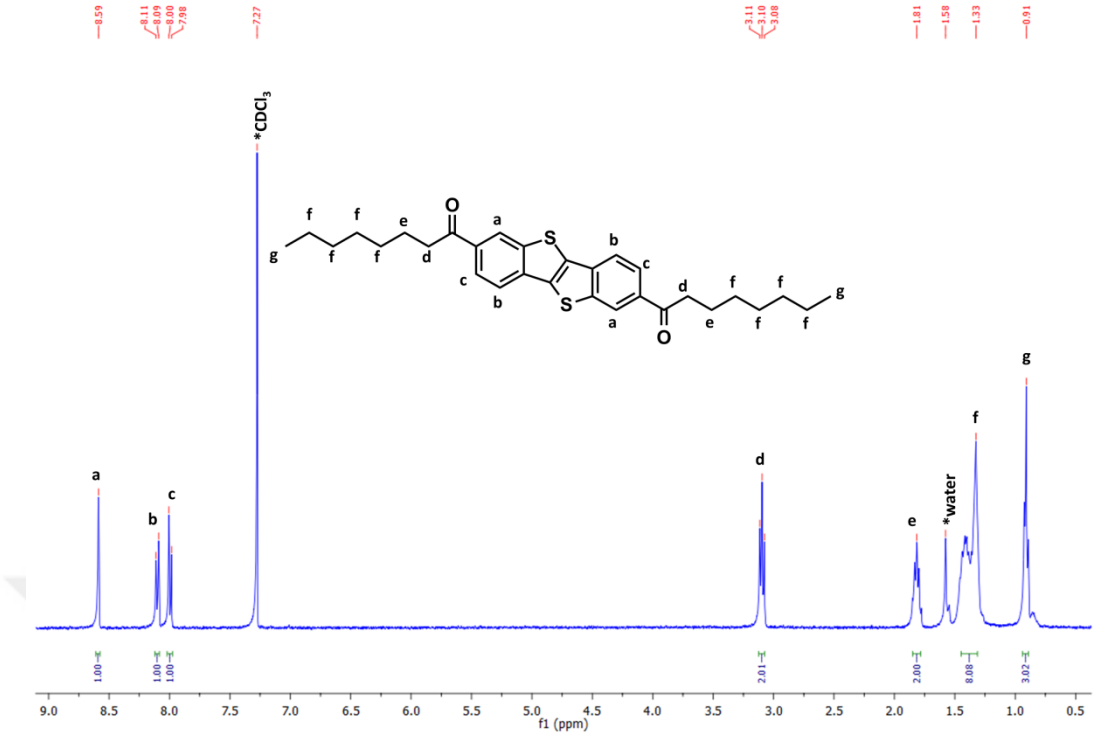

Figure 2.8. ^{1}H NMR spectra of **D(C$_7$CO)-BTBT** measured in $CDCl_3$.

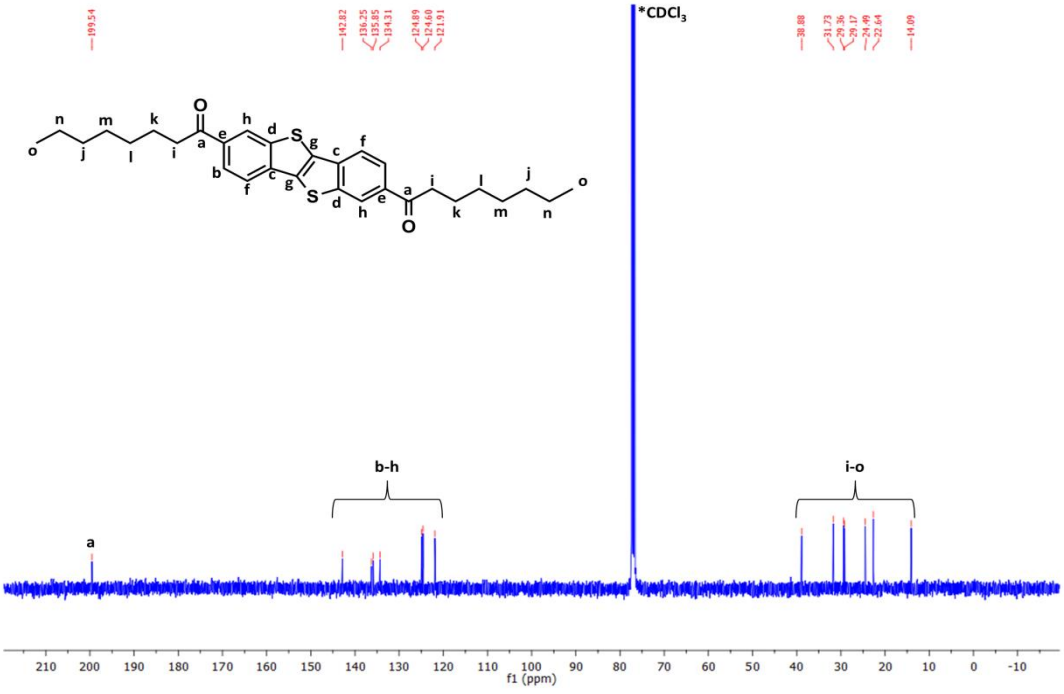

Figure 2.9. ^{13}C NMR spectra of **D(C$_7$CO)-BTBT** measured in $CDCl_3$.

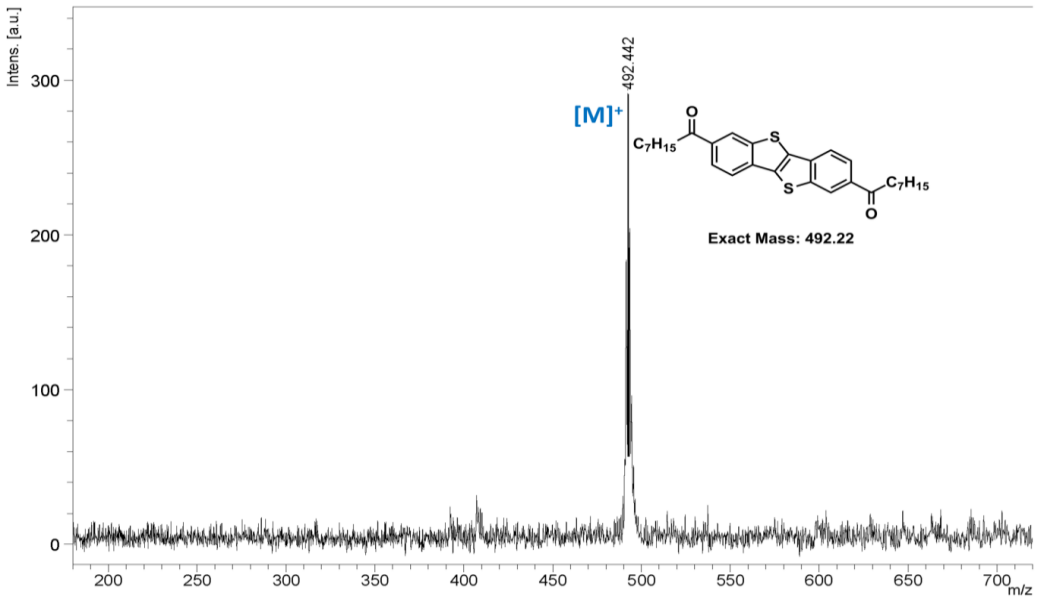

Figure 2.10. Positive ion and linear mode MALDI TOF-MS spectrum of **D(C_7CO)-BTBT**.

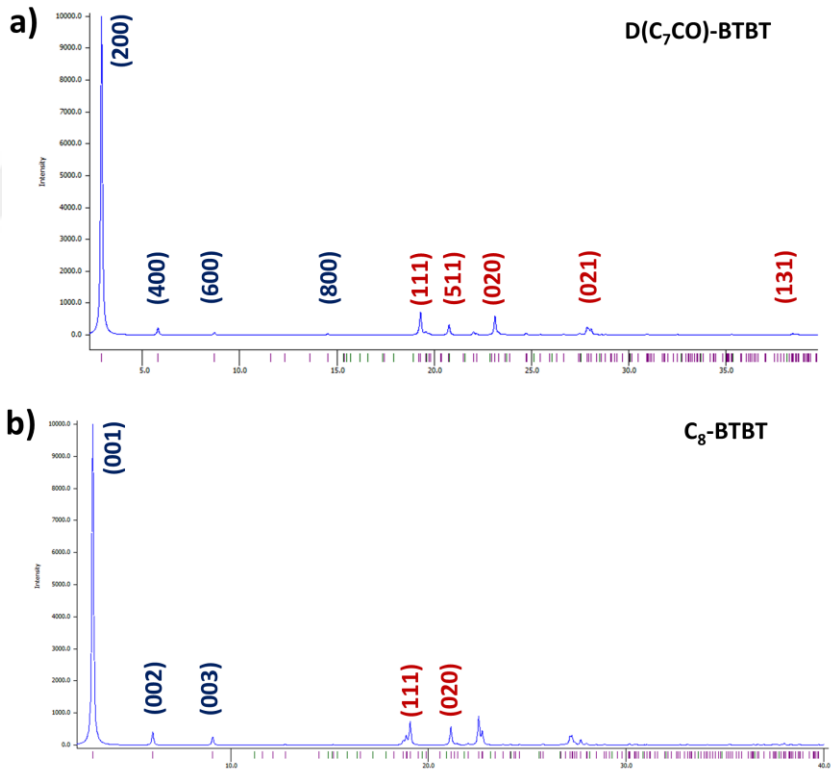

Figure 2.11. Simulated XRD powder patterns based on the single-crystal structures for **D(C_7CO)-BTBT** (a) and **C_8-BTBT** (b) indicating the selected matching diffraction peaks and lattice planes. The dark blue and red assignment colors refer to the edge-on and face-on molecular orientations, respectively, within that lattice plane with respect to the substrate plane.

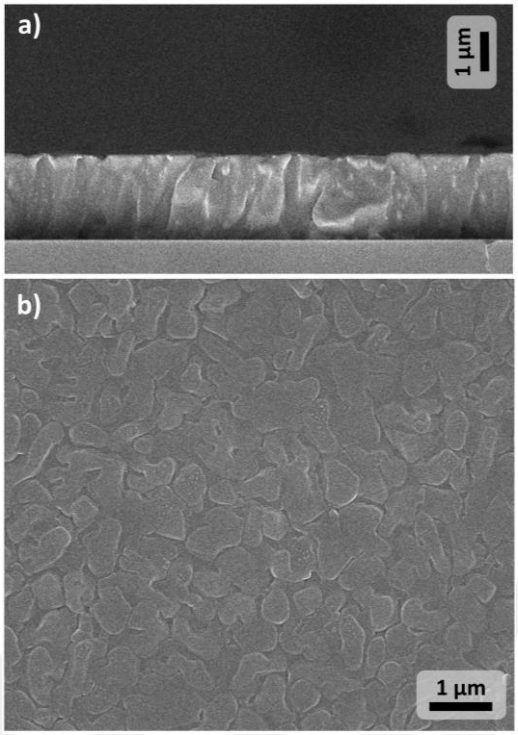

Figure 2.12. Cross-sectional (a) and top-view (b) SEM images of the **BTBT** film deposited via physical vapor deposition method. Scale bars are shown separately for each SEM image.

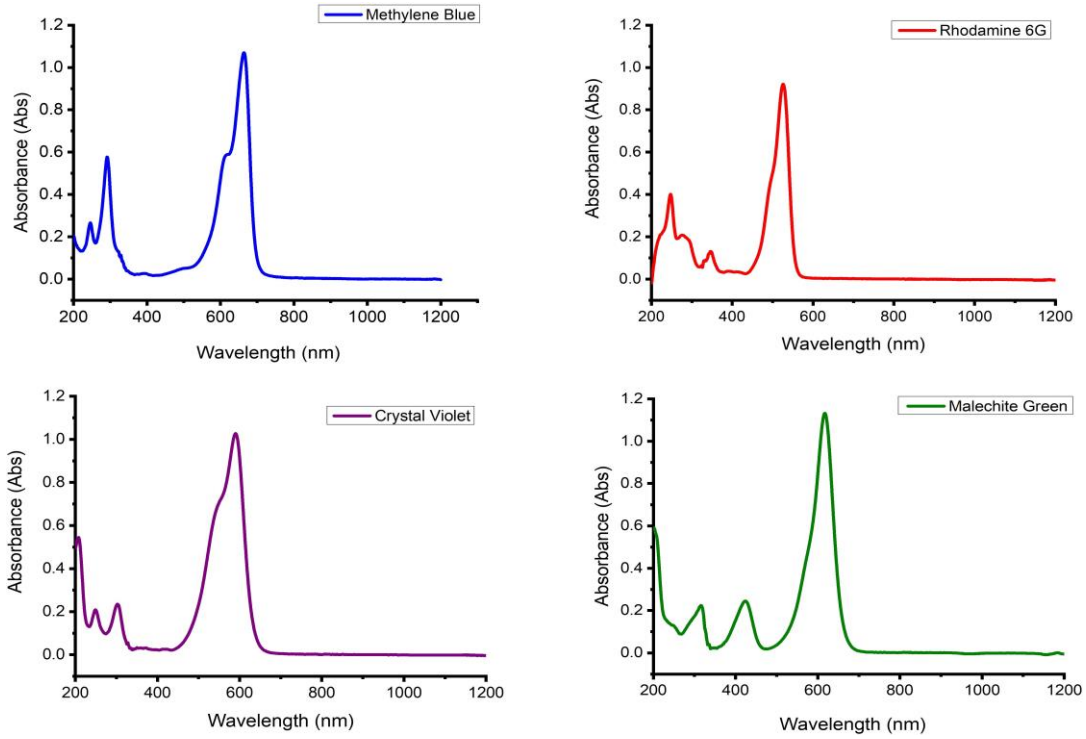

Figure 2.13. UV-vis optical absorption spectra of **MB**, **R6G**, **CV**, and **MG**.

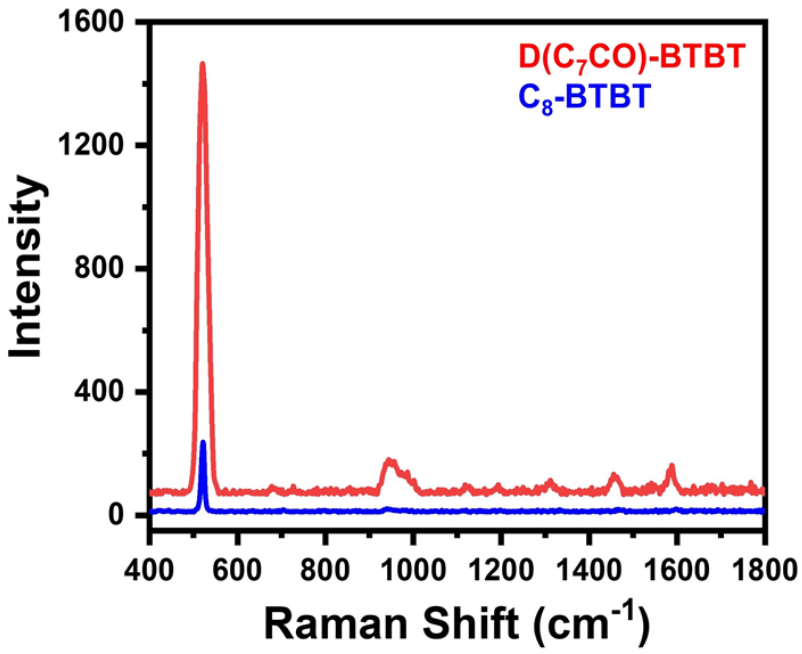

Figure 2.14. Raman spectra for pristine **D(C$_7$CO)-BTBT** and **C$_8$-BTBT** films.

Table 2.1. Band positions (in cm^{-1}) and their assignments for SERS spectra of **MB**, **R6G**, **CV**, and **MG** on **C_8-BTBT** and **D(C_7CO)-BTBT** films.

MB on C_8-BTBT films (cm^{-1})	**MB on D(C_7CO)-BTBT films (cm^{-1})**	**Band Assignments[1,2]**
443	445	δ(C-N-C)
763	766	γ(C-H)
1174	1181	ν(C-N)
1382	1391	α(C-H)
1432	1435	ν(C-N)
1614	1621	ν(C-C)$_{ring}$

ν, stretching; α, in-plane ring deformation; γ, out-of-plane bending; and δ, skeletal deformation.

R6G on C_8-BTBT films (cm^{-1})	**R6G on D(C_7CO)-BTBT films (cm^{-1})**	**Band Assignments[3,4]**
-	612	β(C─C) $_{\text{xanthene ring}}$/β(C─C) $_{\text{phenyl ring}}$
-	774	γ(C─H)
-	1125	β(C─H) $_{\text{xanthene ring}}$/β(C─H)$_{\text{phenyl ring}}$
-	1186	β(C─H) $_{\text{xanthene ring}}$
-	1314	Hybrid mode (xanthene, phenyl ring and NHC_2H_5)
-	1651, 1512, 1360	ν_s(C─C)$_{\text{xanthene ring}}$

CV on C_8-BTBT films (cm^{-1})	**CV on D(C_7CO)-BTBT films (cm^{-1})**	**Band Assignments[5,6]**
-	424	δ(C─N─C)/δ(C─C_{center}─ C)
-	726	ν(C─N)
-	916, 940	δ(C─C_{center}─C)
-	1178	ν_{as}(C─C_{center}─C)
-	1392	$\delta(CH_3)$/α(C─H)/δ(C─C─C)$_{ring}$
-	1540, 1585	ν_s(C_{ring}─N)/$\delta_s(CH_3$
-	1622	ν_s(C─C)

MG on C_8-BTBT films (cm^{-1})	**MG on D(C_7CO)-BTBT films (cm^{-1})**	**Band Assignments[7,8]**
-	436	γ(Ph─C─Ph)
-	799	γ(C─H)$_{ring}$
-	919	Ring skeletal vibration
-	1179	β(C─H)$_{ring}$
-	1223	δ_s(C─C)$_{ring}$
-	1299	ν_s(C─C)$_{ring}$
-	1367, 1398	ν_s(N─Ph─C)
-	1591, 1619	ν_s(C─C)

ν, stretching; β, in-plane bending; γ, out-of-plane bending; and δ, skeletal deformation.

2.3 Discussion

Highly crystalline nanostructured porous organic films comprised of π-electron deficient (low-LUMO) thienoacene molecule **D(C$_7$CO)-BTBT** have been fabricated via PVD and showed great promise in organic-SERS applications. Following our recent breakthroughs with oligothiophenes, a completely different π-framework and a unique functionalization strategy are demonstrated. Different than our previous SERS-active oligothiophenes, the current semiconductor was prepared on the gram-scale in ambient via facile Friedel-Crafts acylation reaction without any high-cost transition-metal catalyst. The purification was also based on simple precipitation/solvent washing (i.e., no need for tedious chromatography/sublimation). On the basis of straight comparison to the non-functionalized analogue, **C$_8$-BTBT**, at molecular level and detailed film characterizations, film growth mechanisms have been revealed, and polar carbonyl functionalization was found to enable proper nanostructured film formation (out-of-plane crystal growth) with face-on π-backbones via dipolar C=O···C=O interactions, hydrogen bonds, and strengthened π-interactions. The analysis of the electronic structures and the ratio of the anti-Stokes to Stokes SERS suggest that the π-extended and stabilized LUMOs with crystalline face-on orientations in varied directions, all of which are the direct results of carbonyl functionalization, are key for the chemical enhancement mechanism to be effective. Instead of running more complicated electronic structure calculations involving analyte/*o*-SERS complexes and excited-state characteristics, as we have previously performed,[31], [41] our analysis based on frontier orbitals vacuum energy levels herein provides a facile guidance to elucidate SERS ability of π-conjugated semiconductors. Using **C$_8$-BTBT** platform with a relatively high-lying LUMO that does not allow for effective π-mixing with the corresponding orbitals of the analytes, molecular sensitivity for Raman enhancement is also achieved on an organic-SERS platform. Employing a future research direction towards carbonyl-functionalized (hetero)acenes having relatively easy synthesis-purification could bring in significant opportunities for organic-SERS platforms such as low materials cost, gram-scale synthesis, structural versatility for potential SERS-based molecular sensors, and solution-based film fabrication. These are envisioned based on

the following facts: (i) Friedel-Crafts acylation is a highly universal reaction that could be performed on most of the π-systems and does not require a pre-existing group (e.g., triaalkylstannyl, boronic esters/acids, or halides in cross-coupling reactions), which gives a great flexibility to employ various (hetero)acenes, (ii) single or multiple ("di-" in this study) functionalization(s) could be performed and the substituent(s) adjacent to the carbonyl unit could be of any chemical structure, which gives a great tuning ability for molecular/electronic structures, and (iii) proper substituents adjacent to the carbonyl unit would increase molecular solubility, which could allow for the fabrication of solution-processed semiconductor thin-films that could be exposed to a post-deposition process (e.g., thermal or solvent annealing) to form nanostructured surfaces. Especially, mono-carbonyl functionalization might give a proper tuning of LUMO (i.e., not as low as di-carbonyl derivatives) for enhanced molecular sensitivity. As another potential future direction from a molecular engineering perspective, different polar EWD-functionalities (e.g., cyano-, dicyanovinylene-, or nitro-) that provides frontier orbital tuning and π-delocalization (negative mesomeric effect) at the same time could also be employed to explore similar nanostructured films and Raman enhancements. Future studies with other polar EWD unit-functionalized (hetero)acenes and additional analyte molecules would provide better understanding of the role of (hetero)acenes, polar EWD units, and substituents in the formation of nanostructured highly crystalline semiconductor films and the role of LUMOs in determining SERS activity and molecular sensitivity

2.4 Methods

Synthesis, chemical characterization, computational/crystal analysis, and fabrication/characterization of organic semiconductor films. BTBT-based π-conjugated semiconductors 1,1'-(benzo[b]benzo[4,5]thieno[2,3-d]thiophene-2,7-diyl)bis(octan-1-one) (**D(C$_7$CO)-BTBT**) and 2,7-dioctyl[1]benzothieno[3,2-*b*][1]benzothiophene (**C$_8$-BTBT**) were used as molecular building blocks in physical vapor deposition. Prior to the semiconductor film fabrication, Si wafers (001 crystallographic orientation and 1-10 Ω resistivity) were cleaned in sonicating bath with acetone and ethanol (10 min each) and dried with nitrogen gas. The wafers were then treated with piranha solution for 1 h, washed with DI water, and dried with nitrogen gas. To further remove contaminants

from the wafer surface, pre-cleaned samples were treated with UV-ozone cleaner for 15 min. For micro-/nanostructured semiconductor film depositions, **D(C_7CO)-BTBT** or **C_8-BTBT** powder (10-20 mg) was placed in a tungsten boat and thermally evaporated using a conventional PVD system (NANOVAK HV) under high vacuum ($1 \pm 0.2 \times 10^{-6}$ Torr). During film deposition, a 90° deposition angle along with an ultrafast deposition rate (~ 40 nm s^{-1}) and a short source-to-substrate distance (~ 7 cm) were employed. The morphology and microstructure of the deposited films were characterized with scanning electron microscope (Zeiss, Gemini-SEM 500 Field Emission SEM) and X-ray diffraction (Malvern Panalytical, Empyrean X-Ray Diffractometer). UV-vis absorption and water contact angle measurements were carried out using a Shimadzu 2600 UV-vis-near-IR spectrophotometer and a Krüss, DSA 100 drop shape analyzer, respectively. PS-SiO_2(300 nm)-Si(100) substrates were prepared by using grafting-to method (ω-hydroxy-terminated poly(styrene) from Polymer Source Inc., Canada, M_n = 5.2 kDa and PDI = 1.06) onto SiO_2(300 nm)-Si(100) substrates and in accordance with the reported procedures.[58], [59] The theoretical morphology for **D(C_7CO)-BTBT** was calculated according to the BFDH (Bravais, Friedel, Donnay, and Harker) method using the program Mercury 2.4 (CCDC).

SERS experiments. Raman signal enhancement behavior of the films was investigated using MB, R6G, CV, and MG as reporter molecules at an excitation wavelength of 785 nm. In a typical experiment, 5.0 μL aqueous analyte solution with a concentration of 10^{-3} M was dripped onto the fabricated films followed by storing in a hood at room temperature until dry. Raman spectra were subsequently collected from at least ten different spots across the entire dried area using a high-resolution confocal Raman spectrometer (Jasco NRS-4500). A 20X objective lens with a laser spot diameter of ~3 μm, and 30 mW laser power were used to obtain all Raman spectra. Acquisition time was also 10 s for SERS investigation of the films and 2 s for Stokes and anti-Stokes Raman investigation.

Synthesis and Structural Characterization. The reactions in ambient were carried out by simply capping the reaction flask with a rubber septum. Conventional Schlenk techniques were used for the reactions performed under N_2 atmosphere. All chemicals were purchased from commercial sources and used without further purification unless otherwise noted. $^1H/^{13}C$ NMR spectra were recorded on a Bruker 400 spectrometer (^1H,

400 MHz; ^{13}C, 100 MHz). Elemental analyses were done on a LecoTruspec Micro model instrument. High-resolution mass spectra were measured on a Bruker Microflex LT MALDI-TOF-MS Instrument. The optimization of the molecular geometries and the analysis of the frontier molecular orbitals were carried out by Gaussian 09 using density functional theory (DFT) at B3LYP/6-31G** level.[77] The synthesis of [1]benzothieno[3,2-b][1]benzothiophene (**BTBT**) and 2,7-dioctyl[1]benzothieno[3,2-*b*][1]benzothiophene (**C_8-BTBT**) were carried out in accordance with the reported procedures.[37], [40]

Synthesis of 1,1'-(benzo[b]benzo[4,5]thieno[2,3-d]thiophene-2,7-diyl)bis(octan-1-one) **(D(C_7CO)-BTBT)**: $AlCl_3$ (3.03 g, 22.76 mmol) was added into a solution of [1]benzothieno[3,2-b][1]benzothiophene (1.5 g, 6.24 mmol) in anhydrous dichloromethane (150 mL) at −10 °C under nitrogen or ambient. The resulting solution was stirred at −10 °C for 30 min. Then, the reaction mixture cooled down to −78 °C. Octanoyl chloride (5.075 g, 31.20 mmol) was subsequently added dropwise, and the mixture was stirred for 1 h at the same temperature. The reaction mixture was then allowed to warm to room temperature and stirred for 2 days under nitrogen or ambient. The reaction mixture was quenched with water and the precipitated solid was collected by vacuum filtration, and washed with water and methanol, respectively. In order to remove mono-acylated by-product from the precipitated solid, small amount (~100 ml) of dichloromethane was used during solvent washing. The product was obtained as a pale yellow solid (2.09 g, 68% yield-under nitrogen), which showed sufficient purity and was directly used in physical vapor deposition. The reaction yield was ~60% when the reaction was carried out in ambient conditions. Melting point: 265-266 °C; ^1H NMR (400 MHz, $CDCl_3$), δ (ppm): 8.59 (s, 2H), 8.09 (d, 2H, J = 8.0 Hz), 7.98 (d, 2H, J = 8.0 Hz), 3.10 (t, 4H, J = 12.0 Hz), 1.78-1.83 (m, 4H), 1.33-1.44 (m, 16H), 0.89-0.92 (t, 6H, J = 16.0 Hz); ^{13}C NMR (100 MHz, $CDCl_3$), δ (ppm): 199.5, 142.8, 136.2, 135.8, 134.3, 124.9, 124.6, 121.9, 38.9, 31.7, 29.4, 29.2, 24.5, 22.6, 14.1; MS (MALDI-TOF) *m/z* calcd for $C_{30}H_{36}O_2S_2$: 492.22 [M^+]; found: 492.44 [M^+]; elemental analysis calcd (%) for $C_{30}H_{36}O_2S_2$: C, 73.13; H, 7.36; found: C, 73.46; H, 7.67.

Chapter 3

Hansen Solubility Approach Towards Green Solvent Processing: N-Channel Organic Field-Effect Transistors in Ambient

3.1 Introduction

Electron deficient π-conjugated small molecules represent a captivating class of organic materials that have shown tremendous potential as semiconductors in *n*-channel organic field-effect transistors (OFETs), as well as electron transport layers in a wide range of optoelectronic devices including photovoltaics and light-emitting diodes/transistors.[78], [79], [80], [81] Although a π-system functionalized with an electron-withdrawing group (e.g., fluoro, imide, carbonyl, cyano, and dicyanovinylene) becomes technically π-electron deficient,[82], [83], [84] the famous examples with high electron mobilites include naphthalene diimide,[85], [86], [87] perylene diimide,[88], [89] quinoidal[90], [91], [92], and indenofluorene[93], [94] π-architectures. Small molecules offer a remarkable fine tuning ability over frontier orbital energetics, optical transitions, physicochemical properties, and solubilities, when compared to polymers and macromolecules.[36], [95], [96] Furthermore, conventional synthesis and purification processes for small molecules enable the reproducible achievement of high purity levels with monodispersity and minimal batch-to-batch variations.[33], [97], [98] Over the past three decades, *n*-type semiconducting molecules have played an essential

role in advancing the functions and performances of organic (opto)electronic devices, which has enabled a plethora of structural, physicochemical, mechanical, and optoelectronic properties that are mostly unattainable with conventional elemental or compound semiconductors.[29], [82], [99], [100] Among these properties, solubility in organic solvents stands out as a unique tunable feature of molecular semiconductors that holds significant potential for large-scale roll-to-toll manufacturing.[30], [100], [101] Molecular semiconductors generally exhibit greater solubility in organic solvents when compared to polymers, primarily due to the increased entropy of mixing effect as dictated by statistical thermodynamics.[102], [103] Despite these advantages, incorporating solubility into *n*-type semiconducting π-architectures, particularly in conjunction with ambient processing and ambient characterization of their corresponding semiconducting thin-films, continues to present challenges from both molecular design and semiconductor device standpoints.[89], [104], [105] As a result, only a limited number of π-structures exhibiting these properties have been reported to date in OFETs.[85], [86], [91], [92], [106]

Solution processable and ambient stable *n*-type semiconducting molecules have been mostly studied by processing their solutions in environmentally dangerous and toxic halogenated/aromatic hydrocarbon solvents such as chloroform, dichloromethane, chlorobenzene, and toluene.[82], [85] These solvents not only pose significant risks to human health and diverse ecosystems but are also predominantly derived from fossil fuels, making them non-sustainable in nature.[102], [107], [108] In recent years, the utilization of green solvents in the solution processing of molecular semiconductors has emerged as a crucial research direction for advancing the future development of organic optoelectronics, yet with very limited examples for *n*-channel OFETs (Table 3.2).[102], [107], [109], [110] In one of these studies, Ho et al.[108] demonstrated green solvent-processed OFETs (μ_e = 0.07-0.13 $cm^2/V{\cdot}s$ measured under vacuum) by shearing the solutions of *n*-type molecules N,N'-dioctyl-3,4,9,10-perylenedicarboximide and N,N'-bis(n-alkyl)-(1,7 and 1,6)-dicyanoperylene-3,4:9,10-bis(dicarboximide) (**PTCDI-C$_8$** and **PDIF-CN$_2$**, respectively, in Table 3.2) in anisole and Purasolv EHL (2-ethylhexyl ester of natural L-Lactic acid). In another study, Harris et al.[111] reported the synthesis of a bay-functionalized PDI-based molecular semiconductor (**X1** in Table 3.2), which exhibited μ_e's ~ 5×10^{-5} $cm^2/V{\cdot}s$ (measured under vacuum) in their green solvent (alcohol/amine binary mixture) processed thin-films in *n*-channel OFETs. In a very

recent study by Corzo et al.,[112] an electron-deficient molecule (**O-IDTBR** in Table 3.2), which is typically used as an acceptor in bulk-heterojunction solar cells, was processed from a terpene biosolvent into an *n*-type semiconducting film in bottom-contact/top-gate OFETs (μ_e ~ 0.37-0.91 $cm^2/V{\cdot}s$ as measured under vacuum). Alternatively, the utilization of green solvents as non-solvent additives to modify semiconductor morphology-crystallinity has also been demonstrated, rather than relying solely on the dissolving capabilities of pure green solvents.[113], [114] In the latest study by Lee et al.,[115] binary semiconductor solution systems were prepared by introducing 2-methyltetrahydrofuran (2-MeTHF) into the chloroform solution of an *n*-type polymer (**P(NDI2OD-T2)** in Table 3.2), and diethyl succinate into the chlorobenzene solution of an *n*-type small molecule (**TU-3** in Table 3.2). This approach led to *n*-channel OFETs with μ_e's ranging from 0.13 to 0.33 $cm^2/V{\cdot}s$, as measured under vacuum conditions.

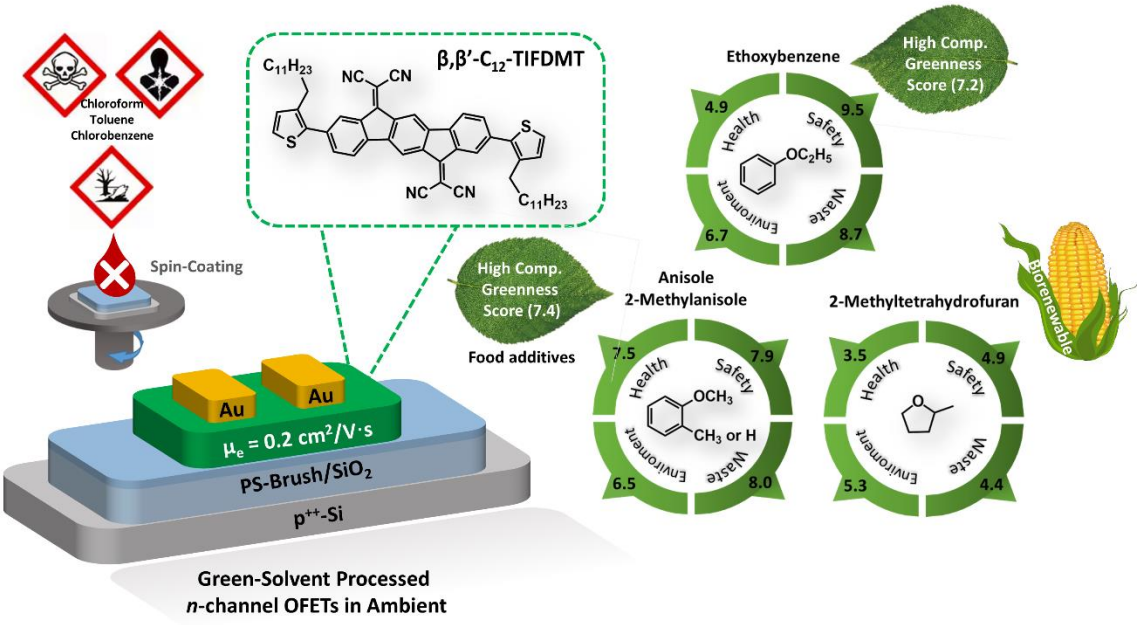

Figure 3.1 The bottom-gate/top-contact OFET device structure (p^{++}-Si/SiO_2/PS-brush/semiconductor/Au) employed in this study to study green solvents, and the chemical structure of ambient-stable *n*-type semiconductor, 2,2'-(2,8-bis(3-dodecylthiophen-2-yl)indeno[1,2-b]fluorene-6,12-diylidene)dimalononitrile (**β,β'-C_{12}-TIFDMT**). The chemical structures for the green solvents, anisole, 2-methylanisole, ethoxybenzene, and 2-methyltetrahydrofuran, are shown with the corresponding GlaxoSmithKline (GSK)'s[116]"Globally Harmonized System of Classification and Labelling of Chemicals" (GHS) are also shown for some toxic and environmentally hazardous solvents (e.g., chloroform, toluene, and chlorobenzene).

Despite the recent efforts, the occurrence of green solvent processed *n*-channel OFETs with favorable electron mobilities (μ_e > 0.1 $cm^2/V{\cdot}s$) and transistor characteristics ($I_{on}/I_{off} \geq 10^5$ and $V_{on} \sim 0$ V) measured in ambient conditions remains highly uncommon, emphasizing the need for further studies. At this point, it is important to highlight that during solution processing, specific solute-solvent interactions, along with solvent properties such as evaporation rate, viscosity/surface wettability, and film-forming capacity, critically influence the molecular self-assembly process.[79], [85], [117], [118] Altering the solvent used for the semiconductor can result in notable changes in the microstructural and morphological characteristics of thin films, subsequently impacting the efficiency of electron transport. Hence, replacing toxic and non-sustainable solvents with environmentally friendly and sustainable alternatives is not a straightforward effort, and it requires a rational approach. Due to the intricate nature of solubility involving a wide range of interaction types, it is essential to conduct rational studies, rather than a trial-and-error approach, in order to determine which green solvents are compatible with a specific semiconductor. For this purpose, utilizing solubility parameters (δ's) proves to be a practical approach. This concept was first introduced by Hildebrand and Scott in the 1950s[119], [120], which is defined as the square root of total cohesive energy density ($\delta = (E_{cohesive}/V_{molar})^{1/2}$), and later extended by Hansen[119], [121] in 1967 to include three distinct interaction contributions of dispersive (δ_D), polar (δ_P), and hydrogen-bonding (δ_H) origins, which are defined as Hansen solubility parameters (HSPs). The fundamental understanding in this theory posits that the total cohesive energy of a molecule comprises three primary intermolecular forces: dispersion, polarity, and hydrogen-bonding, and molecules can only dissolve each other if they possess similar specific interaction strengths. In a similar manner, this principle can be extended to organic semiconductors, with each semiconductor anticipated to show a specific δ_D, δ_P, δ_H coordinate point in the 3D Hansen solubility space. Additionally, a solubility sphere, determined by an interaction radius (R_0), can be defined based on the specific solubility criteria relevant to a given application.[97], [122], [123]

In this study, by employing a HSP analysis-aided rational solubility approach, we explore potential green solvents for an ambient-stable, high-performance *n*-type

semiconducting molecule, **β,β'-C_{12}-TIFDMT** (Figure 1). This semiconductor, synthesized in-house at a half-gram scale, was chosen for this study due to its excellent *n*-channel behavior (μ_e ~ 0.9 $cm^2/V{\cdot}s$, I_{on}/I_{off} ~ 10^7-10^8, and V_{on} ~ 0 V in ambient) in bottom-gate/top-contact OFETs, when processed from chlorinated solvents.[124] The solubility of the semiconductor across a set of 30 organic solvents with diverse chemical structures and HSPs were determined by UV-Vis absorption spectroscopy and gravimetric methods. The solubilities ranged from 7.3 g/L (8.3×10^{-3} M) to 0.03 g/L (3.0×10^{-5} M) and insolubility, and the HSPs were determined to be δ_D = 20.8 $MPa^{1/2}$, δ_P = 5.8 $MPa^{1/2}$, δ_H = 5.5 $MPa^{1/2}$ with a radius (R_0) of 8.3 $MPa^{1/2}$ based on the solubility sphere method using Classic Hansen algorithm in HSPiP software.[125] A green solvent screening analysis was then performed by using the minimal distance constraint ($R_a < R_0$) and the solvent sustainability credits. Accordingly, ethoxybenzene (R_a = 5.19 $MPa^{1/2}$), anisole (R_a = 6.32 $MPa^{1/2}$), 2-methylanisole (R_a = 5.17 $MPa^{1/2}$), and 2-methyltetrahydrofuran (R_a = 7.93 $MPa^{1/2}$) were identified as suitable green solvents for solution-processing, all of which yield sufficient solubilities (≥ 4 g/L) for thin-film processing. In addition, a strong thermodynamic correlation was identified between the solubility and the semiconductor-solvent distance in the 3D Hansen solubility space, from which the maximum solubility limit could be estimated with the semiconductor's thermal properties of melting enthalpy (ΔH_{fusion}) and temperature (T_m). Bottom-gate/top-contact OFETs were fabricated in ambient by spin-coating the semiconductor green solutions onto p^{++}-Si/SiO_2/PS-brush (M_n= 5 kDa) substrates. Clear *n*-channel transistor behaviors were observed in ambient with μ_e's reaching to ~0.2 $cm^2/V{\cdot}s$, I_{on}/I_{off} ~ 10^6-10^7, and V_{on} ~ 0-5 V.

3.2 Experimental Section

3.2.1 Materials and Methods

All reagents and solvents were obtained from commercial vendors and used as received unless otherwise noted. **β,β'-C_{12}-TIFDMT** was synthesized in accordance with the synthesis and purification methods outlined in our previous report.[124] The

structural characterizations were performed by ^{1}H- and ^{13}C-NMR spectroscopy that were recorded using a Bruker 400 spectrometer. MALDI-TOF characterization was performed on Bruker Daltonics (microflex LT) spectrometer by using the matrix-assisted laser desorption/ionization-time-of-flight (MALDI-TOF) method. Differential scanning calorimetry (DSC) was performed under nitrogen at a heating rate of 10 C·min^{-1} on Mettler Toledo DSC822e instrument. Indium and zinc standards (Mettler Toledo, Schwerzenbach, Switzerland) were used for calibration in DSC. UV-Vis absorption spectra were recorded on a Shimadzu, UV-1800 UV-Vis spectrophotometer. Hansen solubility sphere, parameters, and the fitting accuracy were determined by using the classic Hansen algorithm in the HSPiP Program (*5th Edition Version 5.4.08*) with a solubility limit of 2 g/L.[125] Solubility scores of "1" and "0" are assigned for good and bad solvents, respectively. The group contribution methodology was employed using Neural Network techniques in the same HSPiP program.

3.2.2 Solubility Measurements

The semiconductor solubility in varied solvents was measured by UV-Vis absorption spectroscopy method. First, a linear calibration curve was produced at the semiconductor's absorption maximum (λ_{max} = 338 nm) in chloroform by collecting the UV-Vis absorption spectra of standard solutions (4.55×10^{-7}–4.55×10^{-5} M). Then, saturated semiconductor solutions were prepared by weighing a small amount (~5.0 mg) of organic semiconductor solid into a vial and adding 500 μL of a particular solvent via micropipette. Next, the mixture was stirred/sonicated for 30 min at room temperature, filtered through a PTFE syringe filter (VWR, part of Avantor, 0.20 μm pore size), and diluted (200×) with chloroform in order to reach to an optical absorption region in the range of the calibration curve. For each solvent, the absorbance at the absorption maximum is measured, and the corresponding solubility value is calculated by plugging this absorbance value into the calibration curve equation based on the Beer-Lambert law ($A = \varepsilon \cdot b \cdot c$). When solubility exceeds 1.0 g/L in a particular solvent, an additional gravimetric method is also used for confirmation. In the gravimetric method, a small amount (~5.0 mg) of semiconductor solid was precisely weighed into a vial, and incremental volumes (in 50-100 μL portions) of a particular solvent was added via micropipette. After each addition, the solution was stirred/sonicated for 10 min at room

temperature. Solvent addition was continued until complete dissolution was visually observed. Once complete dissolution is confirmed, semiconductor solution was filtered through PTFE syringe filter (VWR, part of Avantor, 0.20 μm pore size) and then evaporated to dryness with a rotary evaporator. The gravimetric solubility was calculated based on the recovered semiconductor solid weight (m_{osc}) and the total amount of solvent ($V_{solvent}$) using the equation (solubility = $m_{osc}/V_{solvent}$). The typical difference in solubilities determined via spectroscopic and gravimetric methods was less than 3-4%.

3.2.3 OFET Device Fabrication and Characterization

β,β'-C_{12}-TIFDMT thin-films (~40−45 nm) were deposited onto the PS-brush-treated substrates, p^{++}-Si/SiO_2/PS-brush (M_n = 5 kDa), by spin-coating the corresponding semiconductor solutions in anisole, 2-methylanisole, ethoxybenzene, and 2-methyltetrahydrofuran (4.0 mg/mL) at 1500, 1700, and 2000 rpm values under ambient conditions. The thin-films were thermally annealed at 170, 190 and 200 °C (for 30 min) in a vacuum oven. The bottom-gate/top-contact OFET devices were finished with thermal evaporation of Au source-drain electrodes (50 nm thick, growth rate of 0.2 Å/s). Semiconducting channel lengths (L) and widths (W) of 30/40/50/60/80 μm and 1000 μm, respectively, were obtained. The transistor characteristics were measured using a Keithley 2614B source-measure unit in an Everbeing BD-6 probe station under ambient conditions (without excluding natural or fluorescent lighting). Electron mobilities (μ_e), threshold voltages (V_T), and I_{on}/I_{off} ratios were calculated in the saturation regime by the formula:

$$\mu_{sat} = \left(\frac{2L}{W \times C_{ox}}\right)\frac{I_{DS}}{(V_G - V_T)^2}$$

where I_{DS} is the source-drain current, L is the channel length, W is the channel width, C_{ox} is the areal capacitance of the gate dielectric with PS-brush interlayer per unit area (taken as 10.5 nF/cm^2)[58], V_G is the gate voltage, and V_T is the threshold voltage. The reported values are the average of at least ten different devices. The surface morphologies and microstructures for the semiconductor thin-films were investigated

by atomic force microscopy on a NanoSurf FlexAFM C3000 instrument, and by grazing incidence X-ray diffraction (GIXRD) on a Malvern Panalytical Empyrean diffractometer.

3.3 Results and Discussion

3.3.1 Study Of Solubility and Determination of Hansen Solubility Parameters

The *n*-type semiconductor, **β,β'-C_{12}-TIFDMT**, was synthesized in-house at a half-gram scale, following the synthesis and purification methods outlined in our previous report.[124] In order to determine the semiconductor HSP sphere and the corresponding parameters, we employed a set of 30 organic solvents (Table 3.1) encompassing diverse structures, including aromatics, alcohols, polar aprotic solvents, nonpolar solvents, chlorinated alkanes/aromatics, terpenes, and esters. These solvents exhibited a wide range of δ_D (14.5-20.0), δ_P (0-18.0), and δ_H (0-26.0) values in the Hansen space to improve the fitting of the semiconductor solubility sphere. The maximum solubility in these solvents were measured by using UV-Vis absorption spectroscopy method. The initial step involved generating a linear calibration curve at the molecular absorption maximum (λ_{max} = 338 nm) with standard semiconductor solutions (4.55×10^{-7}–4.55×10^{-5} M in chloroform) (Figure 3.5). The molar absorptivity value (ε) of 5.85×10^{4} $M^{-1}\cdot cm^{-1}$ was obtained by fitting the calibration curve (Figure 2(a)) using the Beer-Lambert law. The semiconductor solid was dissolved in solvents at a preparation concentration of 10.0 g/L and stirred/sonicated for 30 min at room temperature. Extended sonication/stirring time was found to have a negligible effect on the solubility results. Any undissolved semiconductor solute with a particle size of > 0.20 μm was removed via filtration. The filtrated solutions were diluted (200×) with chloroform in order to reach to an optical absorption region in the range of the calibration curve. Here, it is important to note that the diluted semiconductor solutions show the same spectra in the 325-450 nm region as the original spectrum recorded in pure chloroform (Figure 2(b)). This is a result of the presence of a residual test solvent

in the diluted solutions (0.5% (v/v)), and it highlights the method's ability to give accurate maximum absorbance values. For each solvent, the absorbance at λ_{max} = 338 nm is measured and translated into the corresponding solubility value by using the calibration curve equation. On the other hand, for the solvents in which solubility is ≥ 1.0 g/L, an additional gravimetric method was also employed for confirmation, which yielded solubility results within ~3-4% of the spectroscopic method. In this case, a precisely weighed amount (~5.0 mg) of **β,β'-C_{12}-TIFDMT** solid was added with incremental volumes (in 50-100 μL portions) of a particular solvent. Solvent addition continued until complete dissolution was visually confirmed, and the dissolved semiconductor solid in this solution was then recovered via filtration (0.20 μm pore size) and solvent evaporation.

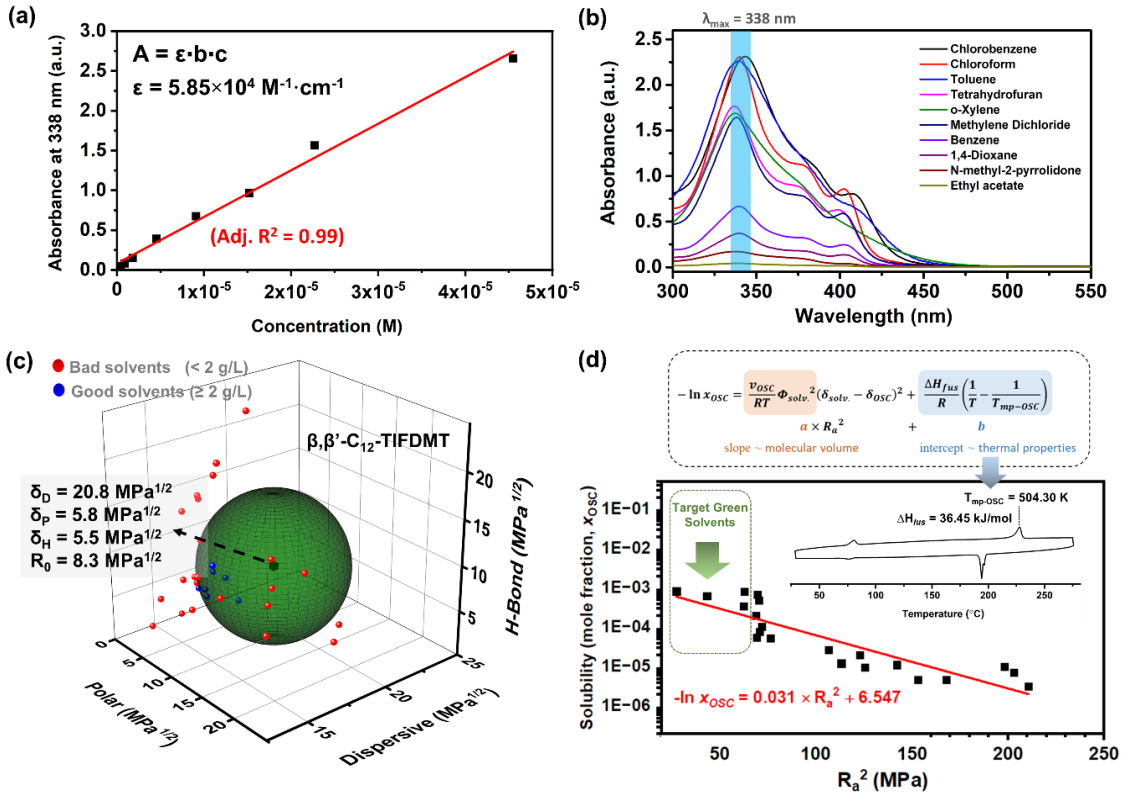

Figure 3.2 (a) The calibration curve based on the absorbance of **β,β'-C12-TIFDMT** in chloroform at varied standard solution concentrations (4.55×10^{-7} M-4.55×10^{-5} M) recorded at absorption maximum (λ_{max} = 338 nm); the linear fitting was performed according to Beer-Lambert law (adjusted R^2 is 0.99). (b) Optical absorption spectra of **β,β'-C12-TIFDMT** for saturated solutions in selected organic solvents after 200× dilutions with chloroform. (c) Hansen solubility sphere and parameters of **β,β'-C12-TIFDMT** as determined by using the classic Hansen algorithm (HSPiP Program) with a solubility limit of 2 g/L. The Hansen solubility parameters (δ_D, δ_P, δ_H, and R_0) are in $MPa^{1/2}$, the bad (23) and the good (7) solvents are shown in the 3D Hansen solubility space with red and blue spheres, respectively. (d) The linear correlation between the semiconductor solubility in mole fraction unit (x_{OSC}) and the squared solute−solvent distance (R_a^2) in the HSP space (correlation coefficient ~ -0.9), and the logarithmic equation derived based on the Scatchard− Hildebrand regular solution theory.[122] Inset shows the differential scanning calorimetry (10 °C/min heating ramp under N_2) scan of **β,β'-C12-TIFDMT** with the corresponding enthalpy of fusion (ΔH_{fus}) and the melting temperature (T_{mp-OSC}) values.

As shown in Table 1, **β,β'-C_{12}-TIFDMT** exhibited a broad spectrum of solubilities in 30 different organic solvents, ranging from complete insolubility to as high as 7.3 g/L (8.3 × 10^{-3} M), with variation dependent on the specific solute-solvent interactions. Especially, chlorinated alkanes/aromatics (4.9-7.3 g/L (5.6-8.3 × 10^{-3} M): chloroform, methylene dichloride, and chlorobenzene) and aromatics (2.0-6.7 g/L (2.3-7.6 × 10^{-3} M): benzene, toluene, *o*-xylene) were found to be the best solvents for **β,β'-C_{12}-TIFDMT**. Also, a good solubility value of 5.3 g/L (6.0 × 10^{-3} M) was recorded in tetrahydrofuran. 1-butanol, cyclopentanone, 1,4-dioxane, methyl iso-butyl ketone, *N*-methyl-2-pyrrolidone**,** *N,N*-dimethylformamide *n*-amyl acetate, ethyl acetate, and *d*-limonene showed solubilities in the range of 0.13-1.11 g/L (0.15-1.26 × 10^{-3} M). The solubilities in the rest of the solvents were ≤ 0.10 g/L. Solubility scores of "1" (indicating a good solvent) and "0" (indicating a nonsolvent) are assigned based on a threshold concentration value of 2.0 g/L at room temperature. Under the assumption of a spherical solubility sphere, the best fitting accuracy (0.999) is attained using the classic Hansen algorithm in the HSPiP program (Figure 3.6).[125] As shown in Figure 2(c), the HSPs for **β,β'-C_{12}-TIFDMT** are determined to be δ_D = 20.8 $MPa^{1/2}$, δ_P = 5.8 $MPa^{1/2}$, δ_H = 5.5 $MPa^{1/2}$ with an interaction radius (R_0) of 8.3 $MPa^{1/2}$. Given that δ_D >> δ_P and δ_H, the major source of cohesive energy in the solid state ($E_{cohesive}$) for **β,β'-C_{12}-TIFDMT** arises from dispersion interactions, with polar and hydrogen-bonding contributions playing a comparatively lesser role. While Hansen's original solubility theory does not explicitly address π-interactions, the dispersion term (δ_D) obtained herein comprises π-interactions (i.e., π···π, C-H···π, and N/S···π) between the relatively large, rod-shaped and polarizable **TIFDMT** donor-acceptor-donor π-backbones, as well as dispersion interactions between aliphatic dodecyl substituents.[126], [127] Note that while the strength of the latter interactions are important for thin-film crystallization and microstructure, the former interactions are essential in establishing an electronic structure for efficient charge transport.[124], [128] The major contribution of the dispersion interactions in the **β,β'-C_{12}-TIFDMT**'s HSP parameters was also evident with the group contribution methodology (Figure 3.7). This approach was employed in the HSPiP using Neural Network techniques,[129], [130] in which the **β,β'-C_{12}-TIFDMT** molecular structure is divided into varied aromatics-aliphatics-functional

group components and the HSPs are estimated as the sum of the contributions from these components. On the basis of the solubility parameters, the best solvents, chlorobenzene (7.3 g/L) and chloroform (6.9 g/L), are calculated to give the closest interaction distances to **β,β'-C$_{12}$-TIFDMT** (R_a = 5.2 $MPa^{1/2}$ and 6.6 $MPa^{1/2}$, respectively) when compared to all other solvents. This serves as additional validation of the precision and reliability of our HSP analysis for the present semiconductor. Given that the δ_D value of our semiconductor is 20.8 $MPa^{1/2}$, solvents with greater solubilities generally have δ_D values exceeding ~ 17-18 $MPa^{1/2}$. This is primarily because the difference in dispersion parameters ($\Delta\delta_D$'s) has a fourfold effect in the R_a calculation, in contrast to the effects of polar ($\Delta\delta_P$) or hydrogen bonding ($\Delta\delta_H$) parameters.[119], [122] Conversely, when considering the moderate δ_P and δ_H values of **β,β'-C$_{12}$-TIFDMT** (5.5-5.8 $MPa^{1/2}$), solvents with extremely high or low δ_P and δ_H values (i.e., very polar and non-polar solvents) tend to result in very low solubility. These observations lay the groundwork for a fundamental understanding of the upcoming green solvent analysis.

Table 3.1 The solubility values (both in g/L and M) of **β,β'-C_{12}-TIFDMT** in 30 different organic solvents determined via spectroscopic (UV-Vis absorption) method, the corresponding Hansen Solubility parameters (δ_D, δ_P, δ_H in $MPa^{1/2}$), and the specific semiconductor-solvent interaction distance ($R_a = (4\Delta\delta_D^2 + \Delta\delta_P^2 + \Delta\delta_H^2)^{1/2}$ in $MPa^{1/2}$, in which $\Delta\delta$ for a specific Hansen parameter is "$\delta_{OSC} - \delta_{solvent}$").

Solvent	Hansen Parameters ($MPa^{1/2}$)			Solubility (g/L)	Molarity ($\times 10^{-3}$ M)	Interaction Distance (R_a) ($MPa^{1/2}$)	Solubility Score
	δ_D	δ_P	δ_H				
Aromatics							
benzene	18.4	0	2.0	2.01	2.29	8.3	1
toluene	18.0	1.4	2.0	6.70	7.60	7.9	1
***o*-xylene**	17.8	1.0	3.1	5.02	5.71	8.0	1
Alcohols							
1-butanol	16.0	5.7	15.8	0.10	0.11	14.1	0
***tert*-butanol**	15.2	5.1	14.7	0.03	0.03	14.5	0
ethanol	15.8	8.8	19.4	insoluble	-	-	0
ethylene glycol	17.0	11.0	26.0	insoluble	-	-	0
methanol	14.7	12.3	22.3	0.03	0.03	21.8	0
2-propanol	15.8	6.1	16.4	insoluble	-	-	0
Polar aprotic							
acetone	15.5	10.4	7.0	0.05	0.06	11.7	0
acetonitrile	15.3	18.0	6.1	insoluble	-	-	0
cyclopentanone	17.9	11.9	5.2	0.79	0.90	8.4	0
diethyl ether	14.5	2.9	4.6	0.04	0.05	13.0	0
dimethyl sulfoxide	18.4	16.4	10.2	insoluble	-	-	0
***N*,*N*-dimethylformamide**	17.4	13.7	11.3	0.13	0.15	11.9	0
1,4-dioxane	17.5	1.8	9	1.11	1.26	8.5	0
ethylene carbonate	18.0	21.7	5.1	insoluble	-	-	0
methyl iso-butyl ketone	15.3	6.1	4.1	0.14	0.16	11.1	0
***N*-methyl-2-pyrrolidone**	18.0	12.3	7.2	0.50	0.57	8.7	0
propylene carbonate	20.0	18.0	4.1	0.05	0.06	12.4	0
tetrahydrofuran	16.8	5.7	8.0	5.30	6.00	8.4	1
Chlorinated alkanes/aromatics							
chloroform	17.8	3.1	5.7	6.92	7.81	6.6	1
methylene dichloride	17.0	7.3	7.1	4.93	5.62	7.9	1
chlorobenzene	19.0	4.3	2.0	7.30	8.30	5.2	1
Esters							
***n*-amyl acetate**	15.8	3.3	6.1	0.16	0.18	10.3	0
ethyl acetate	15.8	5.3	7.2	0.13	0.15	10.2	0
propylene glycol monoethyl ether acetate	15.6	6.3	7.7	0.08	0.09	10.6	0

Terpenes							
***d*-limonene**	17.2	1.8	4.3	0.30	0.34	8.3	0
nonpolar							
cyclohexane	16.8	0	0.2	0.08	0.09	11.2	0
hexane	14.9	0	0	0.05	0.06	14.3	0

3.3.2 Quantitative Correlation of The Semiconductor Solubility and HSP Parameters

A key advantage of a HSP analysis should be the ability to establish a quantitative thermodynamic correlation between solubility values and the interaction distances (R_a's) in the 3D Hansen space for semiconductors. Surprisingly, this still largely remains unexplored in the field of (opto)electronics. Despite several studies exploring HSPs of semiconductors,[97], [112], [116] to the best of our knowledge, such a correlation has been examined in only a few previous reports, and a direct relationship to thermal characteristics has not been established.[122], [131], [132] As the solubilities of our semiconductor ranged over almost three orders of magnitude among 24 solvents, and these solvents gave widely ranged semiconductor-solvent interaction distances (R_a) of 5.2-21.8 $MPa^{1/2}$ (Table 1) in the 3D Hansen space, we were able to study such thermodynamic correlation for **β,β'-C_{12}-TIFDMT**. We note that six solvents are omitted from this analysis since the semiconductor is practically insoluble in these solvents. This correlation was based on a Hansen-adapted Scatchard-Hildebrand regular solution theory,[122], [133] in which the squared difference in the Hildebrand solubility parameters $(\delta_1 - \delta_2)^2$ is replaced by the squared interaction distance (R_a^2) in the HSP space As shown in Equation 1 below where R is the gas constant and T is the solubility measurement temperature (absolute), a logarithmic relationship between the R_a^2 value and the solubility mole fraction (x_{OSC}) would be expected if the Hansen solubility parameters for the semiconductor is accurately determined.

$$-\ln x_{OSC} = \frac{v_{OSC}}{RT}\Phi_{solv.}{}^2 R_a{}^2 + \frac{\Delta H_{fus}}{R}\left(\frac{1}{T} - \frac{1}{T_{mp-OSC}}\right) \quad (1)$$

In this equation, while the slope depends on the molar volume (v_{OSC}) of the subcooled liquid of pure semiconductor solid and the solvent volume fraction ($\Phi_{solv.} \approx 1$ for dilute solutions), the intercept is a function of the thermal properties of the semiconductor solid, which are the semiconductor's enthalpy of fusion (ΔH_{fus}) and the melting temperature ($T_{mp\text{-}OSC}$). The slope indicates the sensitivity of semiconductor solubility to changes in the R_a value, while the intercept represents the maximum solubility limit of the semiconductor in an ideal solvent as R_a approaches 0. The second part of equation (1) shows the solubility equation described for ideal solutions.[134] Additionally, it's important to note that in equation (1), the Flory-Huggins correction term for the entropy of mixing is considered to be significantly smaller than the HSP term, and as a result, it is not included in the calculation.[132] As shown in Figure 2(d), when x_{OSC} is plotted against R_a^2 on a logarithmic scale (see Table 3.3 for data details), a strong negative correlation (correlation coefficient ≈ -0.9) was calculated between these two parameters and the relationship can be regressed to the equation given on Figure 2(d). Most importantly, the intercept is calculated to be 6.547, and it matches very well with the enthalpy of fusion (ΔH_{fus} = 36.45 kJ/mol) and the melting temperature ($T_{mp\text{-}OSC}$ = 504.30 K) of the semiconductor solid obtained via differential scanning calorimetry (DSC) (Figure 3.8). This correspondence between the Scatchard-Hildebrand regular solution theory and DSC characteristics is highly promising, which has the potential to pave the way for a new approach in semiconductors, enabling the prediction of their maximum solubility limits solely based on thermal characteristics.

3.3.3 Exploring Suitable Green Solvents For Semiconductor Processing

In light of the recent regulatory demands concerning chemical substances, the adoption of green solvent processing is undeniably important for solution-based fabrication of organic (opto)electronic devices.[112], [116], [135] The qualification of an organic liquid as a green solvent is a multifaceted concept that reflects diverse, and sometimes controversial, aspects regarding health, safety, environmental impact, and overall sustainability. More specifically, the solvents could be evaluated and classified into ten distinct subcategories of health hazard, exposure potential, flammability & explosion, reactivity & stability, air impact, aqueous impact, incineration, recycling, bio treatment, and volatile organic compounds, according to the regularly updated

GlaxoSmithKline (GSK) solvent sustainability guide.[136], [137] As demonstrated by Larsen et al. in a quantitative methodolody,[116] these subcategories could be converted into four category scores and then combined to generate a composite score value (G). The G value ranges between 1 and 10, and a high score (>7) is desirable for a solvent suggesting a favorable greenness. On the other hand, the green solvent of choice should be able to dissolve the semiconductor at needed concentrations, which is at least 4.0 mg/ml at room temperature or moderately elevated temperatures (~50-60 °C) in our case for spin-coating. According to Hansen solubility approach,[97], [119], [121] the selection of a green solvent to dissolve a semiconducting molecule strictly depends on the similarities between dispersive, polar, and hydrogen-bonding interactions (i.e., δ_D, δ_P, and δ_H values, respectively) of the pure green solvent and the semiconductor structure. In other words, the similarities between these interactions lead to a reduction in interaction distance (R_a), thereby increasing molecular solubility.

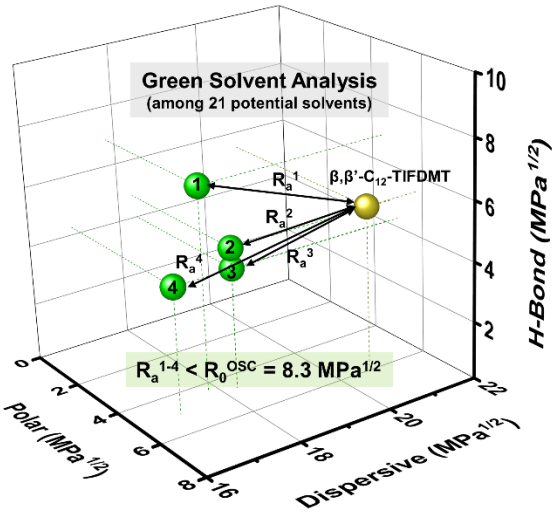

#	Solvent (CAS Number)	δ_D	δ_P	δ_H	R_a	GSK Greenness Scores/GHS of Classification-Labelling of Chemicals
1	Anisole (100-66-3)	17.8	4.4	6.9	6.3	Health = 7.5 Safety = 7.9 Environment = 6.5 Waste = 8.0 Composite Score = 7.4 H226, H315, H319, H336
2	2-Methylanisole (578-58-5)	18.3	4.7	4.8	5.2	Certified Food Additive H226, H302
3	Ethoxybenzene (103-73-1)	18.4	4.5	4	5.2	Health = 4.9 Safety = 9.5 Environment = 6.7 Waste = 8.7 Composite Score = 7.2 H226
4	2-Methyltetrahydrofuran (96-47-9)	16.9	5	4.3	7.9	Health = 3.5 Safety = 4.9 Environment = 5.3 Waste = 4.4 Composite Score = 4.4 H225, H302, H315, H318, H319, H335, H336 Biorenewable

Figure 3.3 Hansen solubility parameters (δ_D, δ_P, δ_H in $MPa^{1/2}$) of four potential green solvents, anisole (1), 2-methylanisole (2), ethoxybenzene (3), and 2-methyltetrahydrofuran (4), and their corresponding semiconductor-solvent interaction distances with respect to **β,β'-C$_{12}$-TIFDMT** ($R_a^{1-4} = (4\Delta\delta_D^2 + \Delta\delta_P^2 + \Delta\delta_H^2)^{1/2}$ in $MPa^{1/2}$, in which $\Delta\delta$ for a specific Hansen parameter is "$\delta_{OSC} - \delta_{solvent}$"). The GlaxoSmithKline (GSK)'s four category scores of health, safety, environment, and waste (disposal) are shown in the table for the green solvents, along with the composite scores and the representative hazard statements based on "Globally Harmonized System of Classification and Labelling of Chemicals" (GHS),[116] in which H225: Highly Flammable liquid and vapor, H226: Flammable liquid and vapor, H302: Harmful if swallowed, H315: Causes skin irritation, H318: Serious eye damage, H319: Serious eye irritation, H335: May cause respiratory irritation, H336: Make cause drowsiness or dizziness.

On the basis of the HSPs determined for **β,β'-C_{12}-TIFDMT** (δ_D = 20.8 $MPa^{1/2}$, δ_P = 5.8 $MPa^{1/2}$, and δ_H = 5.5 $MPa^{1/2}$), a set of potential green solvents (21 green solvents shown in Table 3.4) were screened by using the minimal distance constraint ($R_a < R_0$ = 8.3 $MPa^{1/2}$) in the 3D Hansen solubility space and sustainability credits. Consequently, we identified four solvents with reasonably small interaction distances: ethoxybenzene (R_a = 5.19 $MPa^{1/2}$), anisole (R_a = 6.32 $MPa^{1/2}$), 2-methylanisole (R_a = 5.17 $MPa^{1/2}$), and 2-methyltetrahydrofuran (R_a = 7.93 $MPa^{1/2}$). Here it is noteworthy that these R_a values are expected to align with the high solubility region of the Scatchard-Hildebrand fitting curve in Figure 2(d), aiming to achieve solubilities exceeding 10^{-3} M–sufficient for thin-film fabrication. These solvents exhibit relatively larger δ_D values (16.8-18.4 $MPa^{1/2}$) when compared to other environmentally friendly solvents, which, as previously mentioned, highlights the significant role of dispersion interactions in determining the overall solubility. Moreover, the boiling points of these solvents are in a reasonable temperature range (boiling points ≈ 78-170°C), which is crucial for an effective spin-coating process to achieve favorable semiconducting morphologies and microstructures.[102], [138], [139] With regards to the greenness of these solvents, anisole and 2-methylanisole are well-known food additives,[102], [110], [140] while ethoxybenzene and anisole exhibit excellent sustainability with high G values of 7.2 and 7.4, respectively.[116] In this context, it's worth highlighting that the GSK composite score for ethoxybenzene might potentially be even higher, as a relatively conservative health score (4.9) was assigned to ethoxybenzene due to limited information available in this particular category.[116] In today's industry, although anisole production predominantly relies on petrochemicals, we note that it is also possible to obtain anisole from renewable sources such as lignin and guaiacol.[141] On the other hand, despite its relatively lower greenness compared to our other three green solvents, 2-methyltetrahydrofuran is a biorenewable green solvent and it could be manufactured with a carbon footprint of ~40× reduced CO_2 emission as compared to conventional tetrahydrofuran.[142]

3.3.4 Thin-Film Microstructure/Morphology and Field-Effect Transistor Characterization

After determining four potential green solvents for our *n*-type semiconductor processing, bottom-gate/top-contact OFETs were fabricated by spin coating **β,β'-C_{12}-TIFDMT** green solutions (4.0 g/L) in anisole, 2-methylanisole, ethoxybenzene, and 2-methyltetrahydrofuran onto p^{++}-Si/SiO_2/PS-brush (M_n= 5 kDa) substrates. The ultrathin (~3.6 nm) polystyrene brush (PS-brush) layer was employed since its densely packed (grafting density ≈ 0.45 chains/nm^2) hydrophobic surface facilitates the formation of a proper microstructure for efficient electron trasport.[58], [124] When selecting these green solvents, the similarity of the dispersive, polar, and hydrogen-bonding interactions between the semiconductor and the solvents serves not only to enhance molecular solubility but also to promote uninterrupted molecular arrangement during solution processing. This is because it reduces the likelihood of abrupt and drastic changes in the short-range intermolecular cohesive forces when transitioning from a solution state, where semiconducting molecules are surrounded by solvent molecules, to a thin-film state, where semiconducting molecules interact only with each other. This phenomenon has been evident in the literature, where a majority of the high-performing semiconducting thin-films were fabricated from solvents with favorable solubility parameters (e.g., chloroform, toluene, and chlorobenzene), despite the absence of Hansen Solubility Parameter (HSP) analyses in most of these studies.[82], [118], [143]

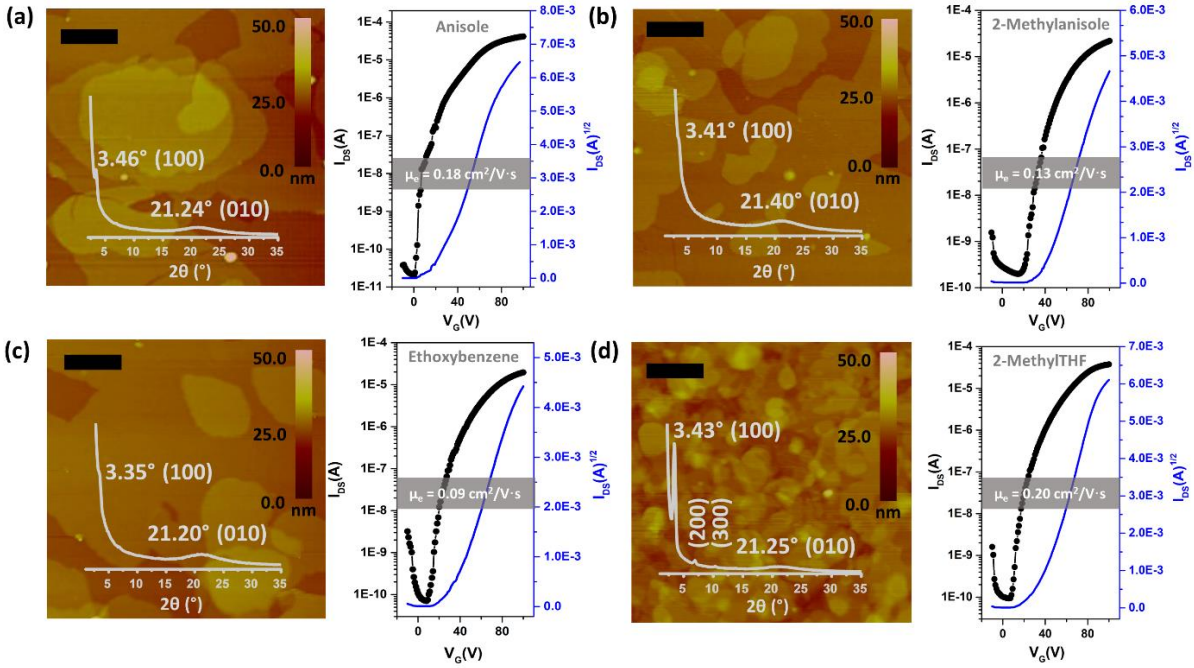

Figure 3.4 For spin-coated thin-films of **β,β'-C12-TIFDMT** on p^{++}-Si/SiO_2/PS-brush (M_n = 5 kDa) from anisole (a), 2-methylanisole (b), ethoxybenzene (c), and 2-methyltetrahydrofuran (d) solutions, top-view atomic force microscopy (AFM) topography images and transfer plots (V_{DS} = 100 V) for the fabricated OFET devices (with Au top-contact electrodes) measured under ambient conditions. The inset in each AFM image shows the corresponding out-of-plane grazing-incidence X-ray diffraction (GIXRD) patterns with the 2θ diffraction angles and the assigned crystallographic planes. Scale bars denote 1 μm. The annealing temperature for each device is 170-190 °C. The electron mobilities are based on the transfer curves shown herein.

In order to completely realize the potential of these green solvents to yield favorable microstructures with efficient electron-transport, spin-coating rates of 1500, 1700, and 2000 rpm were used and the semiconductor thin-films were thermally annealed at temperatures of 170 °C, 190 °C, and 200 °C. Typical transfer and output plots are shown in Figures 4 and S5, and the transistor results for all these conditions are listed in Table 3.5. The OFETs from all four solvents exhibited clear *n*-channel characteristics under ambient conditions. In their best working conditions, while the OFETs processed from anisole and 2-methyltetrahydrofuran gave μ_{max} = 0.18-0.20 $cm^2/V{\cdot}s$ (μ_{avg} = 0.07-0.13 ± 0.04) with I_{on}/I_{off} ratios of ~ 10^6-10^7 and threshold voltages (V_T's) of 2.1-9.4 V, the OFETs from 2-methylanisole and ethoxybenzene yielded μ_{max} = 0.09-0.13 $cm^2/V{\cdot}s$ (μ_{avg} = 0.05 ± 0.03) with I_{on}/I_{off} ratios of ~ 10^5-10^6 and slightly

increased V_T's of 18.4-27.1 V. Especially in the transfer curve for the thin-film fabricated from anisole (Figure 4(a)), a clear near-zero turn-on voltage was evident. Thin-films processed from anisole, 2-methylanisole, and ethoxybenzene showed two dimensional micron-sized (~1−3 μm) grains that are grown in the substrate plane. However, their microstructures did not reveal a large crystallinity in the out-of-plane direction, showing weak (100) peaks in the low-angle region (2θ = 3.35-3.46°) and broad (010) peaks in the higher angle (2θ = 21.20-21.40°) region. On the other hand, thin-films processed from 2-methyltetrahydrofuran yields the highest crystallinity with a slightly different morphology having smaller grains (~400−600 nm). In 2-methyltetrahydrofuran-processed thin-films, long-range ordering in the out-of-plane direction was evident with a strong (100) peak at 2θ = 3.43° along with the presence of (200) and (300) diffraction peaks. Based on the observed broad (010) peaks, we note that short-range π-interactions (~4.1 Å) were present for all thin-films. Among the four green solvents employed in thin-film fabrication, 2-methyltetrahydrofuran has the largest Ra^2 value (62.41) as compared to those of the other green solvents (Ra^2 = 27-39.69 for anisole, 2-methylanisole, and ethoxybenzene). This aligns well with our observation that semiconductor molecules tend to crystallize more efficiently from 2-methyltetrahydrofuran solution, forming a highly crystalline microstructure with long-range order.

Table 3.2. The molecular structures, OFET device configurations/performances, semiconductor thin-film deposition methods, and the green solvents employed during deposition for previously reported solution-processable *n*-type and *p*-type semiconductors. The abbreviated names for each molecular structure are presented as indicated in their respective references.

Molecular Structure	**Solution-based deposition method**	**Green Solvent**	**OFET Performance I_{on}/I_{off}, $\mu(cm^2/V\cdot s)$, $V_{th}(V)$**	**OFET Device Configuration**	**OFET Character. Environment**	**References**
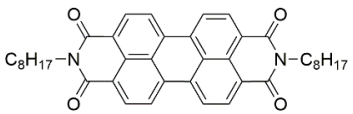 **PTCDI-C_8**	Solution-shearing	Anisole	1.5×10^7, 0.13, 36 (*n*-channel)	Si/SiO_2/PS-brush/**PTCDI-C_8**/Au	Vacuum	
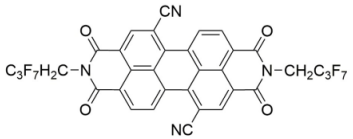	Solution-shearing	Purasolv EHL	2.3×10^3, 0.069, -32 (*n*-channel)	Si/SiO_2/PS-brush/**PDIF-CN_2**/Au	Vacuum	

PDIF-CN_2		Methyl laurate	1.3×10^2, 0.000094, -52 (*n*-channel)			*Ho et al.*[1]
		n-Amyl acetate	3.4×10^2, 0.000010, -52 (*n*-channel)			
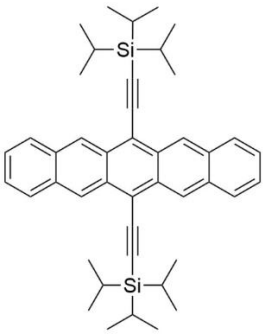 **TIPS-PEN**	Solution-shearing	t-Amyl methyl ether	5.1×10^4, 1.40, -32 (*p*-channel)	Si/SiO_2/PS-brush/**TIPS-PEN**/Au	Vacuum	
		Anisole	4.4×10^5,1.90, -33 (*p*-channel)			
		Isopropyl acetate	2.2×10^4,0.67, -33 (*p*-channel)			
		Isobutyl acetate	3.7×10^4, 2.6, -29 (*p*-channel)			
		Dimethyl Carbonate	4.6×10^4, 1.3, -25 (*p*-channel)			

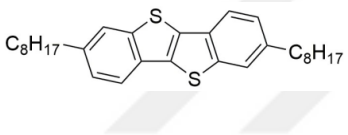 **C_8-BTBT**	Solution-shearing	t-Amyl methyl ether	$3.5\times10^{8,}$ 0.73, -30 (*p*-channel)	Si/SiO_2/PS-brush/**C_8-BTBT** /Au	Vacuum	Ho *et al.*[1]
		Isobutyl acetate	4.6×10^{6}, 0.057, -31 (*p*-channel)			
		Isopropyl acetate	2.0×10^{8}, 0.92, -56 (*p*-channel)			
		Dimethyl Carbonate	2.3×10^{6}, 0.031, -19 (*p*-channel)			
		Anisole	1.1×10^{7}, 0.92, -38 (*p*-channel)			
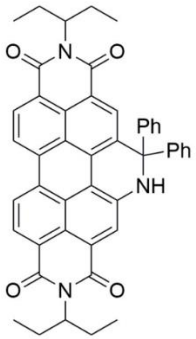 **X1**	Spin-coating	Propanol/n-butylamine	NA, 10^{-5},10 (*n*-channel)	Si/SiO_2/OTCS/**X1**/Au	Vacuum	Harris *et al.*[2]

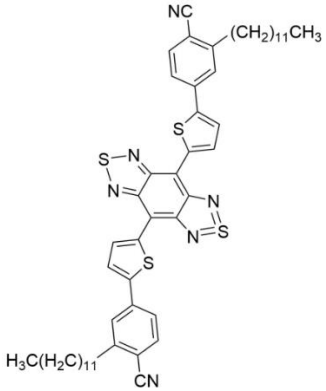 **TU-3**	Solution-shearing	Chlorobenzene /diethyl succinate	6.43×10^{4}-2.84×10^{5}, 0.13-0.33, 0.2-4 (*n*-channel)	Si/SiO_2/PS-brush/**TU-3**/Au	Vacuum	Lee *et al.*[3]
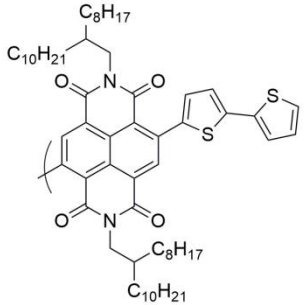 **P(NDI2OD-T2)**	Spin-coating	Chloroform/2-methyl tetrahydro furan	$1.05\text{-}1.25\times10^{4}$, 0.086-0.11, 1.6-1.9 (*n*-channel)	Si/SiO_2/PS-brush/**P(NDI2OD-T2)**/Au	Vacuum	

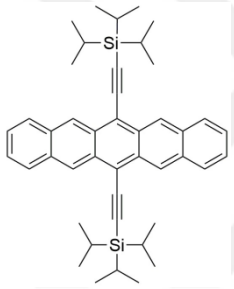 **TIPS-pentacene**	Solution-shearing	Toluene/ n-amyl acetate	1.67-3.31×10^7, 1.71-2.61, -23-(-16) (*p*-channel)	Si/SiO_2/PS-brush/**TIPS-pentacene**/Au	Vacuum	Lee *et al.*[3]
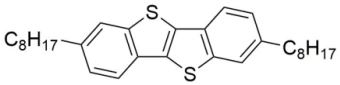 **C_8-BTBT**	Solution-shearing	Chloroform/2-methyl tetrahydro furan	2.85-9.81×10^7, 1.84-2.10, -30 (*p*-channel)	Si/SiO_2/PS-brush/**C_8-BTBT**/Au	Vacuum	

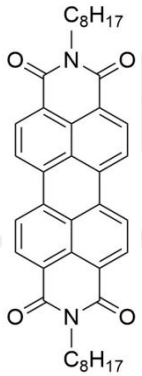 **PTCDI-C8**	Solution-shearing	Anisole	$(1.5 \pm 0.7)\times10^5$, 0.31, 29±0.7 (*n*-channel)	Si/SiO_2/Shellac/**PTCDI-C8**/Au	Vacuum	Lee *et al.*[4]
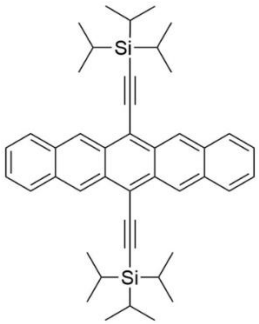	Solution-shearing	Tert-amyl methyl ether	$(7.0\pm3.5)\times10^6$, 0.61, -31±2.3 (*p*-channel)	Si/SiO_2/Shellac/**TIPS-pentacene**/Au	Vacuum	
		Isobutyl acetate	$(19\pm9.1)\times10^6$, 1.52, -30±3.8 (*p*-channel)			

TIPS-pentacene		Anisole	$(4.0\pm2.5)\times10^6$, 1.11, -25±8.0 (*p*-channel)			
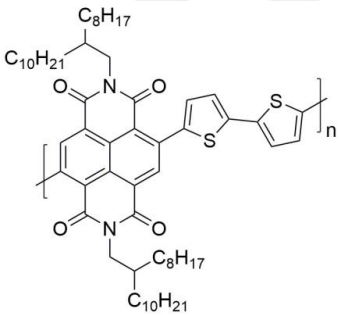 **P(NDI2OD-T2)**	Solution-shearing	Propylene glycol methyl ether acetate / 1,2-dichlorobenzene	NA, 0.28-1.03, 26.8-31.8 (*n*-channel)	Glass/Au-Ni/**P(NDI2OD-T2)**/PMMA/Al	Under N_2	Opoku *et al.*[5]

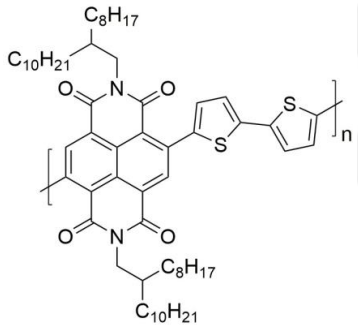 **P(NDI2OD-T2)**	Solution-shearing	Mesitylene/ acetophenone	1.23-2.83×10^3, 0.448-0.574, 19.8-20.6 (*n*-channel)	Glass/Au-Ni/**P(NDI2OD-T2)**/ PMMA/Al	Under N_2	Opoku *et al.*[6]
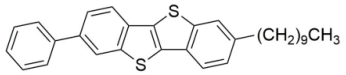 **Ph-BTBT-C_{10}**	Solution-shearing	Anisole	10^4-10^5, 0.01-3.96, -23-(-5) (*p*-channel)	Si/SiO_2/PS-brush/**Ph-BTBT-C_{10}**/Au	Vacuum	Yun *et al.*[7]
		Cyclohexanone	10^4-10^9, 0.01-5.07, -16-(-6) (*p*-channel)			

		Diethyl Carbonate	10^5-10^9, 0.04-3.22, -18-(-6) (*p*-channel)			
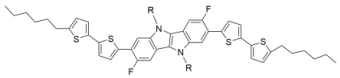 **PEG-IDIDF**	Solution-shearing	Ethanol-water	10^3-10^6, 5.53×10^{-4}-2.01×10^{-3}, (-1±4)-(1±3) (*p*-channel)	Si/SiO_2/PVN/**PEG-IDIDF**/Au	Under N_2	Hong *et al.* [8]
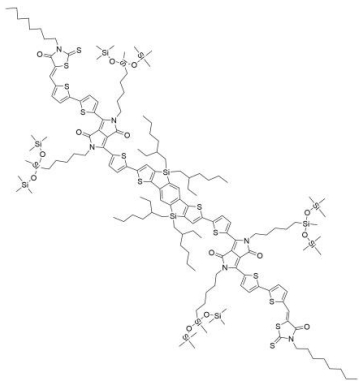 **LGC-D118**	Spin-coating	2-methyl tetrahydro furan	0.82×10^6, 2.60, -5.11±1.58 (*p*-channel)	Glass/Au-Ni/**LGC-D118**/CYTOP/Al	Under N_2	Lim *et al.*[9]

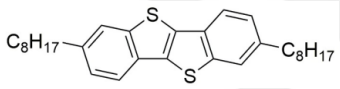 **C_8-BTBT**	Spin-coating	Cyclohexanone	10^7, 4.6, -7.0±1.9 (*p*-channel)	Glass/PVP/Au-Cr/**C_8BTBT**/CYTOP/Al	Vacuum	Sanda *et al.* [10]
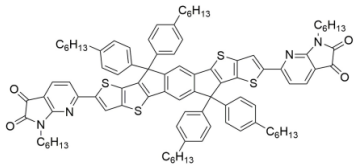 **IDTT-IDD-N**	Spin-coating	Ethyl acetate	2.48×10^7, 1.49, -29.5 (*p*-channel)	Si/SiO_2/OTS/**IDTT-IDD-N**/Au	Vacuum	Zhang *et al.*[11]
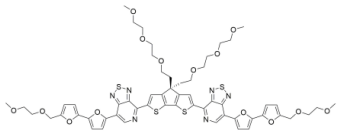 **4**	Spin coating	Ethyl acetate	10^3, 10^{-5}, NA (*p*-channel)	Si/SiO_2/HMDS/**4**/Au	Vacuum	Henson *et al.*[12]

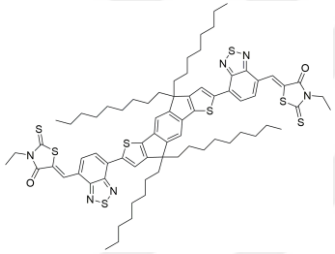 **O-IDTBR**	Blade-coating	Eucalyptol	$>10^5$, 0.37-0.91, 38.8 (*n*-channel)	Glass/Au/**O-IDTBR**/CYTOP CTL-809M/Al	Under N_2	Corzo *et al.* [13]

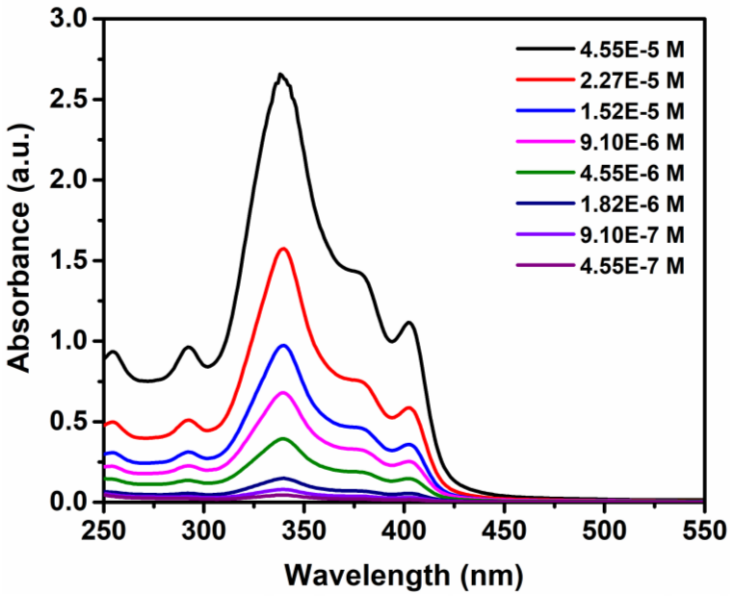

Figure 3.5 Optical absorption of standard **β,β'-C$_{12}$-TIFDMT** solutions (4.55×10^{-7}–4.55×10^{-5} M) in chloroform. Based on the absorbance values recorded at the molecular absorption maximum (λ_{max} = 338 nm) at different concentrations, a calibration curve (shown in Figure 2(a)) was derived.

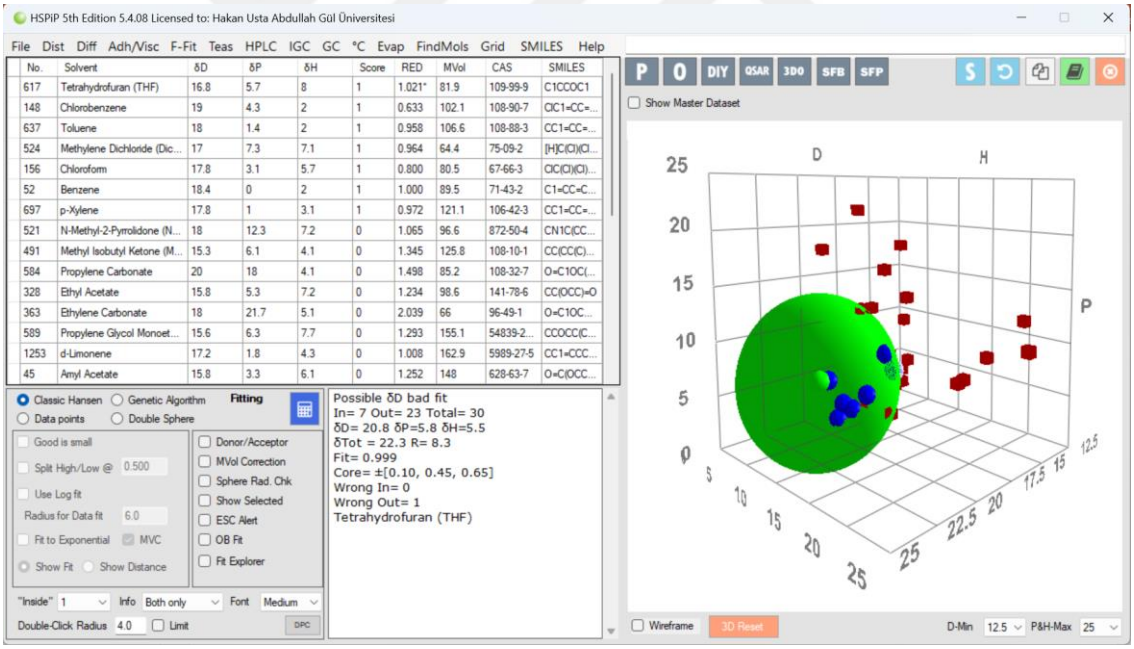

Figure 3.6 Hansen solubility sphere, parameters, and the fitting accuracy of **β,β'-C$_{12}$-TIFDMT** as determined by using the classic Hansen algorithm in the HSPiP Program (*5th Edition Version 5.4.08*) with a solubility limit of 2 g/L. The Hansen solubility parameters (δ_D, δ_P, δ_H, and R_0) are in MPa$^{1/2}$, the bad (23) and the good (7) solvents are shown in the 3D Hansen solubility solubility space with the red and blue spheres, respectively.

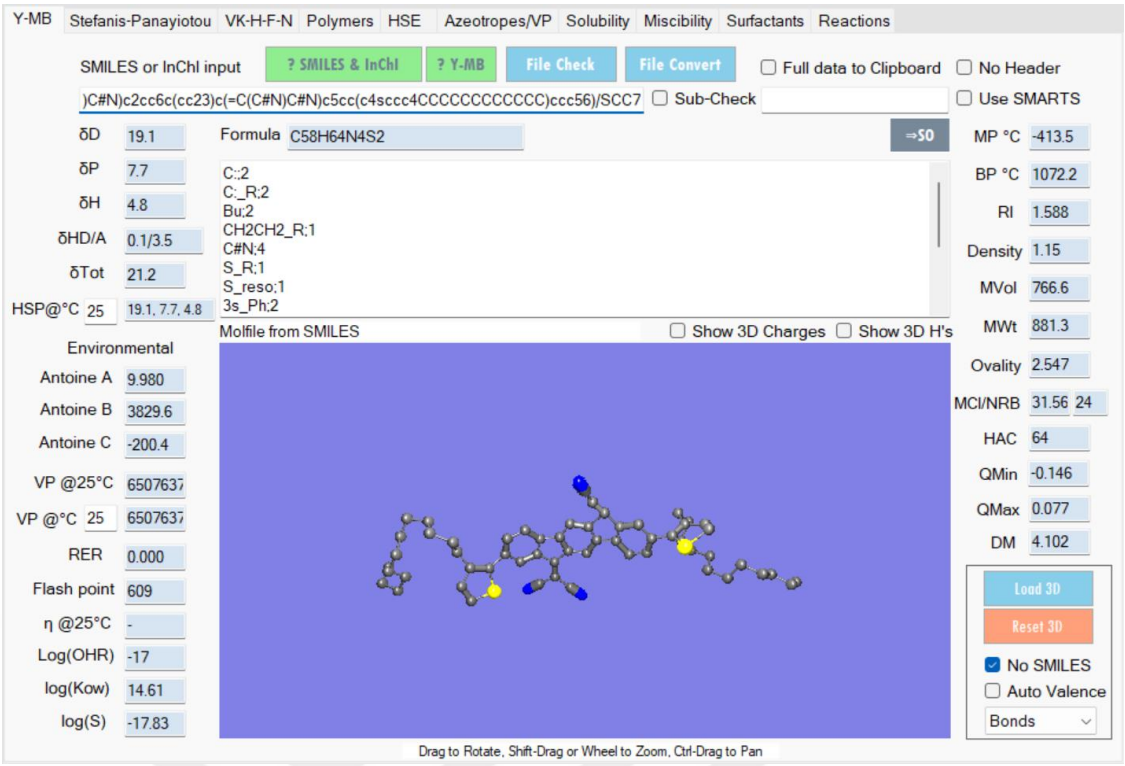

Figure 3.7 Hansen solubility parameters calculated for **β,β'-C$_{12}$-TIFDMT** by group contribution methodology in the HSPiP software (*5th Edition Version 5.4.08*) with DIY and Y-MB modules using simplified molecular-input line-entry system (SMILES).

Table 3.3 The calculation of **β,β'-C_{12}-TIFDMT** mole fraction in varied solvents based on the maximum solubilities measured and the squared interaction distance (Ra^2) between **β,β'-C_{12}-TIFDMT** and the solvent HSPs in the 3D Hansen solubility space.

Solvent	Solvent Density (g/mL)	Solvent Molecular Weight (g/mol)	Max. Solubility (g/L)	Semiconductor Molecular Weight (g/mol)	Semiconductor Mole Fraction	Ra	(Ra)2
Acetone	0.791	58.08	0.05	879.19	4.17576E-06	11.65	135.7225
Acetonitrile	0.786	41.05	0	879.19	0	16.43	269.9449
n-Amyl Acetate	0.87	130.18	0.16	879.19	2.72302E-05	10.32	106.5024
Benzene	0.874	78.11	2.01	879.19	0.000204277	8.3	68.89
1-Butanol	0.81	74.12	0.1	879.19	1.04079E-05	14.08	198.2464
t-Butyl Alcohol	0.775	74.12	0.03	879.19	3.2634E-06	14.51	210.5401
Chloroform	1.492	119.38	6.9	879.19	0.000627562	6.58	43.2964
Cyclohexane	0.779	84.16	0.08	879.19	9.8304E-06	11.21	125.6641
Diethyl Ether	0.706	74.12	0.04	879.19	4.77646E-06	12.96	167.9616
Dimethyl Sulfoxide (DMSO)	1.1	78.13	0	879.19	0	12.54	157.2516
1,4-Dioxane	1.034	88.11	1.11	879.19	0.000107572	8.47	71.7409
Ethanol	0.79	46.07	0	879.19	0	17.38	302.0644
Ethyl Acetate	0.902	88.11	0.13	879.19	1.44435E-05	10.15	103.0225
Ethylene Carbonate	1.32	88.06	0	879.19	0	16.86	284.2596
Ethylene Glycol	1.11	62.07	0	879.19	0	22.47	504.9009
Hexanes	0.659	86.18	0.05	879.19	7.43713E-06	14.25	203.0625
d-Limonene	0.84	136.23	0.3	879.19	5.5336E-05	8.32	69.2224
Methanol	0.791	32.04	0.03	879.19	1.38215E-06	21.75	473.0625
Methyl Iso-Butyl Ketone (MIBK)	0.801	100.16	0.14	879.19	1.99112E-05	11.09	122.9881
N-Methyl-2-Pyrrolidone (NMP)	1.028	99.13	0.5	879.19	5.48372E-05	8.74	76.3876
Methylene Chloride	1.325	84.93	4.9	879.19	0.000357111	7.91	62.5681
N,N-Dimethyl Formamide (DMF)	0.944	73.09	0.13	879.19	1.14483E-05	11.92	142.0864
2-Propanol	0.785	60.1	0	879.19	0	14.79	218.7441
Propylene Carbonate	1.204	102.09	0.05	879.19	4.82216E-06	12.38	153.2644
Propylene Glycol Monoethyl Ether Acetate	0.97	132.16	0.08	879.19	1.23974E-05	10.64	113.2096
Tetrahydrofuran	0.889	72.11	5.3	879.19	0.000488736	8.38	70.2244
Toluene	0.865	92.14	6.7	879.19	0.000811095	7.93	62.8849
Xylene	0.861	106.17	5	879.19	0.00070078	8.35	69.7225
Chlorobenzene	1.106	112.56	7.3	879.19	0.000844311	5.24	27.4576
Cyclopentanone	0.951	84.12	0.79	879.19	7.94746E-05	8.42	70.8964

Theoretical calculation of the intercept in the Hansen-adapted Scatchard-Hildebrand regular solution theory equation (1):

$$-\ln x_{OSC} = \frac{v_{OSC}}{RT}\Phi_{solv.}{}^{2}R_{a}{}^{2} + \frac{\Delta H_{fus}}{R}\left(\frac{1}{T} - \frac{1}{T_{mp-OSC}}\right) \quad (1)$$

By using the thermal properties of the enthalpy of fusion (ΔH_{fusion} = 36.45 kJ/mol) and the melting temperature ($T_{mp\text{-}OSC}$ = 504.30 K) for **β,β'-C$_{12}$-TIFDMT** (Figure 3.8),[14] the intercept in equation (1) is calculated to be 6.01. Note that the melting process at 504.30 K leads to a fully isotropic liquid phase, as visually confirmed through conventional melting point measurement. The end-set of the melting temperature is taken as it represents the completion of the melting process.

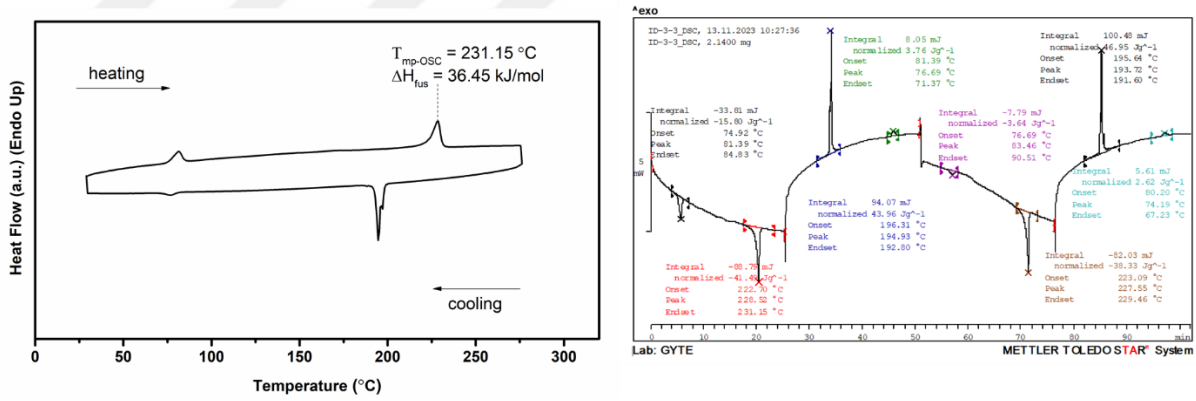

Figure 3.8 Differential scanning calorimetry scan of **β,β'-C$_{12}$-TIFDMT** at a temperature ramp of 10 °C min^{-1} under N_2 and the raw data from the instrument.

Table 3.4 The potential green solvents with Hansen solubility parameters (δ_D, δ_P, δ_H in $MPa^{1/2}$) and the corresponding specific **β,β'-C_{12}-TIFDMT**-solvent interaction distance ($R_a = (4\Delta\delta_D^2 + \Delta\delta_P^2 + \Delta\delta_H^2)^{1/2}$ in $MPa^{1/2}$, in which $\Delta\delta$ for a specific Hansen parameter is "$\delta_{OSC} - \delta_{solvent}$").

	Green Solvent	CAS Number	δ_D	δ_P	δ_H	R_a
1	Water	7732-18-5	15.5	16.0	42.3	39.6
2	Pentyl Acetate	628-63-7	15.8	3.3	6.1	10.3
3	Diethyl Carbonate	105-58-8	15.1	6.3	3.5	11.6
4	Anisole	100-66-3	17.8	4.4	6.9	6.3
5	Dimethyl Carbonate	616-38-6	15.5	8.6	9.7	11.7
6	Butyl Acetate	123-86-4	15.8	3.7	6.3	10.2
7	2-Methylanisole	578-58-5	18.3	4.7	4.8	5.2
8	Isobutyl Acetate	110-19-0	15.1	3.7	6.3	11.6
9	Isopropyl Acetate	108-21-4	14.9	4.5	8.2	12.2
10	2-Methyltetrahyrofuran	96-47-9	16.8	4.8	4.6	7.9
11	Cyclohexanone	108-94-1	17.8	8.4	5.1	6.6
12	Dimethyl Succinate	106-65-0	16.1	7.7	8.8	10.1
13	Diethyl Succinate	123-25-1	16.2	6.8	8.7	9.8
14	Methyl Oleate	112-62-9	16.2	3.8	4.5	9.5
15	Ethoxybenzene	103-73-1	18.4	4.5	4.0	5.2
16	Benzyl Alcohol	100-51-6	18.4	6.3	13.7	9.5
17	Cyclohexanol	108-93-0	17.4	4.1	13.5	10.6
18	Diethylene Glycol	111-46-6	16.6	12.0	19.0	17.0
19	Dimethyl Adipate	627-93-0	16.3	6.8	8.5	9.5
20	Triacetin	102-76-1	16.5	4.5	9.1	9.4
21	Triethylene Glycol	112-27-6	16.0	12.5	18.6	17.5

Table 3.5 The transistor characteristics of p^{++}-Si/SiO_2/PS-brush(M_n = 5 kDa)/**β,β'-C_{12}-TIFDMT**/Au OFET devices having the semiconductor layers processed from anisole, 2-methylanisole, ethoxybenzene, and 2-methyltetrahydrofuran. The average electron mobilities given for each condition are based on at least ten different OFET devices measured.

Green Solvent	**rpm**	**Temperature (°C)**	**μ_{avg} (μ_{max}) ($cm^2V^{-1}s^{-1}$)**	**I_{on}/I_{off}**	**V_T (V)**
Anisole	1500	170	3.87×10^{-3} (6.72×10^{-3})	10^3-10^4	11
		190	0.064 (0.178)	10^6-10^7	2
		200	0.064 (0.122)	10^6	24
	1700	170	0.0706 (0.176)	10^5	10
		190	0.080 (0.155)	10^6-10^7	7
		200	0.032 (0.085)	10^6	10
	2000	170	0.03755 (0.0575)	10^5	18
		190	0.049 (0.136)	10^5	21
		200	0.056 (0.126)	10^5-10^6	33
2-Me-Anisole	1500	170	2.65×10^{-3} (3.98×10^{-3})	10^3-10^4	20
		190	3.81×10^{-3} (8.87×10^{-3})	10^5	15
		200	0.018 (0.022)	10^4-10^5	36
	1700	170	0.011 (0.033)	10^5	7
		190	0.028 (0.052)	10^5	18
		200	0.030 (0.048)	10^6	8
	2000	170	4.00×10^{-3} (9.029×10^{-3})	10^5	17
		190	0.051 (0.125)	10^5	27
		200	0.035 (0.101)	10^6	24

Green Solvent	Rpm	Temperature (°C)	μ_{avg} (μ_{max}) ($cm^2V^{-1}s^{-1}$)	I_{on}/I_{off}	V_T (V)
Ethoxybenzene	1500	170	1.28×10^{-3} (4.94×10^{-3})	10^4-10^5	13
		190	0.030 (0.060)	10^5-10^6	27
		200	0.022 (0.029)	10^5	28
	1700	170	2.24×10^{-3} (3.76×10^{-3})	10^3-10^4	21
		190	0.040 (0.078)	10^6	15
		200	0.014 (0.029)	10^6	12
	2000	170	4.38×10^{-4} (6.72×10^{-4})	10^2-10^4	20
		190	0.052 (0.089)	10^5-10^6	18
		200	0.030 (0.064)	10^5-10^6	29
2-Me-THF	1500	170	1.58×10^{-3} 3.50×10^{-3}	10^4-10^5	16
		190	6.18×10^{-3} (9.35×10^{-3})	10^5	15
		200	0.013 (0.015)	10^5	14
	1700	170	0.035 (0.089)	10^6	22
		190	0.045 (0.094)	10^6	13
		200	0.082 (0.116)	10^6	13
	2000	170	0.122 (0.192)	10^5-10^6	9
		190	0.028 (0.068)	10^6	15
		200	0.038 (0.059)	10^6	21

Figure 3.9 The (*n*-channel) output plots for the p^{++}-Si/SiO_2/PS-brush(M_n = 5 kDa)/**β,β'-C_{12}-TIFDMT**/Au OFET devices, having the semiconductor layers processed from anisole (a), 2-methylanisole (b), ethoxybenzene (c), and 2-methyltetrahydrofuran (d).

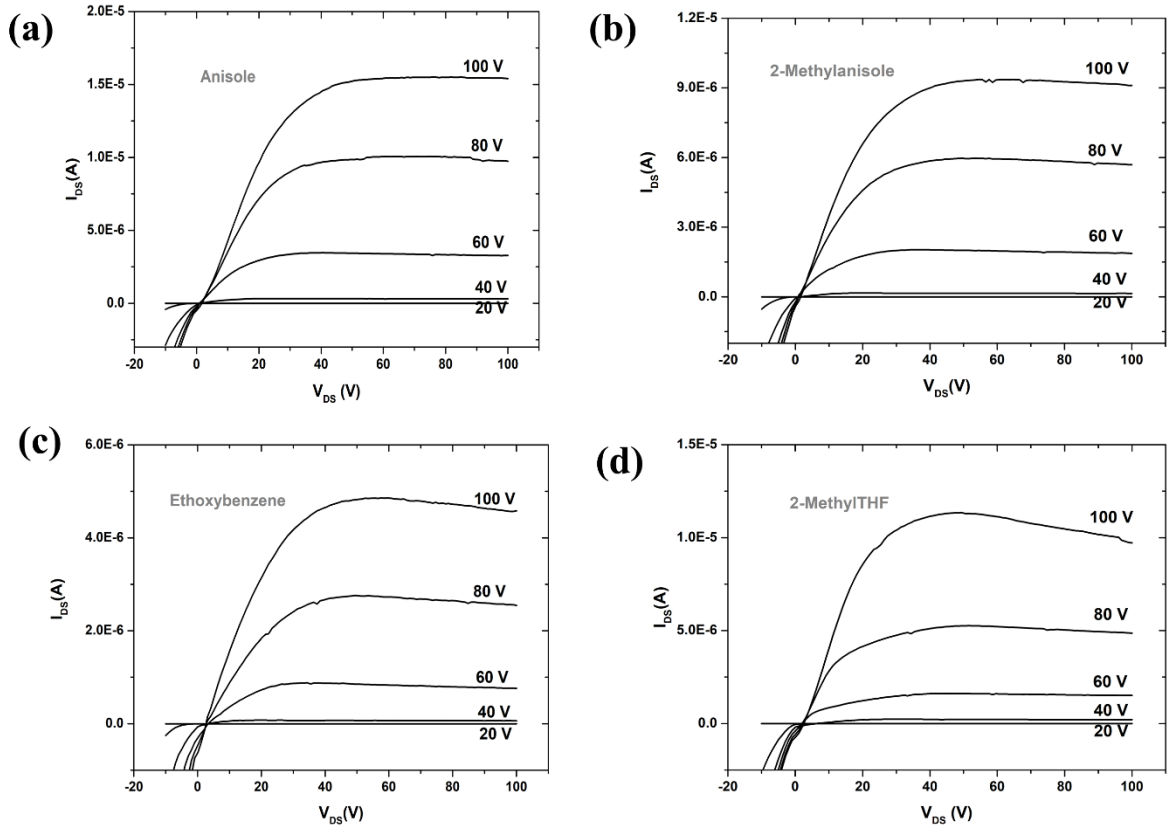

3.3.5 N-type Molecular Thermoelectrics

The development of n-type organic thermoelectric materials, especially π-conjugated small molecules, lags far behind their p-type counterparts, due primarily to the scarcity of efficient electron-transporting molecules and the typically low electron affinities of n-type conjugated molecules which leads to inefficient n-doping[144]. Herein, we demonstrate the n-doping of two functionalized (carbonyl vs. dicyanovinylene) indenofluorene-based conjugated small molecules, 2,8-bis(5-(2-octyldodecyl)thien-2-yl)indeno[1,2-b]fluorene-6,12-dione (**β,β'-C_{12}-TIFDKT**) and 2,2′-(2,8-bis(3-alkylthiophen-2-yl)indeno[1,2-b]fluorene-6,12-diylidene)dimalononitrile

(**β,β'-C_{12}-TIFDMT**), with n-type dopant (4-(2,3-Dihydro-1,3-dimethyl-1H-benzimidazol-2-yl)-N,N-dimethylbenzenamine) N-DMBI (Figure 3.10).

The two small molecules studied herein were synthesized in accordance with the previously reported synthesis and purification methods[124]. **β,β'-C_{12}-TIFDKT** and **β,β'-C_{12}-TIFDMT** were specifically chosen for thermoelectrics based on their highly favorable structural and electronic properties. Firstly, both molecules include a donor-acceptor-donor type of π-backbone with long, linear (-$C_{12}H_{25}$) alkyl substituents. This is critical to achieve solution-processability and proper molecular ordering in thin film. Secondly, the dicyanovinylene vs. carbonyl comparison is crucial to better understand the effect of functional groups on designing molecular thermoelectrics materials. The functional groups have been placed on the indenofluorene unit in a symmetric fashion to achieve a π-system extending to both ends of the indenofluorene unit along the short-axis. Thirdly, we specifically design the π-system with dicyanovinylenes (in TIFDMT) to ensure a more stabilized Lowest Unoccupied Molecular Orbital (LUMO) energy level with an extended orbital wave function (i.e., enhanced mesomeric effect), whereas these characteristics remain more limited (i.e., relatively higher and less π-extended LUMO) with carbonyls (in **β,β'-C_{12}-TIFDKT**). Notably, **β,β'-C_{12}-TIFDMT** exhibits high electron mobilities of over 0.1 $cm^2V^{-1}s^{-1}$ in solution-processed organic field-effect transistors.[105], [124] Finally, incorporating dicyanovinylene units into indenofluorenes is synthetically straightforward, as compared with the introduction of some other electron withdrawing units (e.g., -NO_2 and -F), through Knoevenagel condensations. In this current work, it is discovered that although **β,β'-C_{12}-TIFDMT** is poorly miscible with the dopant, it shows in the n-doped state a several orders of magnitude higher conductivity as compared to the carbonyl-functionalized **β,β'-C_{12}-TIFDKT**. Electron spin resonance (ESR) measurement proves that the n-doping level of TIFDMT is significantly higher than that of **β,β'-C_{12}-TIFDKT**. Interestingly, the molecular ordering for the **β,β'-C_{12}-TIFDMT** thin-film is enhanced by n-doping, as characterized by grazing-incidence wide-angle X-ray scattering (GIWAXS). By revealing the impact of carbonyl vs. dicyanovinylene on the n-doping efficiency, microstructure evolution upon doping, and thermoelectric performance, this work highlights the importance of simultaneous enhancement of molecular ordering and doping level of n-type π-conjugated small molecules for the future design of efficient thermoelectrics.

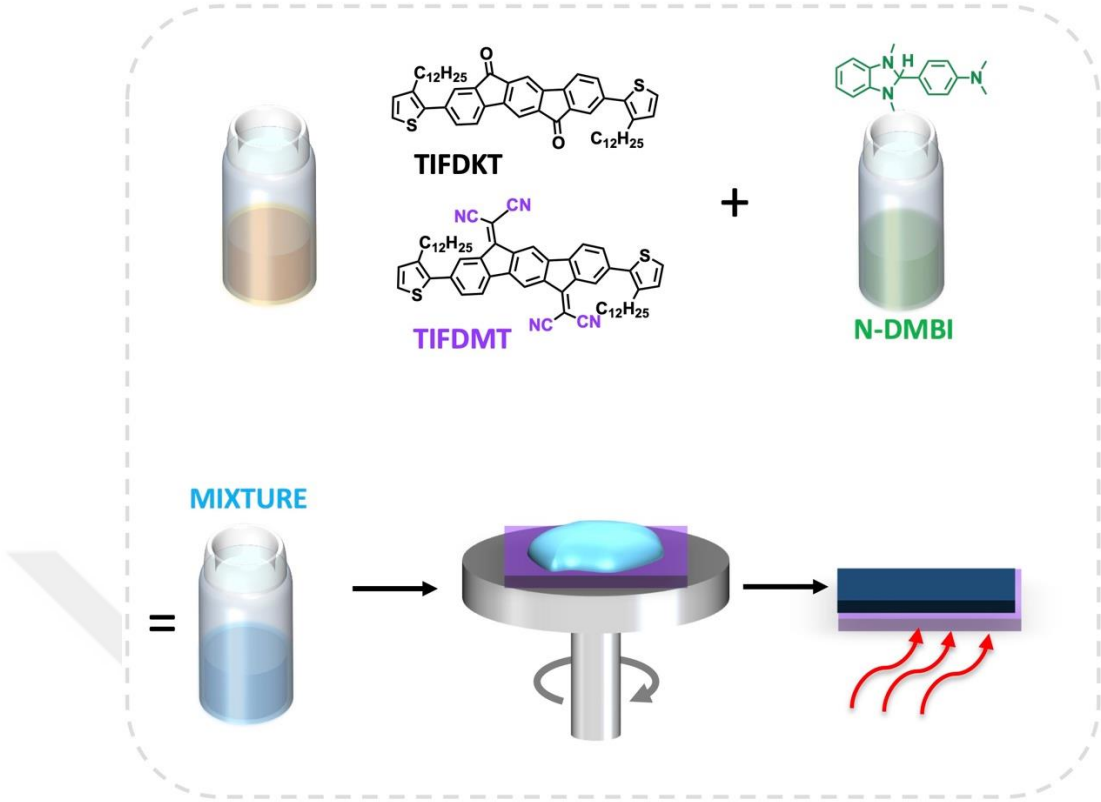

Figure. 3.10 Molecular structures of **β,β'-C_{12}-TIFDKT** and **β,β'-C_{12}-TIFDMT**, and the illustration of mix-solution doping methods.

The evolution of the electrical conductivity for **β,β'-C_{12}-TIFDKT** and **β,β'-C_{12}-TIFDMT** thin films was recorded as a function of the N-DMBI molar ratio, as shown in Figure 3.11A. The conductivities of the pristine **β,β'-C_{12}-TIFDKT** and **β,β'-C_{12}-TIFDMT** thin films are comparable, both on the order of 10^{-6} S cm^{-1}. After doping, the conductivity for the **β,β'-C_{12}-TIFDKT** thin film remains almost unchanged, even at a dopant concentration of 20 mol%. By contrast, the conductivity of the **β,β'-C_{12}-TIFDMT** thin film increases by 3 orders of magnitude with a low dopant concentration of 3 mol%, reaching 2.1 × 10^{-3} S cm^{-1}. The conductivity continues to gradually raise with the increased dopant concentration, and the highest conductivity value of 0.16 S cm^{-1} is achieved with the dopant concentration of 20 mol%. As the dopant concentration further increases above 20 mol%, the conductivity of the **β,β'-C_{12}-TIFDMT** thin-film decreases, which is commonly observed as a result of the disruption of thin film microstructure by excessive dopants.[145] Based on the temperature-dependent conductivity measurements carried out on the 20 mol% N-DMBI-doped

β,β'-C$_{12}$-TIFDMT thin film (Figure 3.11B), the activation energy (EA) is determined to be as low as 0.087 eV, suggesting a highly ordered molecular packing for **β,β'-C$_{12}$-TIFDMT** molecules in the doped thin-film state.

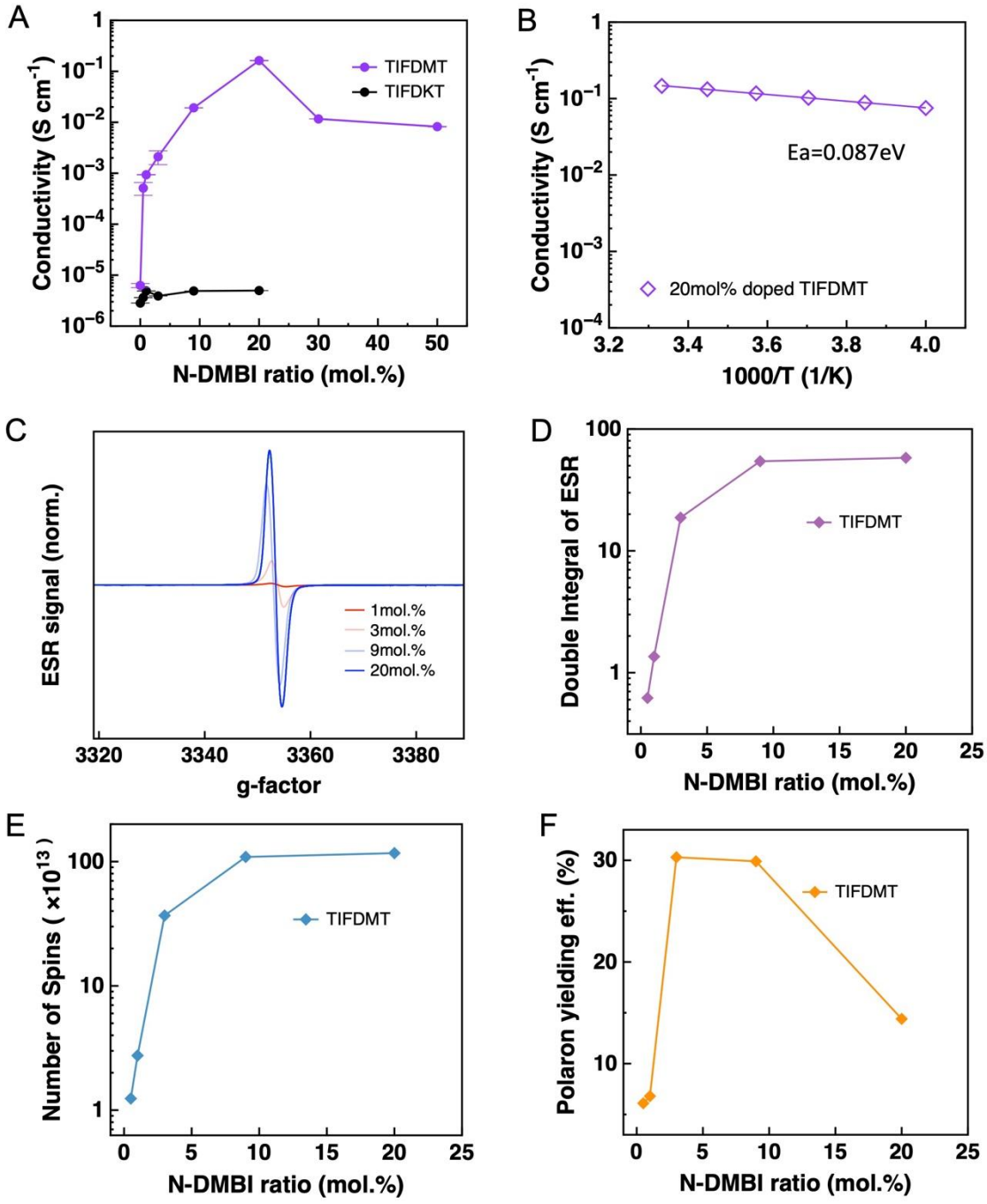

Figure. 3.11 (A) Electrical conductivity of the pristine and the doped **β,β'-C$_{12}$-TIFDKT** and **β,β'-C$_{12}$-TIFDMT** thin films as a function of N-DMBI dopant concentration. (B) Temperature dependence of the electrical conductivity of the 20 mol% doped **β,β'-C$_{12}$-TIFDMT** thin film. (C) ESR spectroscopy of the N-DMBI-doped

β,β'-C12-TIFDMT thin films for different doping concentrations measured at room temperature. (D) Double integral of the ESR signals, (E) the number of spins and (F) the polaron generation efficiency of the N-DMBI-doped **β,β'-C12-TIFDMT** thin film as a function of doping concentration.

We performed electron spin resonance (ESR) measurements on the doped TIFDKT and **β,β'-C12-TIFDMT** thin films (Figure 3.11C). While no noticeable signal is recorded for the doped **β,β'-C12-TIFDKT** thin film even at a doping concentration of 20 mol%, strong ESR signals are observed for the doped **β,β'-C12-TIFDMT** thin film starting from low doping concentrations and becoming stronger as the doping concentration increases.[146] This confirms the successful doping of **β,β'-C12-TIFDMT** thin films and the formation of polarons in the molecular lattice. As shown in Figure 3.11D, the double integral of the ESR signals for the N-DMBI-doped **β,β'-C12-TIFDMT** thin films increases by approx. two orders of magnitude as the doping level rises, eventually saturating at 20 mol%. The spin density in the doped **β,β'-C12-TIFDMT** films is estimated by referring to a standard sample of (2,2,6,6-tetramethylpiperidin-1-yl)oxyl (TEMPO) in toluene with known spin density based on the assumption that each TEMPO molecule has one spin, and the experimental setting parameter and the Q-factor of the resonator should be taken into account, as proposed by Neher et al.[147] It is apparent that N-DMBI induces more spins (i.e., unpaired electrons or polarons) with increasing doping concentration, which is consistent with the evolution of the electrical conductivity as shown in Figure 3.11A. The number of spins for different doping concentrations is shown in Figure 3.11E. The polaron generation efficiency (η_i) is typically defined as the ratio of the number of polarons (spins) to the number of dopants, which represents the efficiency of a dopant to generate polarons. ηi is a crucial metric for assessing the doping capability of a dopant for a particular semiconductor.[148] Considering that not all induced polarons eventually become free carriers, it is noteworthy that ηi is typically higher than the doping efficiency.[6] Figure 3.11F shows the ηi values of the N-DMBI-doped **β,β'-C12-TIFDMT** thin films. Although the number of spins continues to increase up to 20 mol% of doping concentration, the maximum ηi of 30.3% is obtained for the 3 mol% N-DMBI-doped **β,β'-C12-TIFDMT** film.

To understand the change of the morphology upon doping, tapping mode atomic force microscopy (AFM) was performed on both pristine and doped films of **β,β'-C12-**

TIFDKT and **β,β'-C_{12}-TIFDMT**. As shown in **Figure 3.12A**, the pristine **β,β'-C_{12}-TIFDMT** film displays multilayers with an uncontinous top layer. After doping, the layers become more continuous, whereas dopant aggregates appear on the top of the film (**Figure 3.12B**), suggesting a poor miscibility between **β,β'-C_{12}-TIFDMT** and N-DMBI. To gain information about the influence of doping on the microstructure and molecular packing of **β,β'-C_{12}-TIFDMT**, two-dimensional grazing-incidence wide-angle X-ray scattering (GIWAXS) measurements were performed for the pristine and 20 mol% N-DMBI-doped thin films. Interestingly, the patterns in **Figure 3.12C**, **3.12D** significant changes in the molecular arrangement and the crystallinity upon doping. The out-of-plane reflections are related to a layer organization, which is present for both thin-films but with different *d*-spacing values as derived from the main scattering intensity. The layer *d*-spacing is reduced from 31.4 Å to 25.0 Å by the incorporation of the N-DMBI dopant. At the same time, the overall crystallinity for the doped thin-film is increased as implied by the observed smaller full-width-at-half-maximum (fwhm) values of the sharper reflections. The molecular packing is also significantly affected by n-doping. The GIWAXS patterns clearly showed that the location of the corresponding π-stacking reflection shifts from off-meridional to in-plane for doped **β,β'-C_{12}-TIFDMT**. While the pristine **β,β'-C_{12}-TIFDMT** molecules reveal a π-stacking distance of 3.61 Å and arrange in a tiled fashion on the surface as illustrated in **Figure 3.12E**, in the doped state the π-stacking distance decreases to 3.36 Å adopting an edge-on dominant orientation on the surface (**Figure 3.12F**). The observed *d*-spacing along with the in-plane π-stacking interactions clearly suggest that **β,β'-C_{12}-TIFDMT** molecules adopt an edge-on layer packing with alkyl chain interdigitations in the n-doped thin-film state[124]. There is no evidence that the dopants intercalate into the π-π stacks of **β,β'-C_{12}-TIFDMT**. Rather, the dopants form aggregates on top of the **β,β'-C_{12}-TIFDMT** film, as indicated by the AFM image. As suggested by previously reported DFT calculations, the polaron delocalizes between neighbouring molecular backbones resulting in attractive forces that decrease the π-π distance.[149] Such a phenomenon has been observed in the doping of conjugated polymers.[150] Notably, the tighter packing and especially reduced π-stacking distance are important factors for more efficient charge transport.[151] As reported by Kim et al, highly ordered microstructures were formed after doping of a conjugated polymer using a novel solvent combination doping method, leading to an increase of charge carrier mobility by over

three orders of magnitude compared to that of the pristine film. Similarly, the better molecular order and shorter π-stacking distance herein well explain the significantly improved conductivity in the n-doped **β,β'-C12-TIFDMT** thin-film.[151]

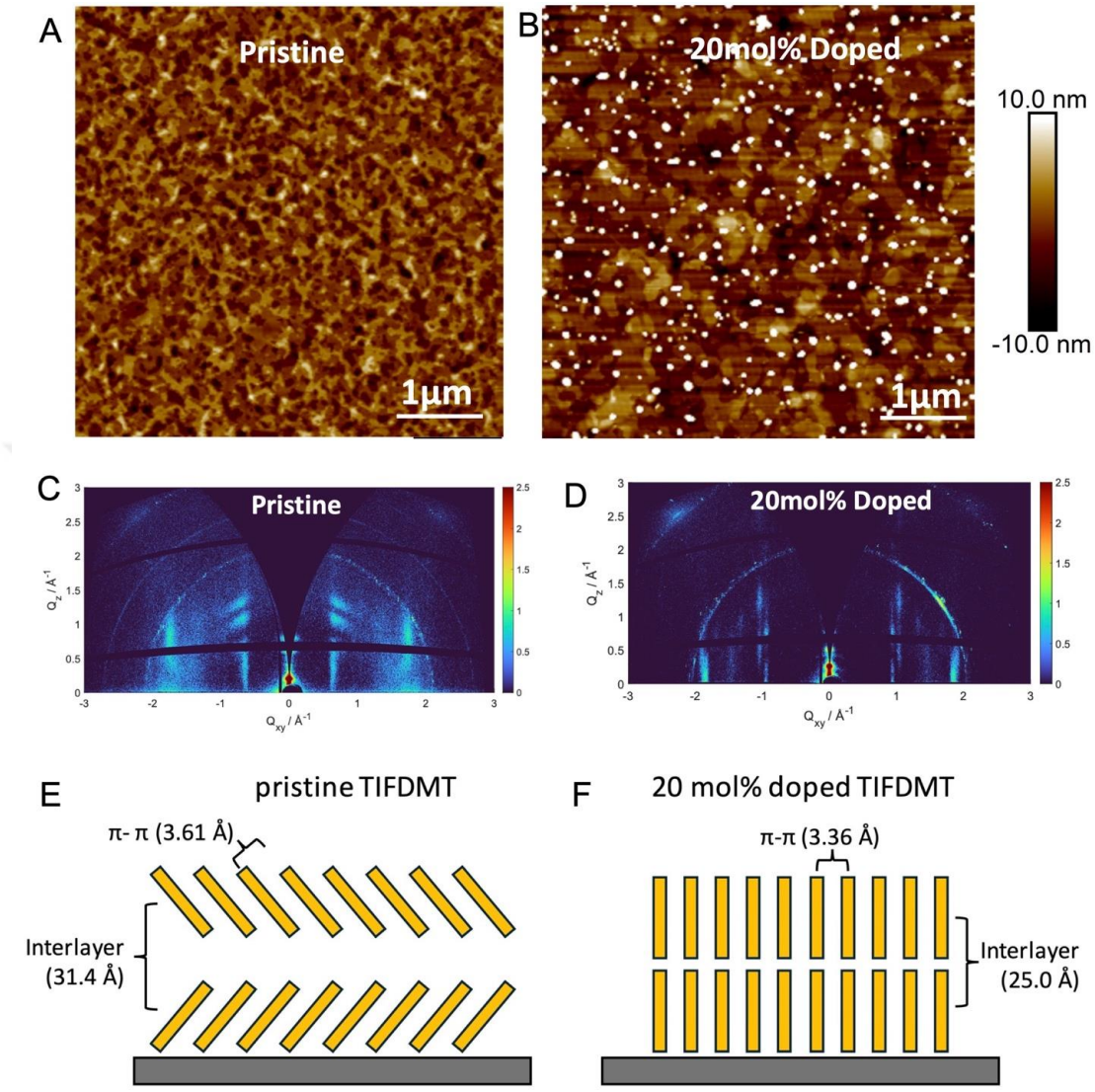

Figure 3.12 AFM tapping mode images of the pristine (A) and the 20 mol% doped (B) **β,β'-C12-TIFDMT** thin films. 2D GIWAXS patterns of the pristine (C) and the 20 mol% doped (D) **β,β'-C12-TIFDMT** thin films. Schematic illustration of the molecular packing for the pristine (E) and the 20 mol% doped (F) **β,β'-C12-TIFDMT** thin films. The yellow rectangles represent the **β,β'-C12-TIFDMT** molecular structures along its short π-molecular axis, forming a layer packing with alkyl chain interdigitations in the out-of-plane direction.

To assess the potential of **β,β'-C12-TIFDMT** in OTE devices, we evaluated the thermoelectric performance of N-DMBI-doped **β,β'-C12-TIFDMT** thin-films. The Seebeck coefficient (*S*) is determined by applying a temperature gradient across the doped thin film and monitoring the thermovoltages. The measured *S* values of **β,β'-C12-**

TIFDMT films with different doping concentrations are presented in **Figure 3.13A**. In theory, the *S* value is influenced by the difference between the Fermi level energy (E_F) and the charge transport energy (E_T).[151] As the doping level rises, more charges are created, shifting E_F toward E_T and altering the absolute *S* value. Indeed, the *S* value of the N-DMBI-doped **β,β'-C$_{12}$-TIFDMT** thin-films changes from -355 μV K^{-1} to -123 μV K^{-1} by increasing the doping concentration from 3 to 20 mol%. The power factor (*PF*) is a crucial statistic for characterizing thermoelectric performance, which is dependent on the interplay between σ and *S*. Using the acquired σ and *S* values, the *PF* values can be calculated from $PF=S^2\sigma$, see **Figure 3.13B**, where the N-DMBI-doped **β,β'-C$_{12}$-TIFDMT** thin-film reveals an optimized *PF* of 0.25 ± 0.006 μWm^{-1}K^{-2} at a doping concentration of 20 mol%.

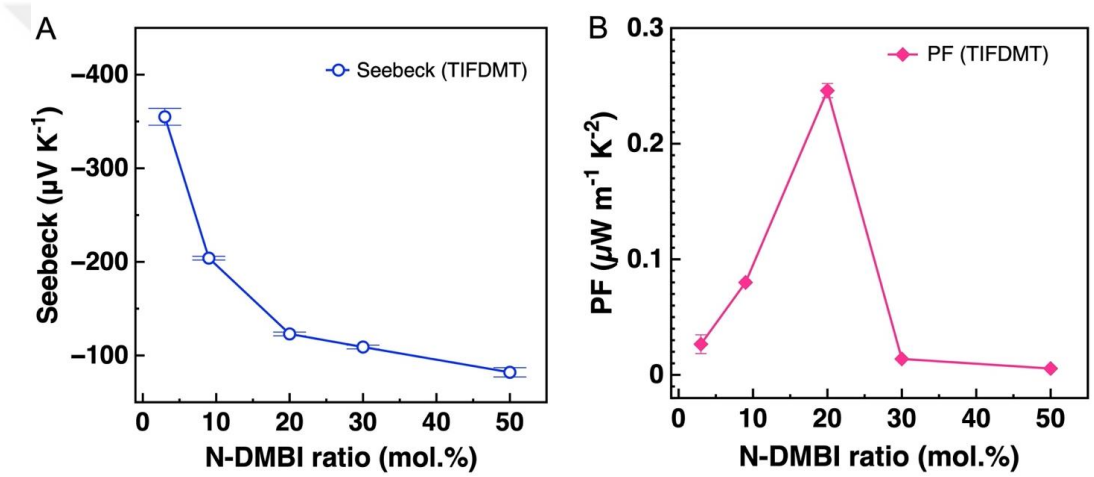

Figure 3.13 (A) Seebeck coefficient and (B) power factor of n-doped TIFDMT films as a function of dopant concentration.

3.4 Conclusions

In summary, the solubility behavior of an ambient-stable *n*-type semiconductor, 2,2'-(2,8-bis(3-dodecylthiophen-2-yl)indeno[1,2-b]fluorene-6,12-diylidene)dimalononitrile (**β,β'-C_{12}-TIFDMT**), was studied based on the solubility sphere method using Classic Hansen algorithm. As the solubility in 30 different solvents ranged from 7.3 g/L (8.3×10^{-3} M) to 0.03 g/L (3.0×10^{-5} M) and insolubility, the HSPs were determined to be δ_D = 20.8 $MPa^{1/2}$, δ_P = 5.8 $MPa^{1/2}$, δ_H = 5.5 $MPa^{1/2}$ with an interaction radius (R_0) of 8.3 $MPa^{1/2}$. A strong thermodynamic correlation based on the Scatchard-Hildebrand regular solution theory was identified between the molecular solubility and the semiconductor-solvent interaction distance R_a. From the fitting curve, it was evident that the maximum solubility limit could be estimated with the semiconductor's thermal properties of enthalpy of fusion (ΔH_{fus}) and melting temperature (T_{mp}). To the best of our knowledge, this relationship is being established for the first time for an organic semiconductor. Using minimal distance constraint in the HSP space and quantitative sustainability score, four suitable green solvents (i.e., ethoxybenzene, anisole, 2-methylanisole, and 2-methyltetrahydrofuran) were identified for **β,β'-C_{12}-TIFDMT** with R_a's of 5.17-7.93 $MPa^{1/2}$ (< R_0). These solvents yielded sufficient solubilities (≥ 4 g/L) for thin-film processing. Bottom-gate/top-contact OFETs were fabricated by spin-coating the semiconductor green solutions, which gave μ_e's reaching to ~0.2 $cm^2/V{\cdot}s$ (I_{on}/I_{off} ~ 10^6-10^7 and V_{on} ~ 0-5 V) in ambient. This *n*-channel device performance, to our knowledge, is the highest reported for an ambient-stable green solvent-processed OFET. Our HSP-based rational approach, an emerging yet underexplored methodology in the field, along with the unique findings presented herein, holds the potential to significantly contribute to integrating green solvents into the solution processing of *n*-channel semiconductors and to the broader development of green optoelectronics. In addition, two π-conjugated small molecules TIFDKT and TIFDMT were n-doped by N-DMBI for the first time and the impact of carbonyl vs dicyanovinylene units on doping efficiency, thin-film microstructure and thermoelectric performance was systematically investigated. Owing to its polar carbonyl groups and

higher solubility, TIFDKT exhibits good miscibility with the polar dopant molecule N-DMBI. However, because of its inadequately low LUMO, the n-doping of TIFDKT remains inefficient. Promisingly, TIFDMT with a significantly deeper LUMO can be effectively n-doped to achieve a respectable electrical conductivity of > 0.1 S cm^{-1} despite its lower miscibility with N-DMBI. The significant energy difference between the LUMOs of the two compounds is confirmed by DFT calculations, which also demonstrate that the polarons in the n-doped TIFDMT are more delocalized. Measurements of electron paramagnetic resonance provide further credence to the efficient n-doping of the dicyanovinylene-based TIFDMT. The GIWAXS results show that the doping significantly improves the molecular order of TIFDMT, resulting in a reorganization and closer edge-on π-π stacking distance, which promotes more effective charge transport in the doped state. In the evaluation of the thermoelectric properties, a respectable thermoelectric power factor of 0.25 μ$Wm^{-1}K^{-2}$ is attained for n-doped TIFDMT. Higher thermoelectric performance may be achievable by introducing polar side chains (e.g. ethylene glycol) facilitating an enhanced molecule-dopant miscibility[42], and/or by applying dopants with smaller size leading to a less disruption of the film microstructure at high dopant concentrations.[43] Our results clearly demonstrate that functionalized indenofluorenes with stabilized and delocalized frontier molecular orbitals are promising candidates for solution-processable n-type thermoelectric materials and sustainable energy solutions.

Chapter 4

Mono-(aryl)carbonyl Functionalization of [1]benzothieno[3,2-*b*][1]benzothiophene (BTBT): A Viable Asymmetric Molecular Engineering for Extremely High Solubility and Green Solvent Processed Organic Field-Effect Transistors

4.1 Introduction

Small molecules based on coplanar diacene-fused thienothiophene (DAcTT) π-scaffolds have emerged as one of the most appealing organic semiconductor family in the past decade.[34], [36] [1]Benzothieno[3,2-*b*][1]benzothiophene (BTBT) π-system in this family enables large frontier orbital coefficients on the sulfur atoms and forms a favorable solid-state electronic structure for efficient hole transport.[152], [153] As a direct result of their phene-like π-electronic structure, BTBTs have much larger band gaps (>3.5 eV) and deeper HOMO levels (< -5.5 eV) than the majority of the high performance molecular semiconductors reported to date.[143] Today, BTBT remains an unprecedented π-framework enabling facile synthetic modification and good solubility in common organic solvents, and showing optical transparency and ambient-stable high hole mobility.[154] In addition, from a materials production standpoint, the synthesis of BTBTs could typically be performed in a small number of steps with convenient chromatographic purifications, which makes these semiconductors quite attractive for industrial scale applications. Over the past decade, a large variety of π-electron rich BTBT semiconductors (Figure 4.1 and Table 4.5) have been developed including mono-

and di-alkyl substituted BTBTs (e.g., **(mono)-C_{13}-BTBT**[155] and **C_8-BTBT**[37]), di-aryl substituted BTBTs (e.g., **DPh-BTBT**[152]), and mono-aryl/mono-alkyl substituted BTBTs (e.g., **C_n-BTBT-Ph**[2] and **BTBT-Ph-$C_{6/12}$**[156], [157]) for use in *p*-channel organic field-effect transistors (OFETs). In these semiconductors, although the BTBT π-core is the active charge-transporting moiety, an alkyl and/or aryl substitution has been employed to realize proper semiconductor thin-film formation with efficient hole transport and solid-state characteristics.[157] Among these BTBTs, some structures have been reported to have good solubility in common organic solvents, and their synthetic purification and thin-film fabrication were carried out using solution-based techniques (Table 4.3). Typically, medium-length linear alkyl chain (-*n*-C_nH_{2n+1} (n = 3-8)) substitution has been employed to realize proper solution-processability, and the highest reported solubility was for dialkyl-substituted BTBTs (**C_8-BTBT**'s[37]) with values up to 90 mg·mL^{-1}, followed by solubilities of up to 9-11 mg·mL^{-1} for **C_n-BTBT-Ph**'s[2].

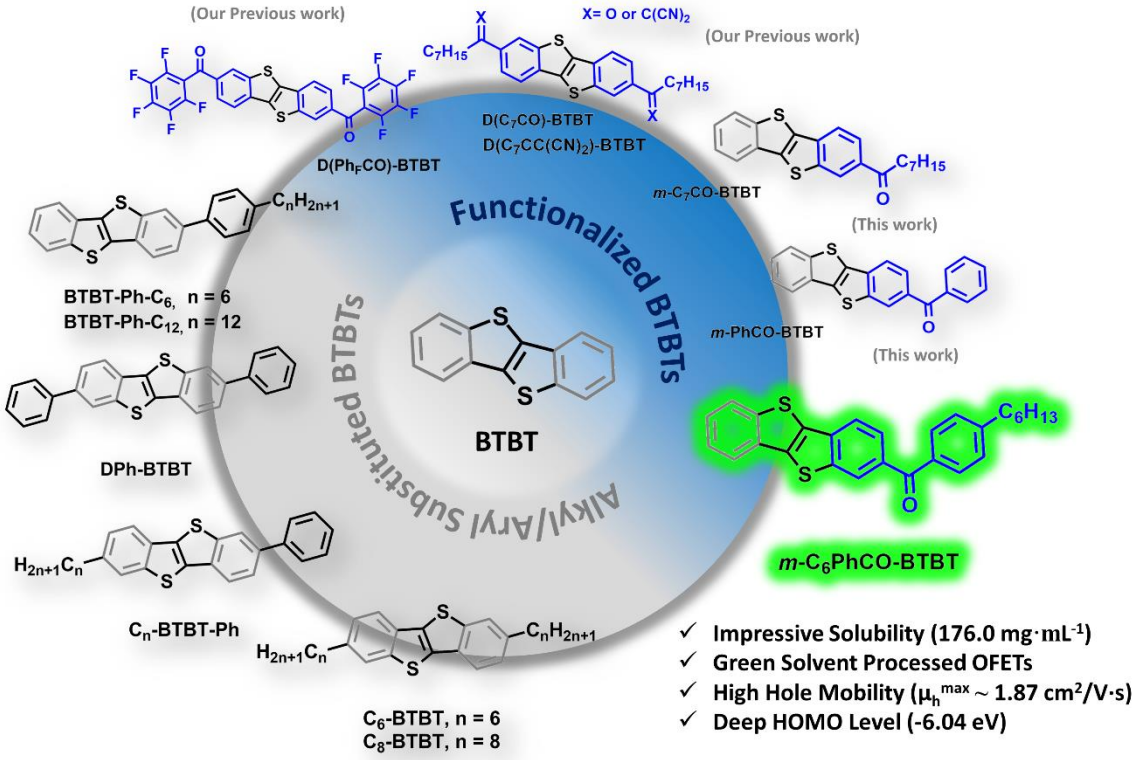

Figure 4.1 The chemical structures of previously developed alkyl/aryl substituted BTBT semiconductors (**BTBT-Ph-C$_{6/12}$,**[156], [157] **DPh-BTBT**,[152] **C$_n$-BTBT-Ph,**[2] and **C$_{6/8}$-BTBT**[37]) and the di-functionalized BTBTs, **D(Ph$_F$CO)-BTBT**,[32] **D(C$_7$CC(CN)$_2$)-BTBT**,[39] and **D(C$_7$CO)-BTBT**,[39] developed in our previous studies, and the mono-(aryl)carbonyl functionalized molecules, ***m*-C$_6$PhCO-BTBT**, ***m*-PhCO-BTBT**, and ***m*-C$_7$CO-BTBT**, developed in this study.

With the goal of expanding further the versatility of the BTBT π-scaffold, we have recently employed a different molecular engineering approach beyond the previously used alkyl/aryl substitutions and explored di-functionalization motif with electron withdrawing units (i.e., **D(Ph$_F$CO)-BTBT** with μ_e = 0.57 cm^2/V·s and **D(C$_7$CO)-BTBT with** μ_h = 0.03 cm^2/V·s, Figure 4.1).[32], [39] This approach allowed us to demonstrate the first examples of both functionalized and electron-transporting (*n*-type) BTBTs in the field of organic semiconductors. In these studies, we demonstrated that carbonyls in di-functionalized "CO-BTBT-CO" π-framework are very effective electron withdrawing functional groups that adopt highly coplanar conformations ($\theta_{torsion}$ ~ 2-4°) to extend the π-conjugation and considerably stabilize frontier orbital energies ($-\Delta E_{HOMO}$ = 0.74-0.86 eV and $-\Delta E_{LUMO}$ = 1.41-1.54 eV) through strong

negative inductive (-*I*)/resonance (-*R*) effects. The energetic stabilization through carbonyl was observed to be even stronger than that of, technically more electron-deficient, dicyanovinylene functional group (i.e., as in **D(C_7CC$(CN)_2$)-BTBT**, Figure 4.1).[39] To the best of our knowledge, our two molecules are the only known examples of carbonyl functionalized BTBT semiconductors reported to date. It is important to note that during the development of novel semiconductor structures in the past few decades, carbonyls have typically been used either to realize electron transport[128], [158], [159], [160] or to reduce the HOMO level of π-electron rich oligothiophenes[161] for ambient-stable hole transport. Therefore, as far as hole transport is concerned, carbonyl functionalization has never been considered as a potential strategy for BTBTs since they already have highly stabilized HOMOs (-5.5 – -5.8 eV, Table 4.3). A critical question remains as to whether carbonyl functionalization would be useful in realizing a high performance BTBT-based *p*-channel OFET. Furthermore, despite BTBT being a fused π-system, considering its highly soluble nature, further structural engineering approaches could introduce unique molecular and electronic properties. This could facilitate eco-friendly green solvent processing and enhance the versatility of DAcTTs in (optoe)electronics in general.

We herein present a unique molecular engineering on the BTBT π-system by employing *mono*-(aryl)carbonyl functionalization with one hexyl (*n*-C_6H_{13}) substituent, and demonstrate the design, synthesis, and characterization of a new asymmetric BTBT semiconductor, ***m*-C_6PhCO-BTBT**. The new molecule was produced in gram-scale through a two-step transition-metal-free synthesis, and the detailed structural, physicochemical, and (opto)electronic characterizations were performed. Mono-(aryl)carbonyl functionalization stabilizes frontier molecular orbitals (ΔE_{HOMO} = -0.29 eV *vs.* ΔE_{LUMO} = -0.65 eV) and induces an asymmetric π-electronic structure having a ground state molecular dipole moment (μ_g) of 3.17 D and a large excited state dipole moment (μ_e) of 12.69 D. Moreover, the asymmetric π-backbone demonstrates a significant degree of polarizability. The new π-electronic structure yields excellent solubility behavior in varied organic solvents, including a number of eco-friendly green solvents. Hansen solubility parameters (HSP) analysis, combined with thermodynamics data from differential scanning calorimetry (DSC), was employed to explore the solubility behavior of the new molecule and to elucidate unique structure-solubility-cohesive energetics relationships. In this analysis, two other novel molecules, ***m*-PhCO-**

BTBT, and ***m*-C$_7$CO-BTBT**, were also synthesized and used as the reference molecules, along with some structurally related BTBT semiconductors from the earlier studies in the literature. The HSPs for ***m*-C$_6$PhCO-BTBT** are determined to be δ_D = 18.9 MPa$^{1/2}$, δ_P = 5.7 MPa$^{1/2}$, and δ_H = 5.8 MPa$^{1/2}$ with an interaction radius (R_0) of 8.0 MPa$^{1/2}$. Strong thermodynamic correlations of the molecular solubility with thermal properties are established for the first time in the literature. ***m*-C$_6$PhCO-BTBT** exhibits prompt dissolution at room temperature in chloroform, displaying a remarkable room temperature solubility of 176.0 mg·mL^{-1} (0.41 M), which, to our knowledge, represents the highest solubility ever reported for a high-performance organic semiconductor. The impressive solubility of the new molecule even allowed for the preparation of semiconductor solutions (solubility up to ~12.5 mg·mL^{-1} at room temperature) in eco-friendly green solvents such as 2-methyltetrahydrofuran, ethyl acetate, ethoxybenzene, acetone, and ethanol, suitable for thin-film solution-processing. In the past few decades, small molecular OFETs have hardly been fabricated from these solvents, and, to the best of our knowledge, BTBT-based semiconducting thin-films are fabricated for the first time from these solvents. The charge-transport characteristics of the new molecule were studied in solution-processed top-contact/bottom-gate (TC/BG) OFETs. In the field of π-conjugated small molecules, ***m*-C$_6$PhCO-BTBT** is now a rare example of a high-mobility *p*-type semiconductor with a deep HOMO level of -6.04 eV. The maximum saturation hole mobilities were achieved for thin-films spin-coated from 2-methyltetrahydrofuran (μ_h^{max} = 1.87 cm^2/V·s, μ_h^{avg} = 1.21 cm^2/V·s (I_{on}/I_{off} = 10^7-10^8)) and ethyl acetate (μ_h^{max} = 0.62 cm^2/V·s, μ_h^{avg} = 0.41 cm^2/V·s (I_{on}/I_{off} = 10^6-10^7)) solutions. Relatively lower μ_h's of 0.07-0.11 cm^2/V·s (I_{on}/I_{off} = 10^5-10^6) were realized for spin-coated thin-films from acetone and ethoxybenzene, while drop-casted thin-films from ethanol yielded μ_h's of ~ 0.001 cm^2/V·s (I_{on}/I_{off} ≈ 10^4). Microstructural and morphological characterizations shed light on the observed transistor behaviors, revealing the key effects of differences in solute-green solvent interactions.

4.2 Experimental Section

4.2.1 Materials and Methods

Friedel-Crafts acylation reactions were conducted under nitrogen atmosphere with conventional Schlenk techniques and all reagents were used as received without any purifications. Chromatographic purification was carried out using 230-400 mesh size silica gel. ^{1}H and ^{13}C NMR spectroscopy characterizations were carried out on Bruker 400 spectrometer (^{1}H, 400 MHz; ^{13}C, 100 MHz). Elemental analyses were recorded on a Thermo Scientific^{TM} FLASH 2000 instrument. Atmospheric pressure chemical ionization mass spectra (APCI-MS) were recorded by using molecular solid sample on Advion-Expression^{L}-CMS instrument. Thermogravimmetric analysis (TGA) and differential scanning calorimetry (DSC) measurements were performed under nitrogen (heating rate ≈ 10 °C/min) using Mettler Toledo-TGA/STDA 851 and Mettler Toledo-DSC 822e model instruments, respectively. For the calibration process in DSC, In and Zn standards (Mettler Toledo, Schwerzenbach, Switzerland) were used. Conventional melting temperatures were recorded on Electrothermal IA9000 instrument. Cyclic voltammograms were recorded on the BAS-Epsilon potentiostat/galvanostat system (Bioanalytical Systems Inc. (Lafayette, IN) equipped with a C3-cell stand electrochemical station) using ferrocene/ferrocenium redox couple (Fc/Fc^{+}: $E_{1/2}$ = +0.40 V) as the internal standard. Pt wire was used as the working and the counter electrodes, and the reference electrode was Ag/AgCl (3 M NaCl). The. UV-vis absorption studies were performed on a Shimadzu UV-1800 spectrophotometer, and photoluminescence (PL) spectra were recorded with an Agilent-Cary Eclipse fluorescence spectrophotometer. Density Functional Theory (DFT) calculations of equilibrium geometry, electrostatic potential map, frontier molecular orbitals, molecular dipole moment, polarizability and single point energy were performed using B3LYP functional and 6-31G** basis set as implemented in Spartan ’24 version 1.0.0 (Wavefunction Inc., 2024, Irvine, CA) [162] The intramolecular reorganization energies for hole (λ_h) and electron (λ_e) transport were calculated by using the standard procedure described in the literature. [163]

4.2.2 Synthesis and Characterization

[1]Benzothieno[3,2-b][1]benzothiophene (**BTBT**), 2,7-dioctyl[1]Benzothieno[3,2-b][1]benzothiophene (**C_8-BTBT**), and 1,1'-(benzo[b]benzo[4,5]thieno[2,3-d]thiophene-2,7-diyl)bis(octan-1-one) **(D(C_7CO)-BTBT)** were synthesized according to the reported procedures.[37], [39]

Synthesis of benzo[b]benzo[4,5]thieno[2,3-d]thiophen-2-yl(4-hexylphenyl)methanone (**m-C_6PhCO-BTBT**): $AlCl_3$ (2.42 g, 18.14 mmol) was added into a solution of [1]benzothieno[3,2-b][1]benzothiophene (BTBT) (0.80 g, 3.32 mmol, 1.0 equiv.) in anhydrous dichloromethane (70 mL) at -10 °C under nitrogen. The resulting solution was stirred at -10 °C for 30 min, and then it was cooled down to -78 °C. 4-Hexylbenzoyl chloride (3.74 g, 16.64 mmol, 5.0 equiv.) was subsequently added dropwise, and the mixture was stirred for 1 h at the same temperature. The reaction mixture was allowed to warm to room temperature and stirred for 2 days. After extraction of the reaction mixture with $CHCl_3$, organic layer was dried with Na_2SO_4, filtered, and concentrated to yield the crude product. The crude was then purified by column chromatography on silica gel using chloroform as the mobile phase to afford the final product as an off-white solid (1.21 g, 84.9% yield). Melting point: 151-152 °C; ^{1}H NMR (400 MHz, $CDCl_3$), δ (ppm): 8.40 (s, 1H), 7.99-7.93 (m, 4H), 7.81 (d, 2H, J = 8.0 Hz), 7.51-7.45 (m, 2H), 7.35 (d, 2H, J = 8.0 Hz), 2.73 (t, 2H, J = 8.0 Hz), 1.69 (m, 2H), 1.35 (m, 6H), 0.91 (m, 3H, J = 8.0 Hz); ^{13}C NMR (100 MHz, $CDCl_3$), δ (ppm): 195.8, 148.2, 142.8, 141.9, 136.7, 135.9, 135.3, 134.4, 133.0, 132.8, 130.3, 128.4, 126.8, 126.5, 125.8, 125.2, 124.1, 122.1, 121.2, 36.1, 31.8, 31.3, 28.8, 22.7, 14.1; MS (APCI) m/z calcd for $C_{27}H_{24}OS_2$: 428.13 [M^+]; found: 428.440 [M^+]; elemental analysis calcd (%) for $C_{27}H_{24}OS_2$: C, 75.66; H, 5.64; found: C, 75.63; H, 5.70.

Synthesis of benzo[b]benzo[4,5]thieno[2,3-d]thiophen-2-yl(phenyl)methanone ***(m-PhCO-BTBT)***: $AlCl_3$ (0.81 g, 6.09 mmol) was added into a solution of [1]benzothieno[3,2-*b*][1]benzothiophene (BTBT) (1.20 g, 4.98 mmol, 1.0 equiv.) in anhydrous dichloromethane (100 mL) at -10 °C under nitrogen. The resulting solution was stirred at -10 °C for 30 min, and then it was cooled down to -78 °C. Benzoyl chloride (3.51 g, 24.96 mmol, 5.0 equiv.) was subsequently added dropwise, and the

mixture was stirred for 1 h at the same temperature. The reaction mixture was allowed to warm to room temperature and stirred for 2 days. After extraction of the reaction mixture with $CHCl_3$, organic layer was dried with Na_2SO_4, filtered, and concentrated to yield the crude product. The crude was then purified by column chromatography on silica gel using chloroform as the mobile phase to afford the final product as an off-white solid (1.22 g, 71.2% yield). Melting point: 224-225 °C; ^{1}H NMR (400 MHz, $CDCl_3$), δ (ppm): 8.41 (s, 1H), 7.97-7.93 (m, 4H), 7.87 (d, 2H, *J* = 6.0 Hz), 7.65 (t, 1H, J = 6.0 Hz), 7.56-7.46 (m, 4H); ^{13}C NMR (100 MHz, $CDCl_3$), δ (ppm): 196.4, 142.9, 141.9, 137.9, 136.9, 136.1, 134.0, 133.1, 132.8, 132.4, 130.1, 128.5, 126.9, 126.8, 125.9, 125.2, 124.2, 122.2, 121.2; MS (APCI) m/z calcd for $C_{21}H_{12}OS_2$: 344.03 [M^+]; found: 344.540 [M^+]; elemental analysis calcd (%) for $C_{21}H_{12}OS_2$: C, 73.23; H, 3.51; found: C, 73.42; H, 3.73.

Synthesis of 1-(benzo[b]benzo[4,5]thieno[2,3-d]thiophen-2-yl)octan-1-one (***m-C$_7$CO-BTBT***): $AlCl_3$ (0.62 g, 4.66 mmol) was added into a solution of [1]benzothieno[3,2-*b*][1]benzothiophene (BTBT) (1.12 g, 4.66 mmol, 1.0 equiv.) in anhydrous dichloromethane (80 mL) at -10 °C under nitrogen. The resulting solution was stirred at -10 °C for 30 min, and then it was cooled down to -78 °C. Octanoyl chloride (0.76 g, 4.66 mmol, 1.0 equiv.) was subsequently added dropwise, and the mixture was stirred for 1 h at the same temperature. The reaction mixture was allowed to warm to room temperature and stirred for 2 days. After extraction of the reaction mixture with $CHCl_3$, organic layer was dried with Na_2SO_4, filtered, and concentrated to yield the crude product. The crude was then purified by column chromatography on silica gel using chloroform as the mobile phase to afford the final product as an off-white solid. (1.24 g, 72.6% yield). Melting point: 179-180 °C; ^{1}H NMR (400 MHz, $CDCl_3$), δ (ppm): 8.56 (s, 1H), 8.06 (d, 1H, *J* = 8.0 Hz), 7.97-7.95 (m, 3H), 7.51-7.46 (m, 2H), 3.08 (t, 2H, *J* = 8.0 Hz), 1.82-1.79 (m, 2H), 1.40-1.32 (m, 8H), 0.92 (t, 3H, *J* = 8.0 Hz); ^{13}C NMR (100 MHz, $CDCl_3$), δ (ppm): 199.7, 142.8, 142.2, 136.8, 136.2, 133.7, 133.0, 132.8, 125.8, 125.1, 124.8, 124.5, 124.2, 122.1, 121.4, 38.8, 31.4, 29.4, 28.7, 24.6, 22.6, 14.1; MS (APCI) m/z calcd for $C_{22}H_{22}OS_2$: 366.11 [M^+]; found: 366.469 [M^+]; elemental analysis calcd (%) for $C_{22}H_{22}OS_2$: C, 72.09; H, 6.05; found: C, 72.33; H, 6.14.

4.2.3 Solubility Measurements and HSP Analysis

UV-Vis absorption spectroscopy method is used in order to determine the semiconductor solubility in different solvents. Initially, a linear calibration curve was generated (R^2 = 0.995-0.997, Figure 4.16) at the semiconductor's absorption peak (λ_{max} = 328 nm for ***m*-C$_6$PhCO-BTBT**, 330 nm for ***m*-PhCO-BTBT**, and 329 nm for ***m*-C$_7$CO-BTBT**) in chloroform. This was achieved by recording the UV-Vis absorption spectra (Figure 4.16) of the semiconductor standard solutions (ranging from 9.3×10^{-7} M to 5.8×10^{-5} M). Subsequently, saturated solutions of the semiconductor were prepared by weighing approximately 10.0 mg of the organic semiconductor solid into a vial and adding 500 μL of a specific solvent using a micropipette. After preparation, the mixture was stirred and sonicated for 10 minutes at room temperature. Subsequently, the mixture was filtered through a PTFE syringe filter with a pore size of 0.20 μm (VWR, part of Avantor). The filtrate was then diluted (up to 100-5000 times depending on the specific solvent) with chloroform to bring the optical absorption within the range of the calibration curve. For each solvent, the absorbance at the absorption peak was measured, and the corresponding solubility value was calculated by substituting this absorbance value into the Beer-Lambert law equation ($A = \varepsilon \cdot b \cdot c$), where A is the absorbance, ε is the molar absorptivity, b is the path length, and c is the concentration. For solubilities exceeding 10.0 mg·mL^{-1}, an additional gravimetric method is employed. In this method, approximately 10.0-15.0 mg of the semiconductor solid is accurately weighed into a vial. Incremental volumes of the solvent (in 50-100 μL portions) are then added using a micropipette. After each addition, the solution is stirred or sonicated for 10 minutes at room temperature. This process continues until complete dissolution is visually confirmed. Once dissolution is complete, the semiconductor solution is filtered through a PTFE syringe filter (VWR, part of Avantor, 0.20 μm pore size) and then evaporated to dryness using a rotary evaporator. The gravimetric solubility was determined by calculating the ratio of the recovered semiconductor solid weight (m_{osc}) to the total amount of solvent ($V_{solvent}$), using the equation "solubility = $m_{osc}/V_{solvent}$". Typically, the difference in solubilities determined via spectroscopic and gravimetric methods was found to be less than 4%. The Hansen solubility sphere parameters and fitting accuracy were determined using the Genetic algorithm in the HSPiP Program (*5th Edition Version 5.4.08*), with a solubility limit of 4.0 mg·mL^{-1}.[125] Solubility scores of

"1" (indicating a good solvent) and "0" (indicating a nonsolvent) were assigned based on the solubility tests described above. The group contribution methodology was employed using Neural Network techniques in the same HSPiP program.

4.2.4 OFET Device Fabrication and Electrical Characterization

Top-contact/bottom-gate (TC/BG) organic field effect transistors (OFETs)[98], [164] were fabricated on heavily *p*-doped (100) silicon substrate (p^{++}-Si) having a 300 nm thermally grown silicon dioxide (SiO_2) as the gate dielectric layer. The substrates were cleaned via sonication in an ultrasonic bath with hexane, acetone, and ethanol, respectively, for 10 minute each, dried with nitrogen and treated with air plasma for 3 min (Harrick Plasma, 30W). An ultrathin (~3.6 nm) polystyrene brush (PS-brush) layer (grafting density ≈ 0.45 chains·nm^{-2}) was formed on the p^{++}-Si/SiO_2 (300 nm) substrates using hydroxyl-terminated polystyrene (M_n = 5.0 kDa, M_w/M_n = *1.05, Polymer Source Inc.*) via a "grafting-to" method, as described in earlier methods.[58], [165], [166] Organic semiconductor films (40-50 nm thick) were spin-coated onto p^{++}-Si/SiO_2 (300 nm)/PS-brush (M_n = 5 kDa) substrates from green solvent solutions (4 mg·mL^{-1} in 2-methyltetrahydrofuran, ethyl acetate, ethoxybenzene, and acetone) at 1200 rpm for 60 s. For deposition from ethanol (1 mg·mL^{-1}), drop-casting method was used at solution and substrate temperatures of 60 °C. The semiconductor thin-films were then annealed at varied temperatures (90-130 °C) under vacuum. The surface morphology and the microstructure of the solution-processed semiconductor thin-films were characterized by using atomic force microscopy (NanoSurf FlexAFM C3000) and X-ray diffraction (Malvern Panalytical Empyrean diffractometer) techniques. Finally, Au source-drain electrodes (50 nm thickness) with variable channel lengths of 30, 40, 50, 60, 80 μm (width = 1000 μm) were deposited via thermal evaporation (growth rate = 0.2 Å/s) under high vacuum (~10^{-6} Torr) using high density deposition masks (Ossila, E322). The electrical characterizations of the p^{++}-Si/SiO_2 (300 nm)/PS-brush (M_n = 5 kDa)/***m*-C$_6$PhCO-BTBT** (40-45 nm)/Au (50 nm) OFET devices was performed in an ambient probe station (Everbeing BD-6) using a Keithley 2614B source-measure unit (without excluding natural or fluorescent lighting). Charge carrier mobility (μ_h) was estimated in the saturation regime from the $I_{DS}^{1/2}$ *vs.* V_{GS} transfer plots based on the conventional metal-oxide-semiconductor field-effect transistor (MOSFET) model using the formula,

$\mu_{sat} = (2I_{DS}L)/[WC_i(V_{GS} - V_{th})^2]$, where I_{DS} is the source−drain current, L is the channel length, W is the channel width, C_i is the areal capacitance of the gate dielectric with the PS-brush layer (10.4 nF/cm^2 based on our large grafting density of 0.45 chains·nm^{-2} and M_n = 5 kDa),[59], [124] V_{GS} is the gate voltage, and V_{th} is the threshold voltage.

4.3 Results and Discussion

4.3.1 Synthesis, Characterization, and Thermal Properties

The syntheses of the new mono-carbonyl molecules, ***m*-C$_6$PhCO-BTBT**, ***m*-PhCO-BTBT**, and ***m*-C$_7$CO-BTBT**, are shown in Figure 4.2. The mono-carbonyl functionalized BTBTs were synthesized in gram scale via regioselective Friedel-Crafts acylation at 2-position of the BTBT π-core using 4-*n*-hexylbenzoyl chloride (4-*n*-C_6H_{13}-PhCOCl), benzoyl chloride (PhCOCl), and 4-*n*-octanoylchloride (*n*-C_7H_{15}-COCl) reagents, respectively, in the presence of $AlCl_3$ Lewis acid catalyst. As the new molecules were found to have excellent solubility (*vide infra*) in common organic solvents, the purifications were performed via column chromatography to yield the final pure solids in gram scale as single batches (~85%, ~71%, ~73% yields, respectively). While a stoichiometric amount (1.0 *equiv.)* of C_7H_{15}-COCl reagent was used to prevent di-carbonyl functionalization, excess (~5.0 *equiv.*) amounts were safely used for 4-*n*-C_6H_{13}-PhCOCl and PhCOCl reagents without any di-carbonyl product formation. This suggests that benzoyl unit deactivates the BTBT π-system towards second acylation,[167] which is quite different than the Friedel-Crafts acylation with alkanoyl chloride (RCOCl) that typically yields di-carbonyl product in good yields (>70%).[37], [39] The molecular structure and the chemical purity of the new molecules were characterized by using ^{1}H and ^{13}C NMR spectroscopies (Figures 4.5, 4.6, 4.8, 4.9, 4.11, and 4.12), atmospheric-pressure chemical ionization mass spectrometry (APCI-MS) (Figures 4.7, 4.10, and 4.13), and elemental analysis. The phene-like electronic structure of the BTBT π-system, which reduces the π-electronic interaction between outer phenyl

rings, was evident in the ^{1}H NMR spectra (Figures 4.5, 4.8, and 4.11) of the new molecular structures. In the case of ***m*-C$_6$PhCO-BTBT**, as shown in Figure 4.2, the chemical shifts of the non-exchangeable aromatic protons "e, g", which are on the outer phenyl ring adjacent to the 4-*n*-hexylbenzoyl unit, show downfield shifts of ~0.5 ppm relative to those of the unfunctionalized BTBT. However, the other outer phenyl ring protons "a-d" show minimal changes in their chemical shifts. This indicates a reduced electron density (π-electron deficiency) on one side of the BTBT unit due to the asymmetric electron withdrawing effect of the mono-carbonyl functionalization. The π-density on the other outer phenyl side remains similar to that of the parent BTBT π-system. The asymmetric π-electronic structure in ***m*-C$_6$PhCO-BTBT** leads to a large ground state molecular dipole moment (Figure 4.2(a), μ_g = 3.17 D) and unique solvent polarity-dependent optoelectronic characteristics with a large excited state (S_1) dipole moment (μ_e) of 12.69 D (*vide infra*). Moreover, the π-backbone demonstrates a significant degree of polarizability, as detailed below.

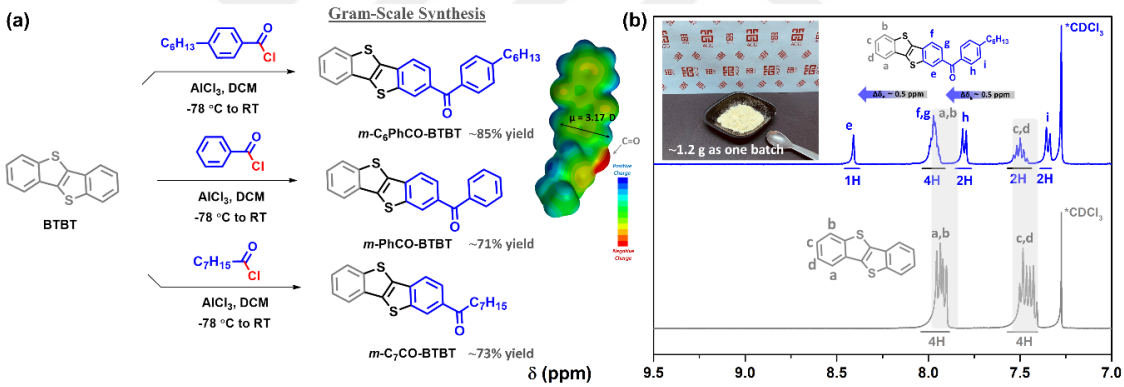

Figure 4.2 (a) Gram-scale syntheses of new mono-carbonyl molecules, ***m*-C$_6$PhCO-BTBT**, ***m*-PhCO-BTBT**, and ***m*-C$_7$CO-BTBT**. Inset shows the DFT(B3LYP/ 6-31 G**)-calculated electrostatic potential map for ***m*-C$_6$PhCO-BTBT** and the ground state dipole moment (μ_g = 3.17 D). (b) ^{1}H NMR spectra of ***m*-C$_6$PhCO-BTBT** (top) and the parent **BTBT** (bottom) molecules in $CDCl_3$ showing the non-exchangeable aromatic protons "a-i" and the downfield shifts for "e and g" ($\Delta\delta$ ~ +0.5 ppm). Inset shows the photo of the gram-scale ***m*-C$_6$PhCO-BTBT** solid.

On the basis of the thermogravimetric analysis, the new mono-carbonyl BTBTs exhibit high thermolysis onset temperatures (T_{onset} ≈ 5% weight loss) of 313-351 °C and nearly quantitative decomposition behavior (Figure 4.14). The inclusion of both alkyl and aryl substitutions in ***m*-C$_6$PhCO-BTBT** results in a higher T_{onset} of ~35-40 °C greater than that of ***m*-PhCO-BTBT** and ***m*-C$_7$CO-BTBT**, indicating enhanced thermal

stability. As shown in Figure 4.15, differential scanning calorimetry (DSC) measurements exhibit one major endothermic transition for each compound at 180.5 °C (84.45 J/g for ***m*-C$_7$CO-BTBT**), 225.0 °C (103.51 J/g for ***m*-PhCO-BTBT**), and 152.7 °C (85.85 J/g for ***m*-C$_6$PhCO-BTBT**). Only in the case of ***m*-C$_7$CO-BTBT**, an endothermic transition prior to melting was observed at 120.8 °C (27.32 J/g), which probably corresponds to a liquid crystalline phase transition.[2], [37], [157], [167] The higher temperature transitions observed in the DSC scans correspond to transitions to an isotropic liquid phase, as confirmed via conventional melting point measurements. The crystallizations were evident in the corresponding cooling scans. The melting temperature of ***m*-C$_6$PhCO-BTBT** is ~30-35 °C higher than those of the previously disclosed high mobility and high solubility dialkyl-BTBTs.[37] The increased melting temperature can be attributed to the removal of one flexible alkyl chain, and the addition of a polar carbonyl and a rigid aryl unit, resulting in an extended π-framework with enhanced solid-state cohesive energetics. Despite its higher melting temperature and the removal of one of the alkyl substituents as compared with dialkyl-BTBTs, ***m*-C$_6$PhCO-BTBT** surprisingly exhibits a much higher solubility as compared to well-known highly soluble dialkyl-BTBTs (e.g., **C$_{6/8}$-BTBTs**[37]: 70-80 mg·mL^{-1}). ***m*-C$_6$PhCO-BTBT** shows an instantaneous dissolution behavior at room temperature in chloroform with a remarkable solubility of 176.0 mg·mL^{-1}. This corresponds to a molarity of 0.41 M, which, to the best of our knowledge, is the highest solubility ever reported for a high performance organic semiconductor.[97], [123], [168], [169], [170], [171], [172] Note that this is >20-40× higher than those of the previously reported **C$_n$-BTBT-Ph**'s (solubility < 9-11 mg·mL^{-1})[2] and **BTBT-Ph-C$_n$**'s (solubility << 5-10 mg·mL^{-1})[156], [157], which carry the same alkyl and phenyl molecular fragments on the BTBT π-system. This suggests that our current asymmetricmono-carbonyl design is very effective to induce an extreme high solubility in common organic solvents. As demonstrated in Figure 4.3(a), based on our analysis on the physicochemical properties of previously reported (i.e., **C$_n$-BTBT**,[37] **C$_n$-BTBT-Ph**,[2] **DPh-BTBT**,[152] and **BTBT-Ph-C$_n$**[156], [157]) and our synthesized (i.e., **BTBT**,[39] **D(Ph$_F$CO)-BTBT**,[32] **D(C$_7$CO)-BTBT**,[39] ***m*-C$_7$CO-BTBT**, and ***m*-PhCO-BTBT**) BTBT molecules, a clear inverse correlation is evident between the melting temperature and the maximum molecular solubility. The increase in solubility with decreasing melting temperature across a large number of BTBT derivatives suggests that thermodynamic

factors linked to the strength of solid-state cohesive energetics, such as thermal transition temperatures and enthalpies, influence the dissolution process.[2] Nevertheless, the solubility value achieved with ***m*-C$_6$PhCO-BTBT** is significantly higher (shown with a gray arrow in Figure 3(a)) than the trend value expected based on its thermal properties. Additionally, the molar solubility achieved for ***m*-C$_6$PhCO-BTBT** (0.41 M) is approximately twice the combined solubility values obtained for either an alkyl or an aryl substituent alone in our other synthesized mono-carbonyl-BTBTs (0.16 M for ***m*-C$_7$CO-BTBT** and 0.06 M for ***m*-PhCO-BTBT**). These observations suggest that the structure of ***m*-C$_6$PhCO-BTBT**, with mono-(*n*-alkyl-aryl)carbonyl functionalization, provides a unique molecular architecture for developing stronger interactions with solvent molecules.

4.3.2 Hansen Solubility Parameters and Structure-Solubility Relationships

To gain insights into molecular design and reveal the key structural components that enable ***m*-C$_6$PhCO-BTBT**'s record-high solubility behavior, we studied the Hansen solubility parameters of ***m*-C$_6$PhCO-BTBT**, along with those of comparative molecules ***m*-PhCO-BTBT** and ***m*-C$_7$CO-BTBT**. The latter two molecules allow for a direct comparison with ***m*-C$_6$PhCO-BTBT**, thereby revealing the individual effects of aryl and alkyl units. The solubility of the new molecules was explored in a diverse set of organic solvents, spanning nonpolar solvents, chlorinated alkanes, aromatics, alcohols, polar aprotic solvents, terpenes, and esters having a wide range of dispersion (δ_D = 14.5-20), polar (δ_D = 0-21.7), and hydrogen-bonding (δ_D = 0-22.3) interactions. UV-Vis absorption spectroscopy and gravimetric methods were employed for this purpose (see the Experimental details).[173] As shown in Table 4.1, the new molecules exhibited solubility across a wide range, from complete insolubility to as high as 176.0 mg·mL^{-1}, in 28 different organic solvents. While chlorinated alkanes and aromatics yield the highest solubilities for all three molecules, reasonable solubility values in a wide range are recorded in polar aprotic solvents, esters, and terpenes as well. On the basis of a threshold concentration value of 4.0 mg·mL^{-1} at room temperature, solubility scores of "1" (indicating a good solvent) and "0" (indicating a nonsolvent) are assigned. Note that

this is a usual spin-coating concentration to yield semiconducting thin-films.[124], [173], [174] The solubility spheres are calculated in the HSPiP program using the Genetic algorithm.[121], [125] The genetic algorithm is a heuristic stochastic global optimization method successfully applied in diverse fields ranging from vehicle routing to quantum control of atomic/molecular dynamics.[175], [176] For our current mono-carbonyl BTBTs, this method yielded the best fitting accuracies (0.929-1.000) with minimum errors in solvent selection, as it aims to find the least number of incorrect solvents within the smallest possible radius.

Table 4.1 The solubility values (in mg·mL^{-1}) of ***m*-C$_7$CO-BTBT**, ***m*-PhCO-BTBT**, and ***m*-C$_6$PhCO-BTBT** in 28 different organic solvents determined via spectroscopic (UV-Vis absorption) and gravimetric methods, and the solvent Hansen Solubility parameters (δ_D, δ_P, δ_H in MPa$^{0.5}$). The solubility scores "1" (for good solvent) and "0" (for nonsolvent) are assigned based on the threshold concentration value of 4.0 mg·mL^{-1}.

Solvent	**Hansen Solubility Parameters, MPa$^{0.5}$**			**Solubility, mg·mL^{-1} (Solubility Score)**		
	δ_D	**δ_P**	**δ_H**	***m*-C$_7$CO-**	***m*-PhCO-**	***m*-C$_6$PhCO-**
Aromatics						
Benzene	18.4	0	2.0	5.50 (1)	3.02 (0)	>4 (1)
Toluene	18.0	1.4	2.0	7.31 (1)	2.37 (0)	34.0 (1)
o-Xylene	17.6	1	3.1	3.07 (0)	1.83 (0)	21.3 (1)
Alcohols						
1-Butanol	16	5.7	15.8	0.34 (0)	0.12 (0)	0.73 (0)
tert-Butanol	15.2	5.1	14.7	0.20 (0)	0.13 (0)	0.54 (0)
Ethanol	15.8	8.8	19.4	0.10 (0)	Insoluble	0.24 (0)
Ethylene glycol	17	11	26	Insoluble	Insoluble	0.04 (0)
Methanol	14.7	12.3	22.3	0.08 (0)	0.06 (0)	0.26 (0)
2-Propanol	15.8	6.1	16.4	0.48 (0)	Insoluble	0.26 (0)
Polar aprotic						
Acetone	15.5	10.4	7.0	1.57 (0)	0.75 (0)	2.70 (0)
Acetonitrile	15.3	18	6.1	0.15 (0)	0.08 (0)	0.77 (0)
Diethyl ether	14.5	2.9	4.6	1.03 (0)	0.25 (0)	2.94 (0)
Dimethyl sulfoxide (DMSO)	18.4	16.4	10.2	0.60 (0)	1.47 (0)	1.52 (0)
N,N-Dimethylformamide (DMF)	17.4	13.7	11.3	2.98 (0)	4.03 (1)	9.26 (1)
1,4-Dioxane	17.5	1.8	9	4.20 (1)	4.02 (1)	>4 (1)
Ethylene carbonate	18	21.7	5.1	0.12 (0)	0.86 (0)	0.36 (0)
Methyl *iso*-butyl ketone (MIBK)	15.3	6.1	4.1	2.40 (0)	1.19 (0)	7.21 (1)
N-Methyl-2-pyrrolidone (NMP)	18	12.3	7.2	4.02 (1)	7.97 (1)	31.2 (1)
Propylene carbonate	20	18	4.1	0.24 (0)	0.27 (0)	0.50 (0)
Tetrahydrofuran	16.8	5.7	8.0	28.3 (1)	6.44 (1)	102.5 (1)
Esters						
n-Amyl acetate	15.8	3.3	6.1	2.68 (0)	0.84 (0)	7.72 (1)
Ethyl Acetate	15.8	5.3	7.2	1.61 (0)	0.90 (0)	8.80 (1)
Propylene glycol monoethyl ether acetate	15.6	6.3	7.7	1.53 (0)	0.90 (0)	5.05 (1)
Chlorinated alkanes						

Chloroform	17.8	3.1	5.7	58.3 (1)	22.2 (1)	176.0 (1)
Methylene dichloride	17	7.3	7.1	25.1 (1)	6.32 (1)	87.5 (1)
Non-polar						
Cyclohexane	16.8	0	0.2	0.53 (0)	0.04 (0)	1.60 (0)
Hexane	14.9	0.0	0.0	0.23 (0)	Insoluble	0.56 (0)
Terpenes						
d-Limonene	17.2	1.8	4.3	2.09 (0)	0.54 (0)	8.02 (1)

As shown in Figure 4.3(b), the HSPs for ***m*-C$_6$PhCO-BTBT** are determined to be δ_D = 18.9 MPa$^{1/2}$, δ_P = 5.7 MPa$^{1/2}$, and δ_H = 5.8 MPa$^{1/2}$ with an interaction radius (R_0) of 8.0 MPa$^{1/2}$. Considering the specific cohesive energy densities (δ^2), the dispersion-based interactions appear to be the major contributor to the solid state cohesive energetics in ***m*-C$_6$PhCO-BTBT**. It is crucial to note that while Hansen's original solubility theory does not identify specific π-interactions, the δ_D term derived herein includes π-interactions (i.e., π···π, C-H···π, and S···π) between the extended mono-carbonyl BTBT π-systems, along with dispersion interactions between aliphatic hexyl substituents.[126], [127] The prevalence of dispersion interactions in the HSPs was additionally verified through the group contribution approach, as depicted in Figure 4.17. This technique, utilized in the HSPiP using Neural Network methods, determines the HSPs by calculating contributions from specific molecular constituents, such as aromatics, aliphatics, and functional groups in ***m*-C$_6$PhCO-BTBT**.[129], [130] On the other hand, the HSPs for the comparative molecules ***m*-PhCO-BTBT** and ***m*-C$_7$CO-BTBT** are determined to be δ_D = 20.5 MPa$^{1/2}$/δ_P = 7.7 MPa$^{1/2}$/δ_H = 9.6 MPa$^{1/2}$ (R_0 = 8.9 MPa$^{1/2}$) and δ_D = 19.2 MPa$^{1/2}$/δ_P = 6.9 MPa$^{1/2}$/δ_H = 6.5 MPa$^{1/2}$ (R_0 = 6.8 MPa$^{1/2}$), respectively (Figure 4.3(b)). Transititoning from either only phenyl (as in ***m*-PhCO-BTBT**) or solely alkyl (as in ***m*-C$_7$CO-BTBT**) substituents to an alkyl-aryl substituent combination (as in ***m*-C$_6$PhCO-BTBT**) results in a decrease in δ_P (-Δ = 1.2-2.0 MPa$^{1/2}$) and δ_H (-Δ= 0.7-3.8 MPa$^{1/2}$) interaction parameters. Because these parameters are directly linked to polarity and hydrogen bonding ability arising from carbonyl units, this reduction is evidently due to volume dilution of carbonyl units by the addition of an alkyl-aryl unit. Changing the substituent from an alkyl to an aryl unit when transitioning from ***m*-C$_7$CO-BTBT** to ***m*-PhCO-BTBT** results in an increase of δ_D by 1.3 MPa$^{1/2}$ and δ_H by 3.1 MPa$^{1/2}$. Given the similar molecular weights of these molecules, the increase

in δ_D reflects a more condensed structure of the phenyl aromatic ring compared to the linear aliphatic heptyl chain. The increase in δ_H, on the other hand, indicates the non-classical hydrogen bonding (C-H$\cdots\pi$) ability of an aryl unit, which an aliphatic chain lacks.[50] It is noteworthy that the aforementioned increase in δ_D and δ_H resembles a similar trend observed for the common solvents hexane, cyclohexane, benzene, respectively (δ_D/δ_H = 14.9/0.0 $MPa^{1/2}$ → 16.8/0.2 $MPa^{1/2}$ → 18.4/2.0 $MPa^{1/2}$) in the HSP space.

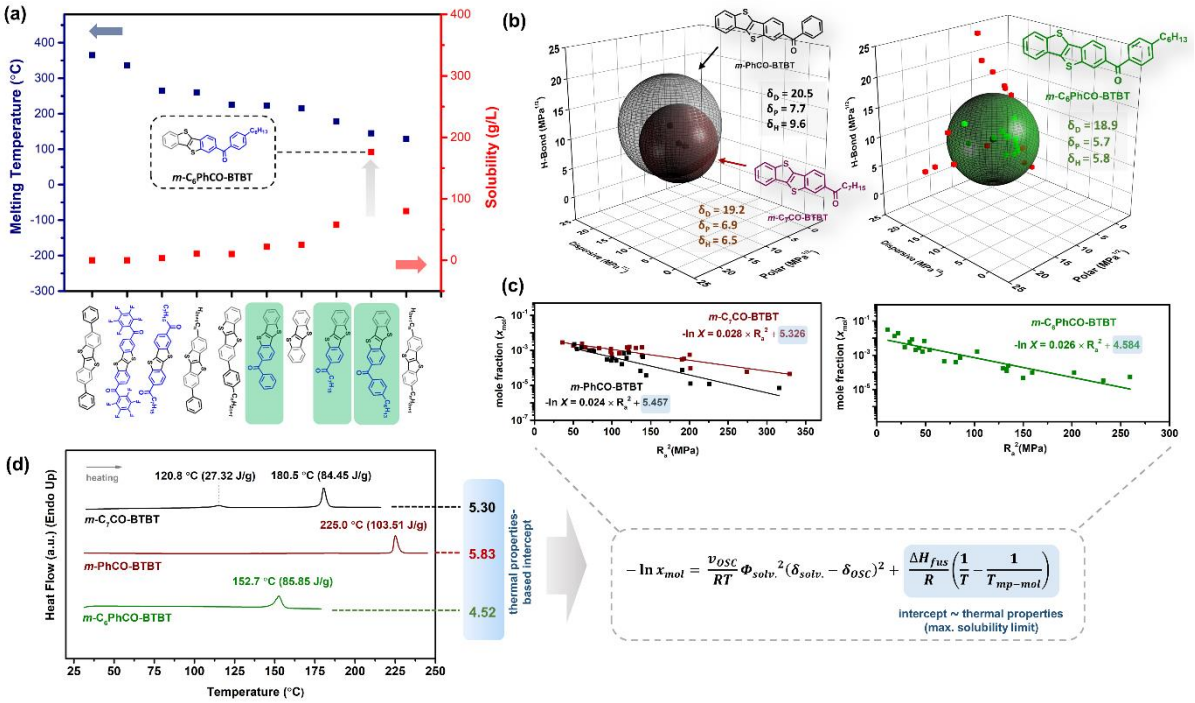

Figure 4.3 (a) The melting temperatures (blue squares) and maximum solubilities (red squares) of previously developed BTBT-based semiconductors, **DPh-BTBT**,[152] **D(Ph$_F$CO)-BTBT**,[32] **D(C$_7$CO)-BTBT**,[39] **C$_n$-BTBT-Ph**,[2] **BTBT-Ph-C$_n$**,[156], [157] **BTBT**,[39] **C$_n$-BTBT**,[37] respectively from left to right, and our synthesized molecules ***m*-PhCO-BTBT**, ***m*-C$_7$CO-BTBT**, and ***m*-C$_6$PhCO-BTBT**, respectively shown in green from left to right. For solids of **DPh-BTBT** and **BTBT-Ph-C$_n$**, which have been purified and processed via non-solution based techniques, solubility values are taken as <10 mg·mL^{-1}. The solubility values of **D(Ph$_F$CO)-BTBT**, **D(C$_7$CO)-BTBT**, and **BTBT** solids (in chloroform) were determined in our laboratory. (b) Hansen solubility spheres and parameters of ***m*-PhCO-BTBT**, ***m*-C$_7$CO-BTBT**, and ***m*-C$_6$PhCO-BTBT**, as determined by using the Genetic algorithm (HSPiP Program) with a solubility limit of 4 mg·mL^{-1}. The Hansen solubility parameters ($\delta_D/\delta_P/\delta_H$) are in MPa$^{1/2}$, and the bad and the good solvents are shown in the 3D Hansen solubility space with red and green spheres, respectively for ***m*-C$_6$PhCO-BTBT**. (c) The logarithmic correlations between the semiconductor solubility in the mole fraction unit (x_{mol}) and the squared solute-solvent distance (R_a^2) in the HSP space (correlation coefficient ≈ -0.91). The corresponding equations are derived based on linear fittings and correspond to the Hansen-adapted Scatchard-Hildebrand regular solution theory equation (v_{OSC} is molar volume of the subcooled liquid of pure molecular solid, $\Phi_{solv.}$ is solvent volume fraction (≈ 1 for dilute solutions), ΔH_{fus} is enthalpy of fusion, T_{mp-mol} is melting temperature, R is the gas constant, and T is the solubility measurement temperature (absolute)).[122] (d) The differential scanning calorimetry (10 °C·min^{-1} heating ramp under N_2) heating scans of ***m*-PhCO-BTBT**, ***m*-C$_7$CO-BTBT**, and ***m*-C$_6$PhCO-BTBT** solids showing the temperature and enthalpy values for the corresponding thermal transitions from solid to isotropic liquid.

On the basis of the calculated HSPs, chloroform, which appears to be the best solvent for all three molecules, gives the closest solute-solvent interaction distances ($R_a = (4\Delta\delta_D^2 + \Delta\delta_P^2 + \Delta\delta_H^2)^{1/2}$), as compared to the rest of the solvents. More importantly, R_a value gradually decreases as 8.05 $MPa^{1/2}$ (for ***m*-PhCO-BTBT**), 4.79 $MPa^{1/2}$ (for ***m*-C$_7$CO-BTBT**), and 3.36 $MPa^{1/2}$ (for ***m*-C$_6$PhCO-BTBT**), which aligns well with the corresponding gradual solubility increase of 0.06 M → 0.16 M → 0.41 M (Table 4.2). Due to the fourfold effect of the difference in dispersion parameters ($\Delta\delta_D$) on R_a, ***m*-C$_6$PhCO-BTBT** with the closest δ_D value to that of chloroform yields the highest solubility. This highlights a key design advantage of alkyl-aryl substitution over either alkyl or aryl substitution alone, particularly in enhancing the molecular solubility of a rigid π-system.

Table 4.2 Summary of Hansen solubility parameters (δ_D, δ_P, δ_H in $MPa^{1/2}$), interaction radii (R_0 in $MPa^{1/2}$), and solubilities (at 25 °C) in chloroform for ***m*-PhCO-BTBT**, ***m*-C$_7$CO-BTBT**, and ***m*-C$_6$PhCO-BTBT**, and the corresponding HSP interaction distances (R_A in $MPa^{1/2}$) with respect to chloroform.

	HSPs and Interaction Radii[a]					Solubility in Chloroform	
Compounds	δ_D	δ_P	δ_H	R_0	Fitting, WI/WO	R_A[b]	Solubility[c] ($mg \cdot mL^{-1}/M$)
***m*-PhCO-BTBT**	20.5	7.7	9.6	8.9	1.000, 0/0	8.05	22.2/0.06
***m*-C$_7$CO-BTBT**	19.2	6.9	6.5	6.8	0.929, 0/2	4.79	58.0/0.16
***m*-C$_6$PhCO-BTBT**	18.9	5.7	5.8	8.0	0.964, 0/1	3.36	176.0/0.41

The excellent solubility of our present molecule ***m*-C$_6$PhCO-BTBT** is compared with that of previously reported **BTBT-Ph-C$_6$/C$_{12}$** semiconductors, which have exactly the same "π-π-σ" subunit sequence as our molecule but lack an electron withdrawing carbonyl unit. It is noteworthy that one of these molecules even has a longer alkyl chain (-*n*-$C_{12}H_{25}$). In the earlier studies with **BTBT-Ph-C$_6$/C$_{12}$**,[156], [157] the material purifications and OFET thin-film depositions have been performed via non-solvent-based techniques, vacuum sublimation and physical vapor deposition. It was also noted that structural engineering is necessary to solubilize these compounds. Therefore, it is evident that the solubility of **BTBT-Ph-C$_6$/C$_{12}$** is well below ~5-10 mg·mL^{-1}, which is typically the minimum requirement for solution processing.[123], [177] This vis-a-vis experimental comparison clearly demonstrates that inserting a mono-carbonyl unit between the π-core and the aryl substituent, transitioning from "π-π-σ" to a "π-CO-π-σ" configuration, notably enhances molecular solubility. On the other hand, transitioning from ***m*-C$_7$CO-BTBT** to **D(C$_7$CO)-BTBT**, which was synthesized in our previous study,[39] although an additional solubilizing alkyl substituent is introduced, the molecular solubility decreases more than tenfold (58.3 mg·mL^{-1} → 3.5 mg·mL^{-1}). One may also compare the di-carbonyl semiconductor **D(C$_7$CO)-BTBT** with the analogous non-carbonyl derivatives of **(di)-C$_{7/8}$-BTBT** that have the same alkyl substituents.[37], [39] Despite having the same alky substituents, di-carbonyl functionalization significantly decreases molecular solubility (70-80 mg·mL^{-1} → 3.5 mg·mL^{-1}). Therefore, it is evident that while single carbonyl functionalization greatly improves solubility, going from an asymmetric mono-carbonyl to a symmetric di-carbonyl configuration ("π-CO-substituent" → "substituent-CO-π-CO-substituent") results in a significant decrease in molecular solubility.

Theoretical calculations aided by DFT have shown that mono-carbonyl functionalization in BTBT results in a substantial ground-state molecular dipole (μ_g = 3.17 D, Figure 4.2(a)). This value is significantly higher than those observed for mono-/di-substituted BTBTs mentioned earlier, which exhibit μ_g = 0 D for **(di)-C$_{6/8}$-BTBTs** and **D(C$_7$CO)-BTBT**, 0.45 D for **C$_n$-BTBT-Ph**, and 0.57 D for **BTBT-Ph-C$_n$** (Figure 4.18). This ground-state molecular dipole is expected to lead to strong dipolar interactions with solvent molecules, particularly with polar green solvents.[102], [178] When the calculations were performed in a solvent medium, it was observed that a larger molecular dipole ($\Delta\mu_g \approx +1$ D in dichloromethane) is induced for ***m*-C$_6$PhCO-**

BTBT, whereas the corresponding $\Delta\mu_g$'s for di-carbonyl-functionalized and aryl/alkyl-substituted BTBTs were minimal ($\Delta\mu_g \approx$ 0-0.1 D) (Figure 4.18). In order to confirm that the observed increase in μ_g is not due to a conformational change in a solvent medium, the DFT calculation was repeated in the gas phase using the molecular geometry optimized in the solvent. This calculation confirmed that the observed $\Delta\mu_g$ is primarily due to an induced dipole via π-polarization of the ***m*-C$_6$PhCO-BTBT** backbone in the solvent dielectric medium. Furthermore, the polarizability of the BTBT molecular π-system was shown to be enhanced in all directions after mono-carbonyl functionalization, with the most significant increase (19.10 Å^3 → 22.08 Å^3) observed along the long molecular axis (Figure 4.18). The large polarizability of the new mono-(aryl)carbonyl-functionalized π-architecture is expected to lead to enhanced dispersion and induced dipole interactions with solvents molecules.[127], [179], [180] DFT studies (Figure 4.18) also showed that the mono-carbonyl insertion in ***m*-C$_6$PhCO-BTBT** twists the phenyl ring out of the BTBT π-plane ($\theta_{dihedral}$ = 51°) as compared to low-solubility molecules in which there is a direct BTBT-Ph bond ($\theta_{dihedral}$ = 2.5/6.2° in **BTBT-Ph-C$_n$/C$_n$-BTBT-Ph** based on single-crystal[1], [2]). This reduces the structural rigidity and solid-state cohesive energetics in ***m*-C$_6$PhCO-BTBT**,[172] and it contributes to enhanced solubility[102]. Consistently, all three Hansen parameters for ***m*-C$_6$PhCO-BTBT**, despite being a larger molecular system, are lower than those of its non-aryl counterpart ***m*-C$_7$CO-BTBT** (*vide supra*), confirming a lower cohesive energy density.

4.3.3 Thermodynamic Correlation of the Molecular Solubility with Thermal Properties

For our new mono-carbonyl BTBTs, a quantitative logarithmic relationship is explored between the measured solubility values and the calculated interaction distances (R_a's) in the HSP space. One could also consider this quantitative relationship as providing further confirmation of the accuracy of the calculated Hansen parameters. As depicted in Figure 4.3(c), strong negative correlations were established when the solubility mole fraction (x_{mol}) in a particular solvent is logarithmically plotted against the specific solvent-molecule R_a^2 value. A different regressed equation was established

for each molecule, as expected. These equations follow a modified version of the original equation proposed by Scatchard and Hildebrand for regular solutions, adapting Hansen parameters as shown in the dashed box in Figure 4.3(c).[122], [133] Here, the R_a values are used to determine the distances for molecule-solvent interactions, rather than relying solely on the relatively simpler Hildebrand solubility parameters distance.[122], [132] On the other hand, we note that the Flory-Huggins correction term for the entropy of mixing in this equation is taken to be significantly smaller than the HSP term. Consequently, it has been excluded from the calculations.[132] Since the slopes for all three molecules are similar (0.024-0.028), the intercept value becomes the most critical aspect of these equations, which represents the maximum molecular solubility in an ideal solvent as R_a^2 approaches 0. According to textbook equations in physical chemistry, this part actually defines a molecule's solubility based on the ideal solution approach, utilizing the solid-to-isotropic liquid transition properties of enthalpy of fusion (ΔH_{fus}) and melting temperature ($T_{mp\text{-}mol}$).[134] The intercept values are found to decrease as 5.457, 5.326, and 4.584 for ***m*-PhCO-BTBT**, ***m*-C$_7$CO-BTBT**, and ***m*-C$_6$PhCO-BTBT**, respectively. This trend matches well the observed solubility trend in organic solvents, as ***m*-C$_6$PhCO-BTBT**, having the smallest intercept value, exhibits the highest solubility. More importantly, these intercept values could be estimated also from the thermal properties measured via DSC measurements. Following the intercept formula in the Hansen-adapted Scatchard-Hildebrand equation and using the enthalpy values and transition temperatures determined via DSC (Figure 4.3(d)), the intercept values are closely estimated as 5.83, 5.30, and 4.52 for ***m*-PhCO-BTBT**, ***m*-C$_7$CO-BTBT**, and ***m*-C$_6$PhCO-BTBT**, respectively. To the best of our knowledge, these values are estimated for the first time in the literature from both Hansen-based solubility studies and thermal characterizations. These quantitative correlations, along with their strong relationship to the thermal properties, could facilitate computer-aided rapid solvent screening to estimate solubility in a specific solvent or solvent mixture before actual experimentation. Such a tool could have practical applications in various industrial settings.

On the other hand, based on the Hansen solubility parameters calculated for the current three molecules, the total cohesive energy density (δ_T^2 ($E_{cohesive}/V_{molar}$) = δ_D^2 + δ_P^2 + δ_H^2) were found to decrease in the order of ***m*-PhCO-BTBT**, ***m*-C$_7$CO-BTBT**, and ***m*-C$_6$PhCO-BTBT**, respectively (δ_T^2 = 23.9 MPa → 21.4 MPa → 20.57 MPa).

Note that the decrease in cohesive energy ($E_{cohesive}$) itself is expected to be more significant as the molecular volume increases going from ***m*-PhCO-BTBT** or ***m*-C_7CO-BTBT** to ***m*-C_6PhCO-BTBT**. This trend closely correlates with the chemical potential changes occurred during solid-to-liquid thermal transitions ($\mu^{\circ}_{(s)} \rightarrow \mu^{\circ}_{(l)}$) at room temperature. These chemical potentials are used to derive the ideal solubility expression at room temperature and are directly related to molecular solubility.[134] $\mu^{\circ}_{(s)} \rightarrow \mu^{\circ}_{(l)}$ at room temperature could be estimated based on the solid-to-liquid transitions observed in the DSC scan, using the formula $\Delta G^{\circ}_{s\rightarrow l} = \sum \Delta H^{\circ}_{trans.}(1\text{-}298.15/T_{trans.})$, where $\Delta H^{\circ}_{trans.}$ is the enthalpy of a specific transition and $T_{trans.}$ is the corresponding transition temperature. Accordingly, following the same trend as the cohesive energies ($E_{cohesive}$'s), $\Delta G^{\circ}_{s\rightarrow l}$ values at room temperature are estimated to be 14.45 kJ/mol *for* ***m*-PhCO-BTBT**, 13.14 kJ/mol for ***m*-C_7CO-BTBT**, and 11.21 kJ/mol for ***m*-C_6PhCO-BTBT**.

4.3.4 Photopysical and Electrochemical Properties

The photophysical and electrochemical properties of ***m*-C_6PhCO-BTBT** were studied by UV-vis absorption and photoluminescence spectroscopies, and cyclic voltammetry. As shown in Figure 4.4(a), consistent with its colorless solution, ***m*-C_6PhCO-BTBT** shows two low-energy absorption maxima at 327/362 nm with the onset wavelength of 391 nm (E_g^{opt} = 3.17 eV) in dichloromethane. The absorption maxima and the onset wavelengths show a significant bathochromic shift ($\Delta\lambda \sim$ 40-55 nm) in the spin-coated thin-film, and a typical vibronic structure (~1200 cm^{-1}) of an aromatic π-system is formed. This indicates that the "PhCO-BTBT" π-scaffold is coplanarized/rigidified in the solid state through intermolecular forces. The observed spectral changes going from a molecular state to a thin-film phase are indicative of J-aggregation.[39] In this arrangement, ***m*-C_6PhCO-BTBT** π-backbones likely assume a slipped-stacked configuration through ground state dipolar interactions.[181] When ***m*-C_6PhCO-BTBT** is excited with an excitation wavelength of 327 nm or 362 nm, the recorded fluorescence spectrum shows a broad emission profile with λ_{fl}^{max} at 435 nm, corresponding to a large Stokes shift of 73 nm. When the solvent polarity is screened from hexane ($f(\varepsilon,n)$ = 0.001) to acetonitrile ($f(\varepsilon,n)$ = 0.305), the fluorescence spectrum

exhibits an additional bathochromic shift of ~36 nm (Figure 4.4(b)). On the other hand, note that the absorption profile for ***m*-C$_6$PhCO-BTBT** exhibits a relatively small bathochromic shift across the same solvents ($\Delta\lambda_{abs}^{max}$ ~ 6-7 nm). This solvatochromic photophysical characteristics are much more pronounced than the unfunctionalized parent BTBT π-backbone (Figure 4.19). This is undoubtedly the result of mono-carbonyl asymmetricπ-electronic structure of the new molecule, and it suggests that the radiative excited state (S_1) possesses higher dipole moment than the ground-state. The excited state (S_1) dipole moment (μ_e) could be estimated from the slope of the Lippert-Mataga plot (Stokes shifts (ν_{abs} - ν_{fl}) against $f(\varepsilon,n)$) using the DFT-calculated ground state dipole moment (μ_g) (see Table 4.5 for data details).[182] Based on the this model, a good linearity between "ν_{abs}-ν_{fl}" and $f(\varepsilon,n)$ was found to retain across the whole solvent polarity region (hexane ($f(\varepsilon,n) = 0.001$) → acetonitrile ($f(\varepsilon,n) = 0.305$)) (Figure 4.4(b) and) yielding a single excitonic character with a relatively large excited-state dipole moment (μ_e) of 12.69 D (~0.26 charge·nm). The frontier orbital topographies for the unoccupied orbitals, LUMO and LUMO+1, show a complete molecular π-backbone delocalization, whereas the occupied frontier orbitals, HOMO and HOMO-1 exhibit more limited delocalization, mainly on the BTBT π-system. These observations, combined with the spectroscopic findings, suggest the presence of a hybridized local and charge transfer (HLCT) excited state for ***m*-C$_6$PhCO-BTBT**.

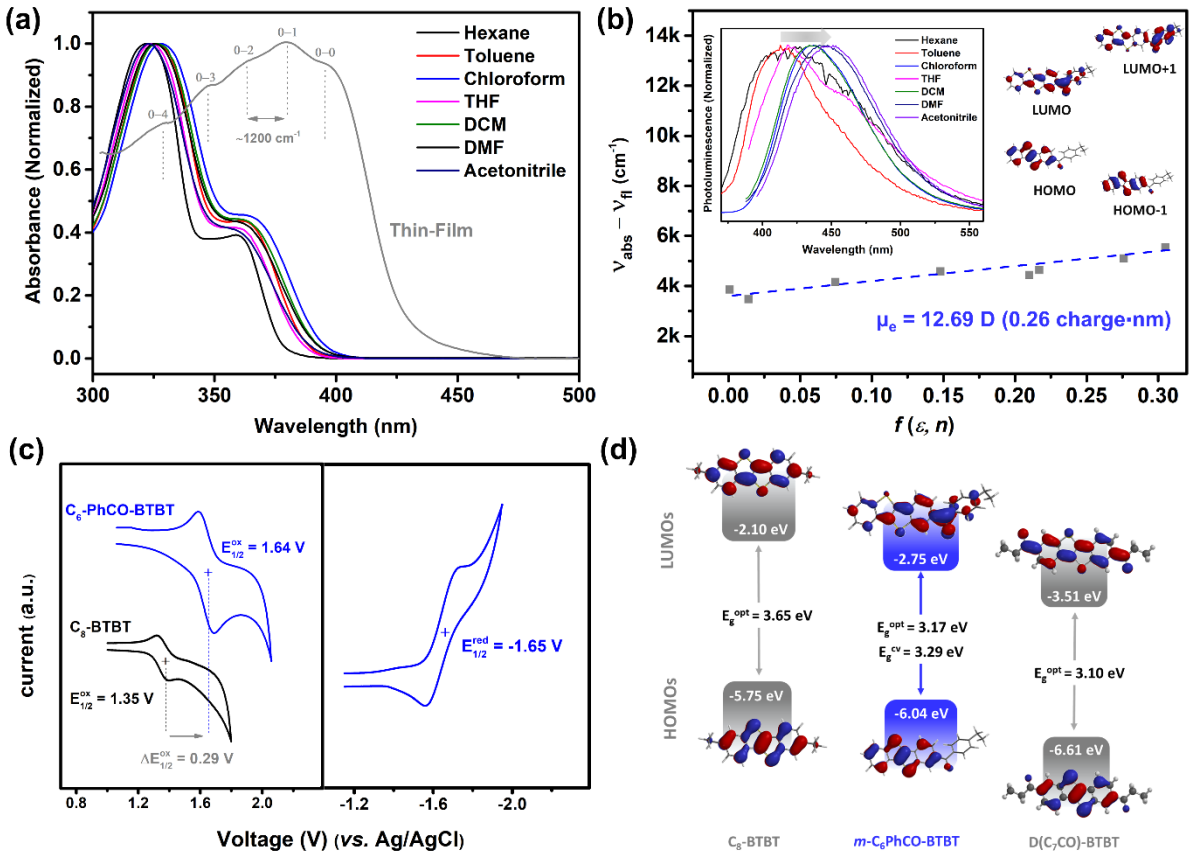

Figure 4.4 (a) Solvatochromic optical absorption spectra of ***m*-C$_6$PhCO-BTBT** in different solvents with increasing polarity (hexanes (*f* (*ε*,*n*) = 0.001) → acetonitrile (*f* (*ε*,*n*) = 0.305)) and solid-state optical absorption spectrum of spin-coated thin-film (annealed at 120 °C) on glass showing vibronic structure. (b) Solvatochromic Lippert-Mataga model for ***m*-C$_6$PhCO-BTBT** showing the fitted linear correlation (ν_{abs}-ν_{fl} *vs. f* (ε,n)) and the corresponding solvatochromic photoluminescence spectra in different solvents with increasing polarity (hexanes (*f* (*ε*,*n*) = 0.001) → acetonitrile (*f* (*ε*,*n*) = 0.305)). (c) Cyclic voltammograms of ***m*-C$_6$PhCO-BTBT** and **C$_8$-BTBT** (measured in house for comparison) showing oxidation and reduction peaks in 0.1 M $TBAPF_6/CH_2Cl_2$ solution *vs.* Ag/AgCl (3.0 M NaCl) at a scan rate of 100 mV/s. (d) The experimental HOMO and LUMO energy levels, frontier orbital topographies (DFT/B3LYP/6-31G**), and optical/electrochemical band gaps.

The cyclic voltammograms in dichloromethane solution shows clear (*quasi*)reversible oxidation and reduction peaks at +1.64 V and -1.65 V (*vs.* Ag/AgCl), respectively (Figure 4.4(c)). Considering that dialkyl-substituted counterpart **C$_8$-BTBT** shows only an oxidation peak at +1.35 V (*vs.* Ag/AgCl) in the same experimental system, the presence of a reduction peak and anodically shifted ($\Delta E_{1/2}^{ox}$ = +0.29 V) oxidation peak undoubtedly reflect the electronic effects of mono-(aryl)carbonyl functionalization. As shown in Figure 4.4(d), HOMO and LUMO energy levels are estimated to be -2.75 eV and -6.04 eV, which falls between those of unfunctionalized

(substituted with alkyl chains) and di-carbonyl functionalized BTBT molecules. The electrochemical band gap is calculated to be 3.29 eV (E_g^{opt} = 3.17 eV, *vide supra*). Our results revealed that mono-(aryl)carbonyl functionalization stabilizes the frontier molecular orbitals in different scales (ΔE_{HOMO} = -0.29 eV and ΔE_{LUMO} = -0.65 eV). This is because while mono-(aryl)carbonyl stabilizes the HOMO only via negative inductive (-*I*) effect (i.e., no π-orbital density on the (aryl)carbonyl moiety), it stabilizes the LUMO via both negative resonance (-*R*) effect and π-extension on the (aryl)carbonyl unit (Figure 4.4(d)).

4.3.5 Green Solvents for Field-Effect Transistor Fabrications and Thin-Film/Electrical Characterizations

Considering the excellent solubility of ***m*-C$_6$PhCO-BTBT** in common organic solvents, a set of potential green solvents have been evaluated for thin-film processing, and ***m*-C$_6$PhCO-BTBT** exhibited reasonable room temperature solubilities of 12.5 mg·mL^{-1} in ethoxybenzene (δ_D = 18.4, δ_P = 4.5, δ_H = 4.0), 10.4 mg·mL^{-1} in 2-methyltetrahydrofuran (δ_D = 16.9, δ_P = 5.0, δ_H = 4.3), 8.80 mg·mL^{-1} in ethyl acetate (δ_D = 15.8, δ_P = 5.3, δ_H = 7.2), and 2.70 mg·mL^{-1} in acetone (δ_D = 15.5, δ_P = 10.4, δ_H = 7.0). The determined HSPs for ***m*-C$_6$PhCO-BTBT** (δ_D = 18.9 MPa$^{1/2}$, δ_P = 5.7 MPa$^{1/2}$, and δ_H = 5.8 MPa$^{1/2}$) indicate that these green solvents have relatively small solute-solvent interaction distances ($R_a = (4\Delta\delta_D^2 + \Delta\delta_P^2 + \Delta\delta_H^2)^{1/2}$) of 2.4 MPa$^{1/2}$, 4.4 MPa$^{1/2}$, 6.4 MPa$^{1/2}$, and 8.3 MPa$^{1/2}$, respectively, which aligns with the observed solubility trend across these green solvents. On the other hand, ***m*-C$_6$PhCO-BTBT** exhibits a room temperature solubility of 0.24 mg·mL^{-1} in ethanol (δ_D = 15.8, δ_P = 8.8, δ_H = 19.4), which is consistent with its relatively larger R_a value of 15.3 MPa$^{1/2}$. However, note that the semiconductor solution in ethanol processed at moderate temperatures (solubility = 1.5 mg·mL^{-1} at ~70 °C) could still yield electro-active thin-films via drop-casting (*vide infra*). Considering that ***m*-C$_6$PhCO-BTBT** does not employ a special oligo(ethylene glycol) side chain[109] or an ionic functional group[183], the observed solubilities in these five different polar green solvents, especially in ethyl acetate, acetone and ethanol, are very attractive. These solvents hold great potential for environmentally friendly processing of ***m*-C$_6$PhCO-BTBT** semiconducting thin films. When compared with highly toxic and environmentally hazardous chlorinated aliphatic/aromatic or non-chlorinated aromatic solvents that are commonly used to prepare semiconductor

solutions, these solvents present much less of a health and environment hazard, and they could potentially be sourced from renewable biomass.[184], [185]

Describing an organic solvent as "green" is a complex notion that needs to consider various factors, including health, safety, environmental impact, and sustainability, which sometimes leads to differing assessment approaches. The selected green solvents for studying ***m*-C$_6$PhCO-BTBT**-based transistor fabrication each have their own strengths and weaknesses in terms of greenness. Among them, ethoxybenzene demonstrates an overall high GlaxoSmithKline (GSK) greenness composite score (G) of 7.2.[116] Here, it is crucial to note that this G value for ethoxybenzene could potentially be even higher, as it received a relatively conservative health score of 4.9 due to limited available information. Another solvent, 2-methyltetrahydrofuran, has a relatively lower G score of 4.4. However, it stands out as a biorenewable green solvent with a reduced life cycle footprint. This compound can be derived from corn cob waste (*eco*MeTHF^{TM}) with a significantly lower carbon footprint (0.150 kg CO_2 production per kg) compared to petrochemical feedstock-based tetrahydrofuran (THF) (5.46 kg CO_2 production per kg).[142] The other solvents, ethyl acetate, acetone, and ethanol have excellent health, environment, and safety subcategory scores of 7.1-8.9.[116] In addition, all three of these solvents could be obtained from renewable, sustainable bio-based materials, leading to a considerable reduction in their environmental impact.[186] These solvents have been listed among the preferred or recommended eco-friendly green solvents for industrial applications including in varied medicinal chemistry laboratories.[135], [184], [185] Especially, ethanol is widely regarded as the most ideal environmentally friendly solvent whenever water is not suitable for processing.[102], [109] To the best of our knowledge, there are very limited examples of small molecular OFETs in general,[109], [186], [187] and no reported examples of a BTBT-based OFET fabricated using the green solvents we are interested in. Only recently, a few reports have demonstrated OFETs based on solution-sheared thin-films of BTBT-based semiconductors from anisole, cyclohexanone, and diethyl carbonate green solvents.[108], [188], [189] The charge transport characteristics of the new mono-(aryl)carbonyl functionalized BTBT molecule was explored in top-contact/bottom-gate (TC/BG) OFETs by spin-coating ***m*-C$_6$PhCO-BTBT** solutions (4.0 mg·mL^{-1}) in 2-methyltetrahydrofuran, ethoxybenzene, ethyl acetate, and acetone, and by drop-casting ***m*-C$_6$PhCO-BTBT** solution in ethanol (1.0 mg·mL^{-1}). The semiconducting thin-films (~40-45 nm) were deposited onto p^{++}-

Si/SiO_2 (300 nm)/PS-brush (M_n = 5 kDa) substrates, which has an ultrathin (~3.6 nm), densely packed (grafting density ≈ 0.45 chains·nm^{-2}), smooth (R_q = 0.17−0.18 nm for a 10 × 10 μm^2 area) hydrophobic surface.[124] This surface promotes the formation of an optimal thin-film microstructure for efficient charge transport.[124], [165], [166] The microstructural and morphological characterizations were performed by atomic force microscopy (AFM) and out-of-plane θ-2θ X-ray diffraction (i.e., in Bragg-Brentano geometry) (Figure 4.5(a) and 4.5(b)). The electrical characterizations conducted under ambient conditions revealed that all transistors based on ***m*-C$_6$PhCO-BTBT**, processed from five different green solvents, exhibit clear *p*-channel semiconductor behavior with high current-modulation characteristics (Figures 4.5(c), 4.20, and 4.21). The transistors function only under negative gate bias. The absence of an *n*-channel transport is attributed to the high-lying LUMO energy level (-2.75 eV) and the relatively larger intramolecular reorganization energy for electron transport *vs.* hole transport (λ_e = 310 meV > λ_h = 265 meV).[163], [190] While poor hole mobilities (μ_h) of ~10^{-4} $cm^2/V{\cdot}s$ were measured for the devices with only spin coated semiconductor layers, μ_h progressively increased to 0.001 $cm^2/V{\cdot}s$ and 0.01 $cm^2/V{\cdot}s$ with thermal annealing at 70 °C and 90 °C, respectively. The highest hole mobility for all green solutions was achieved with the semiconductor thin-films annealed at 120 °C (for 20 min). The highly responsive semiconductor behavior of ***m*-C$_6$PhCO-BTBT** ($\Delta\mu_h$ ≈ 20,000×) to thermal annealing was evident with the morphological characterizations. As shown in Figure 4.5(e), thermal annealing facilitates a progressive growth of smooth and micron-sized terraced 2D islands with sharp edges and well-defined steps, from nanometer-sized (~100-200 nm) small granular domains obtained right after spin-coating process. Also, the crystallinity increases and the molecular packing becomes denser (i.e., decrease in *d*-spacing) in the out-of-plane direction after thermal annealing (Figure 4.5(b)-top scans). Here we note that when the semiconductor thin-films were annealed at a higher temperature ($T_{annealing}$ = 130-140 °C), the transistor characteristics were found to considerably deteriorate (I_{on}/I_{off} < 10). AFM analysis reveals that the semiconductor layer dewets from the PS-surface and forms discontinuous micron-sized domains (~70-80 nm thickness) deterring the OFET semiconducting channel (Figure 4.22).[37]

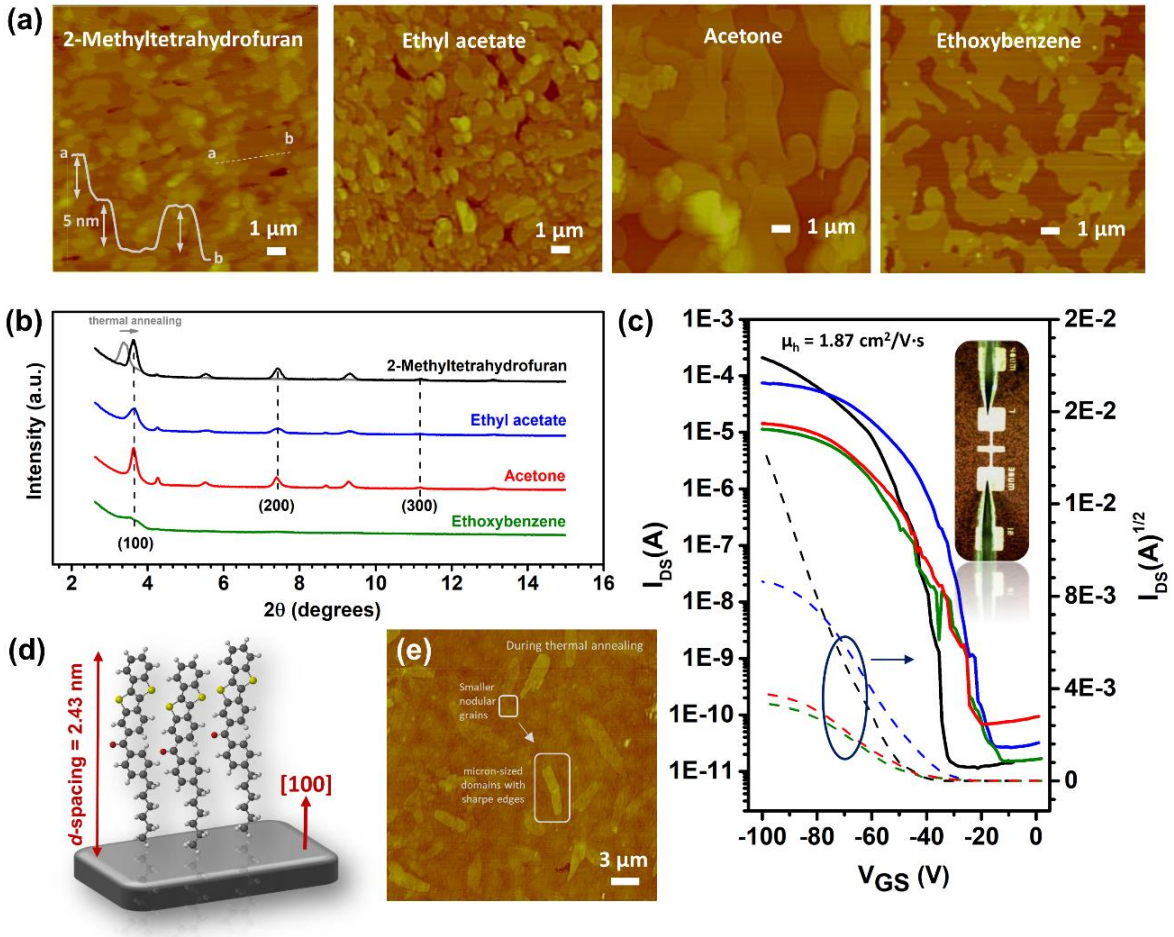

Figure 4.5 Tapping mode atomic force microscopy (AFM) topographic images (a) and θ-2θ out-of-plane X-ray diffraction (Bragg-Brentano configuration) scans with the assigned planes (b) for p^{++}-Si/SiO_2 (300 nm)/PS-brush (M_n = 5 kDa)/***m*-C$_6$PhCO-BTBT** (40-50 nm) thin-films that are spin-coated from four different green solvents (2-methyltetrahydrofuran, ethyl acetate, acetone, and ethoxybenzene), and annealed at 120 °C (for 30 min). Figure 4.5(a)-inset shows the measured step-height profile (~2.5×*n* nm (*n (integer)* ≥ 1)) of the 2D terraced multi-layer molecular islands. In the top XRD scan, the spin-coated sample without thermal annealing (gray solid line) is also provided for comparison. (c) Transfer (V_{DS} = -100 V) characteristics for p^{++}-Si/SiO_2 (300 nm)/PS-brush (M_n = 5 kDa)/***m*-C$_6$PhCO-BTBT** (40-50 nm)/Au (50 nm) OFET devices processed from four different green solvents. The $I_{DS}^{1/2}$ *vs.* V_G plots (dashed curves) are used for hole mobility calculations. The inset shows a representative top-view image of an OFET device during measurement. (d) The molecular arrangement in the out-of-plane [100] direction based on the main (100) diffraction peak and the step-height profile of the 2D crystalline domains. (e) The morphological change from small nodular grains to micron-sized domains with sharp edges, as observed during thermal annealing process for an unfinished sample.

The maximum saturation hole mobilities were achieved for thin-films spin-coated from 2-methyltetrahydrofuran (μ_h^{max} = 1.87 $cm^2/V{\cdot}s$, μ_h^{avg} = 1.21 $cm^2/V{\cdot}s$

(I_{on}/I_{off} = 10^7-10^8)) and ethyl acetate (μ_h^{max} = 0.62 $cm^2/V{\cdot}s$, μ_h^{avg} = 0.41 $cm^2/V{\cdot}s$ (I_{on}/I_{off} = 10^6-10^7)) solutions (Figures 4.5(c) and 4.20). On the other hand, ***m*-C$_6$PhCO-BTBT** thin-films spin-coated from acetone and ethoxybenzene showed relatively lower but still respectable hole mobilities of 0.07-0.11 $cm^2/V{\cdot}s$ (I_{on}/I_{off} = 10^5-10^6) (Figure 4.5(c)). As shown in Figure 4.5(a), semiconductor thin-films processed from all four green solvents exhibited terraced 2D islands that orient along the substrate plane. Despite all being micron-sized grains, the grain sizes for 2-methyltetrahydrofuran and ethyl acetate are observed to be relatively smaller, yet showing a better inter-grain connectivity across large distances (>30 μm). On the other hand, while ethoxybenzene and acetone appear to have larger domains, two different issues were identified with them. Ethoxybenzene thin-film domains exhibited very poor crystallinity (Figure 4.5(b)-green line), and acetone thin-film domains, despite being very crystalline (Figure 4.5(b)-red line), were observed to be isolated from each other and showed poor inter-grain connectivity (R_q = 30.25 nm for a 30 × 30 μm^2 area, Figure 4.23). When the XRD profiles of the thin-films were explored, although all thin-films showed exactly the same crystalline planes, the thin-films processed from 2-methyltetrahydrofuran, ethyl acetate, and acetone showed the best crystallinities with high intensity sharp peaks. Based on the low-angle (100) diffraction peak observed at 2θ = 3.63°, the *d*-spacing value is calculated as 2.43 nm. This *d*-spacing corresponds to the molecular long-axis length having a coplanar and fully extended (i.e., hexyl chain in all-*trans* conformation) structure. This reveals a highly favorable edge-on oriented crystallization behavior in the thin-film, resulting in favorable π-interactions along the source-to-drain charge-transport directions.[118], [143], [190] Note that this conformation is close to the optimized molecular geometry, and all other conformations with increased intramolecular twists and other alkyl chain conformations (e.g., gauche or eclipsed) lead to much shorter molecular lengths (Figure 4.24). The calculated *d*-spacing value matches also perfectly with the measured step-height profiles (~2.5×*n* nm (*n (integer)* ≥ 1)) of the 2D terraced multi-layer molecular islands (Figure 4.5(a)-inset). The higher order diffraction peaks of (200) and (300) were also observed in the same XRD spectra, confirming the presence of a long-range crystal ordering in the out-of-plane direction. Using the Scherrer equation and taking all (100)-(300) diffractions peaks into consideration,[191], [192] the (100) coherence lengths (L) are estimated to be ~34-36 nm for 2-methyltetrahydrofuran, ~27-29 nm for ethyl acetate, and ~40-45 nm for acetone (see Figure 4.25 for Gaussian fittings). The extent of

coherence lengths for all solvents are in the scale of the thin-film thickness, which suggests an excellent degree of molecular ordering in the out-of-plane direction. On the other hand, the absence of any broad peaks at $2\theta \approx 20-25°$ in the out-of-plane direction, which typically corresponds to π-interactions, suggests that all π-interactions are mainly along the thin-film plane, which is important for charge transport in molecular semiconductors. [118], [143], [190], [193]

The high hole mobility and the proper microstructures/morphologies are obtained when the semiconductor is processed from 2-methyltetrahydrofuran and ethyl acetate with a moderate R_a value of 4.4 $MPa^{1/2}$ and 6.4 $MPa^{1/2}$ and reasonable solvent boiling points of 77-78 °C. When R_a decreases in ethoxybenzene (2.4 $MPa^{1/2}$) or increases in acetone (8.3 $MPa^{1/2}$), the mobility and the microstructure/morphology deteriorate. On one hand, poor crystallinity was observed due to the low crystallization tendency in an excellent solvent (i.e., ethoxybenzene, with very small solute-solvent interaction distance). On the other hand, rapid crystallization behavior with poorly connected domain formation was observed in a relatively bad solvent (i.e., acetone, with a relatively larger solute-solvent interaction distance). Herein, one should also note that the low boiling point of acetone (56 °C) and the high boiling point of ethoxybenzene (169 °C) might further characterize these observed crystallization behaviors. This indicates that an optimal solute-solvent interaction distance (R_a) is key to a proper thin-film self-assembly process. In other words, as solvent evaporates during spin-coating, molecules should not immediately precipitate/crystallize due to a large R_a value. Instead, they should gradually saturate, leading to a more controlled thin-film crystallization and molecular self-assembly process.[194], [195] On the other hand, semiconductor thin-films drop-casted from ethanol, which has a much larger R_a value of 15.3 $MPa^{1/2}$, onto p^{++}-Si/SiO_2 (300 nm)/PS-brush (M_n = 5 kDa) substrates yielded OFETs with lower μ_h of ~0.001 $cm^2/V{\cdot}s$ ($I_{on}/I_{off} \approx 10^4$ and V_{th} = -39 V). It is noteworthy that the excellent thin-film crystallization and morphological behaviors of our current semiconductor from 2-methyltetrahydrofuran solution is consistent with our recent observations with an *n*-type small molecule.[173]

To the best of our knowledge, there is very limited examples of OFETs processed from some of these solvents, especially from ethyl acetate, acetone, and ethanol.[109], [186], [187] Also, this is the first time that a BTBT-based OFET is fabricated from these green solvents. The excellent *p*-channel performances, having

high μ_h's and I_{on}/I_{off} ratios, achieved with 2-methyltetrahydrofuran and ethyl acetate green solvents, despite the absence of any meticulous process optimization, rank among the highest reported from a green solvent.[108], [114] Here, it is noteworthy that the V_{th} values for these OFETs typically fall within the range of -30 V to -35 V. Therefore, considering the ideal linear characteristics of the "$I_{DS}^{1/2}$ *vs.* V_{GS}" transfer curves of the green-solvent processed OFETs, yet with noticeable threshold voltages, our saturation hole mobilities could be further evaluated by applying a reliability factor (r_{sat}), as described in recent experimental/modeling studies.[196], [197] The reliability factor is used to define the equivalent electrical performance of an OFET device with a near-zero threshold voltage, following the ideal Shockley equations.[197] This procedure shows that r_{sat}'s for our OFETs are 32-38%, yielding μ_{eff}'s of 0.17-0.35 $cm^2/V{\cdot}s$ for the equivalent ideal transistor according to the Shockley FET equations (i.e., a linear transfer characteristics with V_{th} = 0 V). The large V_{th}'s for the current OFETs are undoubtedly the result of ***m*-C$_6$PhCO-BTBT**'s extremely low-lying HOMO energy level and the unoptimized metal-semiconductor interfaces, as well as possibly the existence of trap states.[198], [199] Further optimizations with regards to metal-semiconductor interface and semiconducting thin-film could significantly reduce the observed V_{th} and further optimize the transistor performance. Among all known high-performance ($\mu_h \geq 0.5$ $cm^2/V{\cdot}s$) *p*-type semiconductors, ***m*-C$_6$PhCO-BTBT** exhibits one of the deepest HOMO energy levels ever recorded at -6.04 eV.[36], [79], [143] This, coupled with its wide optical band gap, excellent processing, and semiconducting characteristics, suggests that it could find many practical applications in multilayer (opto)electronic devices.[81], [140], [200]

Table 4.3 The molecular structures, purification methods, solubility values (if available), highest occupied molecular orbital (HOMO) energy levels, organic field-effect transistor (OFET) semiconductor thin-film processing method, and the maximum field-effect charge carrier mobilities for previously reported BTBT-based semiconductors.

Compound	Molecular Structure	Purification Method (Solubility Value - if available)	HOMO Energy Level	OFET Semiconductor Thin-Film Processing Method (Maximum Field-Effect Charge Carrier Mobility)	Reference
1	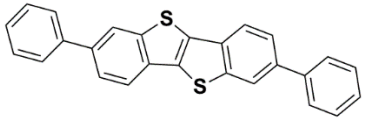	Vacuum Sublimation	-5.6 eV	Thermal Evaporation (1.0-2.0 $cm^2/V.s$)	[152]
2 (C_6-BTBT)	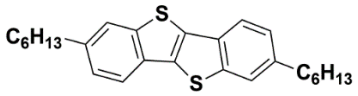	Chromatography (70 g/L in Chloroform)	-5.5 eV	Spin-Coating from chloroform (0.36-0.45 $cm^2/V.s$)	[201]
3 (C_8-BTBT)	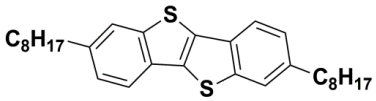	Chromatography (≈10 g/L in toluene, *p*-xylene, and cyclohexanone)	not disclosed	Spin-Coating from toluene:*p*-xylene (4.9 $cm^2/V.s$)	[202]
		Chromatography	not disclosed	Off-Centre Spin-Coating from *o*-dichlorobenzene (25-43 $cm^2/V.s$)	[203]
4 (BTBT-Ph-C_{12})	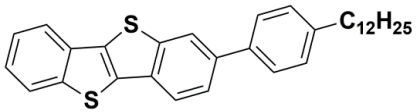	Vacuum Sublimation	-5.64 eV	Thermal Evaporation (8.7 $cm^2/V.s$)	[204]

5	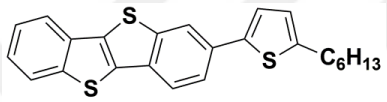	Chromatography	-5.48 eV	Thermal Evaporation (10.5 cm^2/V.s)	[205]
6	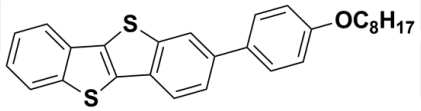	Vacuum Sublimation	-5.51 eV	Thermal Evaporation (8.25 cm^2/V.s)	[1]
7 (BTBT-Ph-C_6)	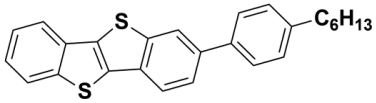	Vacuum Sublimation	-5.65 eV	Thermal Evaporation (4.6 cm^2/V.s)	[157]
8	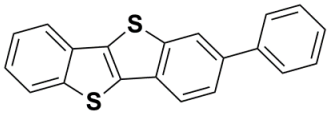	Vacuum Sublimation	-5.68 eV	Thermal Evaporation (0.034 cm^2/V.s)	[157]
9	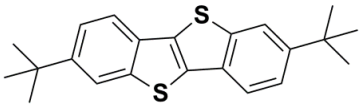	Recrystallization/ Chromatography	-5.7 eV	Physical Vapor Transport/Solution Shearing from tetralin (17/3.7 cm^2/V.s)	[206]
10	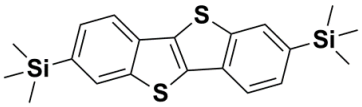	Recrystallization/ Chromatography	-5.6 eV	Physical Vapor Transport (0.6 cm^2/V.s)	[206]
11	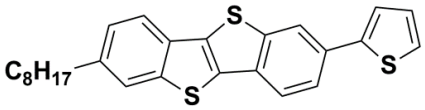	Chromatography	-5.45 eV	Solution Shearing from toluene/1,2,4-trichlorobenzene (0.1 cm^2/V.s)	[207]

12	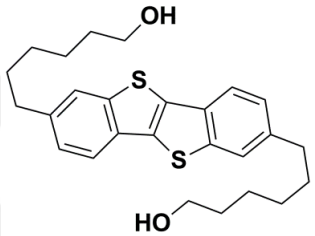	Recrystallization	-5.56 eV	Thermal Evaporation ($0.17\ cm^2/V.s$)	[208]
13	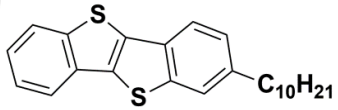	Recrystallization	-5.8 eV	Thermal Evaporation ($6\ cm^2/V.s$)	[209]
14 ((mono)-C_{13}-BTBT)	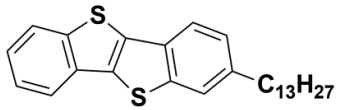	Recrystallization	-5.8 eV	Thermal Evaporation ($17.2\ cm^2/V.s$)	[155]
15 (Ph-BTBT-C_{10})	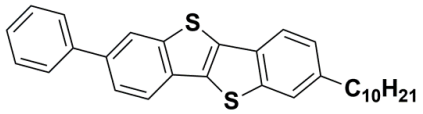	Recrystallization	not disclosed	Spin-Coating from diethylbenzene ($14.7\ cm^2/V.s$)	[210]
16	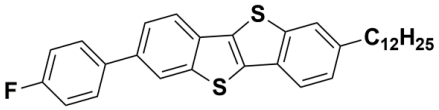	Recrystallization	not disclosed	Solution-Casting from *p*-xylene ($0.42\ cm^2/V.s$)	[211]

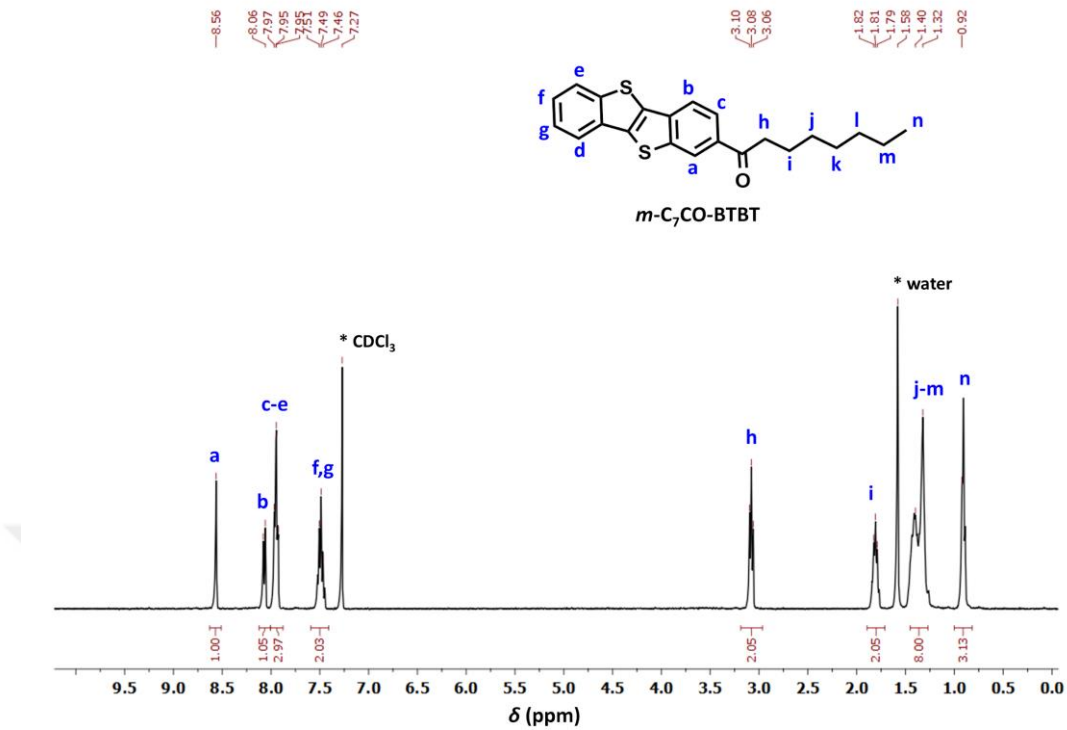

Figure 4.6 ^{1}H NMR spectrum of 1-(benzo[*b*]benzo[4,5]thieno[2,3-*d*]thiophen-2-yl)octan-1-one (***m*-C$_7$CO-BTBT**) in $CDCl_3$ at room temperature.

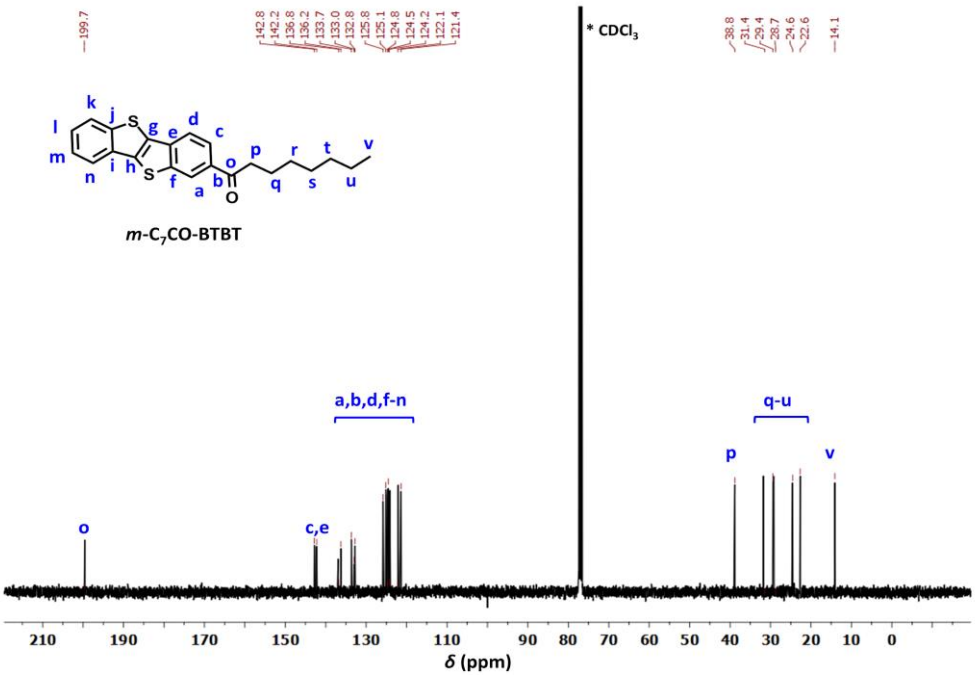

Figure 4.7 ^{13}C NMR spectrum of 1-(benzo[*b*]benzo[4,5]thieno[2,3-*d*]thiophen-2-yl)octan-1-one (***m*-C$_7$CO-BTBT**) in $CDCl_3$ at room temperature.

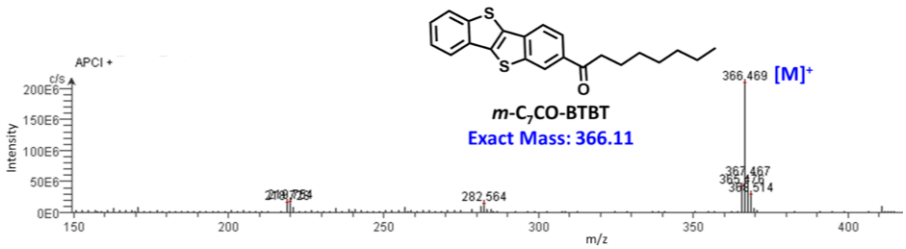

Figure 4.8 Positive ion mass spectrum of 1-(benzo[*b*]benzo[4,5]thieno[2,3-*d*]thiophen-2-yl)octan-1-one (***m*-C$_7$CO-BTBT**) measured by atmospheric pressure chemical ionization mass spectrometer (APCI-MS).

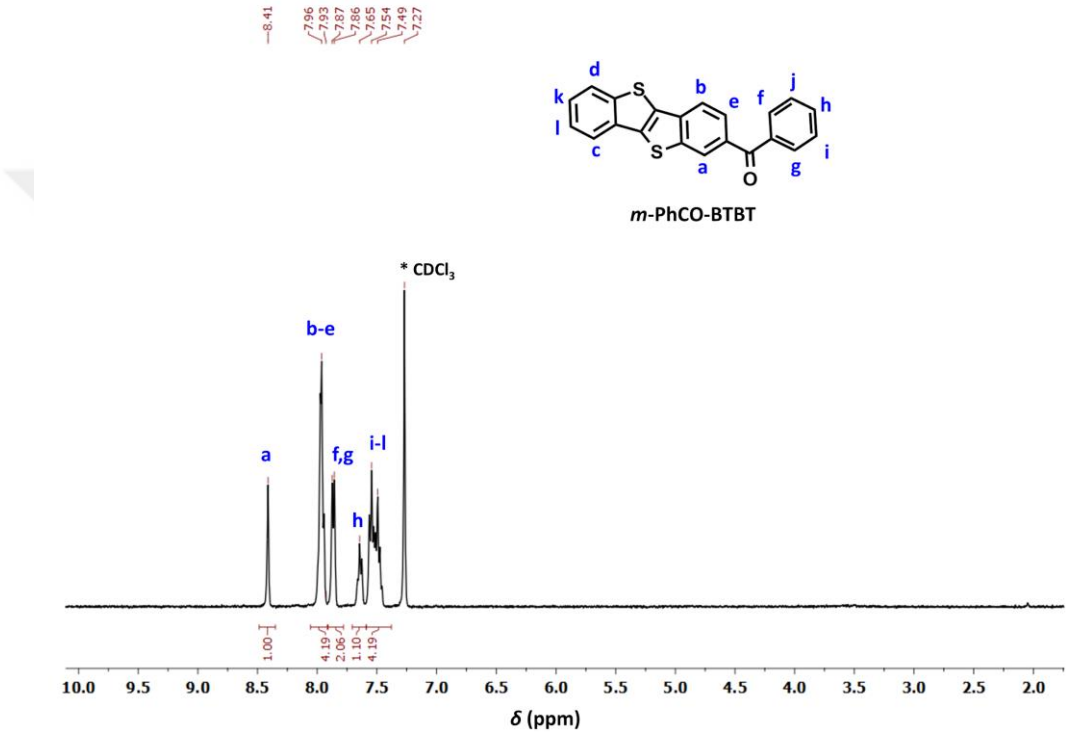

Figure 4.9 ^{1}H NMR spectrum of benzo[*b*]benzo[4,5]thieno[2,3-*d*]thiophen-2-yl(phenyl)methanone (***m*-PhCO-BTBT**) in $CDCl_3$ at room temperature.

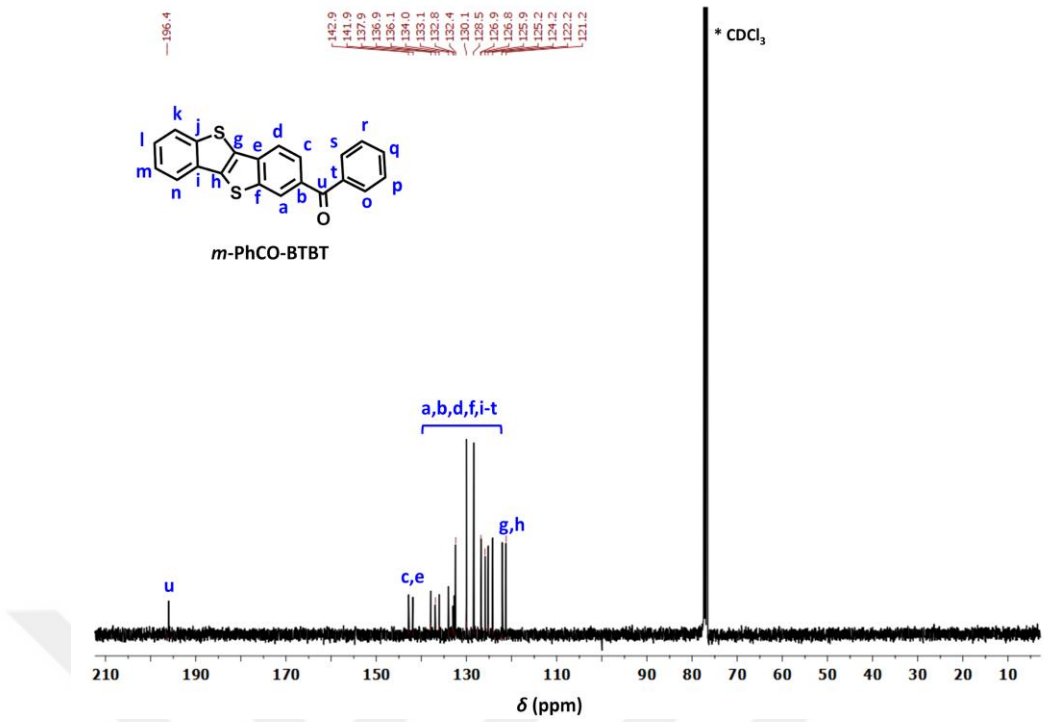

Figure 4.10 ^{13}C NMR spectrum of benzo[*b*]benzo[4,5]thieno[2,3-*d*]thiophen-2-yl(phenyl)methanone (***m*-PhCO-BTBT**) in $CDCl_3$ at room temperature.

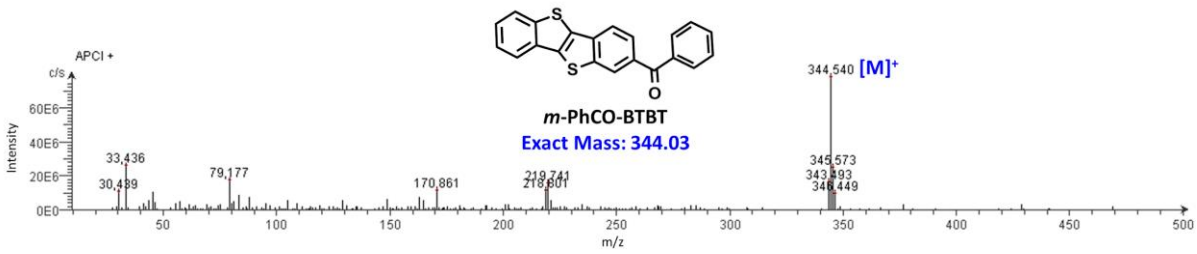

Figure 4.11 Positive ion mass spectrum of benzo[*b*]benzo[4,5]thieno[2,3-*d*]thiophen-2-yl(phenyl)methanone (***m*-PhCO-BTBT**) measured by atmospheric pressure chemical ionization mass spectrometer (APCI-MS).

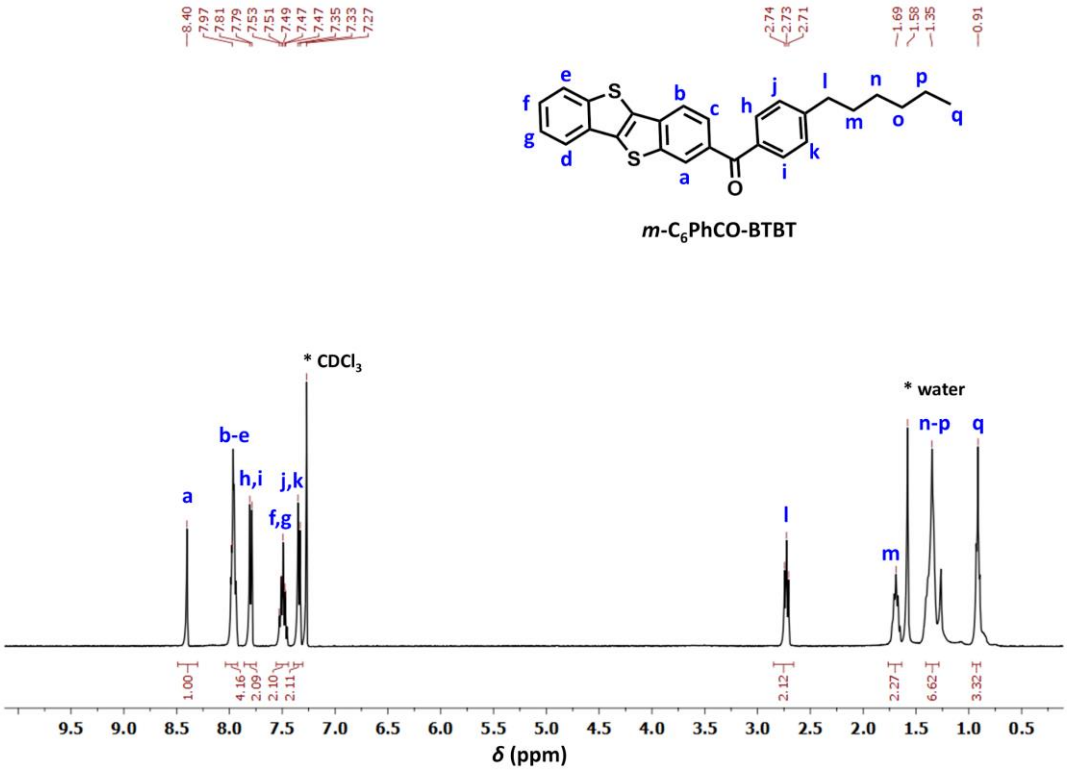

Figure 4.12 ^{1}H NMR spectrum of benzo[*b*]benzo[4,5]thieno[2,3-*d*]thiophen-2-yl(4-hexylphenyl)methanone (***m*-C$_6$PhCO-BTBT**) in $CDCl_3$ at room temperature.

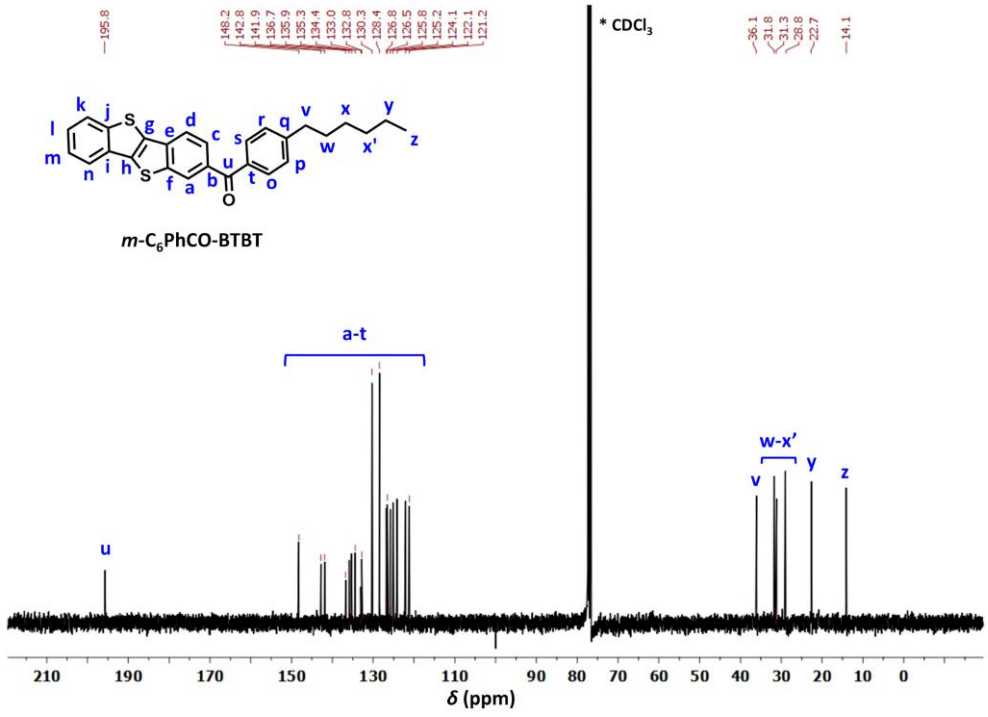

Figure 4.13 ^{13}C NMR spectrum of benzo[*b*]benzo[4,5]thieno[2,3-*d*]thiophen-2-yl(4-hexylphenyl)methanone (***m*-C$_6$PhCO-BTBT**) in $CDCl_3$ at room temperature.

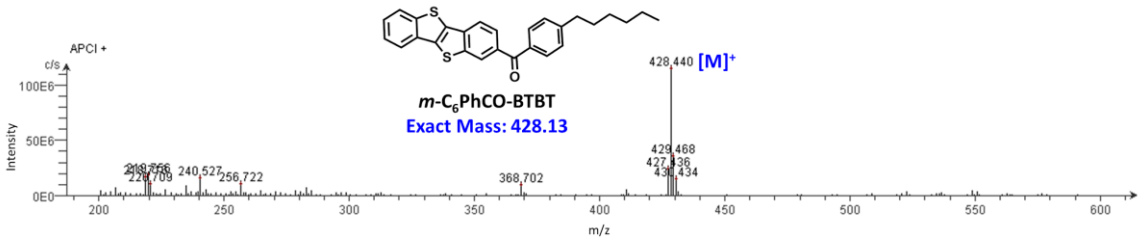

Figure 4.14 Positive ion mass spectrum of benzo[*b*]benzo[4,5]thieno[2,3-*d*]thiophen-2-yl(4-hexylphenyl)methanone (***m*-C$_6$PhCO-BTBT**) measured by atmospheric pressure chemical ionization mass spectrometer (APCI-MS).

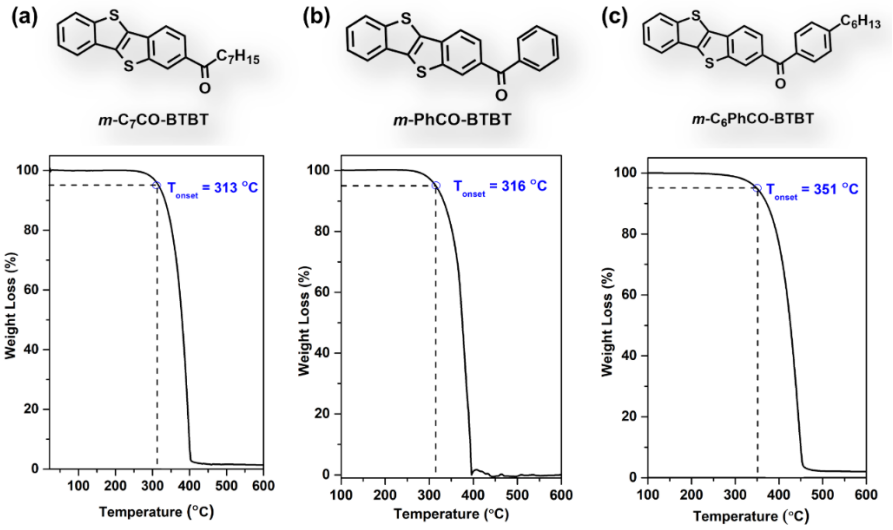

Figure 4.15 Thermogravimetric analysis (TGA) of mono-carbonyl BTBT small molecules ***m*-C$_7$CO-BTBT** (a), ***m*-PhCO-BTBT** (b), and ***m*-C$_6$PhCO-BTBT** (c) at a temperature ramp of 10 °C/min under N_2.

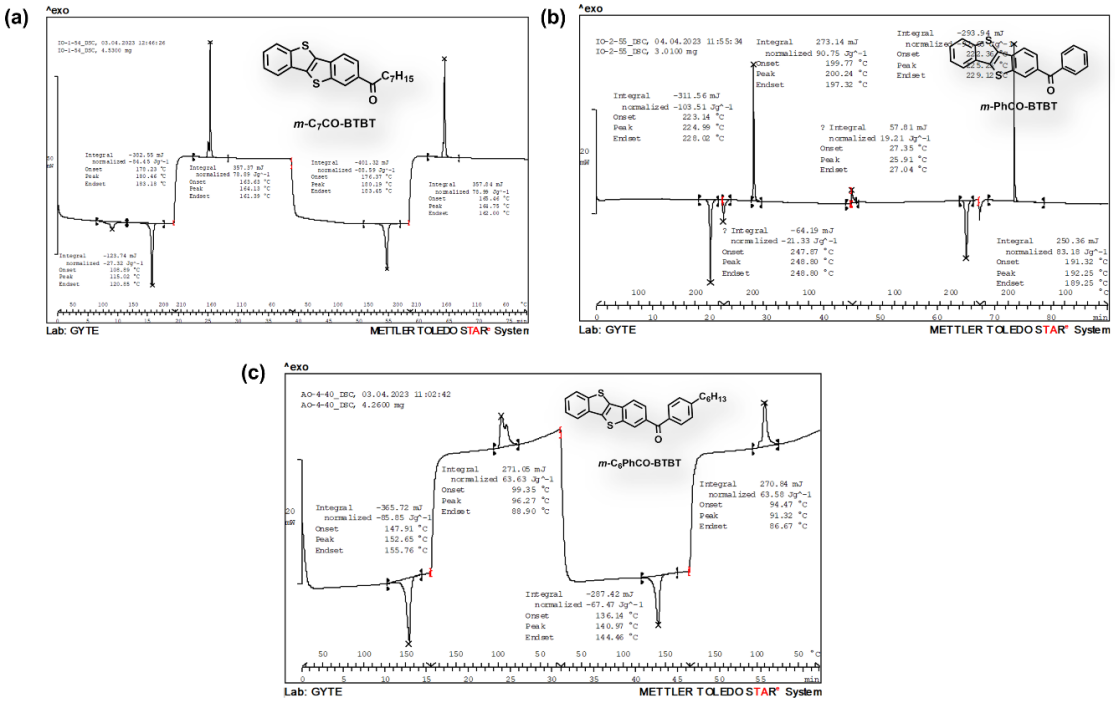

Figure 4.16 Differential scanning calorimetry scans (shown as raw scans from the instrument) of mono-carbonyl BTBT small molecules ***m*-C$_7$CO-BTBT** (a), ***m*-PhCO-BTBT** (b), and ***m*-C$_6$PhCO-BTBT** (c) at a temperature ramp of 10 °C min^{-1} under N_2.

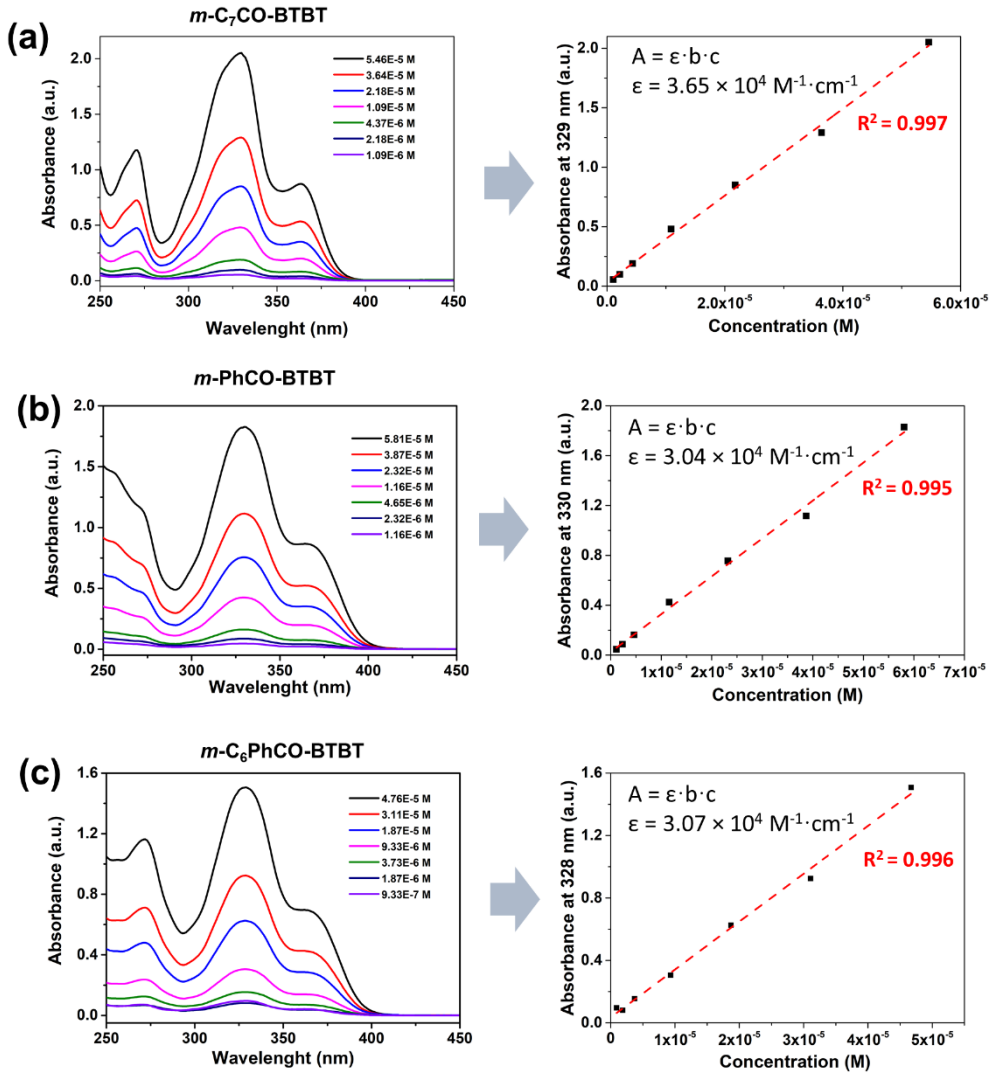

Figure 4.17 The calibration curve based on the absorbance of mono-carbonyl BTBT small molecules ***m*-C$_7$CO-BTBT** (a), ***m*-PhCO-BTBT** (b), and ***m*-C$_6$PhCO-BTBT** (c) in chloroform at varied standard solution concentrations recorded at their corresponding absorption maximum; the linear fitting was performed according to Beer-Lambert law (adjusted R^2's > 0.99).

Theoretical calculation of the intercept in the Hansen-adapted Scatchard-Hildebrand regular solution theory equation (1):

$$-\ln x_{OSC} = \frac{v_{OSC}}{RT}\Phi_{solv.}{}^{2}R_a{}^{2} + \frac{\Delta H_{fus}}{R}\left(\frac{1}{T} - \frac{1}{T_{mp-OSC}}\right) \quad (1)$$

By using the thermal properties of enthalpy of fusion (ΔH_{fus}) and melting temperature ($T_{mp\text{-}OSC}$) measured in the DSC scans of the current molecules (Figure 4.15), the intercept in equation (1) is calculated as shown in Table 4.4. Note that all these melting processes lead to a fully isotropic liquid phase, as visually confirmed through conventional melting point measurement. The endset of the melting temperature and enthalphy of fusion in the first-heating cycle are taken as it represents the completion of the melting process for the polycrystalline solid obtained in the synthesis. Note that the same polycrystalline solid is used for solubility measurements to determine the HSP sphere. When another endothermic transition is observed prior to the main melting process (as seen in the case of ***m*-C$_7$CO-BTBT**, Figure 4.15(a)), this corresponding prior enthalpy value and the thermal transition endset tempearture (27.32 J/g at 120.85 °C) is taken into account for calculating the intercept value, as this endothermic transition is a part of the solid-to-isotropic liquid transition.

Table 4.4 The thermal properties of melting temperature endset ($T_{mp\text{-}endset}$) and enthalpy of fusion (ΔH_{fus}) measured in the DSC scans, molecular weights, and the calculated intercept values based on equation (1) shown above for the mono-carbonyl BTBT small molecules ***m*-C$_7$CO-BTBT**, ***m*-PhCO-BTBT**, and ***m*-C$_6$PhCO-BTBT**.

Molecule	$T_{mp\text{-}endset}$ (° C)	ΔH_{fus} (J/g)	Molecular Weight (g/mol)	ΔH_{fus} (J/mol)	Intercept
m-C$_7$CO-BTBT*	183.18	84.45	366.54	40968.1758	5.30
m-PhCO-BTBT	228.02	103.51	344.45	35654.0195	5.83
m-C$_6$PhCO-BTBT	155.76	85.85	428.61	36796.1685	4.52

* The prior endothermic transition is also taken into account for calculating the intercept value, as explained above.

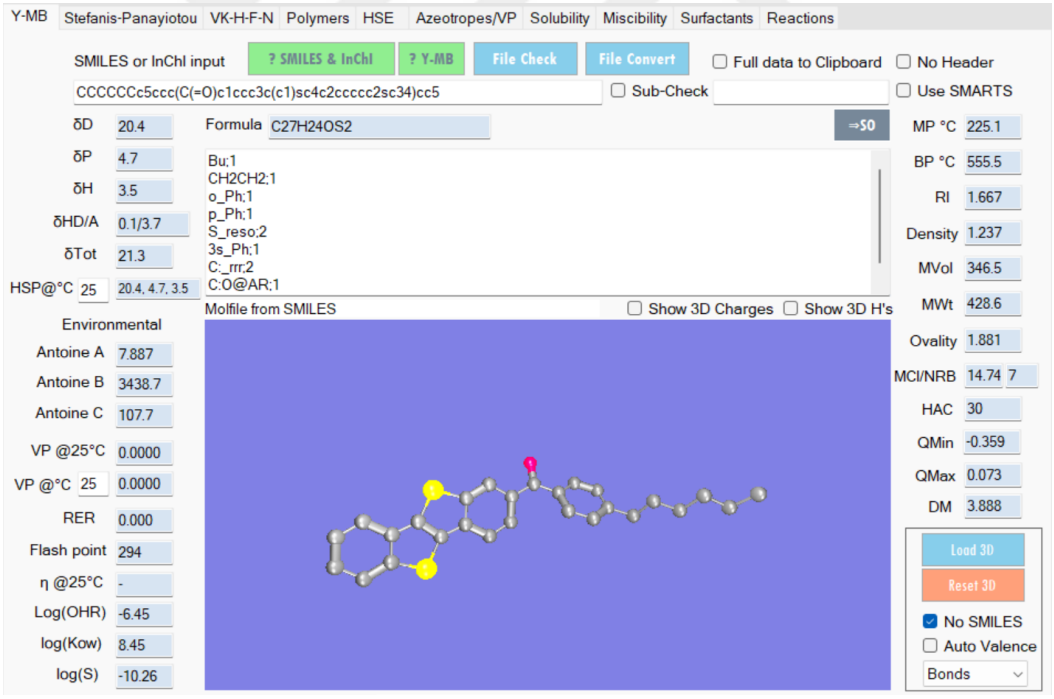

Figure 4.18 Hansen solubility parameters calculated for ***m*-C$_6$PhCO-BTBT** by group contribution methodology in the HSPiP software (*5th Edition Version 5.4.08*) with DIY and YMB modules using simplified molecular-input line-entry system (SMILES).

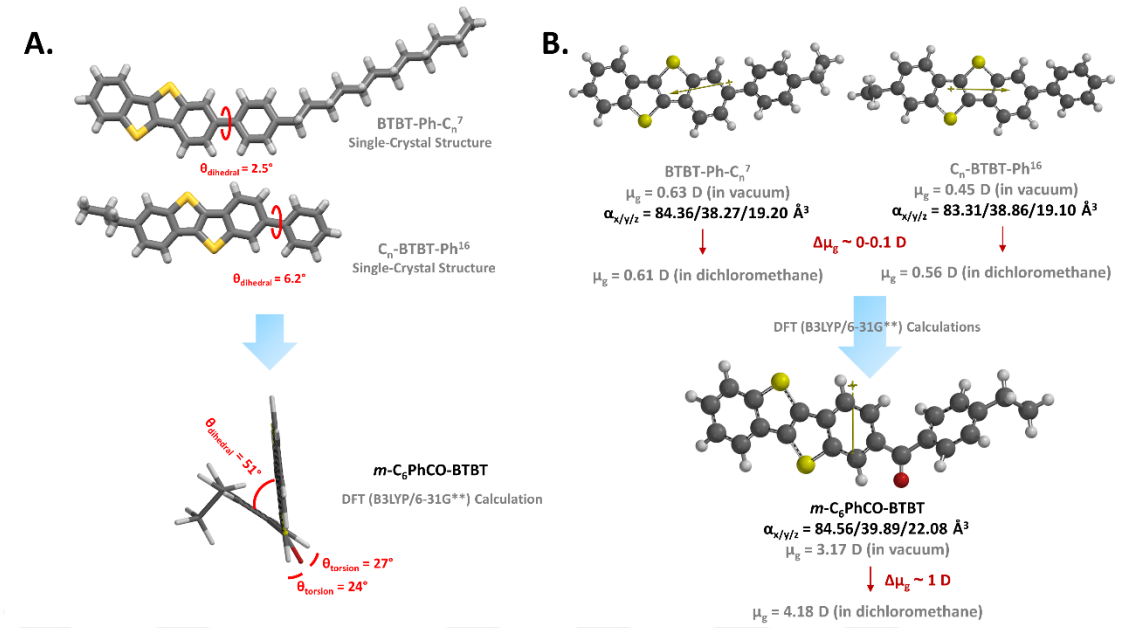

Figure 4.19 A. (*BTBT*)Ph-Ph dihedral angles for structurally similar **BTBT-Ph-Cn** and **Cn-BTBT-Ph** molecules based on their reported single-crystal structures,[1], [2] and the DFT(B3LYP/6-31G**)-optimized molecular conformation of ***m*-C6PhCO-BTBT** showing the (*BTBT*)Ph-Ph dihedral angle and (*BTBT*)Ph-CO/CO-Ph torsion angles. B. DFT(B3LYP/6-31G**)-calculated molecular dipole moments (in vacuum and in dichloromethane) and polarizabilities for **BTBT-Ph-Cn**, **Cn-BTBT-Ph**, and ***m*-C6PhCO-BTBT** indicating a significant increase in ground-state dipole moments (μ_g (D)), dipole changes ($\Delta\mu_g$ (D)) going from vacuum to solution, and polarizabilities (α ($Å^3$)) upon carbonyl insertion.

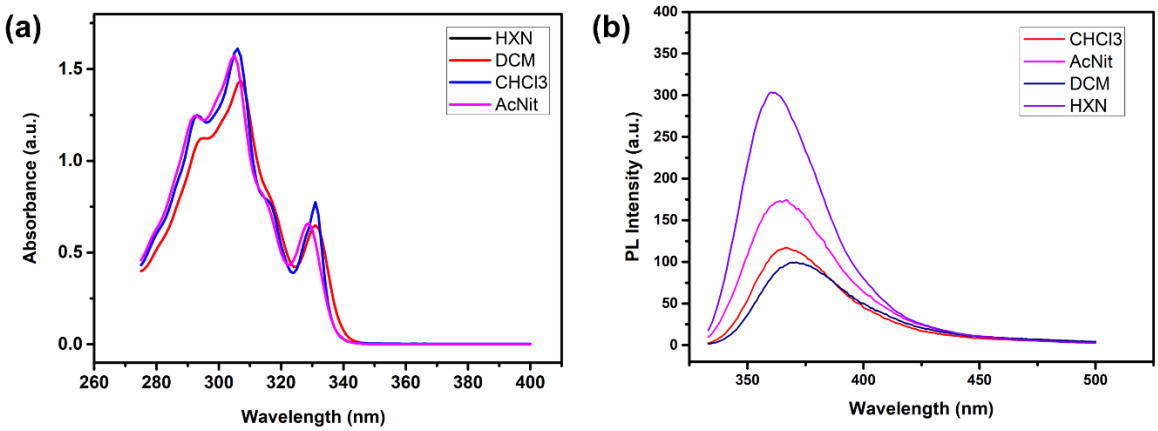

Figure 4.20 UV-Vis optical absorption (a) and photoluminescence ($\lambda_{excitation}$ = 330 nm) (b) spectra of **BTBT** solutions in different solvents with increasing polarity.

The Lippert-Mataga model is used according to the following equation to estimate the dipole moments of S_1 state:

$$\nu_a - \nu_f = \frac{2(\mu_e - \mu_g)^2}{hca^3} f(\varepsilon, n) + (\nu_a^0 - \nu_f^0) \qquad (1)$$

where *h* is Planck constant, *c* is the speed of light in vacuum, $\nu_a^0 - \nu_f^0$ is the Stokes shift when *f* is zero, μ_e and μ_g are dipole moments of excited state and ground state respectively. $f(\varepsilon, n)$ and *a* are the solvent orientation polarizability and the solvent Onsager cavity radius, respectively and can be calculated as follows:

$$f(\varepsilon, n) = \frac{\varepsilon - 1}{2\varepsilon + 1} - \frac{n^2 - 1}{2n^2 + 1}, \quad a = \left(\frac{3M}{4N\pi d}\right)^{1/3} \qquad (2)$$

where ε is the solvent dielectric constant and n is the solvent refractive index. *M* is the molar mass, *N* is the Avogadro's constant, and *d* is the density of the solvents (*d* = 1.0 g/cm^3).

In the Equation (1), $\frac{2(\mu_e - \mu_g)^2}{hca^3}$ is the term corresponding to the slope of the plot of Stokes shift $(\nu_a - \nu_f)$ versus the solvent orientation polarizability $f(\varepsilon, n)$. By estimating the dipole moment of ***m*-C$_6$PhCO-BTBT**'s ground state ($\mu_g = 3.17$ D) from density functional theory (DFT) calculations and the slope from the plot of $(\nu_a - \nu_f)$ vs $f(\varepsilon, n)$, we could calculate the dipole moment of ***m*-C$_6$PhCO-BTBT** in the excited state, μ_e.

Table 4.5 Solvatochromic optical absorption and photoluminescence peak maxima (λ_{abs}^{max} and λ_{fl}^{max}) and Stokes shifts ($\nu_{abs} - \nu_{fl}$) for ***m*-C$_6$PhCO-BTBT** in different

Solvents	***f* (ε,*n*)**	λ_{abs}^{max} **(nm)**	λ_{fl}^{max} **(nm)**	$\nu_{abs} - \nu_{fl}$ **(cm^{-1})**
Hexane	0.001	360	418	3854
Toluene	0.014	362	414	3470
Isopentyl Ether	0.0747	362	426	4160
Chloroform	0.148	364	437	4589
THF	0.210	361	430	4445
DCM	0.217	362	435	4636
DMF	0.276	362	444	5101
Acetonitrile	0.305	360	450	5555

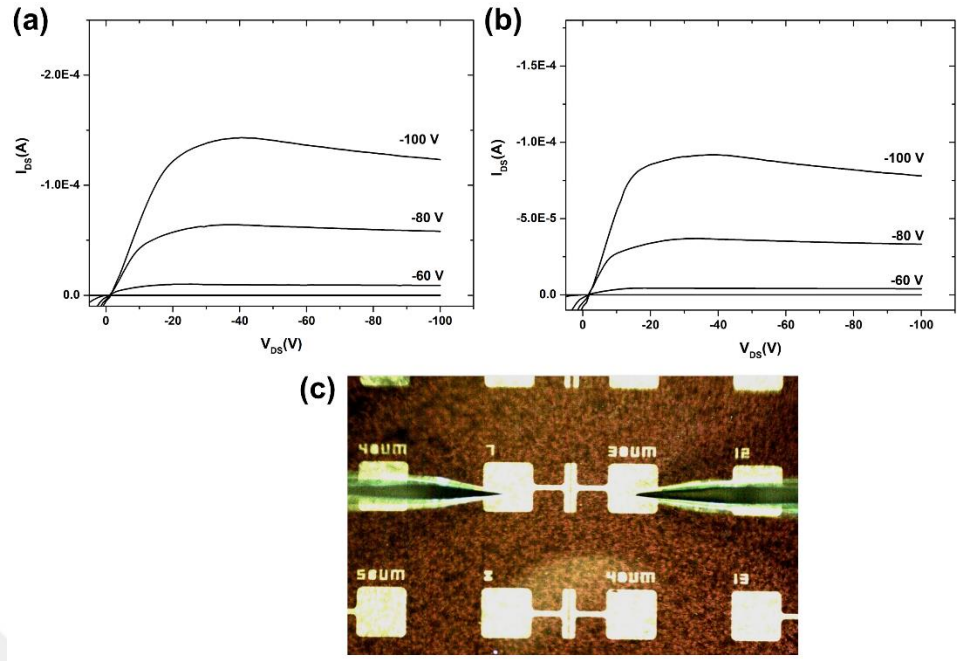

Figure 4.21 Output characteristics (V_{GS} = -100 V, -80 V, -60 V, -40 V, -20 V) for p^{++}-Si/SiO_2 (300 nm)/PS-brush (M_n = 5 kDa)/***m*-C$_6$PhCO-BTBT** (40-50 nm)/Au (50 nm) OFET devices with the semiconductor thin-films spin-coated from 2-methyltetrahydrofuran (a) and ethyl acetate (b), and annealed at 120 °C. (c) The top-view optical image of a section of the OFET devices during electrical characterization under ambient conditions. High density deposition mask (Ossila, E322) is used to define Au source-drain electrodes with variable channel lengths of 30, 40, 50, 60, 80 µm (Width = 1000 µm).

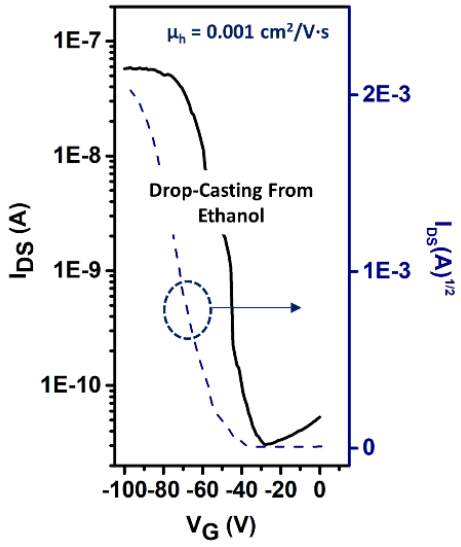

Figure 4.22 Transfer (V_{SD} = -100 V) characteristics for p^{++}-Si/SiO_2 (300 nm)/PS-brush (M_n = 5 kDa)/**m-C$_6$PhCO-BTBT (40-50 nm)**/Au (50 nm) OFET devices based on drop-casted semiconductor thin-films from ethanol solution (annealed at 120 °C). The $I^{1/2}$ *vs.* V_G plots used for the hole mobility calculations are shown in blue.

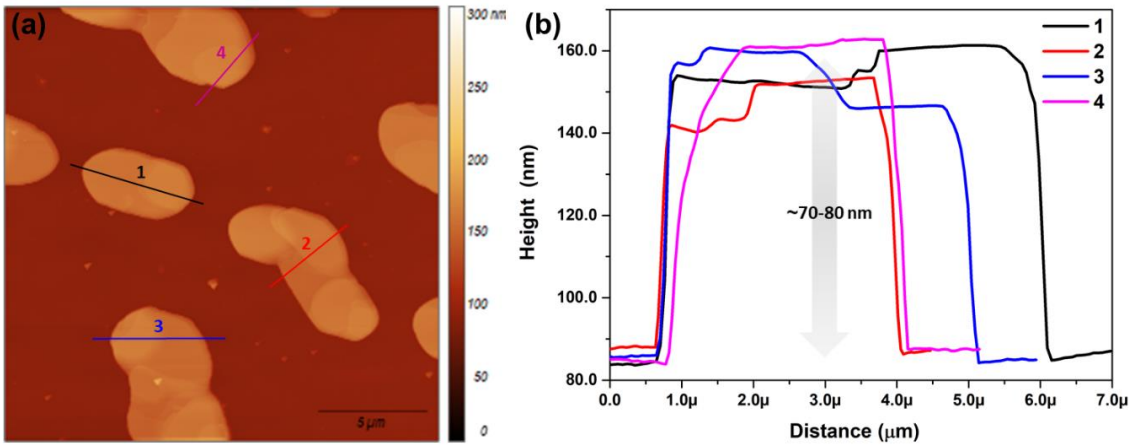

Figure 4.23 Tapping mode atomic force microscopy (AFM) topographic image (a) and the corresponding step-height profiles (b) of the disintegrated micron-sized molecular domains (1-4) for ***m*-C$_6$PhCO-BTBT** thin-film on p^{++}-Si/SiO$_2$ (300 nm)/PS-brush (M_n = 5 kDa) after thermal annealing at 130-140 °C.

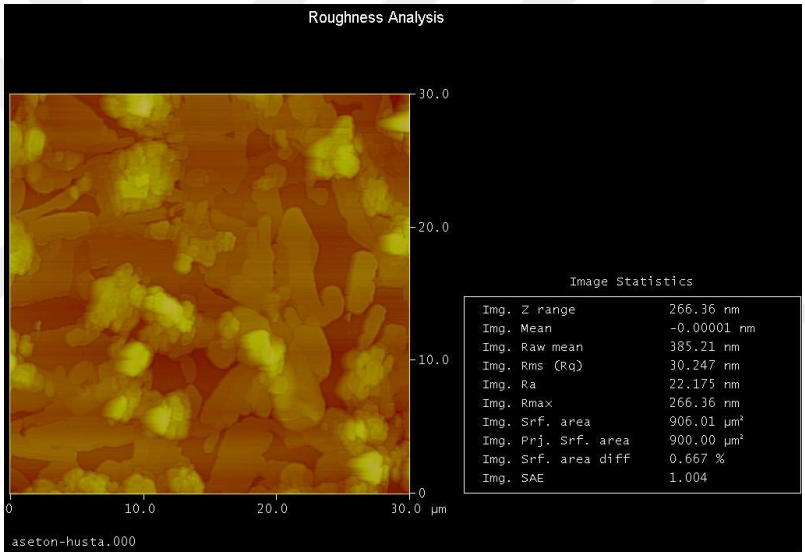

Figure 4.24 Tapping mode atomic force microscopy (AFM) topographic image and the roughness analysis of the spin-coated ***m*-C$_6$PhCO-BTBT** thin-film (annealed at 120 °C) on p^{++}-Si/SiO$_2$ (300 nm)/PS-brush (M_n = 5 kDa).

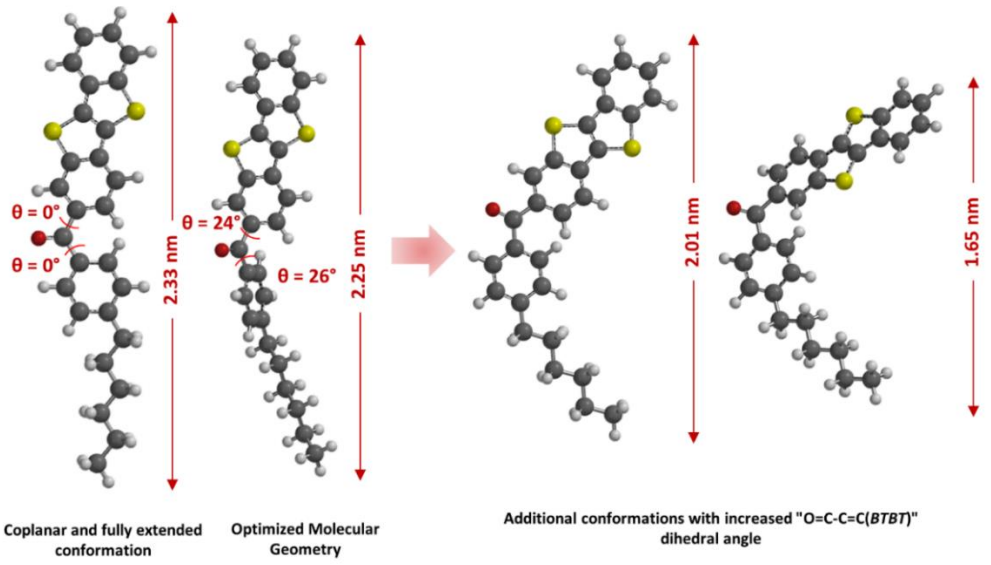

Figure 4.25 DFT-calculated (B3LYP/6-31G**) molecular conformations of ***m*-C$_6$PhCO-BTBT** showing different long-axis molecular lengths depending on the "O=C-C=C(*BTBT*)" dihedral angle. The hexyl chains at the molecular termini display a fully extended all-trans conformation; note that the gauche and eclipsed conformations would further decrease the molecular lengths.

Reliability Factor and Effective Mobility, it is very important to obtain an extended linear region in the $I_{DS}^{1/2}$ *vs.* V_{GS} plots to define the ideal FET device operation and to use the Shockley model as the physical model of the FET operation. The saturation mobilities (μ_{sat}) for our present OFETs (i.e., processed from 2-methyltetrahydrofuran, ethyl acetate, acetone, and ethoxybenzene) are calculated from these extended linear regions in the $I_{DS}^{1/2}$ *vs.* V_{GS} transfer plots over a wide V_{GS} voltage ranges of >50 V. However, a high V_{th} is indicative of high deep trap density and carrier injection problems. Therefore, an electrically equivalent ideal FET is defined to exhibit the same I_{DS}^{max} at the V_{GS}^{max} and to operate as an ideal transistor according to the Shockley FET equations (i.e., a linear transfer characteristics with an ideal V_{th} = 0 V). According to these definitions, a reliability factor (r_{sat}) and effective mobility (μ_{eff}) are defined using the following equation:

$$r_{sat} = \frac{\left(\sqrt{|I_{ds}|^{max}} - \sqrt{|I_{ds}|^{0}} \Big/ |V_{gs}|^{max}\right)^2}{\left(\sqrt{|I_{ds}|} \Big/ V_{gs}\right)^2_{claimed}}$$

Note that the squared slope for the dashed-black and dashed-red linear fits in **Figure 4.26** corresponds to the numerator and denominator, respectively, in the above equation. The effective mobility (μ_{eff}) could be calculated using the equation $\mu_{eff} = r_{sat} \times \mu_{eff}$. Due to our relatively large Vth, the reliability factors reach the highest values of 32-38%.

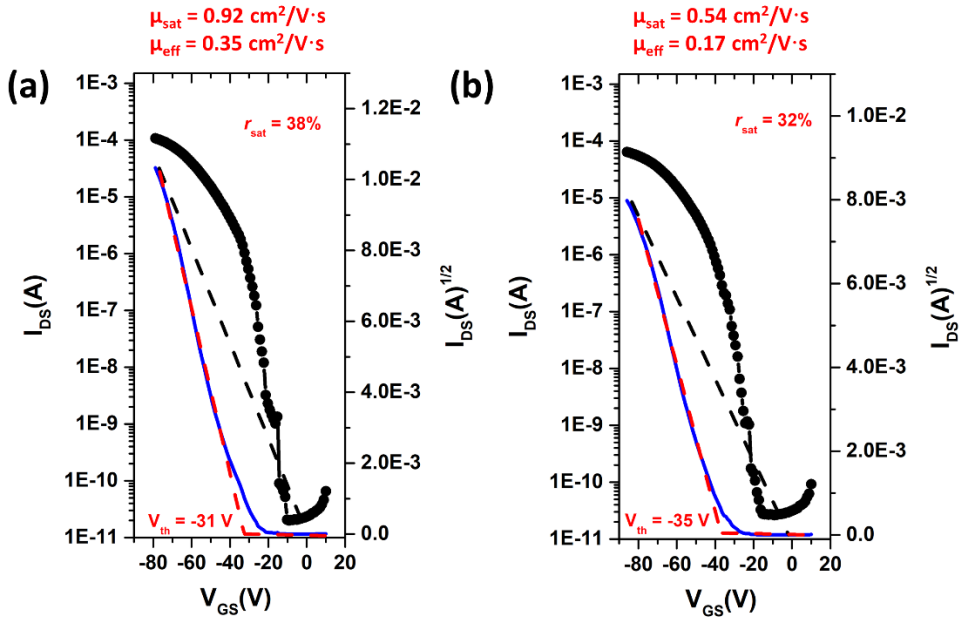

Figure 4.26 The reliability factors (r_{sat}'s) and the effective mobilities (μ_{eff}'s) calculated based on the transfer curves of the p^{++}-Si/SiO_2/PS-brush (M_n = 5 kDa)/***m*-C$_6$PhCO-BTBT**/Au OFET devices in which the semiconductor layer is spin-coated from 2-methyltetrahydrofuran (a) and ethyl acetate (b).

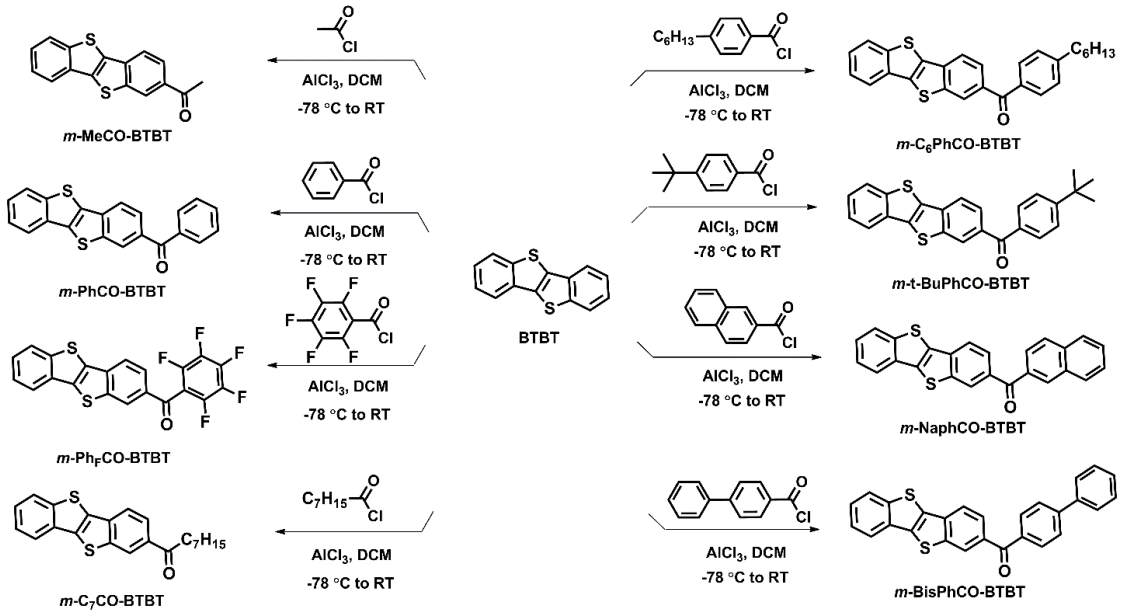

Scheme 1. Synthesis of mono-(aryl/alkyl)carbonyl functionalized semiconductors.

Table 4.6 Mono-(aryl/alkyl)carbonyl functionalized semiconductors, the reaction yields (for the final Friedel-Crafts acylation step), melting temperatures, and the solubilities in chloroform, ethyl acetate, and acetone solvents.

Semiconductor	Reaction Yield (%)	Melting Point (°C)	Solubility (in $CHCl_3$) (mg/mL)	Solubility (in Ethyl Acetate) (mg/mL)	Solubility (in Acetone) (mg/mL)
***m*-MeCO-BTBT**	65	222-223	22.5	2.47	2.43
***m*-PhCO-BTBT**	62	223-224	22.2	0.90	0.75
***m*-Ph_FCO-BTBT**	39	234-235	36.4	4.2	3.42
***m*-C_7CO-BTBT**	73	175-176	58.3	1.61	1.57
***m*-C_6PhCO-BTBT**	83	145-146	176.0	8.8	2.70
***m*-t-BuPhCO-BTBT**	29	224-225	31.3	2.21	1.56
***m*-NaphCO-BTBT**	56	216-217	16.3	1.47	1.43
***m*-BisPhCO-BTBT**	23	247-248	4.5	0.35	0.30

Synthesis of 1-(benzo[b]benzo[4,5]thieno[2,3-d]thiophen-2-yl)ethanone (*m*-MeCO-BTBT): $AlCl_3$ (0.31 g, 2.33 mmol) was added into a solution of [1]benzothieno[3,2-b][1]benzothiophene (0.56 g, 2.33 mmol) in anhydrous dichloromethane (50 mL) at −10 °C under nitrogen. The resulting solution was stirred at −10 °C for 30 min. Then, the reaction mixture was cooled down to −78 °C. Acetyl Chloride (0.18 g, 2.33 mmol) was subsequently added dropwise, and the mixture was stirred for 1 h at the same temperature. The reaction mixture was allowed to warm to room temperature and stirred for 2 days. After extraction with $CHCl_3$, organic layer was dried with Na_2SO_4, filtered and concentrated to obtain the crude product. The crude was then purified through column chromatography on silica gel using chloroform as mobile phase. After column, MeOH leaching was carried out to afford the final product as a white solid (427 mg, 65% yield). Melting point: 222-223 °C; ^{1}H NMR (400 MHz, $CDCl_3$), δ (ppm): 8.55 (s, 1H), 8.07 (d, 1H, J = 8.0 Hz), 8.05 (d, 3H, J = 8.0 Hz), 7.51-7.47 (t, 2H, J = 16.0 Hz),

2.73 (s, 3H); ^{13}C NMR (100 MHz, $CDCl_3$), δ (ppm): 197.1, 142.8, 142.2, 137.0, 136.4, 133.9, 132.9, 132.8, 125.9, 125.1, 124.9, 124.8, 124.2, 122.1, 121.5, 121.4, 26.7; MS (Mass Spec.) m/z calcd for $C_{16}H_{10}OS_2$: 282.02[M^+]; found: 282.487[M^+].

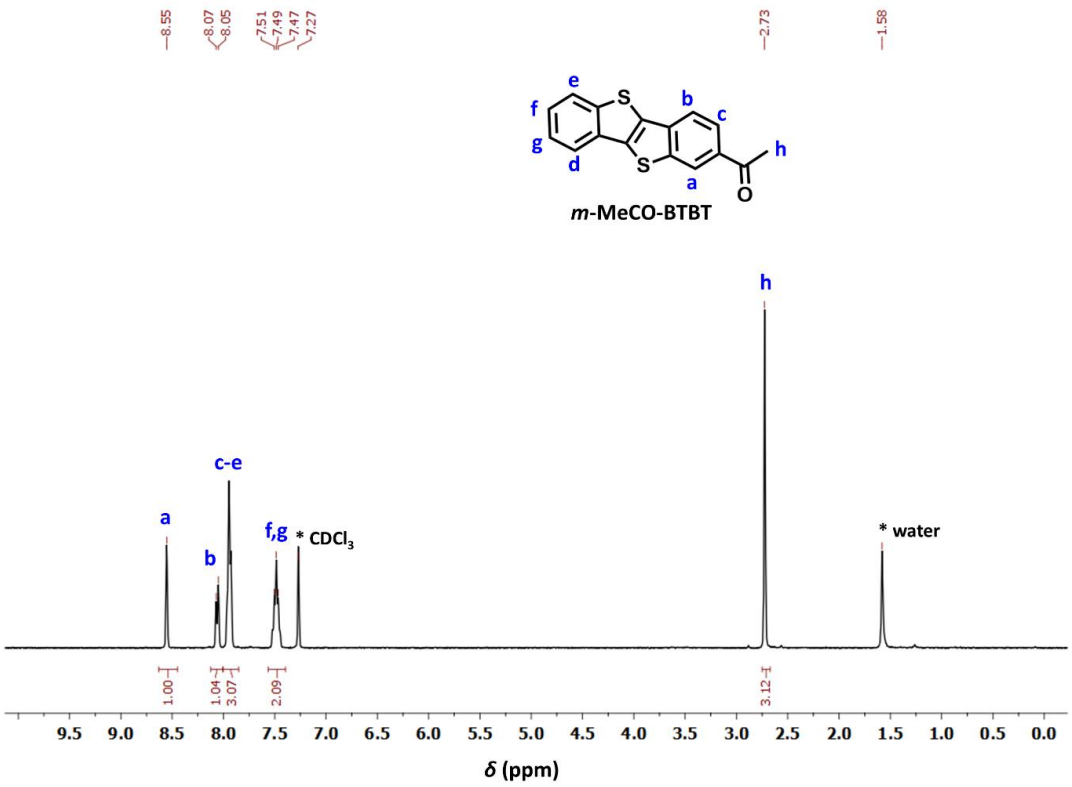

Figure 4.27 ^{1}H NMR spectrum of the molecule 1-(benzo[b]benzo[4,5]thieno[2,3-d]thiophen-2-yl)ethanone (***m*-MeCO-BTBT**) in $CDCl_3$ solvent recorded at room temperature. $CDCl_3$ and H_2O (water) peaks originating from the NMR solvent are marked with an asterisk.

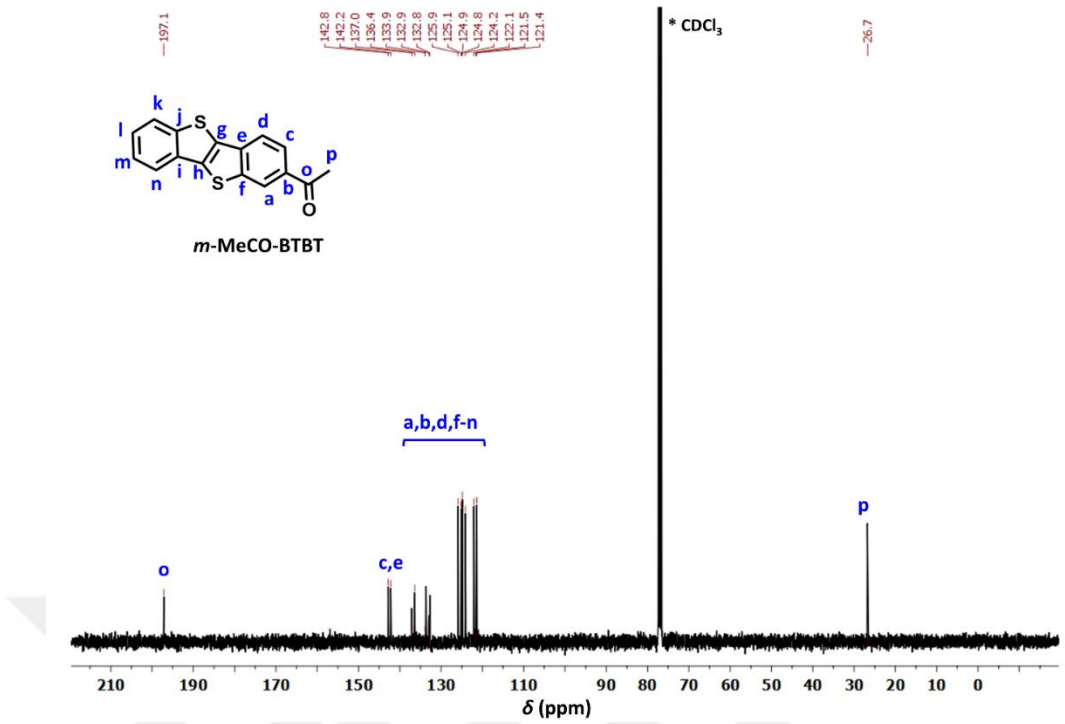

Figure 4.28 ^{13}C NMR spectrum of the molecule 1-(benzo[b]benzo[4,5]thieno[2,3-d]thiophen-2-yl)ethanone (***m*-MeCO-BTBT**) in $CDCl_3$ solvent recorded at room temperature. $CDCl_3$ peak originating from the NMR solvent is marked with an asterisk.

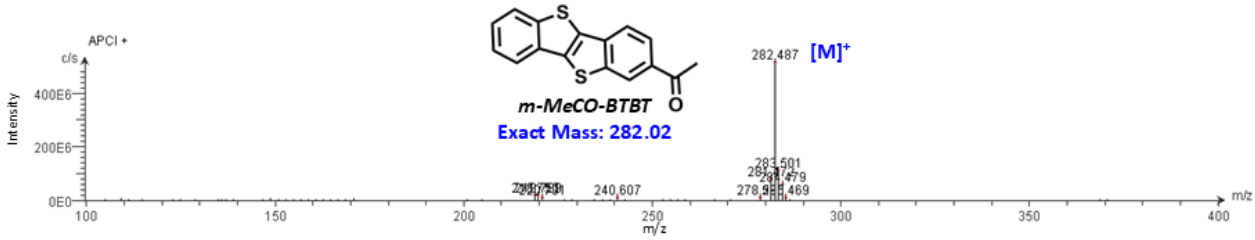

Figure 4.29 Positive ion mass spectrum of the molecule 1-(benzo[b]benzo[4,5]thieno[2,3-d]thiophen-2-yl)ethanone (***m*-MeCO-BTBT**) recorded by atmospheric pressure-chemical ionization method mass spectrometry (APCI-MS) (Advion Expression CMS-L).

Synthesis of benzo[b]benzo[4,5]thieno[2,3-d]thiophen-2yl(perfluorophenyl)methanone (*m*-Ph$_F$CO-BTBT): $AlCl_3$ (0.24 g, 1.83 mmol) was added into a solution of [1]benzothieno[3,2-b][1]benzothiophene (0.40 g, 1.66 mmol) in anhydrous dichloromethane (40 mL) at −10 °C under nitrogen. The resulting solution was stirred at −10 °C for 30 min. Then, the reaction mixture was cooled down to −78 °C. Perfluorobenzoyl Chloride (0.42 g, 1.83 mmol) was subsequently added dropwise, and the mixture was stirred for 1 h at the same temperature. The reaction mixture was allowed to warm to room temperature and stirred for 2 days. After extraction with

$CHCl_3$, organic layer was dried with Na_2SO_4, filtered and concentrated to obtain the crude product. The crude was then purified through column chromatography on silica gel using chloroform:hexane (1:1) as mobile phase. After column, MeOH leaching was carried out to afford the final product as a pale yellow solid (280 mg, 39% yield). Melting point: 234-235 °C; ^{1}H NMR (400 MHz, $CDCl_3$), δ (ppm): 8.41 (s, 1H), 7.98-7.97 (m, 4H), 7.51 (m, 2H); ^{13}C NMR (100 MHz, $CDCl_3$), δ (ppm): 184.1, 143.2, 142.4, 138.6, 137.8, 133.0, 132.5, 132.4, 126.6, 126.4, 126.0, 125.8, 125.3, 124.2, 122.3, 121.9; MS (Mass Spec.) m/z calcd for $C_{21}H_7F_5OS_2$: 433.99[M^+]; found: 434.568[M^+].

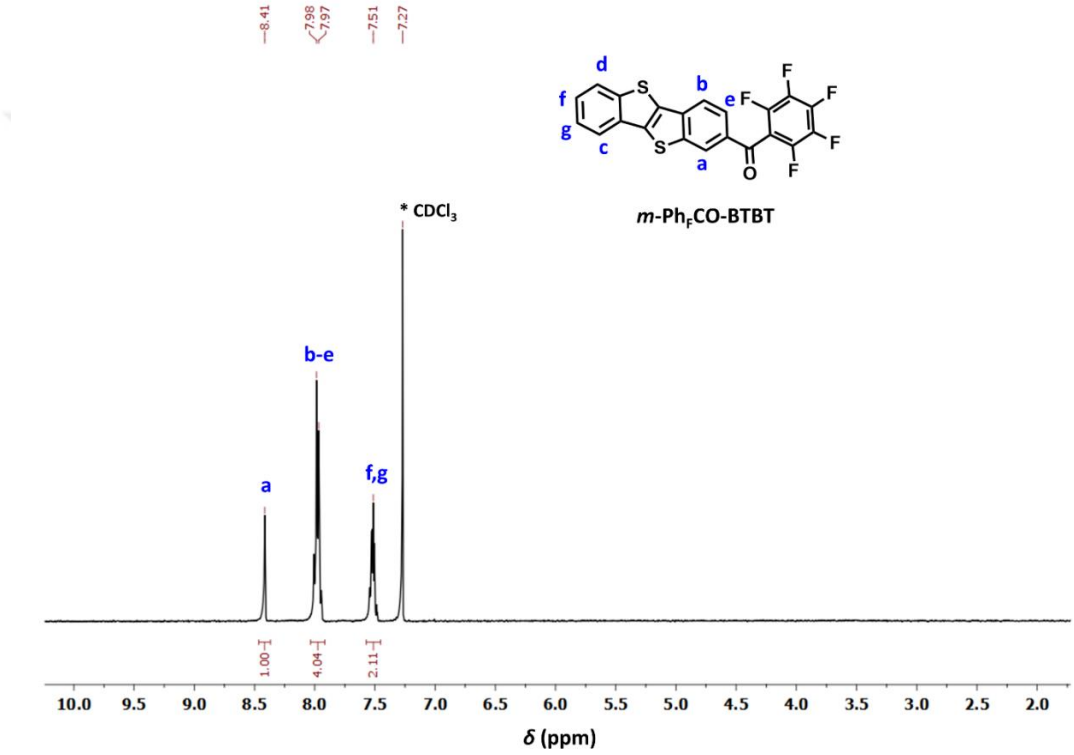

Figure 4.30 ^{1}H NMR spectrum of the molecule benzo[b]benzo[4,5]thieno[2,3-d]thiophen-2 yl(perfluorophenyl)methanone (***m*-Ph$_F$CO-BTBT**) in $CDCl_3$ solvent recorded at room temperature. $CDCl_3$ peak originating from the NMR solvent is marked with an asterisk.

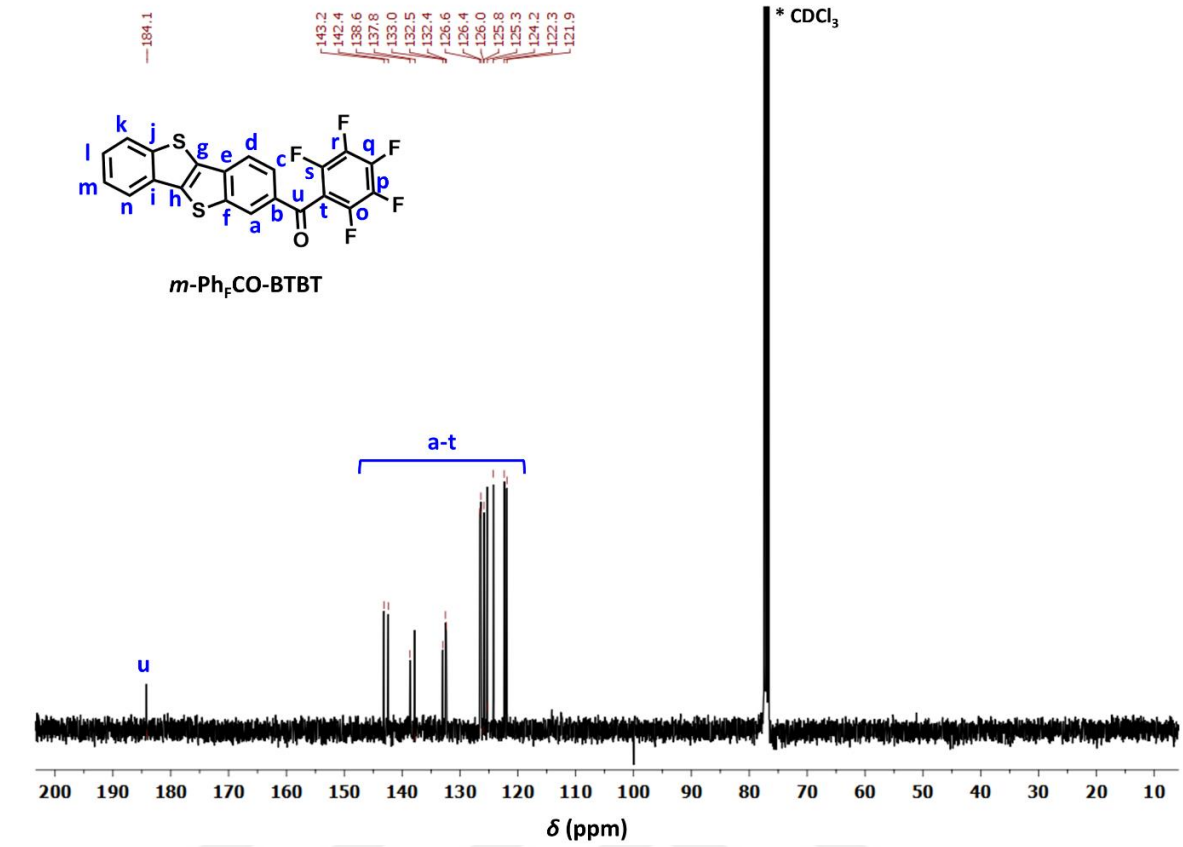

Figure 4.31 ^{13}C NMR spectrum of the molecule benzo[b]benzo[4,5]thieno[2,3-d]thiophen-2 yl(perfluorophenyl)methanone (***m*-Ph$_F$CO-BTBT**) in $CDCl_3$ solvent recorded at room temperature. $CDCl_3$ peak originating from the NMR solvent is marked with an asterisk.

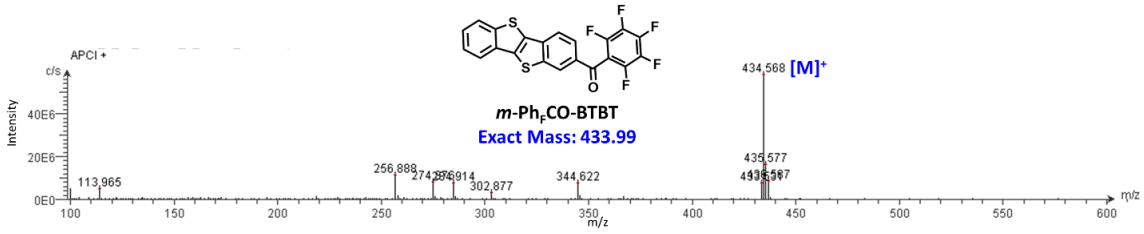

Figure 4.32 Positive ion mass spectrum of the molecule benzo[b]benzo[4,5]thieno[2,3-d]thiophen-2 yl(perfluorophenyl)methanone (***m*-Ph$_F$CO-BTBT**) recorded by atmospheric pressure-chemical ionization method mass spectrometry (APCI-MS) (Advion Expression CMS-L).

Synthesis of benzo[b]benzo[4,5]thieno[2,3-d]thiophen-2-yl(4-(tert-butyl)phenyl)methanone (*m*-t-BuPhCO-BTBT): $AlCl_3$ (0.167 g, 1.25 mmol) was added into a solution of [1]benzothieno[3,2-b][1]benzothiophene (0.25 g, 1.04 mmol) in anhydrous dichloromethane (40 mL) at −10 °C under nitrogen. The resulting solution was stirred at −10 °C for 30 min. Then, the reaction mixture was cooled down to −78

°C. 4-(tert-Butyl)benzoyl chloride (1.02 g, 5.18 mmol) was subsequently added dropwise, and the mixture was stirred for 1 h at the same temperature. The reaction mixture was allowed to warm to room temperature and stirred for 2 days. After extraction with $CHCl_3$, organic layer was dried with Na_2SO_4, filtered and concentrated to obtain the crude product. The crude was then purified through column chromatography on silica gel using chloroform as mobile phase and after column, MeOH leaching was carried out to afford the final product as a white solid (120 mg, 29% yield). Melting point: 224-225 °C; ^{1}H NMR (400 MHz, $CDCl_3$), δ (ppm): 8.42 (s, 1H), 7.98 (m, 4H), 7.97-7.95 (d, 2H, J = 12.0 Hz), 7.57-7.55 (m, 2H), 7.50 (m, 2H, J = 8.0 Hz), 1.41 (m, 9H), ; ^{13}C NMR (100 MHz, $CDCl_3$), δ (ppm): 195.6, 156.2, 142.8, 141.8, 136.7, 135.9, 135.0, 134.3, 133.0, 132.8, 130.1, 126.7, 126.6, 125.8, 125.1, 124.1, 122.0, 121.2, 35.1, 31.1; MS (Mass Spec.) m/z calcd for $C_{25}H_{20}OS_2$: 400.10[M^+]; found: 400.824[M^+].

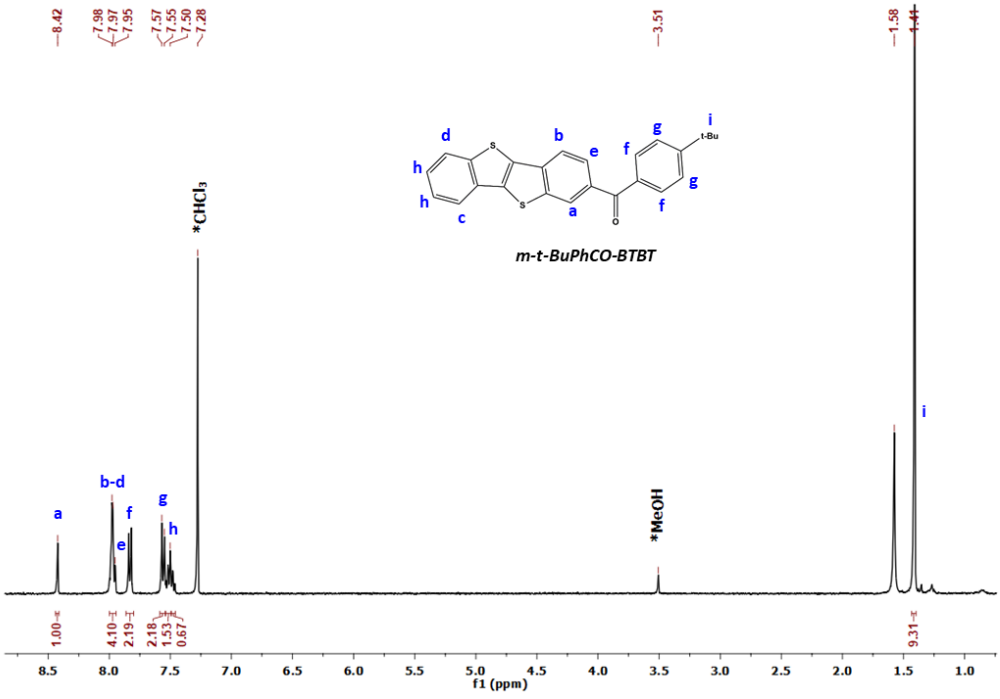

Figure 4.33 ^{1}H NMR spectrum of the molecule benzo[b]benzo[4,5]thieno[2,3-d]thiophen-2-yl(4-(tert-butyl)phenyl)methanone (***m*-t-BuPhCO-BTBT**) in $CDCl_3$ solvent recorded at room temperature. $CDCl_3$ and MeOH peaks originating from the NMR solvent are marked with an asterisk.

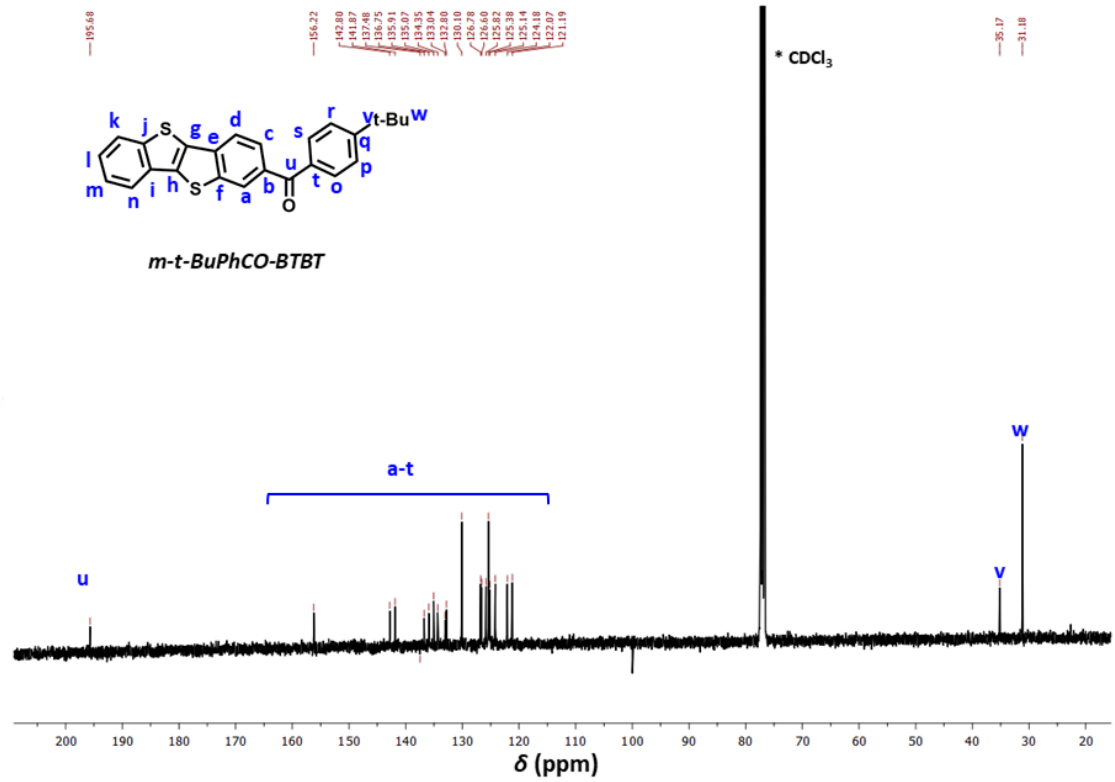

Figure 4.34 ^{13}C NMR spectrum of the molecule benzo[b]benzo[4,5]thieno[2,3-d]thiophen-2-yl(4-(tert-butyl)phenyl)methanone (***m*-t-BuPhCO-BTBT**) in $CDCl_3$ solvent recorded at room temperature. $CDCl_3$ peak originating from the NMR solvent is marked with an asterisk.

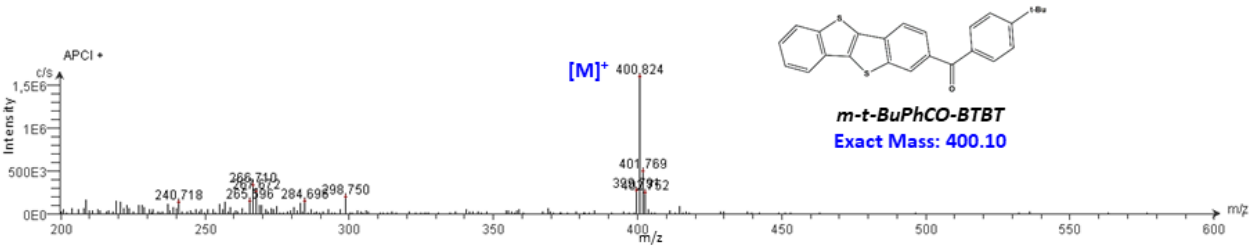

Figure 4.35 Positive ion mass spectrum of the molecule benzo[b]benzo[4,5]thieno[2,3-d]thiophen-2-yl(4-(tert-butyl)phenyl)methanone (***m*-t-BuPhCO-BTBT**) recorded by atmospheric pressure-chemical ionization method mass spectrometry (APCI-MS) (Advion Expression CMS-L).

Synthesis of benzo[b]benzo[4,5]thieno[2,3-d]thiophen-2-yl(naphthalen-2-yl)methanone (*m*-NaphCO-BTBT): $AlCl_3$ (0.167 g, 1.25 mmol) was added into a solution of [1]benzothieno[3,2-b][1]benzothiophene (0.250 g, 1.04 mmol) in anhydrous dichloromethane (40 mL) at −10 °C under nitrogen. The resulting solution was stirred at −10 °C for 30 min. Then, the reaction mixture was cooled down to −78 °C. 2-Naphthoyl chloride (0.991 g, 5.2 mmol) was subsequently added dropwise, and the mixture was stirred for 1 h at the same temperature. The reaction mixture was allowed to warm to room temperature and stirred for 2 days. After extraction with $CHCl_3$, organic layer dried with Na_2SO_4, filtered and concentrated to obtain the crude product. The crude was then purified through column chromatography on silica gel using chloroform:hexane (2:1) as mobile phase and after column, MeOH leaching was carried out to afford the final product as a white solid (230 mg, 56% yield). Melting point: 216-217 °C; ^{1}H NMR (400 MHz, $CDCl_3$), δ (ppm): 8.48 (s, 1H), 8.34 (s, 1H), 8.02 (m, 7H), 7.75 (m, 3H, J = 12.0 Hz), 7.51 (m, 2H); ^{13}C NMR (100 MHz, $CDCl_3$), δ (ppm): 142.8, 142.0, 136.0, 135.2, 135.1, 134.3, 132.7, 132.3, 131.6, 129.4, 128.4, 127.8, 126.9, 126.7, 125.8, 125.1, 124.2, 122.1, 121.2; MS (Mass Spec.) m/z calcd for $C_{25}H_{14}OS_2$: 394.05[M^+]; found: 395.017[M^+].

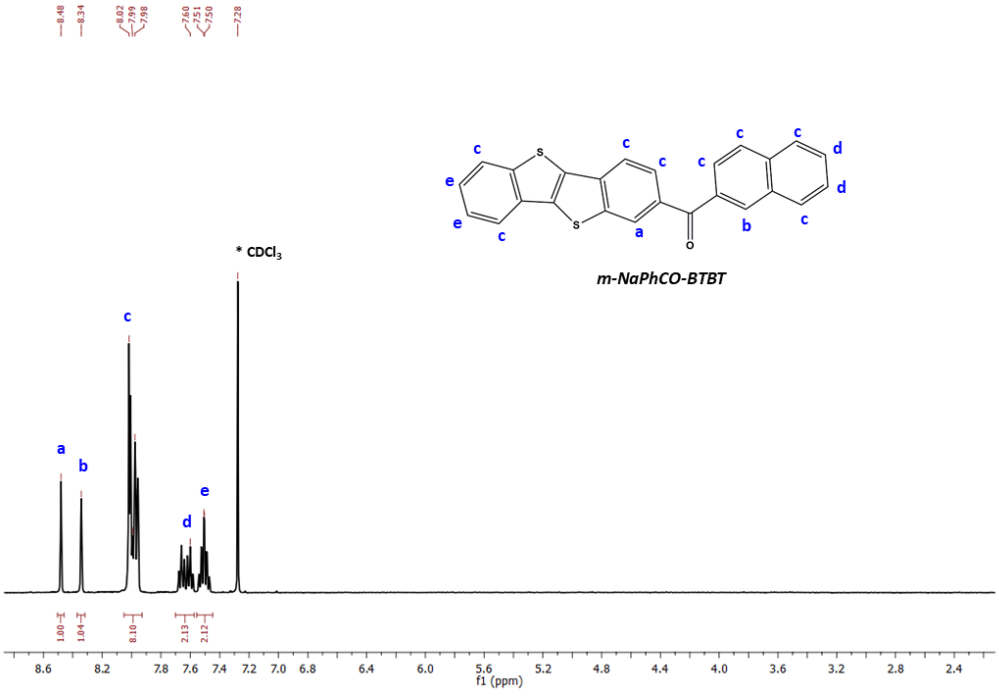

Figure 4.36 ^{1}H NMR spectrum of the molecule benzo[b]benzo[4,5]thieno[2,3-d]thiophen-2-yl(naphthalen-2-yl)methanone (***m*-NaphCO-BTBT**) in $CDCl_3$ solvent recorded at room temperature. $CDCl_3$ peak originating from the NMR solvent is marked with an asterisk.

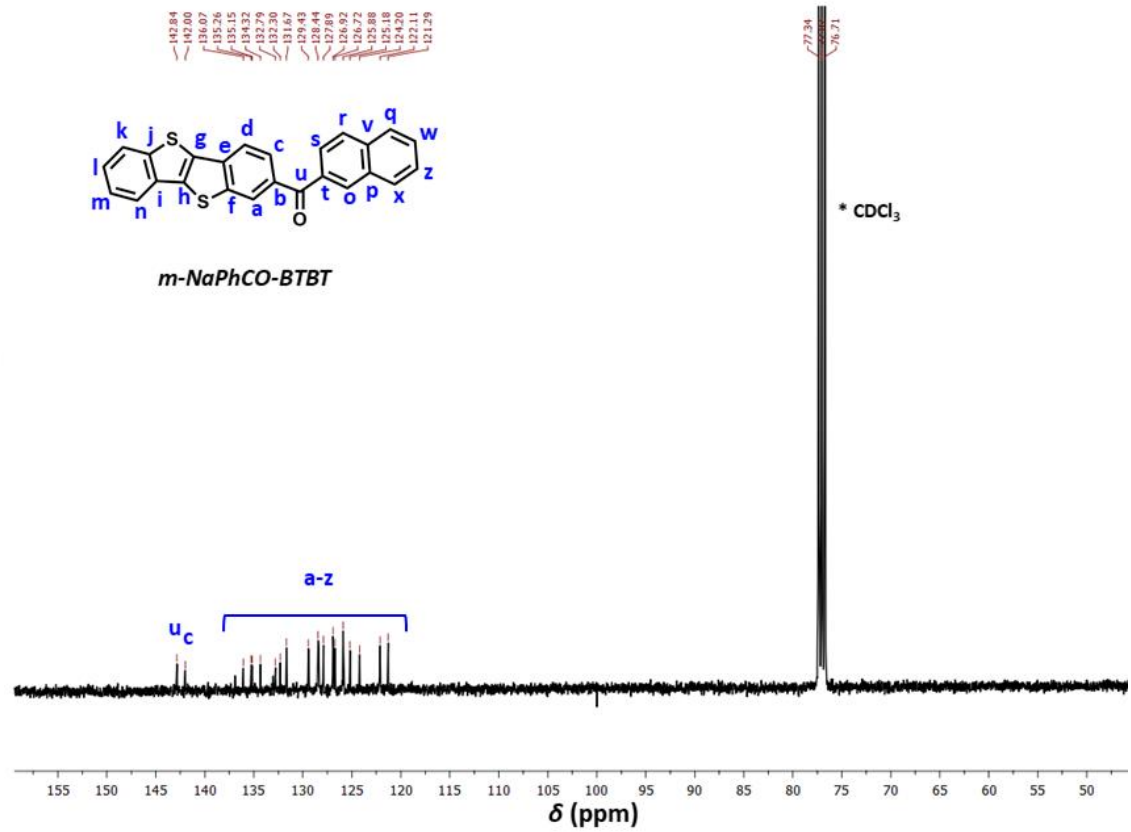

Figure 4.37 ^{13}C NMR spectrum of the molecule benzo[b]benzo[4,5]thieno[2,3-d]thiophen-2-yl(naphthalen-2-yl)methanone (***m*-NaphCO-BTBT**) in $CDCl_3$ solvent recorded at room temperature. $CDCl_3$ peak originating from the NMR solvent i marked with an asterisk.

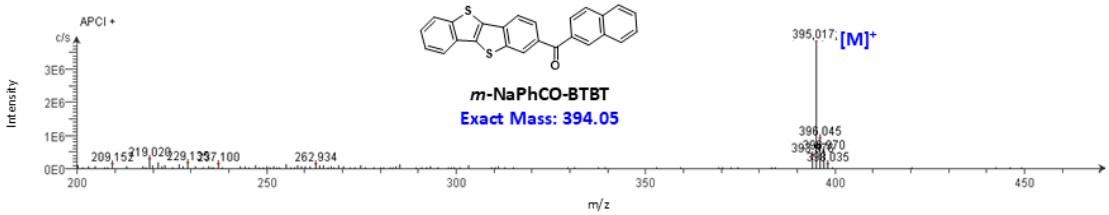

Figure 4.38 Positive ion mass spectrum of the molecule benzo[b]benzo[4,5]thieno[2,3-d]thiophen-2-yl(naphthalen-2-yl)methanone (***m*-NaphCO-BTBT**) recorded by atmospheric pressure-chemical ionization method mass spectrometry (APCI-MS) (Advion Expression CMS-L).

Synthesis of [1,1'-biphenyl]-4-yl(benzo[b]benzo[4,5]thieno[2,3-d]thiophen-2-yl)methanone (*m*-BisPhCO-BTBT): $AlCl_3$ (0.167 g, 1.25 mmol) was added into a solution of [1]benzothieno[3,2-b][1]benzothiophene (0.250 g, 1.04 mmol) in anhydrous dichloromethane (40 mL) at −10 °C under nitrogen. The resulting solution was stirred at −10 °C for 30 min. Then, the reaction mixture was cooled down to −78 °C. Biphenyl-4-carbonyl chloride (1.13 g, 5.2 mmol) was subsequently added dropwise, and the mixture was stirred for 1 h at the same temperature. The reaction mixture was allowed to warm to room temperature and stirred for 2 days. After extraction with $CHCl_3$, organic layer was dried with Na_2SO_4, filtered and concentrated to obtain the crude product. The crude was then purified through column chromatography on silica gel using chloroform:hexane (2:1) as mobile phase and after column, MeOH leaching was carried out to afford the final product as a white solid (100 mg, 23% yield). Melting point: 247-248 °C; ^{1}H NMR (400 MHz, $CDCl_3$), δ (ppm): 8.46 (s, 1H), 8.00-7.97 (m, 6H), 7.78 (d, 2H, J = 12.0 Hz), 7.71 (d, 2H), 7.52-7.74 (m, 5H); ^{13}C NMR (100 MHz, $CDCl_3$), δ (ppm): 195.5, 145.2, 142.8, 141.9, 139.9, 136.9, 136.5, 136.0, 134.1, 133.0, 132.7, 130.7, 129.0, 128.2, 127.3, 126.7, 126.6, 125.8, 125.1, 124.2, 122.1, 121.2; MS (Mass Spec.) m/z calcd for $C_{27}H_{16}OS_2$: 420.06[M^+]; found: 420.731[M^+].

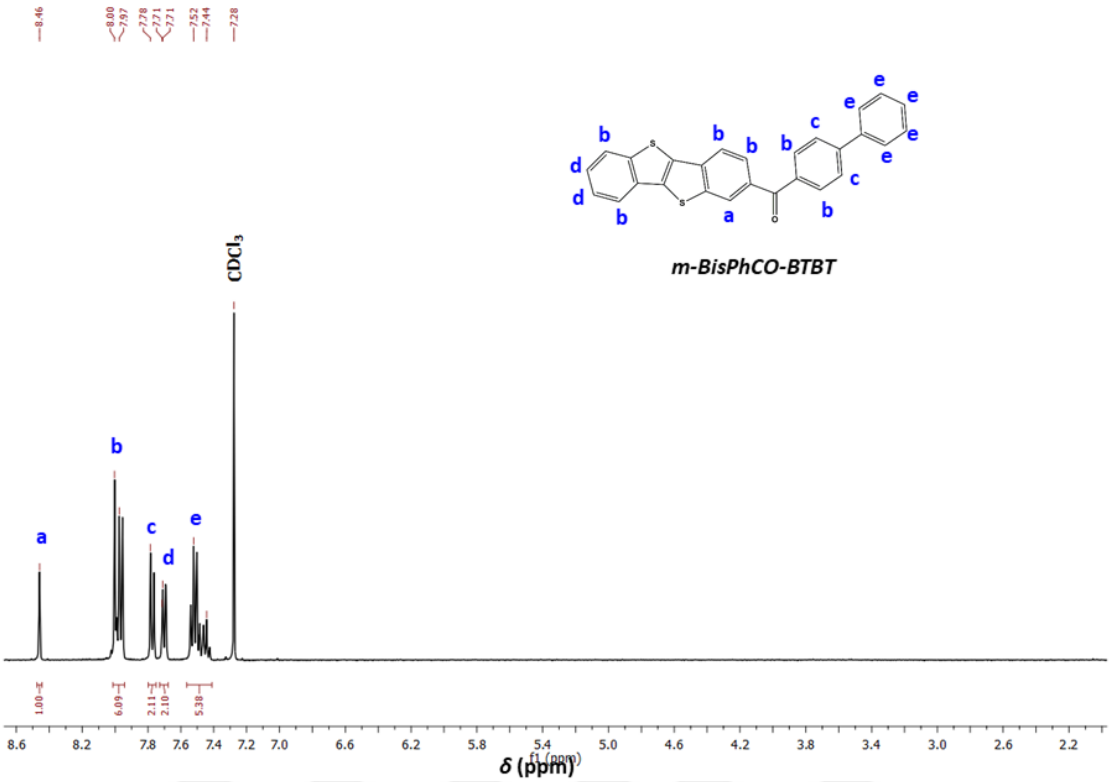

Figure 4.39 ^{1}H NMR spectrum of the molecule [1,1'-biphenyl]-4-yl(benzo[b]benzo[4,5]thieno[2,3-d]thiophen-2-yl)methanone (***m*-BisPhCO-BTBT**) in $CDCl_3$ solvent recorded at room temperature. $CDCl_3$ peak originating from the NMR solvent is marked with an asterisk.

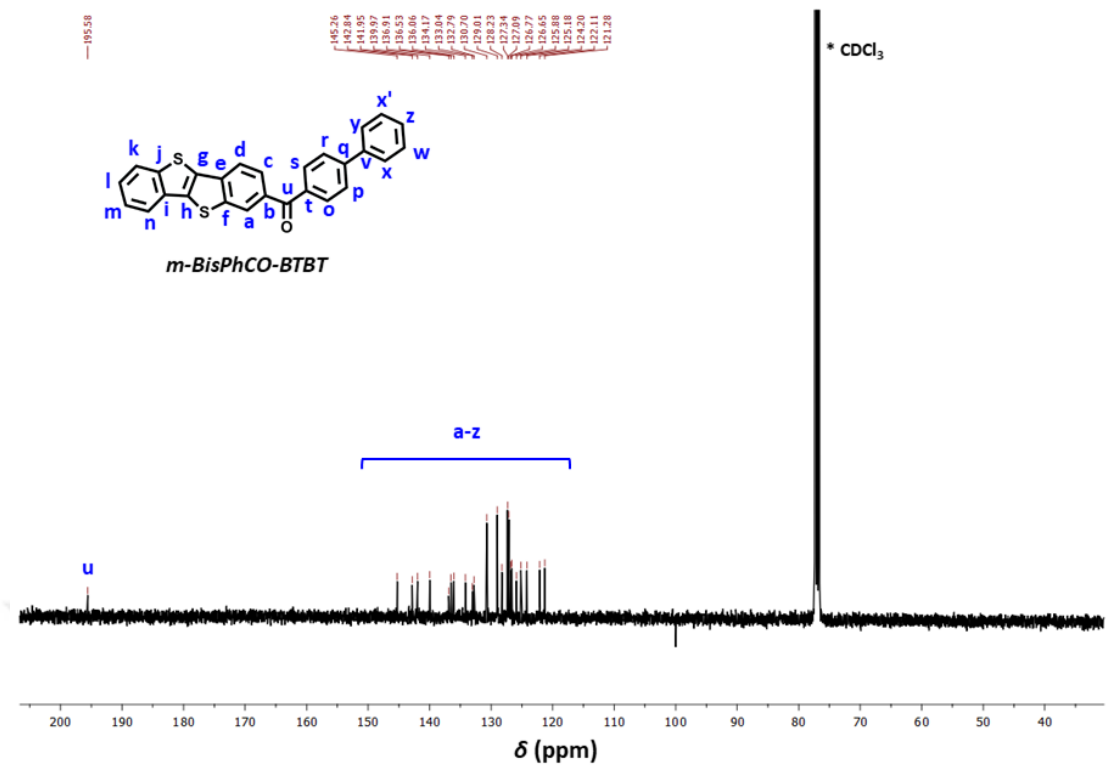

Figure 4.40 ^{13}C NMR spectrum of the molecule [1,1'-biphenyl]-4-yl(benzo[b]benzo[4,5]thieno[2,3-d]thiophen-2-yl)methanone (***m*-BisPhCO-BTBT**) in $CDCl_3$ solvent recorded at room temperature. $CDCl_3$ peak originating from the NMR solvent is marked with an asterisk.

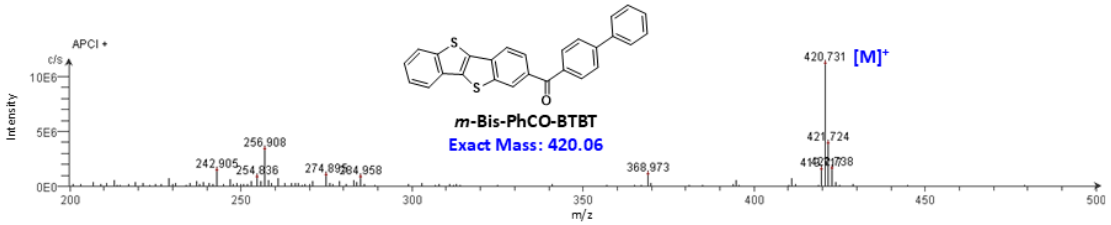

Figure 4.41 Positive ion mass spectrum of the molecule [1,1'-biphenyl]-4-yl(benzo[b]benzo[4,5]thieno[2,3-d]thiophen-2-yl)methanone (***m*-BisPhCO-BTBT**) recorded by atmospheric pressure-chemical ionization method mass spectrometry (APCI-MS) (Advion Expression CMS-L).

4.4 Conclusion

In summary, we have developed a novel asymmetric mono-(aryl)carbonyl functionalization approach for the synthesis of a new highly soluble [1]benzothieno[3,2-*b*][1]benzothiophene (BTBT) semiconductor, ***m*-C$_6$PhCO-BTBT**. The new asymmetric molecule was produced in gram-scale through a two-step transition-metal-free synthesis, and the detailed structural, physicochemical, and (opto)electronic characterizations were performed. Significant structure-molecular properties-charge-transport relationships are established for the first time in a DAcTTs with regards to mono-functionalization. An asymmetric π-electronic structure was obtained with a ground state molecular dipole moment (μ_g) of 3.17 D and a large excited state dipole moment (μ_e) of 12.69 D. Additionally, the asymmetric π-backbone demonstrates a significant degree of polarizability. The frontier orbitals were stabilized by 0.29-0.65 eV in comparison to the parent BTBT π-system. Hansen Solubility Parameters (HSP) analysis, coupled with thermodynamic data from differential scanning calorimetry (DSC), was utilized to investigate the solubility characteristics of the new molecule and to reveal distinctive relationships between structure, solubility, and cohesive energetics. Additionally, two other novel molecules, ***m*-PhCO-BTBT** and ***m*-C$_7$CO-BTBT**, were synthesized and employed as reference compounds, alongside structurally related BTBT semiconductors from previous literature studies. The new π-electronic structure exhibits an outstanding solubility performance in various organic solvents, including a number of eco-friendly green solvents. Most importantly, ***m*-C$_6$PhCO-BTBT** exhibits an instant dissolution behavior at room temperature in chloroform, displaying a record high room temperature solubility of 176.0 mg·mL^{-1} (0.41 M). To the best of our knowledge, this is the highest solubility ever reported for a high-performance organic semiconductor. The structure of ***m*-C$_6$PhCO-BTBT**, with mono-(*n*-alkyl-aryl)carbonyl functionalization, provides a unique molecular architecture for developing stronger interactions with solvent molecules. The HSPs for ***m*-C$_6$PhCO-BTBT** were determined to be δ_D = 18.9 MPa$^{1/2}$, δ_P = 5.7 MPa$^{1/2}$, and δ_H = 5.8 MPa$^{1/2}$ with an interaction radius (R_0) of 8.0 MPa$^{1/2}$. Strong thermodynamic correlations of the molecular solubility with thermal properties are established for the first time in the literature. The significant solubility of the new molecule enabled the preparation of semiconductor solutions (solubility up to ~12.5 mg·mL^{-1} at room temperature) in eco-

friendly green solvents of 2-methyltetrahydrofuran, ethyl acetate, ethoxybenzene, acetone, and ethanol. To the best of our knowledge, these solvents have never been employed in the processing of a BTBT-based semiconductor, and have hardly been used in small molecular semiconductor processing in general. Top-contact/bottom-gate (TC/BG) OFETs were fabricated by solution processing of ***m*-C$_6$PhCO-BTBT** in these five green solvents. The maximum saturation hole mobilities were achieved for thin-films spin-coated from 2-methyltetrahydrofuran (μ_h^{max} = 1.87 cm^2/V·s, μ_h^{avg} = 1.21 cm^2/V·s (I_{on}/I_{off} = 10^7-10^8)) and ethyl acetate (μ_h^{max} = 0.62 cm^2/V·s, μ_h^{avg} = 0.41 cm^2/V·s (I_{on}/I_{off} = 10^6-10^7)) solutions. Relatively lower μ_h's of 0.07-0.11 cm^2/V·s (I_{on}/I_{off} = 10^5-10^6) were realized for spin-coated thin-films from acetone and ethoxybenzene, while drop-casted thin-films from ethanol yielded μ_h's of ~ 0.001 cm^2/V·s ($I_{on}/I_{off} \approx 10^4$). ***m*-C$_6$PhCO-BTBT** has now become a rare example of a high-mobility *p*-type semiconductor with a deep HOMO level of -6.04 eV. The solute-green solvent interaction distances were revealed to play a key role in determining the microstructural and morphological properties of the thin-films. We note that expanding the processing strategies by including additional green solvents, optimizing film-deposition/thermal-annealing conditions (e.g., optimizing viscosity, surface tension, and solvent evaporation rate), and introducing solvent vapor treatment could further increase the hole mobility from these green solvents. The good solubility of the present semiconductor in polar solvents (e.g., ethanol, ethyl acetate, and acetone) that are typically orthogonal to most π-conjugated materials, when combined with its widely separated HOMO-LUMO energetics, wide optical band gap, and efficient hole transport ability, makes this molecular π-framework highly attractive as solution-processable hole-transport/electron-blocking or host material for use in multilayer optoelectronic devices.[212], [213], [214] Our findings in this study demonstrated that mono-(aryl)carbonyl functionalization on the BTBT π-core is a viable approach to realize high solubility, green-solvent processability, and high semiconductor performance. We envision that our current viable *mono*-(aryl)carbonyl functionalization approach may give new semiconductor design perspectives for future solubility approaches and green solvent processing in organic semiconductors. It could be extended to other instrinsically insoluble DAcTTs and (hetero)acenes (e.g., DNTT and pentance). This study provides key information and unique insights into the design and development of green solvent-processable π-conjugated molecules, and could open new directions in the

field of green-optoelectronics, biosensors, and bioelectronics. Given that further green solvent-based processing and molecular engineering optimizations could be employed in this new molecular architecture, it is very reasonable to expect that much higher hole mobilities and novel physicochemical/optoelectronic properties could be achieved in green-optoelectronics. Further studies on ***m*-C$_6$PhCO-BTBT**-based green-OFET device fabrications and molecular engineering on this π-architecture by tailoring alkyl/aryl units are currently underway in our laboratory.

Chapter 5

Conclusions and Future Prospects

5.1 Conclusions

As clearly summarized in the first chapter, molecular engineering via functionalization has been a great tool to tune noncovalent intermolecular interactions. Herein, we demonstrate three-dimensional highly crystalline nanostructured **D(C_7CO)-BTBT** films via carbonyl-functionalization of a fused thienoacene π-system, and strong Raman signal enhancements in Surface-Enhanced Raman Spectroscopy (SERS) are realized. The small molecule could be prepared on the gram scale with a facile synthesis-purification. In the engineered films, polar functionalization induces favorable out-of-plane crystal growth via zigzag motif of dipolar C=O···C=O interactions and hydrogen bonds, and strengthens π-interactions. A unique two-stage film growth behavior is identified with an edge-on-to-face-on molecular orientation transition driven by hydrophobicity. The analysis of the electronic structures and the ratio of the anti-Stokes/Stokes SERS signals suggests that the π-extended/stabilized LUMOs with varied crystalline face-on orientations provide the key properties in the chemical enhancement mechanism. A molecule-specific Raman signal enhancement is also demonstrated on a high-LUMO organic platform. Our results demonstrate a promising guidance towards realizing low-cost SERS-active semiconducting materials, increasing structural

versatility of organic-SERS platforms, and advancing molecule-specific sensing via molecular engineering.

The adoption of green solvents is of utmost importance for the solution-based fabrication of semiconductor thin-films and for the commercialization of (opto)electronic devices, especially in response to evolving regulatory mandates for handling organic materials. Despite increasing interest in this area, the scarcity of green solvent-processed *n*-channel OFETs, especially functioning in ambient conditions, highlights the need for further research. In this study, we demonstrated the Hansen solubility approach to study the solubility behavior of an ambient-stable *n*-type semiconductor, 2,2'-(2,8-bis(3-dodecylthiophen-2-yl)indeno[1,2-b]fluorene-6,12-diylidene)dimalononitrile (**β,β'-C$_{12}$-TIFDMT**), and to analyze potential green solvents for thin-film processing. The Hansen solubility parameters were determined to be δ_D = 20.8 MPa$^{1/2}$, δ_P = 5.8 MPa$^{1/2}$, δ_H = 5.5 MPa$^{1/2}$ with a radius (R_0) of 8.3 MPa$^{1/2}$. A green solvent screening analysis based on minimal distance constraint and quantitative sustainability score identified ethoxybenzene, anisole, 2-methylanisole, and 2-methyltetrahydrofuran as suitable green solvents (R_a's = 5.17-7.93 MPa$^{1/2}$ < R_0). A strong thermodynamic correlation was identified between the solubility and the semiconductor-solvent distance in the 3D Hansen solubility space, in which the maximum solubility limit could be estimated with the semiconductor's enthalpy of fusion (ΔH_{fus}) and melting temperature (T_{mp}). To the best of our knowledge, this relationship between maximum solubility limit and thermal properties is being established for the first time for an organic semiconductor. Bottom-gate/top-contact OFETs fabricated by spin-coating the semiconductor green solutions exhibited μ_e's reaching to ~0.2 cm^2/V·s (I_{on}/I_{off} ~ 10^6-10^7 and V_{on} ~ 0-5 V) in ambient. This device performance, to our knowledge, is the highest reported for an ambient-stable green solvent-processed *n*-channel OFET. Our HSP-based rational approach and unique findings presented in this study can shed a critical light on how green solvents can be efficiently incorporated in solution processing in organic (opto)electronics, and whether ambient-stable *n*-type semiconductors can continue to play an important role in green-OFETs.

Our findings demonstrate that mono-(aryl)carbonyl functionalization along with a medium-length alkyl chain (-n-C_6H_{13}) is a very effective strategy to solubilize the BTBT π-framework, which is attributed to the formation a molecular dipole (μg = 3.17

D) and twisted carbonyl/aryl units. Our findings demonstrated that mono-carbonyl functionalization could be an effective strategy to solubilize BTBT-based molecular semiconductors, increase hole mobility, and fine tune HOMO energy level. To the best of our knowledge, C_6-PhCO-BTBT is the only known example of a mono-carbonyl functionalized BTBT semiconductor reported to date and a rare example of an efficient p-type semiconductor (μh > 0.1-0.2 cm2/V·s) having a deep HOMO energy level (-6 eV). Future molecular design efforts, such as alkyl-chain and aryl unit engineering, could further tune physicochemical/optoelectronic properties of the mono-functionalized BTBTs and may open up new avenues in varied (opto)electronic applications. Based on the promising results achieved with C_6-PhCO-BTBT, our findings in this study clearly demonstrate the remarkable potential of mono-carbonyl functionalization strategy in BTBT-based semiconducting π-systems for highly soluble good mobility p-type semiconductors. Critical structure-molecular properties-charge-transport relationships are established in this study with regards to mono-functionalization of the BTBT π-core. to guide future designs on BTBTs and related diacene-fused thienothiophenes (DAcTTs). To this best of our knowledge, this is the highest solubility value reported to date for a BTBT semiconductor. On the basis of these comparative solubility analysis, the observed large solubility for C_6-PhCO-BTBT originates from the mono-(aryl)carbonyl functionalization yielding an asymmetricπ-electronic structure and the presence of "p-alkyl-aryl" substituent adjacent to the carbonyl functionality has an important contribution. As compared with previously reported mono-/di-substituted unfunctionalized BTBT semiconductors, the resulting asymmetricπ-electronic structure with an electron withdrawing (aryl)carbonyl unit yielded a relatively large molecular polarizability and dipole (μg = 3.17 D), which significantly enhanced the solubility of the new molecule in organic solvents via effective dispersion and dipolar interactions. The two-step transition-metal-free synthesis of C_6-PhCO-BTBT in a good yield, combined with its impressive solubility – especially in green solvents– makes this molecular architecture and mono-(aryl)carbonyl functionalization a highly viable approach for the development of industrially relevant organic semiconductors.

5.2 Societal Impact and Contribution to Global Sustainability

Since the 1950s, scientific research and technological advancements in the fields of micro- and opto-electronics have rapidly progressed. Consequently, semiconductor-based devices such as thin-film/field-effect transistors (FETs/TFTs), photovoltaics (PVs), and light-emitting diodes (LEDs) have become integral components in numerous technological applications. The primary motivation in this field is to utilize carbon-based organic semiconductors instead of traditional inorganic semiconductors (such as Si, Ge, and GaAs) to create cost-effective, flexible (compatible with plastic substrates), and lightweight (opto)electronic devices. Organic semiconductors offer a much richer synthetic chemistry than conventional elemental semiconductors and do not require expensive micro-fabrication techniques. As a result, numerous π-conjugated small molecular and polymeric semiconductors have been developed to date.

The increased structural diversity of organic semiconductors significantly enhances their applicability across various fields beyond traditional optoelectronics. This diversity contributes to improved device performances and its relevance to a broader range of applications, including biological sensors and spectroscopic applications. Biological Sensor Devices, sensitivity and Selectivity, organic semiconductors can be engineered to have specific interactions with biological molecules, leading to highly sensitive and selective biosensors. For instance, organic field-effect transistors (OFETs) can be functionalized with biological recognition elements (e.g., antibodies, enzymes) to detect specific analytes. Flexibility and Biocompatibility, the inherent flexibility and potential biocompatibility of organic semiconductors make them ideal for wearable and implantable sensors. These sensors can monitor physiological parameters in real-time, providing valuable data for healthcare applications. Low-Cost and Disposable, organic semiconductors enable the production of low-cost, disposable sensors. This is particularly useful in medical diagnostics, where single-use sensors can prevent cross-contamination and ensure

accurate readings. Tunable Optical Properties, the ability to tailor the optical properties of organic semiconductors through chemical modifications allows for the design of materials with specific absorption and emission wavelengths. This tunability is crucial for applications in spectroscopy, where precise control over light-matter interactions is required. Light Harvesting and Detection, organic semiconductors can be used in photodetectors and light-harvesting systems. Their ability to absorb light over a broad spectrum makes them suitable for applications ranging from environmental monitoring to advanced imaging techniques. Raman and Fluorescence Spectroscopy, organic semiconductors can enhance the performance of Raman and fluorescence spectroscopy by providing strong, tunable signals. These techniques are widely used in chemical analysis, materials science, and biological research.

The structural diversity of organic semiconductors directly contributes to improved device performance through several mechanisms: Optimized Electronic Properties, by varying the molecular structure, researchers can optimize the HOMO-LUMO gap, charge mobility, and stability of the organic semiconductor. This optimization leads to better performance in electronic devices such as transistors, solar cells, and LEDs. Tailored Intermolecular Interactions, the ability to fine-tune intermolecular interactions through structural modifications allows for the design of materials with enhanced charge transport properties. Proper stacking arrangements and π-π interactions are crucial for high-performance organic electronics. Versatile Processing Techniques, organic semiconductors can be processed using various low-cost and scalable techniques, including solution processing, printing, and coating. These techniques are compatible with flexible substrates, enabling the production of large-area, lightweight, and flexible electronic devices.

The structural diversity of organic semiconductors plays a pivotal role in advancing the field of optoelectronics and expanding its applications. By leveraging the unique properties of organic materials, researchers and engineers can develop high-performance devices for a wide range of applications, from biological sensors to spectroscopic tools. This versatility, combined with cost-effective fabrication methods, positions organic semiconductors as a transformative technology in modern electronics and beyond.

5.3 Future Prospects

Organic small molecule semiconductors, particularly those based on benzothieno[3,2-b]benzothiophene (BTBT) and indeno[1,2-b]fluorene-6,12-dione (IFDM) cores, are garnering significant attention due to their promising electronic properties and versatility. These materials have potential for various advanced applications, and ongoing research is likely to yield exciting developments. The future prospects and potential applications of BTBT and IFDM-based organic semiconductors crucial due to the enhanced electronic properties such as charge mobility, BTBT and IFDM cores are known for their high charge mobility, making them suitable for high-performance organic field-effect transistors (OFETs). Future research aims to further optimize their molecular structures to enhance charge transport properties. And also their synthesis and scalability properties ensures, advancements in synthetic methods will likely make BTBT and IFDM-based semiconductors more accessible and cost-effective to produce on a large scale. Green synthesis approaches and more efficient reaction pathways will be key areas of development.

It is also important to integrate the research and development of organic semiconductors with today's hot topics. Such as, Internet of Things (IoT), as IoT devices proliferate, BTBT and IFDM-based semiconductors can be used to create low-cost, flexible, and high-performance components that are essential for widespread IoT deployment. Artificial Intelligence (AI),the potential for these materials to be used in neuromorphic computing and other AI-related hardware could open new avenues for organic semiconductors, offering efficient, adaptive, and low-power solutions.

The future prospects for organic small molecule semiconductors based on BTBT and IFDM cores are bright and multifaceted. Continued research and development will likely unlock new applications and improve the performance of existing technologies. These materials offer promising solutions for high-performance electronics, flexible devices, energy harvesting, and sensing applications, positioning them as key components in the next generation of advanced materials and devices.

BIBLIOGRAPHY

[1] S. Guo *et al.*, "Alkoxy substituted [1]benzothieno[3,2-b][1]benzothiophene derivative with improved performance in organic thin film transistors," *Org. Electron.*, vol. 56, no. February, pp. 68–75, May 2018, doi: 10.1016/j.orgel.2018.02.003.

[2] S. Inoue *et al.*, "Effects of Substituted Alkyl Chain Length on Solution-Processable Layered Organic Semiconductor Crystals," *Chem. Mater.*, vol. 27, no. 11, pp. 3809–3812, Jun. 2015, doi: 10.1021/acs.chemmater.5b00810.

[3] Y. Takeda *et al.*, "Fabrication of Ultra-Thin printed organic TFT CMOS logic circuits optimized for low-voltage wearable sensor applications," *Sci. Rep.*, vol. 6, no. March, pp. 1–9, 2016, doi: 10.1038/srep25714.

[4] H. Klauk, "Organic thin-film transistors," *Chem. Soc. Rev.*, vol. 39, no. 7, pp. 2643–2666, 2010, doi: 10.1039/b909902f.

[5] A. Tsumura, H. Koezuka, and T. Ando, "Macromolecular electronic device: Field-effect transistor with a polythiophene thin film," *Appl. Phys. Lett.*, vol. 49, no. 18, pp. 1210–1212, Nov. 1986, doi: 10.1063/1.97417.

[6] A. F. Paterson *et al.*, "Recent Progress in High-Mobility Organic Transistors: A Reality Check," *Adv. Mater.*, vol. 30, no. 36, pp. 1–33, Sep. 2018, doi: 10.1002/adma.201801079.

[7] Y. Galagan *et al.*, "Technology development for roll-to-roll production of organic photovoltaics," *Chem. Eng. Process. Process Intensif.*, vol. 50, no. 5–6, pp. 454–461, 2011, doi: 10.1016/j.cep.2010.07.012.

[8] A. Pron and P. Rannou, "Processible conjugated polymers: From organic semiconductors to organic metals and superconductors," *Prog. Polym. Sci.*, vol. 27, no. 1, pp. 135–190, 2002, doi: 10.1016/S0079-6700(01)00043-0.

[9] G. Horowitz, "Organic Semiconductors for new electronic devices," *Adv. Mater.*, vol. 2, no. 6–7, pp. 287–292, 1990, doi: 10.1002/adma.19900020604.

[10] C. D. Dimitrakopoulos and P. R. L. Malenfant, "Organic thin film transistors for large area electronics," *Adv. Mater.*, vol. 14, no. 2, pp. 99–117, 2002, doi: 10.1002/1521-4095(20020116)14:2<99::AID-ADMA99>3.0.CO;2-9.

[11] A. J. Heeger, "Semiconducting and metallic polymers: The fourth generation of polymeric materials," *Curr. Appl. Phys.*, vol. 1, no. 4–5, pp. 247–267, 2001, doi: 10.1016/S1567-1739(01)00053-0.

[12] A. G. MacDiarmid and A. J. Epstein, "'Synthetic metals': A novel role for organic polymers," *Makromol. Chemie. Macromol. Symp.*, vol. 51, no. 1, pp. 11–28, 1991, doi: 10.1002/masy.19910510104.

[13] S. R. Forrest, “Excitons and the lifetime of organic semiconductor devices,” *Philos. Trans. R. Soc. A Math. Phys. Eng. Sci.*, vol. 373, no. 2044, 2015, doi: 10.1098/rsta.2014.0320.

[14] J. E. Anthony, A. Facchetti, M. Heeney, S. R. Marder, and X. Zhan, “N-Type organic semiconductors in organic electronics,” *Adv. Mater.*, vol. 22, no. 34, pp. 3876–3892, 2010, doi: 10.1002/adma.200903628.

[15] J. E. Anthony, “Functionalized acenes and heteroacenes for organic electronics,” *Chem. Rev.*, vol. 106, no. 12, pp. 5028–5048, 2006, doi: 10.1021/cr050966z.

[16] M. Kus, T. Y. Alic, C. Kirbiyik, C. Baslak, K. Kara, and D. A. Kara, “Synthesis of Nanoparticles,” in *Handbook of Nanomaterials for Industrial Applications*, Elsevier, 2018, pp. 392–429. doi: 10.1016/B978-0-12-813351-4.00025-0.

[17] C. Sutton, C. Risko, and J.-L. Brédas, “Noncovalent Intermolecular Interactions in Organic Electronic Materials: Implications for the Molecular Packing vs Electronic Properties of Acenes,” *Chem. Mater.*, vol. 28, no. 1, pp. 3–16, Jan. 2016, doi: 10.1021/acs.chemmater.5b03266.

[18] R. Paulini, K. Müller, and F. Diederich, “Orthogonal Multipolar Interactions in Structural Chemistry and Biology,” *Angew. Chemie Int. Ed.*, vol. 44, no. 12, pp. 1788–1805, Mar. 2005, doi: 10.1002/anie.200462213.

[19] A. Karshikoff, *Non-Covalent Interactions in Proteins*. PUBLISHED BY IMPERIAL COLLEGE PRESS AND DISTRIBUTED BY WORLD SCIENTIFIC PUBLISHING CO., 2006. doi: 10.1142/p477.

[20] A. Rahim, P. Saha, K. K. Jha, N. Sukumar, and B. K. Sarma, “Reciprocal carbonyl–carbonyl interactions in small molecules and proteins,” *Nat. Commun.*, vol. 8, no. 1, p. 78, Dec. 2017, doi: 10.1038/s41467-017-00081-x.

[21] T. K. Pal and R. Sankararamakrishnan, “Quantum Chemical Investigations on Intraresidue Carbonyl−Carbonyl Contacts in Aspartates of High-Resolution Protein Structures,” *J. Phys. Chem. B*, vol. 114, no. 2, pp. 1038–1049, Jan. 2010, doi: 10.1021/jp909339r.

[22] L. Strekowski and B. Wilson, “Noncovalent interactions with DNA: An overview,” *Mutat. Res. Mol. Mech. Mutagen.*, vol. 623, no. 1–2, pp. 3–13, Oct. 2007, doi: 10.1016/j.mrfmmm.2007.03.008.

[23] R. L. Baldwin, “Weak Interactions in Protein Folding: Hydrophobic Free Energy, van der Waals Interactions, Peptide Hydrogen Bonds, and Peptide Solvation,” in *Protein Folding Handbook*, Weinheim, Germany: Wiley-VCH Verlag GmbH, 2005, pp. 127–162. doi: 10.1002/9783527619498.ch6.

[24] A. A. Virkar, S. Mannsfeld, Z. Bao, and N. Stingelin, “Organic semiconductor growth and morphology considerations for organic thin-film transistors,” *Adv. Mater.*, vol. 22, no. 34, pp. 3857–3875, 2010, doi: 10.1002/adma.200903193.

[25] J. Martín *et al.*, “On the Effect of Confinement on the Structure and Properties of Small-Molecular Organic Semiconductors,” *Adv. Electron. Mater.*, vol. 4, no. 1, p. 1700308, Jan. 2018, doi: 10.1002/aelm.201700308.

[26] N. Stingelin-Stutzmann *et al.*, “Organic thin-film electronics from vitreous solution-processed rubrene hypereutectics,” *Nat. Mater.*, vol. 4, no. 8, pp. 601–606, 2005, doi: 10.1038/nmat1426.

[27] J. C. Yang, J. Mun, S. Y. Kwon, S. Park, Z. Bao, and S. Park, “Electronic Skin: Recent Progress and Future Prospects for Skin-Attachable Devices for Health Monitoring, Robotics, and Prosthetics,” *Adv. Mater.*, vol. 31, no. 48, p. 1904765, Nov. 2019, doi: 10.1002/adma.201904765.

[28] J.-O. Kim *et al.*, “Highly Ordered 3D Microstructure-Based Electronic Skin Capable of Differentiating Pressure, Temperature, and Proximity,” *ACS Appl. Mater. Interfaces*, vol. 11, no. 1, pp. 1503–1511, Jan. 2019, doi: 10.1021/acsami.8b19214.

[29] M. N. Le *et al.*, “Versatile Solution-Processed Organic–Inorganic Hybrid Superlattices for Ultraflexible and Transparent High-Performance Optoelectronic Devices,” *Adv. Funct. Mater.*, vol. 31, no. 29, p. 2103285, Jul. 2021, doi: 10.1002/adfm.202103285.

[30] H. Zhu, E. Shin, A. Liu, D. Ji, Y. Xu, and Y. Noh, “Printable Semiconductors for Backplane TFTs of Flexible OLED Displays,” *Adv. Funct. Mater.*, vol. 30, no. 20, p. 1904588, May 2020, doi: 10.1002/adfm.201904588.

[31] M. Yilmaz *et al.*, “Nanostructured organic semiconductor films for molecular detection with surface-enhanced Raman spectroscopy,” *Nat. Mater.*, vol. 16, pp. 918–924, Sep. 2017, doi: 10.1038/nmat4957.

[32] H. Usta *et al.*, “High Electron Mobility in [1]Benzothieno[3,2-b][1]benzothiophene-Based Field-Effect Transistors: Toward n-Type BTBTs,” *Chem. Mater.*, vol. 31, pp. 5254–5263, Jul. 2019, doi: 10.1021/acs.chemmater.9b01614.

[33] H. Usta and A. Facchetti, “Polymeric and Small-Molecule Semiconductors for Organic Field-Effect Transistors,” in *Large Area and Flexible Electronics*, Weinheim, Germany: Wiley-VCH Verlag GmbH & Co. KGaA, 2015, pp. 1–100. doi: 10.1002/9783527679973.ch1.

[34] K. Takimiya, I. Osaka, T. Mori, and M. Nakano, “Organic Semiconductors Based on [1]Benzothieno[3,2- b][1]benzothiophene Substructure,” *Acc. Chem. Res.*, vol. 47, no. 5, pp. 1493–1502, May 2014, doi: 10.1021/ar400282g.

[35] H. Usta and A. Facchetti, “Organic Semiconductors for Transparent Electronics,” in *Flexible Carbon-based Electronics*, Weinheim, Germany: Wiley-VCH Verlag GmbH & Co. KGaA, 2018, pp. 13–49. doi: 10.1002/9783527804894.ch2.

[36] K. Takimiya, S. Shinamura, I. Osaka, and E. Miyazaki, “Thienoacene-Based

Organic Semiconductors," *Adv. Mater.*, vol. 23, no. 38, pp. 4347–4370, Oct. 2011, doi: 10.1002/adma.201102007.

[37] H. Ebata *et al.*, "Highly Soluble [1]Benzothieno[3,2-b]benzothiophene (BTBT) Derivatives for High-Performance, Solution-Processed Organic Field-Effect Transistors," *J. Am. Chem. Soc.*, vol. 129, pp. 15732–15733, Dec. 2007, doi: 10.1021/ja074841i.

[38] H. Usta *et al.*, "High Electron Mobility in [1]Benzothieno[3,2- b][1]benzothiophene-Based Field-Effect Transistors: Toward n-Type BTBTs," *Chem. Mater.*, vol. 31, no. 14, pp. 5254–5263, Jul. 2019, doi: 10.1021/acs.chemmater.9b01614.

[39] R. Ozdemir *et al.*, "Engineering functionalized low LUMO [1]benzothieno[3,2- b][1]benzothiophenes (BTBTs): unusual molecular and charge transport properties," *J. Mater. Chem. C*, 2020, doi: 10.1039/D0TC02945A.

[40] B. Kosata, V. Kozmik, J. Svoboda, V. Novotná, P. Vanek, and M. Glogarová, "Novel liquid crystals based on [1]benzothieno[3,2- b][1]benzothiophene," *Liq. Cryst.*, vol. 30, pp. 603–610, May 2003, doi: 10.1080/0267829031000097484.

[41] G. Demirel *et al.*, "Molecular engineering of organic semiconductors enables noble metal-comparable SERS enhancement and sensitivity," *Nat. Commun.*, vol. 10, p. 5502, Dec. 2019, doi: 10.1038/s41467-019-13505-7.

[42] Y. Zhang *et al.*, "Intrinsic and Extrinsic Parameters for Controlling the Growth of Organic Single-Crystalline Nanopillars in Photovoltaics," *Nano Lett.*, vol. 14, no. 10, pp. 5547–5554, Oct. 2014, doi: 10.1021/nl501933q.

[43] F. H. Allen, C. A. Baalham, J. P. M. Lommerse, and P. R. Raithby, "Carbonyl–Carbonyl Interactions can be Competitive with Hydrogen Bonds," *Acta Crystallogr. Sect. B Struct. Sci.*, vol. 54, no. 3, pp. 320–329, Jun. 1998, doi: 10.1107/S0108768198001463.

[44] K. B. Muchowska *et al.*, "Reconciling Electrostatic and n→π* Orbital Contributions in Carbonyl Interactions," *Angew. Chemie Int. Ed.*, vol. 59, no. 34, pp. 14602–14608, Aug. 2020, doi: 10.1002/anie.202005739.

[45] R. R. Fayzullin, S. A. Shteingolts, O. A. Lodochnikova, V. L. Mamedova, D. E. Korshin, and V. A. Mamedov, "Intermolecular head-to-head interaction of carbonyl groups in bicyclic hydrogen-bonded synthon based on β-hydroxy ketones," *CrystEngComm*, vol. 21, no. 10, pp. 1587–1599, 2019, doi: 10.1039/C8CE02132E.

[46] Z. Zhang, X. Tao, J. Zhang, Y. Sun, C. Zhang, and B. Li, "Synthesis, crystal growth, and characterization of the orthorhombic BaTeW2O9: a new polymorph of BaTeW2O9," *CrystEngComm*, vol. 15, no. 47, pp. 10197–10204, 2013, doi: 10.1039/c3ce41272e.

[47] M. Yilmaz *et al.*, "Micro-/Nanostructured Highly Crystalline Organic

Semiconductor Films for Surface-Enhanced Raman Spectroscopy Applications," *Adv. Funct. Mater.*, vol. 25, pp. 5669–5676, Sep. 2015, doi: 10.1002/adfm.201502151.

[48] M. Nishio, "The CH/π hydrogen bond in chemistry. Conformation, supramolecules, optical resolution and interactions involving carbohydrates," *Phys. Chem. Chem. Phys.*, vol. 13, no. 31, p. 13873, 2011, doi: 10.1039/c1cp20404a.

[49] G. R. Desiraju, "The C−H···O Hydrogen Bond: Structural Implications and Supramolecular Design," *Acc. Chem. Res.*, vol. 29, no. 9, pp. 441–449, Sep. 1996, doi: 10.1021/ar950135n.

[50] S. Thomas, "The Hydrogen Bond in the Solid State," *Angew. Chemie Int. Ed.*, vol. 41, no. 1, pp. 48–76, 2002.

[51] A. Bondi, "van der Waals Volumes and Radii," *J. Phys. Chem.*, vol. 68, no. 3, pp. 441–451, Mar. 1964, doi: 10.1021/j100785a001.

[52] K. J. Kamer, A. Choudhary, and R. T. Raines, "Intimate Interactions with Carbonyl Groups: Dipole–Dipole or n →π*?," *J. Org. Chem.*, vol. 78, no. 5, pp. 2099–2103, Mar. 2013, doi: 10.1021/jo302265k.

[53] H. Kwon *et al.*, "Comparison of semiconductor growth and charge transport on hydrophobic polymer dielectrics of organic field-effect transistors: Cytop vs. polystyrene," *Org. Electron.*, vol. 77, no. August 2019, p. 105485, Feb. 2020, doi: 10.1016/j.orgel.2019.105485.

[54] D. Nabok, P. Puschnig, and C. Ambrosch-Draxl, "Cohesive and surface energies of π-conjugated organic molecular crystals: A first-principles study," *Phys. Rev. B*, vol. 77, no. 24, p. 245316, Jun. 2008, doi: 10.1103/PhysRevB.77.245316.

[55] S. R. Narayan *et al.*, "Comparative Study of Surface Energies of Native Oxides of Si(100) and Si(111) via Three Liquid Contact Angle Analysis," *MRS Adv.*, vol. 3, no. 57–58, pp. 3379–3390, Nov. 2018, doi: 10.1557/adv.2018.473.

[56] B. Zuo, S. Zhang, C. Niu, H. Zhou, S. Sun, and X. Wang, "Grafting density dominant glass transition of dry polystyrene brushes," *Soft Matter*, vol. 13, no. 13, pp. 2426–2436, 2017, doi: 10.1039/C6SM02790C.

[57] C. Kim, A. Facchetti, and T. J. Marks, "Gate Dielectric Microstructural Control of Pentacene Film Growth Mode and Field-Effect Transistor Performance," *Adv. Mater.*, vol. 19, no. 18, pp. 2561–2566, Sep. 2007, doi: 10.1002/adma.200700101.

[58] S. H. Park *et al.*, "A polymer brush organic interlayer improves the overlying pentacene nanostructure and organic field-effect transistor performance," *J. Mater. Chem.*, vol. 21, no. 39, pp. 15580–15586, 2011, doi: 10.1039/c1jm11607j.

[59] S. Lee, M. Jang, and H. Yang, "Optimized Grafting Density of End-

Functionalized Polymers to Polar Dielectric Surfaces for Solution-Processed Organic Field-Effect Transistors," *ACS Appl. Mater. Interfaces*, vol. 6, no. 22, pp. 20444–20451, Nov. 2014, doi: 10.1021/am506024s.

[60] L. F. Drummy and D. C. Martin, "Thickness-driven orthorhombic to triclinic phase transformation in pentacene thin films," *Adv. Mater.*, vol. 17, no. 7, pp. 903–907, 2005, doi: 10.1002/adma.200400189.

[61] K. H. Ji *et al.*, "Comparative Photocatalytic Ability of Nanocrystal-Carbon Nanotube and -TiO 2 Nanocrystal Hybrid Nanostructures," *J. Phys. Chem. C*, vol. 113, no. 46, pp. 19966–19972, Nov. 2009, doi: 10.1021/jp906476m.

[62] H. Sun *et al.*, "Pressure-induced SERS enhancement in a MoS 2 /Au/R6G system by a two-step charge transfer process," *Nanoscale*, vol. 11, no. 44, pp. 21493–21501, 2019, doi: 10.1039/C9NR07098B.

[63] M. V. Cañamares, C. Chenal, R. L. Birke, and J. R. Lombardi, "DFT, SERS, and Single-Molecule SERS of Crystal Violet," *J. Phys. Chem. C*, vol. 112, no. 51, pp. 20295–20300, Dec. 2008, doi: 10.1021/jp807807j.

[64] Z. Li, M. Smeu, S. Afsari, Y. Xing, M. A. Ratner, and E. Borguet, "Single-Molecule Sensing of Environmental pH-an STM Break Junction and NEGF-DFT Approach," *Angew. Chemie Int. Ed.*, vol. 53, no. 4, pp. 1098–1102, Jan. 2014, doi: 10.1002/anie.201308398.

[65] J. R. Lombardi and R. L. Birke, "A Unified View of Surface-Enhanced Raman Scattering," *Acc. Chem. Res.*, vol. 42, no. 6, pp. 734–742, Jun. 2009, doi: 10.1021/ar800249y.

[66] J. R. Lombardi, "Enhanced by organic surfaces," *Nat. Mater.*, vol. 16, no. 9, pp. 878–880, Sep. 2017, doi: 10.1038/nmat4958.

[67] S. Cong, X. Liu, Y. Jiang, W. Zhang, and Z. Zhao, "Surface Enhanced Raman Scattering Revealed by Interfacial Charge-Transfer Transitions," *Innov.*, vol. 1, no. 3, p. 100051, Nov. 2020, doi: 10.1016/j.xinn.2020.100051.

[68] J. R. Lombardi and R. L. Birke, "Theory of Surface-Enhanced Raman Scattering in Semiconductors," *J. Phys. Chem. C*, vol. 118, no. 20, pp. 11120–11130, May 2014, doi: 10.1021/jp5020675.

[69] J. R. Lombardi, "The theory of surface-enhanced Raman spectroscopy on organic semiconductors: J-aggregates," *Chem. Phys. Lett.*, vol. 751, p. 137553, Jul. 2020, doi: 10.1016/j.cplett.2020.137553.

[70] J. R. Lombardi, "The theory of surface-enhanced Raman scattering on semiconductor nanoparticles; toward the optimization of SERS sensors," *Faraday Discuss.*, vol. 205, pp. 105–120, 2017, doi: 10.1039/C7FD00138J.

[71] Y. Kashimoto *et al.*, "The Evolution of Intermolecular Energy Bands of Occupied and Unoccupied Molecular States in Organic Thin Films," *J. Phys.*

Chem. C, vol. 122, no. 22, pp. 12090–12097, Jun. 2018, doi: 10.1021/acs.jpcc.8b02581.

[72] C. Boerigter, R. Campana, M. Morabito, and S. Linic, "Evidence and implications of direct charge excitation as the dominant mechanism in plasmon-mediated photocatalysis," *Nat. Commun.*, vol. 7, no. 1, p. 10545, Apr. 2016, doi: 10.1038/ncomms10545.

[73] S. Hogiu, W. Werncke, M. Pfeiffer, and T. Elsaesser, "Mode specific vibrational kinetics after intramolecular electron transfer studied by picosecond anti-Stokes Raman spectroscopy," *Chem. Phys. Lett.*, vol. 312, no. 5–6, pp. 407–414, Oct. 1999, doi: 10.1016/S0009-2614(99)00959-8.

[74] R. C. Maher, C. M. Galloway, E. C. Le Ru, L. F. Cohen, and P. G. Etchegoin, "Vibrational pumping in surface enhanced Raman scattering (SERS)," *Chem. Soc. Rev.*, vol. 37, no. 5, p. 965, 2008, doi: 10.1039/b707870f.

[75] K. Kneipp, Y. Wang, H. Kneipp, I. Itzkan, R. R. Dasari, and M. S. Feld, "Population Pumping of Excited Vibrational States by Spontaneous Surface-Enhanced Raman Scattering," *Phys. Rev. Lett.*, vol. 76, no. 14, pp. 2444–2447, Apr. 1996, doi: 10.1103/PhysRevLett.76.2444.

[76] T. L. Haslett, L. Tay, and M. Moskovits, "Can surface-enhanced Raman scattering serve as a channel for strong optical pumping?," *J. Chem. Phys.*, vol. 113, no. 4, pp. 1641–1646, Jul. 2000, doi: 10.1063/1.481952.

[77] M. J. Frisch *et al.*, "Gaussian 09." Gaussian Inc., Wallingford, CT, USA, 2010.

[78] C. Lee, S. Lee, G.-U. Kim, W. Lee, and B. J. Kim, "Recent Advances, Design Guidelines, and Prospects of All-Polymer Solar Cells," *Chem. Rev.*, vol. 119, no. 13, pp. 8028–8086, Jul. 2019, doi: 10.1021/acs.chemrev.9b00044.

[79] O. Ostroverkhova, "Organic Optoelectronic Materials: Mechanisms and Applications," *Chem. Rev.*, vol. 116, no. 22, pp. 13279–13412, Nov. 2016, doi: 10.1021/acs.chemrev.6b00127.

[80] X. Gao and Y. Hu, "Development of n-type organic semiconductors for thin film transistors: A viewpoint of molecular design," *J. Mater. Chem. C*, vol. 2, no. 17, pp. 3099–3117, 2014, doi: 10.1039/c3tc32046d.

[81] S. Moschetto *et al.*, "Interplay between Charge Injection, Electron Transport, and Quantum Efficiency in Ambipolar Trilayer Organic Light-Emitting Transistors," *Adv. Mater. Interfaces*, vol. 9, no. 5, p. 2101926, Feb. 2022, doi: 10.1002/admi.202101926.

[82] H. Usta, A. Facchetti, and T. J. Marks, "n -Channel Semiconductor Materials Design for Organic Complementary Circuits," *Acc. Chem. Res.*, vol. 44, no. 7, pp. 501–510, Jul. 2011, doi: 10.1021/ar200006r.

[83] A. Riaño *et al.*, "The unusual electronic structure of ambipolar dicyanovinyl-

substituted diketopyrrolopyrrole derivatives," *J. Mater. Chem. C*, vol. 2, no. 31, p. 6376, Jul. 2014, doi: 10.1039/C4TC00714J.

[84] Y. Wang *et al.*, "Ladder-type Heteroarenes: Up to 15 Rings with Five Imide Groups," *Angew. Chemie Int. Ed.*, vol. 56, no. 33, pp. 9924–9929, Aug. 2017, doi: 10.1002/anie.201702225.

[85] F. Zhang *et al.*, "Critical Role of Alkyl Chain Branching of Organic Semiconductors in Enabling Solution-Processed N-Channel Organic Thin-Film Transistors with Mobility of up to 3.50 cm 2 V –1 s –1," *J. Am. Chem. Soc.*, vol. 135, no. 6, pp. 2338–2349, Feb. 2013, doi: 10.1021/ja311469y.

[86] Y. Hu *et al.*, "One-pot synthesis of core-expanded naphthalene diimides: Enabling N-substituent modulation for diverse n-type organic materials," *Org. Lett.*, vol. 14, no. 1, pp. 292–295, 2012, doi: 10.1021/ol203059r.

[87] B. A. Jones, A. Facchetti, T. J. Marks, and M. R. Wasielewski, "Cyanonaphthalene Diimide Semiconductors for Air-Stable, Flexible, and Optically Transparent n-Channel Field-Effect Transistors," *Chem. Mater.*, vol. 19, no. 11, pp. 2703–2705, May 2007, doi: 10.1021/cm0704579.

[88] J. Zhang, L. Tan, W. Jiang, W. Hu, and Z. Wang, "N-Alkyl substituted di(perylene bisimides) as air-stable electron transport materials for solution-processible thin-film transistors with enhanced performance," *J. Mater. Chem. C*, vol. 1, no. 19, pp. 3200–3206, 2013, doi: 10.1039/c3tc30156g.

[89] B. A. Jones, M. J. Ahrens, M.-H. Yoon, A. Facchetti, T. J. Marks, and M. R. Wasielewski, "High-Mobility Air-Stable n-Type Semiconductors with Processing Versatility: Dicyanoperylene-3,4:9,10-bis(dicarboximides)," *Angew. Chemie*, vol. 116, no. 46, pp. 6523–6526, Nov. 2004, doi: 10.1002/ange.200461324.

[90] C. Zhang *et al.*, "Two-dimensional π-expanded quinoidal terthiophenes terminated with dicyanomethylenes as n-type semiconductors for high-performance organic thin-film transistors," *J. Am. Chem. Soc.*, vol. 136, no. 46, pp. 16176–16184, 2014, doi: 10.1021/ja510003y.

[91] Q. Wu, R. Li, W. Hong, H. Li, X. Gao, and D. Zhu, "Dicyanomethylene-substituted fused tetrathienoquinoid for high-performance, ambient-stable, solution-processable n-channel organic thin-film transistors.," *Chem. Mater.*, vol. 23, no. 13, pp. 3138–3140, 2011, doi: 10.1021/cm201326c.

[92] A. Velusamy *et al.*, "Thienoisoindigo (TII)-Based Quinoidal Small Molecules for High-Performance n-Type Organic Field Effect Transistors," *Adv. Sci.*, vol. 8, no. 1, p. 2002930, Jan. 2021, doi: 10.1002/advs.202002930.

[93] H. Usta *et al.*, "Design, Synthesis, and Characterization of Ladder-Type Molecules and Polymers. Air-Stable, Solution-Processable n -Channel and Ambipolar Semiconductors for Thin-Film Transistors via Experiment and Theory," *J. Am. Chem. Soc.*, vol. 131, no. 15, pp. 5586–5608, Apr. 2009, doi:

10.1021/ja809555c.

[94] A. Can, A. Facchetti, and H. Usta, “Indenofluorenes for organic optoelectronics: the dance of fused five- and six-membered rings enabling structural versatility,” *J. Mater. Chem. C*, vol. 10, no. 22, pp. 8496–8535, 2022, doi: 10.1039/D2TC00684G.

[95] M. M. Torrent and C. Rovira, “Novel small molecules for organic field-effect transistors: Towards processability and high performancens,” *Chem. Soc. Rev.*, vol. 37, no. 4, pp. 827–838, 2008, doi: 10.1039/b614393h.

[96] S. Ma *et al.*, “n-Type Polymer Semiconductors Based on Dithienylpyrazinediimide,” *ACS Appl. Mater. Interfaces*, vol. 15, no. 1, pp. 1639–1651, Jan. 2023, doi: 10.1021/acsami.2c17969.

[97] I. Burgués-Ceballos *et al.*, “Solubility Based Identification of Green Solvents for Small Molecule Organic Solar Cells,” *Adv. Funct. Mater.*, vol. 24, no. 10, pp. 1449–1457, Mar. 2014, doi: 10.1002/adfm.201301509.

[98] G.-S. Ryu, Z. Chen, H. Usta, Y.-Y. Noh, and A. Facchetti, “Naphthalene diimide-based polymeric semiconductors. Effect of chlorine incorporation and n-channel transistors operating in water,” *MRS Commun.*, vol. 6, no. 01, pp. 47–60, Mar. 2016, doi: 10.1557/mrc.2016.4.

[99] B. J. Jung, N. J. Tremblay, M.-L. Yeh, and H. E. Katz, “Molecular Design and Synthetic Approaches to Electron-Transporting Organic Transistor Semiconductors,” *Chem. Mater.*, vol. 23, no. 3, pp. 568–582, Feb. 2011, doi: 10.1021/cm102296d.

[100] S. E. Root, S. Savagatrup, A. D. Printz, D. Rodriquez, and D. J. Lipomi, “Mechanical Properties of Organic Semiconductors for Stretchable, Highly Flexible, and Mechanically Robust Electronics,” *Chem. Rev.*, vol. 117, no. 9, pp. 6467–6499, May 2017, doi: 10.1021/acs.chemrev.7b00003.

[101] T. Kim *et al.*, “Flexible, highly efficient all-polymer solar cells,” *Nat. Commun.*, vol. 6, no. 1, p. 8547, Dec. 2015, doi: 10.1038/ncomms9547.

[102] J. Lee, S. A. Park, S. U. Ryu, D. Chung, T. Park, and S. Y. Son, “Green-solvent-processable organic semiconductors and future directions for advanced organic electronics,” *J. Mater. Chem. A*, vol. 8, no. 41, pp. 21455–21473, 2020, doi: 10.1039/d0ta07373c.

[103] J. Lee *et al.*, “Efficient, Thermally Stable, and Mechanically Robust All-Polymer Solar Cells Consisting of the Same Benzodithiophene Unit-Based Polymer Acceptor and Donor with High Molecular Compatibility,” *Adv. Energy Mater.*, vol. 11, no. 5, p. 2003367, Feb. 2021, doi: 10.1002/aenm.202003367.

[104] H. Usta, A. Facchetti, and T. J. Marks, “Air-Stable, Solution-Processable n -Channel and Ambipolar Semiconductors for Thin-Film Transistors Based on the Indenofluorenebis(dicyanovinylene) Core,” *J. Am. Chem. Soc.*, vol. 130, no. 27,

pp. 8580–8581, Jul. 2008, doi: 10.1021/ja802266u.

[105] R. Ozdemir *et al.*, "A Solution-Processable Liquid-Crystalline Semiconductor for Low-Temperature-Annealed Air-Stable N-Channel Field-Effect Transistors," *ChemPhysChem*, vol. 18, no. 7, pp. 850–861, Apr. 2017, doi: 10.1002/cphc.201601430.

[106] L. Wang *et al.*, "Impact of Chlorination Patterns of Naphthalenediimide-Based Polymers on Aggregated Structure, Crystallinity, and Device Performance of All-Polymer Solar Cells and Organic Transistors," *ACS Appl. Mater. Interfaces*, vol. 12, no. 50, pp. 56240–56250, Dec. 2020, doi: 10.1021/acsami.0c18351.

[107] F. Campana, C. Kim, A. Marrocchi, and L. Vaccaro, "Green solvent-processed organic electronic devices," *J. Mater. Chem. C*, vol. 8, no. 43, pp. 15027–15047, 2020, doi: 10.1039/D0TC03610B.

[108] D. Ho *et al.*, "Green solvents for organic thin-film transistor processing," *J. Mater. Chem. C*, vol. 8, no. 17, pp. 5786–5794, 2020, doi: 10.1039/D0TC00512F.

[109] T. L. Nguyen *et al.*, "Ethanol-Processable, Highly Crystalline Conjugated Polymers for Eco-Friendly Fabrication of Organic Transistors and Solar Cells," *Macromolecules*, vol. 50, no. 11, pp. 4415–4424, Jun. 2017, doi: 10.1021/acs.macromol.7b00452.

[110] S. Pang *et al.*, "High-efficiency organic solar cells processed from a real green solvent," *Mater. Horizons*, vol. 10, no. 2, pp. 473–482, 2023, doi: 10.1039/D2MH01314B.

[111] D. H. Harris, S. Brixi, B. S. Gelfand, B. H. Lessard, and G. C. Welch, "A N–H functionalized perylene diimide with strong red-light absorption for green solvent processed organic electronics," *J. Mater. Chem. C*, vol. 8, no. 29, pp. 9811–9815, 2020, doi: 10.1039/D0TC02284E.

[112] D. Corzo *et al.*, "High-performing organic electronics using terpene green solvents from renewable feedstocks," *Nat. Energy*, vol. 8, no. 1, pp. 62–73, Dec. 2023, doi: 10.1038/s41560-022-01167-7.

[113] H. Opoku, B. Nketia-Yawson, E. S. Shin, and Y.-Y. Noh, "Controlling organization of conjugated polymer films from binary solvent mixtures for high performance organic field-effect transistors," *Org. Electron.*, vol. 41, pp. 198–204, Feb. 2017, doi: 10.1016/j.orgel.2016.11.004.

[114] H. Opoku, B. Nketia-Yawson, E.-S. Shin, and Y.-Y. Noh, "Organic field-effect transistors processed by an environmentally friendly non-halogenated solvent blend," *J. Mater. Chem. C*, vol. 6, no. 3, pp. 661–667, 2018, doi: 10.1039/C7TC04823H.

[115] Y. Lee *et al.*, "Improving the charge transport performance of solution-processed organic field-effect transistors using green solvent additives," *J. Mater. Chem. C*,

vol. 9, no. 46, pp. 16506–16515, 2021, doi: 10.1039/D1TC03782J.

[116] C. Larsen *et al.*, "A tool for identifying green solvents for printed electronics," *Nat. Commun.*, vol. 12, no. 1, p. 4510, Jul. 2021, doi: 10.1038/s41467-021-24761-x.

[117] J. Rivnay, S. C. B. Mannsfeld, C. E. Miller, A. Salleo, and M. F. Toney, "Quantitative Determination of Organic Semiconductor Microstructure from the Molecular to Device Scale," *Chem. Rev.*, vol. 112, no. 10, pp. 5488–5519, Oct. 2012, doi: 10.1021/cr3001109.

[118] C. Wang, H. Dong, W. Hu, Y. Liu, and D. Zhu, "Semiconducting π-Conjugated Systems in Field-Effect Transistors: A Material Odyssey of Organic Electronics," *Chem. Rev.*, vol. 112, no. 4, pp. 2208–2267, Apr. 2012, doi: 10.1021/cr100380z.

[119] A. F. M. Barton, "Solubility parameters," *Chem. Rev.*, vol. 75, no. 6, pp. 731–753, Dec. 1975, doi: 10.1021/cr60298a003.

[120] J. H. Hildebrand, "A Critique of the Theory of Solubility of Non-Electrolytes.," *Chem. Rev.*, vol. 44, no. 1, pp. 37–45, Feb. 1949, doi: 10.1021/cr60137a003.

[121] C. M. Hansen, *Hansen solubility parameters: A user's handbook: Second edition*. 2007. doi: 10.1201/9781420006834.

[122] Y. Takebayashi *et al.*, "Solubility of N,N ′-Di(1-naphthyl)- N,N ′-diphenyl Benzidine (NPB) in Various Organic Solvents: Measurement and Correlation with the Hansen Solubility Parameter," *Ind. Eng. Chem. Res.*, vol. 54, no. 35, pp. 8801–8808, Sep. 2015, doi: 10.1021/acs.iecr.5b01219.

[123] F. Machui, S. Langner, X. Zhu, S. Abbott, and C. J. Brabec, "Determination of the P3HT:PCBM solubility parameters via a binary solvent gradient method: Impact of solubility on the photovoltaic performance," *Sol. Energy Mater. Sol. Cells*, vol. 100, pp. 138–146, May 2012, doi: 10.1016/j.solmat.2012.01.005.

[124] A. Can, I. Deneme, G. Demirel, and H. Usta, "Solution-Processable Indenofluorenes on Polymer Brush Interlayer: Remarkable N-Channel Field-Effect Transistor Characteristics under Ambient Conditions," *ACS Appl. Mater. Interfaces*, vol. 15, no. 35, pp. 41666–41679, Sep. 2023, doi: 10.1021/acsami.3c07365.

[125] S. Abbott and Y. Hiroshi, "Hansen Solubility Parameters in Practice, (software) Version 5.4.08, 2008–2023, Copyright © 2008/23 Professor Steven Abbott & Dr. Yamamoto Hiroshi (accessed: August 2023)," *Hansen Solubility Parameters in Practice, (software) Version 5.4.08, Copyright © 2008/23 Prof. Steven Abbott & Dr. Yamamoto Hiroshi (accessed: August 2023).*

[126] E. M. Pérez and N. Martín, "π–π interactions in carbon nanostructures," *Chem. Soc. Rev.*, vol. 44, no. 18, pp. 6425–6433, 2015, doi: 10.1039/C5CS00578G.

[127] J. P. Wagner and P. R. Schreiner, "London Dispersion in Molecular Chemistry-

Reconsidering Steric Effects," *Angew. Chemie Int. Ed.*, vol. 54, no. 42, pp. 12274–12296, Oct. 2015, doi: 10.1002/anie.201503476.

[128] R. Ozdemir *et al.*, "Triisopropylsilylethynyl-substituted indenofluorenes: carbonyl versus dicyanovinylene functionalization in one-dimensional molecular crystals and solution-processed n-channel OFETs," *Org. Chem. Front.*, vol. 5, no. 20, pp. 2912–2924, 2018, doi: 10.1039/C8QO00856F.

[129] A. Randová and L. Bartovská, "Group contribution method: Surface tension of linear and branched alkanes," *Fluid Phase Equilib.*, vol. 429, pp. 166–176, Dec. 2016, doi: 10.1016/j.fluid.2016.09.007.

[130] E. Stefanis and C. Panayiotou, "Prediction of Hansen Solubility Parameters with a New Group-Contribution Method," *Int. J. Thermophys.*, vol. 29, no. 2, pp. 568–585, Apr. 2008, doi: 10.1007/s10765-008-0415-z.

[131] X.-Z. Shao, L.-S. Wang, and M.-Y. Li, "Measurement and Correlation of the Solubilities of 2-[(6-Oxido-6 H -dibenz[c,e][1,2]oxaphosphorin-6-yl)methyl]butanedioic Acid in Selected Solvents," *Ind. Eng. Chem. Res.*, vol. 51, no. 13, pp. 5082–5089, Apr. 2012, doi: 10.1021/ie202640z.

[132] Y. Takebayashi, K. Sue, T. Furuya, and S. Yoda, "Solubilities of Organic Semiconductors and Nonsteroidal Anti-inflammatory Drugs in Pure and Mixed Organic Solvents: Measurement and Modeling with Hansen Solubility Parameter," *J. Chem. Eng. Data*, vol. 63, no. 10, pp. 3889–3901, Oct. 2018, doi: 10.1021/acs.jced.8b00536.

[133] G. Scatchard, "Equilibria in Non-electrolyte Solutions in Relation to the Vapor Pressures and Densities of the Components.," *Chem. Rev.*, vol. 8, no. 2, pp. 321–333, Apr. 1931, doi: 10.1021/cr60030a010.

[134] P. W. Atkins and J. De Paula, *Atkins' Physical Chemistry, 8th Ed.* London, England: Oxford University Press, 2006.

[135] F. P. Byrne *et al.*, "Tools and techniques for solvent selection: green solvent selection guides," *Sustain. Chem. Process.*, vol. 4, no. 1, p. 7, Dec. 2016, doi: 10.1186/s40508-016-0051-z.

[136] R. K. Henderson *et al.*, "Expanding GSK's solvent selection guide – embedding sustainability into solvent selection starting at medicinal chemistry," *Green Chem.*, vol. 13, no. 4, p. 854, 2011, doi: 10.1039/c0gc00918k.

[137] C. M. Alder *et al.*, "Updating and further expanding GSK's solvent sustainability guide," *Green Chem.*, vol. 18, no. 13, pp. 3879–3890, 2016, doi: 10.1039/C6GC00611F.

[138] D. Chen, A. Nakahara, D. Wei, D. Nordlund, and T. P. Russell, "P3HT/PCBM Bulk Heterojunction Organic Photovoltaics: Correlating Efficiency and Morphology," *Nano Lett.*, vol. 11, no. 2, pp. 561–567, Feb. 2011, doi: 10.1021/nl103482n.

[139] H. Lee, C. Park, D. H. Sin, J. H. Park, and K. Cho, “Recent Advances in Morphology Optimization for Organic Photovoltaics,” *Adv. Mater.*, vol. 30, no. 1800453, pp. 1–39, Aug. 2018, doi: 10.1002/adma.201800453.

[140] J. Lee *et al.*, “Green-Solvent-Processable, Dopant-Free Hole-Transporting Materials for Robust and Efficient Perovskite Solar Cells,” *J. Am. Chem. Soc.*, vol. 139, no. 35, pp. 12175–12181, Sep. 2017, doi: 10.1021/jacs.7b04949.

[141] F. G. Delolo, E. N. dos Santos, and E. V. Gusevskaya, “Anisole: a further step to sustainable hydroformylation,” *Green Chem.*, vol. 21, no. 5, pp. 1091–1098, 2019, doi: 10.1039/C8GC03750G.

[142] C. S. Slater, M. J. Savelski, D. Hitchcock, and E. J. Cavanagh, “Environmental analysis of the life cycle emissions of 2-methyl tetrahydrofuran solvent manufactured from renewable resources,” *J. Environ. Sci. Heal. Part A*, vol. 51, no. 6, pp. 487–494, May 2016, doi: 10.1080/10934529.2015.1128719.

[143] H. Dong, X. Fu, J. Liu, Z. Wang, and W. Hu, “25th Anniversary Article: Key Points for High-Mobility Organic Field-Effect Transistors,” *Adv. Mater.*, vol. 25, no. 43, pp. 6158–6183, Nov. 2013, doi: 10.1002/adma.201302514.

[144] A. M. Glaudell, J. E. Cochran, S. N. Patel, and M. L. Chabinyc, “Impact of the doping method on conductivity and thermopower in semiconducting polythiophenes,” *Adv. Energy Mater.*, vol. 5, no. 4, 2015, doi: 10.1002/aenm.201401072.

[145] J. Duan *et al.*, “Enhancing the Performance of N-Type Thermoelectric Devices via Tuning the Crystallinity of Small Molecule Semiconductors,” *Adv. Sci.*, vol. 10, no. 3, pp. 1–9, 2023, doi: 10.1002/advs.202204872.

[146] H. Wei *et al.*, “Low-Cost Nucleophilic Organic Bases as n-Dopants for Organic Field-Effect Transistors and Thermoelectric Devices,” *Adv. Funct. Mater.*, vol. 31, no. 30, pp. 1–10, 2021, doi: 10.1002/adfm.202102768.

[147] M. Arvind *et al.*, “Quantitative Analysis of Doping-Induced Polarons and Charge-Transfer Complexes of Poly(3-hexylthiophene) in Solution,” *J. Phys. Chem. B*, vol. 124, no. 35, pp. 7694–7708, 2020, doi: 10.1021/acs.jpcb.0c03517.

[148] C. D. Dong, F. Bauch, Y. Hu, and S. Schumacher, “Charge transfer in superbase n-type doping of PCBM induced by deprotonation,” *Phys. Chem. Chem. Phys.*, vol. 26, no. 5, pp. 4194–4199, 2024, doi: 10.1039/d3cp05105f.

[149] W. Liu *et al.*, “Origin of the π-π Spacing Change upon Doping of Semiconducting Polymers,” *J. Phys. Chem. C*, vol. 122, no. 49, pp. 27983–27990, 2018, doi: 10.1021/acs.jpcc.8b10845.

[150] A. Hamidi-Sakr *et al.*, “A Versatile Method to Fabricate Highly In-Plane Aligned Conducting Polymer Films with Anisotropic Charge Transport and Thermoelectric Properties: The Key Role of Alkyl Side Chain Layers on the Doping Mechanism,” *Adv. Funct. Mater.*, vol. 27, no. 25, pp. 1–13, 2017, doi:

10.1002/adfm.201700173.

[151] S. E. Yoon *et al.*, “Enhancing dopant diffusion for ultrahigh electrical conductivity and efficient thermoelectric conversion in conjugated polymers,” *Joule*, vol. 7, no. 10, pp. 2291–2317, 2023, doi: 10.1016/j.joule.2023.09.002.

[152] K. Takimiya, H. Ebata, K. Sakamoto, T. Izawa, T. Otsubo, and Y. Kunugi, “2,7-Diphenyl[1]benzothieno[3,2-b]benzothiophene, a new organic semiconductor for air-stable organic field-effect transistors with mobilities up to 2.0 cm2 V-1 s-1,” *J. Am. Chem. Soc.*, vol. 128, no. 39, pp. 12604–12605, 2006, doi: 10.1021/ja064052l.

[153] H. Ebata *et al.*, “Highly Soluble [1] Benzothieno [3 , 2-b] benzothiophene (BTBT) Derivatives for,” *J. Am. Chem. Soc.*, vol. 129, no. Table 1, pp. 15732–15733, 2007.

[154] M. A. Khalily *et al.*, “The design and fabrication of supramolecular semiconductor nanowires formed by benzothienobenzothiophene (BTBT)-conjugated peptides,” *Nanoscale*, vol. 10, no. 21, pp. 9987–9995, 2018, doi: 10.1039/C8NR01604F.

[155] A. Y. Amin, A. Khassanov, K. Reuter, T. Meyer-Friedrichsen, and M. Halik, “Low-Voltage Organic Field Effect Transistors with a 2-Tridecyl[1]benzothieno[3,2- b][1]benzothiophene Semiconductor Layer,” *J. Am. Chem. Soc.*, vol. 134, no. 40, pp. 16548–16550, Oct. 2012, doi: 10.1021/ja307802q.

[156] Y. He *et al.*, “High Performance OTFTs Fabricated Using a Calamitic Liquid Crystalline Material of 2-(4-Dodecyl phenyl)[1]benzothieno[3,2- b][1]benzothiophene,” *Adv. Electron. Mater.*, vol. 2, no. 9, p. 1600179, Sep. 2016, doi: 10.1002/aelm.201600179.

[157] Y. He *et al.*, “Molecular phase engineering of organic semiconductors based on a [1]benzothieno[3,2-b][1]benzothiophene core,” *RSC Adv.*, vol. 6, no. 97, pp. 95149–95155, 2016, doi: 10.1039/C6RA22999A.

[158] J. A. Letizia, A. Facchetti, C. L. Stern, M. A. Ratner, and T. J. Marks, “High Electron Mobility in Solution-Cast and Vapor-Deposited Phenacyl−Quaterthiophene-Based Field-Effect Transistors: Toward N-Type Polythiophenes,” *J. Am. Chem. Soc.*, vol. 127, no. 39, pp. 13476–13477, Oct. 2005, doi: 10.1021/ja054276o.

[159] V. Figa *et al.*, “Symmetric naphthalenediimidequaterthiophenes for electropolymerized electrochromic thin films,” *J. Mater. Chem. C*, vol. 3, no. 23, pp. 5985–5994, 2015, doi: 10.1039/C5TC00746A.

[160] V. Figà *et al.*, “Electrochemical polymerization of ambipolar carbonyl-functionalized indenofluorene with memristive properties,” *Opt. Mater. (Amst).*, vol. 94, no. January, pp. 187–195, Aug. 2019, doi: 10.1016/j.optmat.2019.05.017.

[161] M.-H. Yoon, S. A. DiBenedetto, A. Facchetti, and T. J. Marks, “Organic Thin-Film Transistors Based on Carbonyl-Functionalized Quaterthiophenes: High Mobility N-Channel Semiconductors and Ambipolar Transport,” *J. Am. Chem. Soc.*, vol. 127, no. 5, pp. 1348–1349, Feb. 2005, doi: 10.1021/ja045124g.

[162] “Spartan ’24 version 1.0.0 (Wavefunction Inc., 2024, Irvine, CA).”

[163] J.-L. Brédas, D. Beljonne, V. Coropceanu, and J. Cornil, “Charge-Transfer and Energy-Transfer Processes in π-Conjugated Oligomers and Polymers: A Molecular Picture,” *Chem. Rev.*, vol. 104, no. 11, pp. 4971–5004, Nov. 2004, doi: 10.1021/cr040084k.

[164] F. Loffredo *et al.*, “Photosensing Properties of Pentacene OFETs Based on a Novel PMMA Copolymer Gate Dielectric,” *J. Disp. Technol.*, vol. 11, no. 6, pp. 533–540, Jun. 2015, doi: 10.1109/JDT.2014.2363685.

[165] K. Park *et al.*, “Polymer Brush As a Facile Dielectric Surface Treatment for High-Performance, Stable, Soluble Acene-Based Transistors,” *Chem. Mater.*, vol. 22, no. 18, pp. 5377–5382, Sep. 2010, doi: 10.1021/cm1018234.

[166] H. S. Lee *et al.*, “Surface Viscoelasticity of an Organic Interlayer Affects the Crystalline Nanostructure of an Organic Semiconductor and Its Electrical Performance,” *J. Phys. Chem. C*, vol. 116, no. 41, pp. 21673–21678, Oct. 2012, doi: 10.1021/jp305820r.

[167] B. Košata, V. Kozmík, and J. Svoboda, “Reactivity of [1]Benzothieno[3,2-b][1]benzothiophene - Electrophilic and Metallation Reactions,” *Collect. Czechoslov. Chem. Commun.*, vol. 67, no. 5, pp. 645–664, 2002, doi: 10.1135/cccc20020645.

[168] M. M. Payne, S. R. Parkin, J. E. Anthony, C.-C. Kuo, and T. N. Jackson, “Organic Field-Effect Transistors from Solution-Deposited Functionalized Acenes with Mobilities as High as 1 cm2/V·s,” *J. Am. Chem. Soc.*, vol. 127, no. 14, pp. 4986–4987, Apr. 2005, doi: 10.1021/ja042353u.

[169] Y. Yamaguchi *et al.*, “Solution-Processable Organic Semiconductors Featuring S-Shaped Dinaphthothienothiophene (S-DNTT): Effects of Alkyl Chain Length on Self-Organization and Carrier Transport Properties,” *Chem. Mater.*, vol. 32, no. 12, pp. 5350–5360, Jun. 2020, doi: 10.1021/acs.chemmater.0c01740.

[170] M. J. Kang *et al.*, “Alkylated Dinaphtho[2,3-b:2′,3′-f]Thieno[3,2-b]Thiophenes (Cn-DNTTs): Organic Semiconductors for High-Performance Thin-Film Transistors,” *Adv. Mater.*, vol. 23, no. 10, pp. 1222–1225, Mar. 2011, doi: 10.1002/adma.201001283.

[171] P. A. Troshin *et al.*, “Material Solubility-Photovoltaic Performance Relationship in the Design of Novel Fullerene Derivatives for Bulk Heterojunction Solar Cells,” *Adv. Funct. Mater.*, vol. 19, no. 5, pp. 779–788, Mar. 2009, doi: 10.1002/adfm.200801189.

[172] K. Kawabata, S. Usui, and K. Takimiya, “Synthesis of Soluble Dinaphtho[2,3-b :2′,3′- f]thieno[3,2- b]thiophene (DNTT) Derivatives: One-Step Functionalization of 2-Bromo-DNTT,” *J. Org. Chem.*, vol. 85, no. 1, pp. 195–206, Jan. 2020, doi: 10.1021/acs.joc.9b02585.

[173] I. Deneme, T. A. Yıldız, N. Kayaci, and H. Usta, “The Hansen solubility approach towards green solvent processing: n-channel organic field-effect transistors under ambient conditions,” *J. Mater. Chem. C*, 2024, doi: 10.1039/D4TC00324A.

[174] A. Velusamy *et al.*, “Diselenophene-Dithioalkylthiophene Based Quinoidal Small Molecules for Ambipolar Organic Field Effect Transistors,” *Adv. Sci.*, vol. 11, no. 9, pp. 1–12, Mar. 2024, doi: 10.1002/advs.202305361.

[175] G. C. Vebber, P. Pranke, and C. N. Pereira, “Calculating hansen solubility parameters of polymers with genetic algorithms,” *J. Appl. Polym. Sci.*, vol. 131, p. 39696, Jan. 2014, doi: 10.1002/app.39696.

[176] C. M. Hansen, *Hansen Solubility Parameters: A User’s Hand- book*, 2nd edn. Boca Raton, FL: CRC Press, 2007. doi: 10.1201/9781420006834.

[177] F. Zhang *et al.*, “Ultrathin Film Organic Transistors: Precise Control of Semiconductor Thickness via Spin-Coating,” *Adv. Mater.*, vol. 25, no. 10, pp. 1401–1407, Mar. 2013, doi: 10.1002/adma.201204075.

[178] Z. Ma, B. Zhao, Y. Gong, J. Deng, and Z. Tan, “Green-solvent-processable strategies for achieving large-scale manufacture of organic photovoltaics,” *J. Mater. Chem. A*, vol. 7, no. 40, pp. 22826–22847, 2019, doi: 10.1039/C9TA09277C.

[179] J. M. Olsen, K. Aidas, and J. Kongsted, “Excited States in Solution through Polarizable Embedding,” *J. Chem. Theory Comput.*, vol. 6, no. 12, pp. 3721–3734, Dec. 2010, doi: 10.1021/ct1003803.

[180] H.-J. Schneider, “Dispersive Interactions in Solution Complexes,” *Acc. Chem. Res.*, vol. 48, no. 7, pp. 1815–1822, Jul. 2015, doi: 10.1021/acs.accounts.5b00111.

[181] J. H. Kim, T. Schembri, D. Bialas, M. Stolte, and F. Würthner, “Slip-Stacked J-Aggregate Materials for Organic Solar Cells and Photodetectors,” *Adv. Mater.*, vol. 34, no. 22, p. 2104678, Jun. 2022, doi: 10.1002/adma.202104678.

[182] X. Qiu *et al.*, “Novel 9,9-dimethylfluorene-bridged D–π–A-type fluorophores with a hybridized local and charge-transfer excited state for deep-blue electroluminescence with CIE y ∼ 0.05,” *J. Mater. Chem. C*, vol. 7, no. 3, pp. 592–600, 2019, doi: 10.1039/C8TC05469J.

[183] K. Yao, L. Chen, Y. Chen, F. Li, and P. Wang, “Influence of water-soluble polythiophene as an interfacial layer on the P3HT/PCBM bulk heterojunction organic photovoltaics,” *J. Mater. Chem.*, vol. 21, no. 36, pp. 13780–13784, 2011,

doi: 10.1039/c1jm12016f.

[184] K. Alfonsi *et al.*, “Green chemistry tools to influence a medicinal chemistry and research chemistry based organisation,” *Green Chem.*, vol. 10, no. 1, pp. 31–36, 2008, doi: 10.1039/B711717E.

[185] C. Capello, U. Fischer, and K. Hungerbühler, “What is a green solvent? A comprehensive framework for the environmental assessment of solvents,” *Green Chem.*, vol. 9, no. 9, pp. 927–934, 2007, doi: 10.1039/b617536h.

[186] Z. B. Henson, P. Zalar, X. Chen, G. C. Welch, T.-Q. Nguyen, and G. C. Bazan, “Towards environmentally friendly processing of molecular semiconductors,” *J. Mater. Chem. A*, vol. 1, no. 37, pp. 11117–11120, 2013, doi: 10.1039/c3ta12690k.

[187] G. Zhang *et al.*, “Acceptor–donor–acceptor molecule processed using polar non-halogenated solvents for organic field-effect transistors,” *J. Mater. Chem. C*, vol. 8, no. 19, pp. 6496–6502, 2020, doi: 10.1039/C9TC07117B.

[188] S. Yun, A. Marrocchi, L. Vaccaro, and C. Kim, “Effects of solution-shearing process parameters on charge carrier mobility in green solvent-processed organic field-effect transistors,” *Synth. Met.*, vol. 291, no. September, p. 117209, Dec. 2022, doi: 10.1016/j.synthmet.2022.117209.

[189] S. Yun *et al.*, “Brewers’ spent grain (BSG)-based green dielectric materials for low-voltage operating solution-processed organic field-effect transistors,” *J. Mater. Chem. C*, vol. 10, no. 40, pp. 15194–15199, 2022, doi: 10.1039/D2TC02240K.

[190] V. Coropceanu, J. Cornil, D. A. da Silva Filho, Y. Olivier, R. Silbey, and J.-L. Brédas, “Charge Transport in Organic Semiconductors,” *Chem. Rev.*, vol. 107, no. 4, pp. 926–952, Apr. 2007, doi: 10.1021/cr050140x.

[191] Y. Liu *et al.*, “Aggregation and morphology control enables multiple cases of high-efficiency polymer solar cells,” *Nat. Commun.*, vol. 5, no. 1, p. 5293, Nov. 2014, doi: 10.1038/ncomms6293.

[192] S. Izawa *et al.*, “Crystallization and Polymorphism of Organic Semiconductor in Thin Film Induced by Surface Segregated Monolayers,” *Sci. Rep.*, vol. 8, no. 1, p. 481, Dec. 2018, doi: 10.1038/s41598-017-18881-y.

[193] C. P. Yu *et al.*, “Approaching isotropic charge transport of n-type organic semiconductors with bulky substituents,” *Commun. Chem.*, vol. 4, no. 1, p. 155, Dec. 2021, doi: 10.1038/s42004-021-00583-2.

[194] K. Wei Chou *et al.*, “Late stage crystallization and healing during spin-coating enhance carrier transport in small-molecule organic semiconductors,” *J. Mater. Chem. C*, vol. 2, no. 28, pp. 5681–5689, 2014, doi: 10.1039/C4TC00981A.

[195] D. Choi, B. Ahn, S. H. Kim, K. Hong, M. Ree, and C. E. Park, “High-

Performance Triisopropylsilylethynyl Pentacene Transistors via Spin Coating with a Crystallization-Assisting Layer," *ACS Appl. Mater. Interfaces*, vol. 4, no. 1, pp. 117–122, Jan. 2012, doi: 10.1021/am201074n.

[196] H. H. Choi, K. Cho, C. D. Frisbie, H. Sirringhaus, and V. Podzorov, "Critical assessment of charge mobility extraction in FETs," *Nat. Mater.*, vol. 17, no. 1, pp. 2–7, Jan. 2018, doi: 10.1038/nmat5035.

[197] O. Yildiz *et al.*, "Optimized Charge Transport in Molecular Semiconductors by Control of Fluid Dynamics and Crystallization in Meniscus-Guided Coating," *Adv. Funct. Mater.*, vol. 32, no. 2, Jan. 2022, doi: 10.1002/adfm.202107976.

[198] Z. A. Lamport *et al.*, "A simple and robust approach to reducing contact resistance in organic transistors," *Nat. Commun.*, vol. 9, no. 1, p. 5130, Dec. 2018, doi: 10.1038/s41467-018-07388-3.

[199] C. Liu, Y. Xu, and Y.-Y. Noh, "Contact engineering in organic field-effect transistors," *Mater. Today*, vol. 18, no. 2, pp. 79–96, Mar. 2015, doi: 10.1016/j.mattod.2014.08.037.

[200] J. C. S. Costa and L. M. N. B. F. Santos, "Hole Transport Materials Based Thin Films: Topographic Structures and Phase Transition Thermodynamics of Triphenylamine Derivatives," *J. Phys. Chem. C*, vol. 117, no. 21, pp. 10919–10928, May 2013, doi: 10.1021/jp4002274.

[201] H. Ebata *et al.*, "Highly soluble [1]benzothieno[3,2-b]benzothiophene (BTBT) derivatives for high-performance, solution-processed organic field-effect transistors," *J. Am. Chem. Soc.*, vol. 129, no. 51, pp. 15732–15733, 2007, doi: 10.1021/ja074841i.

[202] S. Sanda *et al.*, "Effect of non-chlorinated solvents on the enhancement of field-effect mobility in dioctylbenzothienobenzothiophene-based top-gate organic transistors processed by spin coating," *Org. Electron.*, vol. 69, pp. 181–189, Jun. 2019, doi: 10.1016/j.orgel.2019.02.004.

[203] Y. Yuan *et al.*, "Ultra-high mobility transparent organic thin film transistors grown by an off-centre spin-coating method.," *Nat. Commun.*, vol. 5, p. 3005, 2014, doi: 10.1038/ncomms4005.

[204] Y. He *et al.*, "High Performance OTFTs Fabricated Using a Calamitic Liquid Crystalline Material of 2-(4-Dodecyl phenyl)[1]benzothieno[3,2- b][1]benzothiophene," *Adv. Electron. Mater.*, vol. 2, no. 9, p. 1600179, Sep. 2016, doi: 10.1002/aelm.201600179.

[205] K. He *et al.*, "Asymmetric Conjugated Molecules Based on [1]Benzothieno[3,2-b][1]benzothiophene for High-Mobility Organic Thin-Film Transistors: Influence of Alkyl Chain Length," *ACS Appl. Mater. Interfaces*, vol. 9, no. 40, pp. 35427–35436, Oct. 2017, doi: 10.1021/acsami.7b10675.

[206] G. Schweicher *et al.*, "Bulky End-Capped [1]Benzothieno[3,2- b

]benzothiophenes: Reaching High-Mobility Organic Semiconductors by Fine Tuning of the Crystalline Solid-State Order," *Adv. Mater.*, vol. 27, no. 19, pp. 3066–3072, May 2015, doi: 10.1002/adma.201500322.

[207] M. R. Reddy, H. Kim, C. Kim, and S. Seo, "2-Thiopene[1]benzothieno[3,2- b]benzothiophene derivatives as solution-processable organic semiconductors for organic thin-film transistors," *Synth. Met.*, vol. 235, no. October 2017, pp. 153–159, Jan. 2018, doi: 10.1016/j.synthmet.2017.12.012.

[208] G. H. Roche *et al.*, "The role of H-bonds in the solid state organization of [1]benzothieno[3,2-b][1]benzothiophene (BTBT) structures: bis(hydroxy-hexyl)-BTBT, as a functional derivative offering efficient air stable organic field effect transistors (OFETs)," *J. Mater. Chem. C*, vol. 4, no. 28, pp. 6742–6749, 2016, doi: 10.1039/C6TC01814A.

[209] M. Ullah, R. Wawrzinek, R. C. R. Nagiri, S.-C. Lo, and E. B. Namdas, "UV-Deep Blue-Visible Light-Emitting Organic Field Effect Transistors with High Charge Carrier Mobilities," *Adv. Opt. Mater.*, vol. 5, no. 8, p. 1600973, Apr. 2017, doi: 10.1002/adom.201600973.

[210] H. Iino, T. Usui, and J.-I. Hanna, "Liquid crystals for organic thin-film transistors," *Nat. Commun.*, vol. 6, no. 1, p. 6828, Nov. 2015, doi: 10.1038/ncomms7828.

[211] H. Monobe, L. An, P. Hu, B.-Q. Wang, K.-Q. Zhao, and Y. Shimizu, "Charge transport property of asymmetric Alkyl-BTBT LC semiconductor possessing a fluorophenyl group," *Mol. Cryst. Liq. Cryst.*, vol. 647, no. 1, pp. 119–126, Apr. 2017, doi: 10.1080/15421406.2017.1289443.

[212] X. Lian, J. Chen, Y. Zhang, G. Wu, and H. Chen, "Inverted Perovskite Solar Cells Based on Small Molecular Hole Transport Material C 8 -Dioctylbenzothienobenzothiophene," *Chinese J. Chem.*, vol. 37, no. 12, pp. 1239–1244, Dec. 2019, doi: 10.1002/cjoc.201900317.

[213] C. Zhong, C. Duan, F. Huang, H. Wu, and Y. Cao, "Materials and Devices toward Fully Solution Processable Organic Light-Emitting Diodes †," *Chem. Mater.*, vol. 23, no. 3, pp. 326–340, Feb. 2011, doi: 10.1021/cm101937p.

[214] Z. Xu, B. Z. Tang, Y. Wang, and D. Ma, "Recent advances in high performance blue organic light-emitting diodes based on fluorescence emitters," *J. Mater. Chem. C*, vol. 8, no. 8, pp. 2614–2642, 2020, doi: 10.1039/C9TC06441A.

CURRICULUM VITAE

2008 – 2013	B.Sc., Metallurgical and Materials Engineering, Yildiz Technical University, İstanbul, TURKEY
2016 – 2018	M.Sc., Advanced Materials and Nanotechnology, Abdullah Gül University, Kayseri, TURKEY
2024 – Present	Ph.D. Candidate, Materials Science and Mechanical Engineering, Abdullah Gül University, Kayseri, TURKEY

Selected Publications and Presentations

J1) R. Ozdemir, S. Park, **İ. Deneme**, Y. Park, Y. Zorlu, H. A. Alidağı, K. Harmandar, C. Kim*, H. Usta* "Triisopropylsilylethynyl-Substituted Indenofluorenes: Carbonyl versus Dicyanovinylene Functionalization in One-Dimensional Molecular Crystals and Solution-Processed N-Channel OFETs" *Organic Chemistry Frontiers*, 2018, 5, 2912-2924. (**Selected as the Cover**)

J2) R. Ozdemir, K. Ahn, **İ. Deneme**, Y. Zorlu, D. Kim, M. G. Kim, H. Usta,. "Engineering Functionalized Low LUMO [1] Benzothieno [3, 2-b][1] Benzothiophenes (BTBTs): Unusual Molecular and Charge Transport Properties. " *Journal of Materials Chemistry C*, 2020, 8(43), 15253-15267.

J3) I. Deneme, G. Liman, A. Can, G.Demirel, H. Usta,. "Enabling Three-Dimensional Porous Architectures via Carbonyl Functionalization and Molecular-Specific Organic-SERS Platforms. " *Nature Communications*, 2021, 12(1), 6119.

J4) A. Can, G. S. Choi, R. Ozdemir, S. Park, J. S. Park, Y. Lee, **İ. Deneme,** E. Mutlugun, H. Usta. "Meso-π-Extended/Deficient BODIPYs and Low-Band-Gap Donor–Acceptor Copolymers for Organic Optoelectronics. " *ACS Applied Polymer Materials*, 2022, 4(3), 1991-2005.

J5) A. Can, **I. Deneme**, G. Demirel, H. Usta. "Solution-Processable Indenofluorenes on Polymer Brush Interlayer: Remarkable N-Channel Field-Effect Transistor Characteristics under Ambient Conditions. " *ACS Applied Materials & Interfaces*, 2023, 15(35), 41666-41679. (**Selected as the Cover**)

J6) İ. Deneme, T. A. Yıldız, N. Kayaci, H. Usta,. "Hansen Solubility Approach Towards Green Solvent Processing: N-Channel Organic Field-Effect Transistors in Ambient. " *Journal of Materials Chemistry C*. 2024, 12, 3854-3864 (**Selected as the Cover**)

C1) İ. Deneme, R. Ozdemir, M. Ozdemir, H. Usta "Ambipolar Small Molecular Semiconductors For Field Effect Transistor And Complementary Like Inverter Applications" 3rd International Conference on Material Science and Technology in Cappadocia (IMSTEC), September 2017, Nevşehir, Turkey.

C2) İ. Deneme, H. Usta "BTBT-Organic-SERS Platforms" VIII. International Istanbul Scientific Research Congress on March, 2022, İstanbul (online), Turkey.

C3) İ. Deneme, H. Usta "Solution-Processable Indenofluorenes: N-Channel Field-Effect Transistors" 10thInternational Conference on Materials Science and Nanotechnology For Next Generation (MSNG) September 2023 / TÜRKİYE